Temperature dependence of plant photosynthesis and respiration using the Macromolecular Rate Theory (MMRT)

A thesis

Submitted in fulfilment

of the requirements for the degree

of

Doctor of Philosophy in Biological Sciences

at

The University of Waikato

by

Darwin L. Moreno-Echeverry

2026

Abstract

This thesis quantifies the temperature dependence of key traits that determine leaf carbon balance in C_3 plants, using Sunflower as a model system, with emphasis on the photorespiratory CO_2 compensation point (Γ*), the rate of CO_2 release in the light (D_L), the maximal carboxylation capacity (V_{cmax}), the maximal electron transport capacity (J_{max}), and the components of dark respiration (R_{dark}). The central objective was to identify temperature dependence models for each trait that were both parsimonious and physiologically interpretable.

The research combined controlled leaf gas exchange across wide ranges of temperature and CO_2 with comparative model fitting. I evaluated constant-Q_{10} relationships, simple and peaked Arrhenius formulations, and macro molecular rate theory (MMRT), with and without an explicit high temperature deactivation term. Γ* increased approximately exponentially across the measurement range from 4 to 42 °C, and a constant-Q_{10} model best captured this behaviour. The temperature dependence of D_L was well represented by MMRT. For the photosynthetic capacities, I used an MMRT formulation that used inflection-point temperature (T_{inf}) as parameters and included explicit deactivation terms. That approach captured the curvature at cool to moderate temperatures and the decline at supra-optimal temperatures, with J_{max} exhibiting a cooler inflection and a cooler optimum than V_{cmax}. For R_{dark} and its components, an MMRT anchored at the observed inflection temperature and fitted without a deactivation term captured the smooth warm side curvature expected from progressive changes in mitochondrial coupling and accelerated substrate use with increasing temperature.

This thesis provides a unified framework for selecting temperature dependence models for leaf gas exchange traits. It introduces D_L as the light linked composite flux of CO_2 release, rather than a proxy of dark respiration alone, and it presents a published

refinement for estimating Γ* and D_L using the Laisk method based on gas-exchange measurements at low light and low intercellular CO_2 concentrations. The refined methodology explicitly used photosynthetic theory in our parameter estimation and reduced systematic bias in estimating Γ* and D_L. These advances improve the parameterisation of photosynthesis models and strengthens the transfer to crop and land-surface modelling under variable thermal environments.

The thesis is organised in seven chapters. Chapter 3 has been published, and when it is cited elsewhere in the thesis it is referenced as Moreno-Echeverry *et al*., 2026.

Chapter 1. General introduction. It sets the global climate and carbon cycle context, frames leaf carbon balance as the net outcome of photosynthesis and respiration, and explains why accurate parameterisation of Γ*, D_L, V_{cmax} and J_{max} matters for models. It defines temperature as a primary driver of gas-exchange rates, outlines the limit of Arrhenius and constant-Q_{10} functions, introduces MMRT as a thermodynamic alternative, and states the thesis aims.

Chapter 2. Background. It reviews photosynthesis and respiration at the leaf scale, outlines gas exchange principles, describes the FvCB model and presents methods used to estimate Γ* and D_L. It summarises temperature response models, including the constant-Q_{10} function, two variants of the Arrhenius equation and MMRT. The chapter also identifies the knowledge gaps that motivate the specific work described in the thesis.

Chapter 3. Estimating Γ* and D_L using the Laisk method combined with photosynthetic theory. It examines the classical Laisk approach, identifies sources of bias arising from linearisation of inherently curvilinear A_{net}-C_c responses, and formalises estimation of Γ* and D_L within the FvCB framework. It uses simulations and leaf gas exchange measurements to test performance and uncertainty of the modified approach and compares it with the performance and uncertainty of the original Laisk approach. This chapter is based on the published methodological study.

Chapter 4. Temperature dependence of Γ* and D_L. It quantifies how Γ* and D_L vary with temperature over the range from 4 to 42 °C. It compares the constant-Q_{10}, simple and peaked Arrhenius, and MMRT, with and without explicit high temperature deactivation term. It reports model selection, parameter estimates and presents relevant diagnostics.

Chapter 5. Temperature dependence of V_{cmax} and J_{max}. The chapter derives these parameters from A_{net}-C_i curves. It compares the Arrhenius formulations with MMRT, evaluates curvature, inflection and optimum temperatures, and contrast the thermal responses of carboxylation and electron transport.

Chapter 6. Temperature dependence of the components of leaf CO_2 release in the dark. It separates and analyses the different components of dark respiration, post illumination burst, light enhanced dark respiration and dark respiration in steady-state across temperature and integrates metabolite profiling across the light-dark transition to relate CO_2 fluxes to substrate availability. It tests the Arrhenius and MMRT formulations and identifies the model that best capture warm side curvature without deactivation terms.

Chapter 7. Conclusions and perspectives. It synthesises the finding across chapters, and temperature response models, discusses implications for photosynthesis and respiration modelling, and outlines priorities for future research.

Preface

This thesis represents the culmination of my doctoral research on the temperature dependence of plant photosynthesis and respiration using the Macromolecular Rate Theory. The work was conducted at the Bioeconomy Science Institute, Manaaki Whenua Landcare Research, and at the University of Waikato, New Zealand. My motivation for this research stems from a longstanding interest in understanding plant physiological processes under varying environmental conditions, particularly those influenced by climate change. Collaborative research undertaken at the French National Research Institute for Agriculture, Food and Environment (INRAE) and at the University of Angers, France, contributed valuable experimental data and analysis to the thesis. This document presents the experimental design, data analysis, and modelling approaches used, and discusses their implications for plant ecophysiology. The thesis is organised into chapters covering the theoretical background, experimental methods, results, and a comprehensive discussion of the findings.

This research was funded by the interdisciplinary project (MFP-UOW1904) of New Zealand's Marsden Fund and by the Strategic Science Investment Fund (SSIF) of New Zealand's Ministry of Business, Innovation and Employment.

Statement regarding published work: Chapter 3 of this thesis is based on a peer-reviewed article that has been published. The full citation is:

Moreno-Echeverry, D. L., Kirschbaum, M. U. F., Barbour, M. M., and Liáng, L. L. 2026. Estimating the Photorespiratory CO_2 Compensation Point and CO_2 Release in the Light Using the Laisk Method Combined With Photosynthetic Theory. *Plant, Cell and Environment*, 49: 80-93.

Acknowledgements

I am deeply grateful to my supervisors: Miko Kirschbaum, Lìyǐn Liáng, Margaret Barbour, Vic Arcus, and Louis Schipper. Their constant and high-quality supervision, combined with their expertise, guidance, and encouragement, has been fundamental to the successful completion of my PhD. I feel privileged to have benefited from their unwavering support and commitment throughout every stage of this research.

I am grateful to Professor Guillaume Tcherkez for offering me the opportunity to undertake a research stay at INRAE and at the University of Angers, France. His guidance in sample processing and analysis during my time in France enriched this research. I am also grateful to María Dolores Pérez García for her generous assistance with sample processing throughout the project conducted in France.

My sincere thanks go to Kishor Kumar for constructing the Plant Growth Unit, and to Thilak Palmada, Sujatha Senanayake, Peter Berben, and Ngaire Foster for their logistical assistance with laboratory resources at the Bioeconomy Science Institute – Manaaki Whenua Landcare Research. I am also grateful to Yanfei Zhou from Plant & Food Research for his expertise and help with freeze-drying samples.

I gratefully acknowledge David Whitehead for providing access to the LI-6400XT portable photosynthesis system, which enabled a substantial part of the experimental work presented in this thesis. Special thanks are due to Katharina Siebke from Walz in Germany for her exceptional technical support in operating the GFS-3000 gas exchange analyser.

To my parents, Leonel and Clara, my sister Yessika, and my niece and nephew, Verónica and Sebastián: your unwavering love and support have been the steady foundation of my life. You have witnessed and supported every step of my academic journey, from early aspirations to fulfilling my dream of becoming a research scientist through this PhD. This achievement is shared; it rests on your faith in me and your encouragement in times of triumph and difficulty. My work reflects the values you taught me, and I hope it will continue to contribute meaningfully to science and to the common good.

Symbols and abbreviations

A_c	Rubisco-limited assimilation rate
A_j	RuBP regeneration-limited assimilation rate
A_{net}	Net CO_2 assimilation rate
ATP	Adenosine triphosphate
C_c	Chloroplastic CO_2 partial pressure
C_i	Intercellular CO_2 partial pressure
C_i*	Apparent Γ*
D_L	CO_2 released in the light from processes other than photorespiration
E_a	Activation energy
$E_{a\,(Kc)}$	Activation energy for K_c.
$E_{a\,(Ko)}$	Activation energy for K_o.
FvCB	Farquhar, von Caemmerer, and Berry model
H_d	Deactivation energy
IRGA	Infrared gas analyser
J_{max}	Maximum rate of electron transport
K_a	Michaelis-Menten constant for activation of Rubisco by CO_2 at a given Mg^{2+} concentration and pH
K_c	Michaelis-Menten constant for CO_2
K_o	Michaelis-Menten constant for O_2
LMA	Leaf mass per area
LEDR	Light-enhanced dark respiration
LEDRamp	LEDR amplitude
g_m	Mesophyll conductance
MMRT	Macromolecular Rate Theory

O_2	Partial pressure of oxygen.
P	Atmospheric pressure
PIB	Post-illumination burst
PPFD	Photosynthetic photon flux density
R_{dark}	Leaf dark respiration
RuBP	Ribulose 1,5 biphosphate
ROS	Reactive oxygen species
TCA	Tricarboxylic acid cycle
T_{leaf}	Leaf temperature
T_{opt}	Optimal temperature
T_{inf}	Inflection temperature
V_{cmax}	Maximum rate of carboxylation by Rubisco
^{1}H-NMR	Proton nuclear magnetic resonance
^{13}C-NMR	Carbon 13 nuclear magnetic resonance
α	Quantum yield of electron transport
Γ*	Estimated photorespiratory CO_2 compensation point
Γ^*_{ref}	Reference photorespiratory CO_2 compensation point
Γ^*_{exp}	Expected photorespiratory CO_2 compensation point
θ	Curvature parameter of the electron transport nonrectangular hyperbola
$\Delta G^{‡}$	Activation free energy
$\Delta H^{‡}$	Enthalpy of activation
$\Delta S^{‡}$	Entropy of activation
$\Delta C_p^{‡}$	Change in heat capacity between the ground and transition states
$\Delta H^{‡}_{T0}$	Change in enthalpy at a reference temperature T_0
$\Delta S^{‡}_{T0}$	Change in entropy at a reference temperature T_0
ΔH_{eq}	Deactivation enthalpy change
ΔS	Entropy term of deactivation

Contents

Abstract ..... *ii*

Preface ..... *v*

Acknowledgements ..... *vi*

Symbols and abbreviations ..... *vii*

1 General Introduction *1*

1.1 Global context, climate change and the carbon cycle **1**

1.2 Photosynthesis and respiration in leaf carbon exchange **2**

1.3 Temperature as a primary driver of plant metabolism **3**

1.4 Research importance and objectives **4**

2 Background *5*

2.1 Photosynthesis **5**

2.1.1 Light reactions: organisation and photoprotection 5

2.1.2 Carbon fixation: Rubisco activation, carboxylation and regulation 7

2.1.3 Photorespiration: oxygenation cost and metabolic integration 8

2.1.4 CO_2 supply and diffusional conductances 8

2.2 Respiration **10**

2.2.1 Pathways, compartmentation and flexibility 11

2.2.2 Energy conversion and mitochondrial efficiency 12
2.2.3 Respiration in darkness and in the light 12
2.2.4 Environmental and metabolic control 13
2.3 Gas exchange measurements: principles and equations 13
2.4 The FvCB model 15
2.5 Methods to estimate Γ* and D_L 19
2.5.1 Biochemical estimates of Γ* 19
2.5.2 Gas-exchange methods to estimate Γ* and D_L: Laisk method 20
2.5.3 Kok, Yin and isotopic approaches 21
2.6 The steady versus non steady states of leaf dark respiration 23
2.7 Temperature dependence of biological rates 24
2.7.1 Arrhenius-type formulations: scope and limits 24
2.7.2 Macromolecular Rate Theory (MMRT): a thermodynamic alternative 25
2.8 Knowledge gaps and expected contributions 27
2.8.1 Estimation of Γ* and D_L with the Laisk method. 27
2.8.2 Transient and steady components of dark respiration with distinct temperature dependencies 27
2.8.3 Empirical temperature functions lack mechanistic interpretability 28
3 Estimating Γ* and D_L using the Laisk method combined with photosynthetic theory 29
3.1 Introduction 29
3.2 Materials and Methods 34
3.2.1 Growth Conditions and Experimental Data Collection 34

3.2.2 Definitions of Γ used in this chapter* 34

3.2.3 Estimation of Γ* and D_L Using the Laisk Method 35

3.2.4 Common Considerations in Laisk Analyses: Environmental Dependence of g_m and D_L 36

3.2.5 Simulations for Quantifying the Bias of Laisk Method 39

3.2.6 Simulations of Modelled Intercepts for Linear Regressions and FvCB Model 42

3.2.7 Application of the Photosynthetic Model to Experimental Data 43

3.3 Results 44

3.3.1 Bias in Determining Γ* and D_L Using Linear Regressions from 5 to 40 °C. 44

3.3.2 Sensitivity Analysis of Γ* and D_L Across Different C_c Range from 5 to 40 °C. 48

3.3.3 Estimates of Γ* and D_L from Monte Carlo Simulations Using Linear Regressions and the FvCB Model 50

3.3.4 Estimation of Γ* and D_L Using the FvCB Model and Linear Regressions Applied to Experimental Data 54

3.4 Discussion 55

3.4.1 Methodological Limitation of the Classical Laisk Approach 56

3.4.2 Effects of CO_2 Range and Inclusion of the Expected Γ* 56

3.4.3 Influence of Temperature and Published Discrepancies 57

3.4.4 Uncertainty Analysis via Monte Carlo Simulations 58

3.4.5 Advantages of Integrating the FvCB Model into the Laisk Method 59

3.5 Conclusion 61

4 Temperature dependence of Γ* and D_L 62

4.1 Introduction 62

4.2 Materials and Methods 65

4.2.1 Plant Growth Conditions and Gas Exchange Measurements 65
4.2.2 Determination of Γ* and D_L 65
4.2.3 Temperature-response models for Γ* and D_L 66
4.2.4 Apparent parameters for cross-model comparison (E_a* and Q_{10}*) 68
4.2.5 Arrhenius-coordinate diagnostic 70
4.2.6 Statistical analysis 70
4.3 Results 72
4.4 Discussion 80
4.4.1 Interpreting the temperature dependence of Γ* 80
4.4.2 Interpreting the temperature dependence of D_L 81
4.5 Conclusion 84
5 Temperature dependence of V_{cmax} and J_{max} 85
5.1 Introduction 85
5.2 Materials and Methods 88
5.2.1 Plant Growth Conditions and Gas Exchange Measurements 88
5.2.2 Estimation of V_{cmax} and J_{max} from A–C_i Curves 89
5.2.3 Temperature dependence modelling of V_{cmax} and J_{max} 89
5.2.4 Linearity diagnostic in Arrhenius coordinates 92
5.2.5 Statistical analysis 92
5.3 Results 93
5.4 Discussion 107
5.4.1 Thermodynamic and physiological interpretation 108

5.4.2 Deactivation dynamics at high temperature (Hd, ΔS) and their interpretation 110

5.4.3 From enzyme kinetics to leaf assimilation: a thermodynamic continuum. 111

5.4.4 Model evidence and selection. 112

5.5. Conclusion 113

6 Temperature dependence of the components of leaf CO_2 release in the dark. 114

6.1 Introduction 114

6.2 Materials and Methods 118

6.2.1 Plant Growth Conditions and Gas Exchange Measurements 118

6.2.2 Partitioning of dark respiration components 118

6.2.3 LEDR modelling and area calculation 119

6.2.4 Temperature dependence modelling of R_{dark} and LEDR 121

6.2.5Linearity diagnostic in Arrhenius coordinates 123

6.2.6 Metabolite time courses and sampling 123

6.2.7 Extraction for metabolic analysis 125

6.2.8 NMR analysis 125

6.2.9 Quantification and unit conversion for malate 126

6.2.10 Statistical analysis 126

6.3 Results 128

6.3.1 Thermal responses of the CO_2 flux in the dark 128

6.3.2 Temperature dependence of PIB 128

6.3.3 Temperature dependence of basal respiration R_{dark} 130

6.3.4 Temperature dependence of LEDR 135

6.3.5 Metabolic analysis during PIB and LEDR 147

6.4 Discussion 156

6.4.1 Scope and modelling framework 156

6.4.2 R_{dark}: monotonic warming with warm side curvature 156

6.4.3 LEDR as a light conditioned response 157

6.4.4 PIB: a qualitative window on residual photorespiratory flux 159

6.4.5 Mechanistic integration 160

6.4.6 Metabolic evidence against a single organic acid mechanism in LEDR 161

6.5 Conclusions 163

7 Conclusions and perspectives 164

7.1 Temperature optimum 165

7.2 Guidelines to resolve the metabolic origin of LEDR 166

References 168

Appendix A 213

1 General Introduction

1.1 Global context, climate change and the carbon cycle

Climate change is one of the most pressing environmental challenges of the twenty first century, with direct consequences for biodiversity, ecosystem functioning and global food security (IPCC, 2023). Among the drivers of global warming, the accumulation of atmospheric carbon dioxide (CO_2) plays a central role because it traps outgoing infrared radiation near the surface, strengthening the greenhouse effect (Lacis et al., 2010). Understanding how carbon moves into, out of and within the Earth's reservoirs has therefore become a scientific and political priority, reflected in the annually update Global Carbon Budget and its companion datasets that quantify sources, sinks and associated flux uncertainties (Friedlingstein et al., 2025).

Plants are a central component of the global cycle, acting both as a sink and a source of CO_2 through the coupled processes of photosynthesis and respiration observed across ecosystems (Canadell et al., 2021). Through photosynthesis, leaves capture atmospheric CO_2 and convert it into biomass, temporarily storing carbon (Farquhar et al., 1980). However, this gain is offset by CO_2 release through respiration and photorespiration (Bauwe et al., 2010). The net outcome is a dynamic balance between carbon gain and carbon loss, often called net carbon exchange, that is strongly influenced by environmental factors such as temperature, water and nutrient availability and atmospheric CO_2 (Baldocchi, 2020; Beer et al., 2010).

Accurate quantification of these fluxes is essential for understanding plant physiology and for improving land surface components of climate models (Katavouta et al., 2020; Pastorello et al., 2020). Because the capacity of terrestrial ecosystems to absorb or release

carbon is a key determinant of climate regulation, plants need to be understood both as organisms with measurable metabolic limits and as elements of a connected global network that governs the Earth's biogeochemical balance (Baldocchi, 2014; Pastorello et al., 2020).

1.2 Photosynthesis and respiration in leaf carbon exchange

Photosynthesis and respiration regulate the exchange of carbon between plants and the atmosphere. During photosynthesis, CO_2 is fixed in the chloroplast and, using solar energy, is incorporated into organic compounds through light-driven biochemical reactions (Li et al., 2023). This process underpins plant growth and is the foundation of terrestrial primary productivity (Knauer et al., 2023).

Respiration, in contrast, involves the oxidation of organic substrates to produce ATP for maintenance, biosynthesis and transport, releasing CO_2 back to the atmosphere, and it occurs in darkness and in the light (Ren et al., 2024). The release of CO_2 in the light is critical for leaf carbon balances but is difficult to quantify because it overlaps with CO_2 uptake by photosynthesis and with CO_2 release from photorespiration (Bräutigam & Gowik, 2016; Busch, 2020). Understanding the complex interplay between these processes is essential for accurately modelling net carbon balance at the leaf, plant and ecosystem scales (Sun et al., 2023). However, the precise estimation of these fluxes is constrained by significant methodological limitations (Moreno-Echeverry et al., 2026; Wehr et al., 2016; Yin & Amthor, 2024).

Biochemical models such as that of Farquhar, von Caemmerer and Berry (FvCB) require robust estimates of key parameters, including the maximum carboxylation rate of Rubisco (V_{cmax}), the maximum electron transport rate that supports RuBP regeneration (J_{max}), the photorespiratory CO_2 compensation point (Γ^*) and the rate of CO_2 release in the light (D_L). The accuracy of these parameter estimates directly affects the predictive reliability

of physiological models, and thereby the land-surface components of climate models that use them (Rogers et al., 2017).

1.3 Temperature as a primary driver of plant metabolism

Temperature is a powerful driver of plant metabolism because most reactions are catalysed by enzymes whose activity and structural stability vary with temperature (Arcus et al., 2016). Consequently, both photosynthesis and respiration exhibit non-linear responses to temperature (O'sullivan et al., 2017). For photosynthesis, V_{cmax} and J_{max} show clear temperature dependences, with optima that vary across species, environments and plant physiological status (Cox et al., 2023; Kumarathunge et al., 2019). Similarly, respiration rates increase with temperature, but the sensitivity varies with tissue, development and stress status. At supra optimal temperatures, respiration can decline because of enzyme denaturation, membrane instability and shifts in cellular redox balance (Atkin & Tjoelker, 2003; Smith et al., 2019).

The temperature dependence of plant processes has often been described with empirical models, notably Arrhenius formulations and the constant-Q_{10} approach. These models are simple and useful, but they impose constraints (Atkin & Tjoelker, 2003; Yin, 2021). They tend to assume monotonic rate increases with temperature and cannot account for physiological optima or high temperature declines. These limitations call for the use of frameworks that can represent both the rise and the decline in rates, and that connect to quantities with physical meaning (Arcus & Mulholland, 2025). Such frameworks help to compare processes and treatments in ways that are more than purely descriptive.

The macromolecular rate theory (MMRT) provides a thermodynamically grounded alternative to empirical formulations (Liang et al., 2018). Originating from mechanistic understanding of enzyme functioning, MMRT incorporates the change in the heat capacity between ground and transitions states, $\Delta C_p^{\ddagger}$. This parameter enables MMRT to capture the curvature of temperature reaction rate relationships, including the decline in activity

beyond the thermal optimum (Arcus et al., 2016; Liang et al., 2018). MMRT therefore allows estimation of intrinsic thermal metrics, such as optimum temperature and local temperature sensitivity, which vary with temperature.

1.4 Research importance and objectives

Given the strong influence of temperature on photosynthesis and respiration, understanding their thermal sensitivity has become a research priority in the context of climate change. This knowledge is essential for anticipating the impacts of temperature stress on crop productivity, identifying thermally resilient species and improving predictions of terrestrial carbon balances under future climate scenarios.

Accordingly, this thesis aims to:

- Refine and apply an improved method to obtain more accurate estimates of the photorespiratory CO_2 compensation point and non-photorespiratory CO_2 release in the light, and to quantify their temperature dependencies.
- Evaluate the temperature dependence of V_{cmax}, J_{max}, and the components of dark respiration using thermodynamically grounded models, with an emphasis on MMRT.
- Further explore the dynamics of respiration components during the early dark period using metabolomics, linking observed gas exchange patterns to substrate availability and pathway engagement.

2 Background

2.1 Photosynthesis

Photosynthesis arose in the Archean period and underpins life on Earth by converting solar radiation into chemical energy usable by organisms (Oliver et al., 2025; Sánchez-Baracaldo & Cardona, 2020). In plants, absorbed light drives reduction reactions that conserve energy in the chemical bonds of carbohydrates and other compounds (Leister, 2023). This stored energy is then released in controlled amounts to meet metabolic demand (O'Leary et al., 2019). At the leaf scale, photosynthesis comprises two main sets of reactions: the light reactions, which transduce energy to generate adenosine triphosphate (ATP) and reducing power in the form of NADPH (Leister, 2023), and carbon reduction and fixation reactions of the Calvin cycle, which assimilate carbon into organic molecules (Raines, 2022).

2.1.1 Light reactions: organisation and photoprotection

In the reactions that capture energy, several steps transform light energy into chemical energy (Leister, 2023). Light is absorbed by the antenna pigments of photosystem II, which contains hundreds of chlorophyll a and b molecules (Cao et al., 2018; Stirbet et al., 2020). The excitation energy is transferred to chlorophyll P680 in photosystem II, promoting an electron to a primary electron acceptor, pheophytin (Holzwarth et al., 2006). The electrons removed from P680 are replaced by electrons derived from the splitting of water, which also releases O_2 and protons (Gupta, 2020; H. Li et al., 2024).

From pheophytin, the electron moves to plastoquinone QA, which is bound to the D2 protein, then to plastoquinone QB on the D1 protein (De Causmaecker et al., 2019;

Komenda et al., 2024; Saito et al., 2013). A mobile plastoquinone is then reduced and diffuses within the thylakoid membrane to the cytochrome b6f complex, where it donates the electron (Emrich-Mills et al., 2025; Malone et al., 2021). In linear electron transport, the electron then passes to plastocyanin, which carries it through the lumen to photosystem I (Milrad et al., 2025). There it replaces the electron that is excited from chlorophyll P700 and transferred to ferredoxin (Mondal & Bruce, 2018; Si et al., 2024). Finally, $NADP^+$ is reduced by ferredoxin via ferredoxin-$NADP^+$ reductase (FNR) to form NADPH (Kozuleva et al., 2016; Moreno et al., 2024).

Electron transport is coupled with proton movement from the stroma into the thylakoid lumen, which becomes positively charged and acidified (Davis & Kramer, 2020; Rühle et al., 2024). The resulting electrochemical gradient drives the synthesis of ATP from ADP by ATP synthase, a process known as photophosphorylation (Sekiguchi et al., 2024). The light reactions therefore conserve energy in the form of ATP, while simultaneously generating reducing power in form of NADPH (Leister, 2023; Rühle et al., 2024).

In cyclic electron transport around photosystem I, electrons excited from P700 do not reduce $NADP^+$ but return via plastoquinone to the cytochrome b_6f complex, generating ATP without producing NADPH (Emrich-Mills et al., 2025; Yamori & Shikanai, 2016). Linear transport predominates when stromal $NADP^+$ is available and the Calvin cycle draws down reducing power, producing both ATP and NADPH (Leister, 2023; Strand et al., 2017). By contrast, cyclic transport becomes more prominent when the metabolic demand for ATP exceeds that for NADPH or when photoprotection is required, such as under low CO_2, high light, or other stress conditions (Emrich-Mills et al., 2025).

Because these primary photochemical steps in photosystem II and I occur far faster than subsequent electron transport, which itself proceeds faster than the stromal carbon reduction reactions, excitation can accumulate when the Calvin cycle is limited (Holzwarth et al., 2006). Chloroplasts therefore deploy photoprotective mechanisms, including non-photochemical quenching in the antenna, enhanced cyclic electron transport

to raise proton motive force, rapid repair of photosystem II through D1 turnover, and metabolic shuttles that export reducing equivalents via malate/oxaloacetate valve (Arshad et al., 2022; Malnoë, 2018; Ruban, 2016; Selinski & Scheibe, 2019; Wilson & Ruban, 2020).

2.1.2 Carbon fixation: Rubisco activation, carboxylation and regulation

Ribulose-1,5-bisphosphate carboxylase/oxygenase (Rubisco) is an enzyme that requires activation by light-dependent changes in the chloroplast stroma (Amaral et al., 2024; Portis et al., 2008). Activation involves carbamylation, in which an activator CO_2 binds to a lysine residue in the catalytic site (Amaral et al., 2024; Perdomo et al., 2017). Mg^{2+} then coordinates this carbamate to form the catalytically competent complex (Ishijima et al., 2003). In the activated state, Rubisco binds ribulose-1,5-bisphosphate (RuBP) and catalyses carboxylation to yield two molecules of 3-phosphoglycerate, which feed the Calvin cycle (Prywes et al., 2023).

Rubisco activase is the ATP-dependent chaperone that reopens catalytic sites and removes tight-binding inhibitors, maintaining a high activation state in the light (Waheeda et al., 2023). Its activity responds to the stromal environment like pH alkalinisation, higher Mg^{2+}, redox status and the ADP to ATP ratio (Trinh & Masuda, 2022). Isoforms of Rubisco activase differ in regulatory properties and thermal sensitivity, so temperature shifts alter the balance between Rubisco activation, deactivation and spontaneous inhibitor release (Amaral et al., 2024; Carmo-Silva & Salvucci, 2013). As leaves warm, changes in redox state, nucleotide balance and Mg^{2+} availability modulate both activase function and carbamylation, shaping the fraction of Rubisco that is catalytically competent at any moment (Perdomo et al., 2017; Trinh & Masuda, 2022).

At saturating light, linear electron transport raises the proton motive force and increases stromal pH and Mg^{2+}, conditions that favour Rubisco activase and carbamylation (Trinh & Masuda, 2022). Under fluctuating light or heat, activase may become limiting, increasing the lag between illumination and full carboxylation capacity (Wang, 2024).

Together, these controls mean that the instantaneous carboxylation rate depends not only on Rubisco amount and kinetics but also on its activation state, which is dynamically set by the stromal environment (Amaral et al., 2024).

2.1.3 Photorespiration: oxygenation cost and metabolic integration

Rubisco can also catalyse oxygenation when O_2 competes with CO_2 at the catalytic site (Flamholz et al., 2019; Prywes et al., 2023). In oxygenation, RuBP reacts with O_2 to form one molecule of 3-phosphoglycerate and one molecule of 2-phosphoglycolate (Dellero et al., 2016). The latter is dephosphorylated to glycolate, which enters the peroxisome and then the mitochondria, where glycine is converted to serine with the concomitant release of CO_2 and ammonia (Dellero et al., 2016). This photorespiratory pathway consumes ATP and reducing equivalents. It lowers the net CO_2 assimilation via two routes: RuBP is diverted to oxygenation rather than carboxylation, reducing the substrate available for CO_2 fixation, and part of the previously fixed carbon is released again as CO_2 during photorespiration (Walker et al., 2016).

The ratio of carboxylation to oxygenation depends on substrate concentrations at the catalytic site and on Rubisco's specificity for CO_2 relative to O_2 (Farquhar et al., 1980; Jordan & Ogren, 1984; Oh et al., 2023; Sakata et al., 2024). Low chloroplastic CO_2, or high O_2 concentrations shift the balance towards oxygenation (Busch et al., 2024; Haworth et al., 2022). Because each carboxylation event requires four electrons from the thylakoid chain whereas each CO_2 released by photorespiration is associated with additional electron transport demand, changes in this balance also alter ATP and NADPH requirements downstream (Foyer et al., 2012; Kramer & Evans, 2011; Timm et al., 2024; Walker et al., 2014).

2.1.4 CO_2 supply and diffusional conductances

The instantaneous photosynthetic rate reflects the balance between the supply of CO_2 to the chloroplast and the biochemical demand for CO_2 by the Calvin cycle (Busch et al.,

2024; Elferjani et al., 2021; Song & Zhu, 2024). Supply follows a diffusive pathway from ambient air to the carboxylation site, first across the leaf boundary layer, then through the stomata into the intercellular air spaces, and finally across the mesophyll liquid phase to the chloroplast stroma, crossing the cell wall, plasma membrane, cytosol and the two membranes of the chloroplast envelope (Elferjani et al., 2021; Evans et al., 2009; Evans & Von Caemmerer, 1996; Viveros et al., 2024). The corresponding state variables are the ambient concentration C_a, the intercellular concentration C_i and the chloroplastic concentration C_c at Rubisco (Elferjani et al., 2021; Farquhar, von Caemmerer, et al., 1980; Ubierna et al., 2018). Demand is set by the capacity to regenerate RuBP and to carboxylate it, which is controlled by light-driven electron transport, temperature and activation state of Rubisco and Rubisco activase (Farquhar, von Caemmerer, et al., 1980; Song & Zhu, 2024; Yin & Struik, 2009). Because these controls respond differently to the environment, the operating point where diffusive supply matches biochemical demand shifts across the day and with stress (Busch et al., 2024; Song & Zhu, 2024).

Stomatal conductance determines the gas phase step from the leaf surface to the substomatal cavity, whereas mesophyll conductance governs the liquid phase step from C_i to C_c (Tholen et al., 2012; Vrábl et al., 2009; Yin & Struik, 2009). Together, they define the effective conductance of the leaf for CO_2 uptake (Barbour et al., 2010, 2016; Flexas et al., 2008). By Fick's law, net CO_2 assimilation at steady state equals the flux down the concentration gradient multiplied by conductance (Busch et al., 2024). In practice, the conductance for water vapour is often used to infer the conductance for CO_2 by accounting for the faster diffusivity of water in air, which is about 1.6 times that of CO_2, and by separating the boundary layer component from the stomatal component (Evans & Von Caemmerer, 1996; Song & Zhu, 2024). From the substomatal cavity towards the chloroplast interior, mesophyll conductance reflects several steps: CO_2 dissolves in the liquid phase, is partly converted to bicarbonate by carbonic anhydrase, diffuses through the cell water and then crosses the cell wall, plasma membrane and the two membranes of the chloroplast envelope to reach the stroma (Barbour, 2017; Barbour et al., 2016; Pons et

al., 2009). Anatomical traits such as chloroplast surface area exposed to intercellular air spaces and cell wall thickness influence this pathway, and physiological agents such as aquaporins can modulate it rapidly (Flexas et al., 2012; Sonawane & Cousins, 2019; Tania et al., 2025). Crucially, carbonic anhydrase catalyses rapid interconversion between CO_2 and HCO_3^-, keeping these pools near equilibrium at the chloroplast surface and in the stroma. Without this catalyst, equilibration is too slow for physiological fluxes, constraining mesophyll conductance and Rubisco carboxylation (Badger & Price, 1994; Momayyezi et al., 2020; Tholen & Zhu, 2011).

Supply and demand are commonly separated with an A_{net}-C_c response curve under saturating steady irradiance (Busch et al., 2024). At low CO_2, the curve rises steeply because Rubisco carboxylation is substrate limited while RuBP is effectively saturating. This initial slope reflects carboxylation efficiency and is informative about Rubisco amount, kinetics and activation state (Burnett et al., 2019; Lu et al., 2020; Suganami et al., 2021; Yamori et al., 2006). As CO_2 increases the curve bends toward a plateau where RuBP regeneration limits assimilation. In this regime the thylakoid chain determines the rate by supplying ATP and NADPH to the Calvin cycle (Farquhar, von Caemmerer, et al., 1980; Yin & Struik, 2009). At very high CO_2 and high light a further ceiling can appear when triose phosphate utilisation constrains inorganic phosphate recycling and export (Gregory et al., 2021; McClain et al., 2023; Rogers et al., 2021). Across the curve, rising CO_2 suppresses the competing oxygenation reaction of Rubisco, so net assimilation can continue to increase slightly even when electron transport is near its maximum because photorespiratory loss declines (Zhou et al., 2023).

In many conditions leaves operate near co-limitation by carboxylation and RuBP regeneration, which allows efficient use of both the light reactions and the Calvin cycle (Busch et al., 2024; Song & Zhu, 2024). Environmental drivers shift this operating point, by altering electron transport, stromal conditions for activation and substrate availability (Perdomo et al., 2017; Portis et al., 2008; Waheeda et al., 2023; Yamori et al., 2006).

2.2 Respiration

Respiration oxidises carbohydrate to release energy in a controlled manner that can be conserved as ATP (Ghifari et al., 2023; Tasnim et al., 2021). The process supports biosynthesis, transport, repair and cellular maintenance (van Aken, 2021; Vera-Vives et al., 2024). Because the energy content of glucose is high, the pathway proceeds through many small enzyme-mediated steps that channel energy into conserved intermediates rather than releasing it abruptly (Zhang et al., 2023). The overall design couples substrate oxidation to the creation of a proton motive force across the inner mitochondrial membrane and then uses that gradient to power ATP formation (Chadee et al., 2021; Ghifari et al., 2023; Maldonado et al., 2023). In this way, respiration provides a controlled and adaptable energy supply that can follow cellular demand across changing conditions (O'Leary et al., 2023).

2.2.1 Pathways, compartmentation and flexibility

Carbohydrate enters respiration through glycolysis in the cytosol, where glucose is converted to pyruvate with a small yield of ATP and reduced cofactors (Zheng et al., 2025). Pyruvate is then imported into mitochondria and converted to acetyl-CoA, a step that releases CO_2 and positions the substrate for complete oxidation (Le et al., 2021; O'Leary, 2021). Acetyl-CoA feeds the TCA cycle in the matrix, which generates CO_2 and transfers most of the available free energy of the nicotinamide and flavin pools (Zhang et al., 2023). The reduced cofactors donate electrons to the inner-membrane electron transport chain, where electrons pass through a sequence of carriers to oxygen, generating water. Energy released along the chain is used to pump protons from the matrix to the intermembrane space, establishing the gradient that drives ATP synthase (Ghifari et al., 2023; Kühlbrandt et al., 2025; Maldonado et al., 2023).

Plant mitochondria add flexibility by using noncyclic TCA operation, alternative electron routes and redox shuttles, so they can prioritise ATP yield, precursor supply or redox balance as conditions change (Shameer et al., 2019a; Zheng et al., 2025). Alternative electron routes, including the alternative oxidase pathway (AOX) and external or internal dehydrogenases, allow electrons to bypass energy-conserving steps when redox balance or metabolite export is prioritised over maximum ATP yield (Barreto et al., 2022; McDonald, 2023). Mitochondria also exchange reducing equivalents and metabolites with chloroplasts and peroxisomes through the malate-oxaloacetate shuttle, which exports excess reductant from the chloroplast in the light and helps stabilise the NAD(P)H balance across compartments (Dao et al., 2022; van Aken, 2021; Vera-Vives et al., 2024; Voon et al., 2021).

2.2.2 Energy conversion and mitochondrial efficiency

Most ATP generated by respiration is produced by oxidative phosphorylation when electrons from NADH and $FADH_2$ are transferred to oxygen via the electron transport chain (Ghifari et al., 2023; Kühlbrandt et al., 2025; Vera-Vives et al., 2024). Proton pumping at multiple sites builds an electrochemical gradient, and ATP synthase couples proton return to phosphorylation of ADP (Ghifari et al., 2023; Kühlbrandt et al., 2025). Smaller amounts of ATP arise directly in glycolysis and in the TCA cycle. The effective recovery of energy from glucose is well below the theoretical maximum because part of the free energy is channelled into maintenance cost, ion homeostasis and transport, and a substantial fraction is dissipated as heat (Amthor, 2025; Bathe et al., 2023; G. Li et al., 2021; Xiao et al., 2024).

2.2.3 Respiration in darkness and in the light

Mitochondrial respiration proceeds continuously in both darkness and light, but its apparent contribution to net CO_2 exchange depends on what photosynthesis and photorespiration are doing at the same time (Niu et al., 2025; Vera-Vives et al., 2024). During the day, chloroplast activity changes stromal pH, Mg^{2+} and adenylate balance and

alters the redox state of the cell (Voon et al., 2021; Xiao et al., 2024). These changes feedback to mitochondrial substrate supply and the partitioning of electron flow through the cytochrome pathway and the AOX (McDonald, 2023; Selinski et al., 2018; Shameer et al., 2019a). When lights are switched off, leaves often show a burst of CO_2 release followed by a transient enhancement of dark respiration that may reflect the size and redox state of metabolites pools accumulated in the light (Fan et al., 2024). Subsequently, respiration rates usually decline towards a lower steady level as those pools relax and control shifts to substrate availability and enzyme activation states (Xiao et al., 2024).

2.2.4 Environmental and metabolic control

Leaf respiration is sensitive to temperature, water status, nutrient supply and recent light history (Fan et al., 2024; Li et al., 2025; Needham et al., 2025). Warming accelerates enzyme kinetics within limits but can also increase proton leak and shift the balance of ATP supply and demand (de Souza et al., 2025; Kühlbrandt et al., 2025). Drought and low nitrogen constrain substrate availability and modify the cost of maintenance (Li et al., 2025; Quetin et al., 2024). Prior irradiance sets the starting conditions for the night by building or depleting carbohydrate and organic acid pools and by altering the cellular redox environment (Fan et al., 2024; Shameer et al., 2019a). At the regulatory level, adenylate energy charge, inorganic phosphate availability, matrix pH and redox state coordinate flux through glycolysis, the TCA cycle and the electron transport chain (He et al., 2023; Xiao et al., 2024; Zheng et al., 2025). In high light the chloroplast can overproduce reducing power relative to ATP, and the leaf compensates by exporting reductant through malate shuttles and by increasing cyclic electron flow and mitochondrial engagement (Shameer et al., 2019a; Voon et al., 2021; Xiao et al., 2024). This coordination keeps the ATP and NAD(P)H supply aligned with the work of biosynthesis and repair while limiting the accumulation of damaging reactive intermediates (He et al., 2023; Xiao et al., 2024).

2.3 Gas exchange measurements: principles and equations

Having outlined the processes that consume and generate CO_2 in the leaf, I now describe how these fluxes are measured and calculated. In an open gas exchange system, a flow of gas with known composition enters the leaf chamber, interacts with the leaf and exits with modified mole fraction of CO_2 and H_2O (Heinz Walz GmbH, 2019). The analyser continuously measures the sample and reference signals to obtain inlet and outlet mole fractions for both gases and the molar flow, then converts these values to fluxes per unit leaf area. The CO_2 differential is handled with a time delay that aligns sample and reference signals, whereas H_2O is treated without delay because it varies more slowly in the system (Heinz Walz GmbH, 2019). These definitions provide the differentials used below for transpiration and assimilation.

Transpiration per leaf area is

$$E = \frac{u_e(w_a - w_e)}{LA\ (1 - w_a)}, \tag{2.1}$$

where, u_e is the inlet molar flow, w_a and w_e are the outlet and inlet H_2O mole fractions, and LA is leaf area.

The $(1\text{-}w_a)$ term corrects for dilution by water vapour in open systems. The air to leaf vapour pressure deficit is computed from chamber and intercellular H_2O mole fractions

$$VPD = \frac{w_i - w_a}{1 - \frac{w_i + w_a}{2}}, \tag{2.2}$$

with w_i assumed saturated at leaf temperature

$$w_i = \frac{SVP\ (T_{leaf})}{P_{cuv}} \approx \frac{SVP\left(T_{leaf}\right)}{P_{amb}}. \tag{2.3}$$

These relations provide a closed form for VPD as a function of T_{leaf}, chamber pressure and w_a. Total water vapour conductance follows directly as

$$G_{H_2O} = \frac{E}{VPD}. \quad [mmol\ m^{-2}s^{-1}]. \tag{2.4}$$

Net CO_2 assimilation includes the water vapour dilution correction

$$A = \frac{w_e(c_e - c_o)}{LA} - E\ c_a, \tag{2.5}$$

where c_e and c_0 are inlet and outlet CO_2 mole fractions and c_a is the chamber CO_2 mole fraction. In operational form

$$A = \frac{Flow\ \left(dCO_{2zp} - dCO_{2MP}\right)}{Area} - E\ c_a \quad [\mu mol\ m^{-2}s^{-1}]. \tag{2.6}$$

The second term removes the apparent CO_2 flux caused by dilution with transpired water vapour and is essential for open path calculations. Intercellular CO_2 mole fraction is obtained from Fick's law with the customary water vapour term

$$C_i = \frac{gCO_2 - \frac{E}{2}}{gCO_2 + \frac{E}{2}}\ C_a - \frac{A}{gCO_2 + \frac{E}{2}}, \quad [ppm] \tag{2.7}$$

where gCO_2 is the total conductance for CO_2 from leaf internal airspace to atmosphere. The relation between water and CO_2 conductance is

$$gCO_2 = \frac{G_{H_2O}}{1.56}, \tag{2.8}$$

which uses the ratio of diffusivities of water vapour and CO_2 in air. Substituting G_{H2O} gives a fully operational expression for C_i (Heinz Walz GmbH, 2019).

2.4 The FvCB model

The following section uses the Farquhar, von Caemmerer and Berry model to link measured assimilation to its biochemical drivers. The FvCB model of C_3 photosynthesis is the most widely used for quantifying carbon fixation in terrestrial C_3 plants and consists of three components that together determine the CO_2 exchange at the leaf level (Farquhar et al., 1980): the carboxylation by Rubisco (gross photosynthesis), the oxygenation by Rubisco (photorespiration), and D_L (CO_2 released in the light from processes other than photorespiration) (Ubierna et al., 2019; Tcherkez et al., 2024). While it was traditionally believed that CO_2 release under light conditions was exclusively due to respiratory processes, it is now understood that anabolic pathways also make a significant contribution (Abadie et al., 2024; Tcherkez et al., 2024; Tcherkez & Atkin, 2021). These include the decarboxylation of pyruvate during fatty acid biosynthesis, the conversion of glucose-6-phosphate to ribose-5-phosphate via the pentose phosphate pathway for sucrose production, and the decarboxylation of isocitrate to 2-oxoglutarate (2-OG) during amino acid biosynthesis (Abadie et al., 2024; Tcherkez et al., 2024). Gas exchange methods estimate the total CO_2 release under light conditions and therefore cannot differentiate between the contributions of respiratory processes and other decarboxylation processes, making the use of terms like R_{day} or R_L conceptually misleading. By incorporating these metabolic processes into the definition of D_L, I aim to more accurately capture the full scope of CO_2 released in the light.

Net photosynthesis can be calculated in terms of the rate of Rubisco carboxylation, as:

$$A_{net} = V_c\,(1 - \Gamma^*/C_c) - D_L \tag{2.9}$$

where V_c is the rate of carboxylation, Γ* is the photorespiratory CO_2 compensation point and C_c is the chloroplast CO_2 partial pressure. V_c can be determined as the minimum rate of three possible limiting factors: the Rubisco-limited carboxylation rate (W_c), the

carboxylation rate limited by RuBP (Ribulose 1,5-bisphosphate) regeneration or electron transport rate (W_j), and the carboxylation rate constrained by phosphate availability (W_p). Therefore, at a given chloroplastic CO_2 partial pressure, A_{net} is modelled as the minimum of these three limiting rates (W_c, W_j, W_p) as shown in Equation 2.11 (Kirschbaum & Farquhar, 1984; Ubierna et al., 2019).

$$V_c = \min \{W_c, W_j, W_p\} \tag{2.10}$$

Since W_p was not limiting under our experimental conditions, this term was omitted. Measurements were conducted across a wide range of CO_2 concentrations, extending up to approximately 2000 ppm. However, net assimilation (A_{net}) did not show further increases at the highest CO_2 levels, indicating that triose phosphate utilisation did not impose a limitation under these conditions. Because TPU limitation typically becomes evident at high CO_2 concentrations through a characteristic response of A_{net}, the absence of such behaviour in our measurements suggests that photosynthesis was not limited by W_p. Therefore, W_c was calculated as:

$$W_c = \frac{V'_{cmax} \text{ x } C_c}{C_c + K_m} \tag{2.11}$$

where $V_c'_{max}$ is the apparent maximum carboxylation rate and K_m is the effective Michaelis-Menten constant for CO_2 that also considers competitive inhibition by oxygen. In the calculation of K_m, the partial pressure of oxygen (O_2), the Michaelis-Menten constants for CO_2 (K_c) and for O_2 (K_o) are incorporated as seen in Equation 2.13.

$$K_m = K_c \left(1 + \frac{O_2}{K_o}\right) \tag{2.12}$$

V'_{cmax} is calculated as:

$$V'_{cmax} = \frac{V_{cmax} \times C_c}{C_c + K_a} \tag{2.13}$$

where V_{cmax} is the maximum carboxylation rate, and K_a is the Michaelis-Menten constant for activation of Rubisco by CO_2 at a given Mg^{2+} concentration and pH (Kirschbaum & Farquhar, 1984).

W_j is calculated as:

$$W_j = \frac{J * C_c}{4(C_c + 2\Gamma^*)} \tag{2.14}$$

where J is the potential electron transport rate. I used the factor of 2 here instead of 7/3 by assuming that NADPH reduction, rather than ATP production, is the limiting step in the regeneration of RuBP (Kirschbaum & Farquhar, 1987). The regeneration of one molecule of RuBP requires two molecules of NADPH, each of which requires two electrons.

J is calculated as:

$$J = \frac{(\alpha * I + J_{max}) - \sqrt{(\alpha * I + J_{max})^2 - 4\theta\ (\alpha * I * J_{max})}}{2\theta} \tag{2.15}$$

where J_{max} is the maximum electron transport rate, α is the quantum yield of electron transport, I is the photon flux density of photosynthetically active radiation and θ describes the curvature of the light response of photosynthesis (Buckley & Farquhar, 2004).

However, the transition between these limitations on V_c is not as abrupt as implied by Equation 2.11. The intrinsic nature of enzymatic kinetics and the variability in leaf tissue properties result in a region on the A_{net}-C_c curve where different factors can co-limit the overall rates (Kirschbaum & Farquhar, 1984) as multiple processes simultaneously restrict the current rate of photosynthesis. Consequently, Equation 2.10 was rearranged by introducing an empirical factor (e), which transforms the function into a smooth hyperbola (Equation 2.17).

$$V_c^2 - V_c\ (W_c + W_j + e) + W_c W_j = 0 \tag{2.16}$$

The resulting V_c from Equation 2.18 is then substituted into Equation 2.10. The estimated assimilation rate is thus calculated based on the FvCB model, incorporating modifications proposed by Kirschbaum and Farquhar (1984), and further refinements by Ubierna et al. (2019).

$$V_c = \frac{(W_c + W_j + e) \pm \sqrt{(W_c + W_j + e)^2 - 4(W_c W_j)}}{2} \tag{2.17}$$

2.5 Methods to estimate Γ* and D_L

2.5.1 Biochemical estimates of Γ*

Biochemically, Γ* is defined as the chloroplastic CO_2 partial pressure at which Rubisco carboxylation is exactly balanced by photorespiratory CO_2 release when other decarboxylation processes are excluded, which at steady state implies $V_c = 0.5V_O$. Under these conditions the classical expression is:

$$\Gamma^* = \frac{O}{2\,S_{C/O}} \tag{2.18}$$

where O is the chloroplastic O_2 partial pressure and $S_{c/o}$ is Rubisco's CO_2 over O_2 specificity factor (Farquhar, Von Caemmerer, et al., 1980; Yin et al., 2021). This identity follows from the competitive kinetics of Rubisco for CO_2 and O_2 and from the stoichiometry of one CO_2 released per two oxygenations in the photorespiratory pathway (Farquhar, Von Caemmerer, et al., 1980; Jordan & Ogren, 1984; Laing et al., 1974). Farquhar, von Caemmerer and Berry embedded this definition in the biochemical model of C_3 photosynthesis, and subsequent syntheses retain the same expression for Γ* as a function of O and $S_{c/o}$ (Farquhar, Von Caemmerer, et al., 1980; Yin et al., 2021).

Classically, Γ* is obtained by determining $S_{c/o}$ in vitro with purified Rubisco under controlled gas composition, pH, Mg^{2+} and RuBP, then substituting the measured $S_{c/o}$ together with the target O_2 into equation 2.19. Pivotal experiments established the CO_2 and O_2 competition at Rubisco's active site and developed assays that quantify carboxylase and oxygenase activities, enabling robust estimation of $S_{c/o}$ (Jordan & Ogren, 1984; Laing et al., 1974). Jordan and Ogren showed large interspecific differences in $S_{c/o}$, and documented its strong decline with increasing temperature, while reporting only weak pH effects and little dependence on RuBP within experimental ranges. These findings imply that Γ* increases with warming at fixed O_2 (Jordan & Ogren, 1984). Brooks and Farquhar (1985) linked the temperature dependence of $S_{c/o}$ to leaf-level estimates of Γ*, providing temperature functions that became widely used in modelling studies.

2.5.2 Gas-exchange methods to estimate Γ* and D_L: Laisk method

The Laisk method estimates the photorespiratory CO_2 compensation point (Γ*) and the rate of CO_2 release in the light (D_L), from a group of low CO_2 response curves measured at several sub-saturating irradiances (Farquhar, von Caemmerer, et al., 1980; Laisk, 1977). Net CO_2 assimilation is recorded across a restricted low CO_2 range at each light level, straight lines are fitted to the A_{net}-C_c curves, and these lines intersect at a common point (Laisk, 1977). The x-intercept gives Γ* and the y-intercept yields D_L. Practical descriptions converge on the same operational steps: three or more irradiances, a low CO_2 partial pressure, and regression to the intersection point (Schmiege et al., 2023).

Implementation rests on several explicit assumptions and measurement choices. First, local linearity is assumed in the chosen low-CO_2 window, but the true A_{net}-C_c relation is intrinsically curvilinear under the FvCB biochemistry (Walker & Ort, 2015). Consequently, linear regression must be confined to a CO_2 span to minimise curvature bias, which becomes more pronounced at cooler temperatures. Second, the original method is usually conducted with A_{net}-C_i curves, but finite mesophyll conductance means that C_i is not equal to the chloroplastic CO_2 partial pressure C_c, so using C_i can return an

apparent compensation point and can shift the intersection (Douthe et al., 2011; Ubierna et al., 2018). Third, D_L is assumed not to change with light, but studies report that both light and CO_2 can influence the release of CO_2 under light conditions (Tcherkez et al., 2017).

Two relevant limitations have been identified in this method. The first arises from diffusion and reassimilation. The apparent intersection can be displaced when a fraction of respired or photorespired CO_2 is reassimilated, and when the location of mitochondrial sources relative to chloroplast alters the effective path length for CO_2 (Berghuijs et al., 2019; Gong et al., 2018). Reaction-diffusion analyses show how reassimilation and mesophyll resistance modulate the estimates obtained from classical Lasik protocols and provide ways to interpret or correct these effects (Gong et al., 2018). The second relates to protocol domain, very low CO_2 or large light steps can shift C_c and can change the oxygenation to carboxylation ratio, while cooler temperatures accentuate curvature and can move the intersection (Walker & Ort, 2015). However, linearity and the selection of the CO_2 range are also pivotal considerations for evaluating and improving the Laisk method.

2.5.3 Kok, Yin and isotopic approaches

The Kok method estimates the CO_2 released under illuminated conditions by exploiting the change in the slope of the net photosynthesis versus irradiance curve close to the light compensation point ('Kok effect") (Tcherkez et al., 2017; Yin et al., 2020). The classical interpretation is that the break in slope reflects light-induced inhibition of mitochondrial respiration, such that extrapolation of the low-light linear portion to zero irradiance provides an estimate of D_L. The approach is simple and uses only gas exchange, but it is sensitive to the assumption of a constant quantum yield and to a stable chloroplastic CO_2 concentration (C_c) during the light steps (Gauthier et al., 2020; Yin et al., 2011). Recent analyses show that part of the Kok effect can be explained by changes in C_c and by

increasing contribution of photorespiration with irradiance, which biases D_L estimates if unaccounted for (Buckley et al., 2017; Farquhar & Busch, 2017).

On the other hand, the Yin method combines gas exchange with chlorophyll fluorescence to partition electron transport and explicitly account for photorespiratory effects, thereby estimating D_L without relying on the Kok break (Tcherkez et al., 2017; Yin et al., 2011). Operationally, it uses the electron transport yield (J) derived from fluorescence to constrain RuBP regeneration and then derives D_L from a linearised form of the photosynthesis model under defined light conditions (Yin et al., 2011; Yin & Amthor, 2024). Across species and conditions, Yin-method estimates tend to be higher than Kok-based estimates and are often comparable to values from carefully implemented Laisk-type protocols (Schmiege et al., 2023; Sun et al., 2023). Methodological reviews and recent evaluations indicate that Yin-base D_L estimates are typically about 20 percent higher than Kok, consistent with the view that the Kok approach underestimate D_L when photorespiration and chloroplastic CO_2 vary across the light steps (Yin & Amthor, 2024).

A mechanistic re-analysis using the mathematical description of photosynthesis proposes that much of the Kok effect arises from changes in C_c rather than a direct inhibition of mitochondrial processes (Farquhar & Busch, 2017; Yin et al., 2020). Under this view, variation in Γ^*/C_c with irradiance alters the apparent quantum yield at very low light, producing a slope change even if mitochondrial respiration is not strongly inhibited (Buckley et al., 2017; Farquhar & Busch, 2017). This interpretation helps explain why Kok-base D_L estimates depend on the photorespiratory regime, measurement CO_2 and leaf temperature, and why approaches that constrain C_c or partition electron transport reduce bias (Yin et al., 2020; Yin & Amthor, 2024).

Isotopic methods estimate D_L by exploiting the ^{13}C signal of the leaf CO_2 efflux and its disequilibrium with leaf organic matter (Ghashghaie & Badeck, 2014; C. Y. Xu et al., 2004). In the isotopic disequilibrium approach, D_L is derived from the constrain ^{13}C signatures of metabolically produced CO_2 versus CO_2 near the exchange surfaces, thereby

avoiding very low irradiance or low CO_2 during measurement (Gong et al., 2018; Sun et al., 2023). Applications have shown that isotopic disequilibrium often yields higher D_L than the Kok method and can track responses to irradiance and CO_2 without requiring a Kok break (Gong et al., 2018; Yin & Amthor, 2024). Labelling and natural-abundance studies further indicate that multiple carbon sources contribute to CO_2 release in the light and that leaf-respirated CO_2 can be ^{13}C-enriched relative to bulk leaf carbon, consistent with a composite efflux interacting with photosynthesis (Tcherkez & Atkin, 2021; C. Y. Xu et al., 2004). Methodological critiques emphasise the need for rigorous isotope mass balance, characterisation of internal CO_2 pools, and accounting for back-diffusion and reassimilation (Gong et al., 2018; Ubierna et al., 2022).

In practice, the Kok method is attractive for its simplicity but is susceptible to bias when the quantum yield changes or when C_c varies near the light-compensation point (Farquhar & Busch, 2017; Gauthier et al., 2020; Yin et al., 2011). The Yin method reduces these issues by using fluorescence-derived electron transport to constrain calculation and generally yields larger and more stable D_L estimates across conditions (Schmiege et al., 2023; Yin et al., 2011; Yin & Amthor, 2024). Isotopic approaches provide an independent line of evidence that D_L varies with light and CO_2, and they help separate metabolic versus diffusive components of CO_2 release in the light, although they require specialised instrumentation and rigours isotope mass balance (Gong et al., 2018; Sun et al., 2023; Tcherkez & Atkin, 2021; Ubierna et al., 2022; C. Y. Xu et al., 2004).

2.6 The steady versus non steady states of leaf dark respiration

When lights are switched off, leaf CO_2 efflux passes through a non-steady state and then approaches a steady-state rate (Bruhn et al., 2025; Griffin & Turnbull, 2012). Across the early transient phase, processes primed during illumination are released as photochemistry ceases (Atkin et al., 1998; Lehmann et al., 2016). Two features dominate this window. First, the post-illumination burst (PIB) is a brief spike linked to rapid rebalancing of electron acceptors and carriers, together with the sudden drop in chloroplastic CO_2

refixation, which allows a short surge of CO_2 to escape, consistent with a photorespiratory origin (Vines et al., 1983; Walker & Cousins, 2013). Second, the light enhanced dark respiration (LEDR) is a slower relaxation driven by oxidation and redistribution of metabolites that accumulated in the light (Barbour et al., 2007; Reddy et al., 1991). During this relaxation, pools of photorespiratory intermediates, organic acids and carbohydrates decline toward new dark equilibria, while the adenylate energy state, inorganic phosphate availability and cellular redox poise adjust to the loss of light-driven ATP and NADPH supply (Noctor & Foyer, 2000; Shameer et al., 2019b). As these pools and control variables stabilise, the system settles into a steady state in which the mitochondrial network supplies ATP at a quasi-constant rate set by substrate delivery, enzyme activation and proton leak (Fan et al., 2024; Scafaro et al., 2021).

Measurements taken during the non-steady interval therefore merge transient decarboxylation with the sustained respiratory baseline (Reddy et al., 1991; Vines et al., 1983). For thermal analyses, this distinction is critical, because the non-steady phase shortens and changes shape with temperature, and its inclusion can steepen or flatten apparent temperature responses in ways that do not represent the intrinsic steady-state behaviour of dark respiration (Bruhn et al., 2025). Accordingly, measurements made during LEDR overestimate the steady-state dark respiration rate, because LEDR is an excess above the dark baseline.

Metabolite dynamics underlie the transition between phases and determine how long dark acclimation must be before steady state is reached (Atkin & Tjoelker, 2003; Noctor & Foyer, 2000). In the light, operation of the Calvin cycle and photorespiration builds glycine and serine pools and elevates turnover of the glycine-decarboxylase complex, which releases CO_2 and ammonia (Rosa-Téllez et al., 2024; Tcherkez et al., 2017). Organic acids such as malate and fumarate accumulate through the malate-oxaloacetate shuttle that exports reducing equivalents from chloroplast, and TCA cycle intermediates shift to support biosynthesis (Dao et al., 2022; Selinski & Scheibe, 2019; Xiao et al., 2024). Sucrose and starch metabolism sets the supply of hexose phosphates that feed

glycolysis at lights-off (Stitt & Zeeman, 2012). Once illumination ceases, oxidation of these pools and reconfiguration of pathway engagement cause the LEDR (Barbour et al., 2007; Reddy et al., 1991). The relative use of the cytochrome pathway and the alternative oxidase (AOX) shapes the efficiency and heat dissipation of this recovery (Chadee et al., 2021; McDonald, 2023). Because pool sizes an enzyme activities are temperature-dependent, the magnitude and duration of the non-steady phase change with leaf temperature and recent light history (Atkin & Tjoelker, 2003; Fan et al., 2024).

2.7 Temperature dependence of biological rates

2.7.1 Arrhenius-type formulations: scope and limits

Temperature is a first-order driver of metabolic rate because enzyme-catalysed reactions accelerate as thermal energy lowers the effective barrier to the transition state (Arcus et al., 2016; Arcus & Mulholland, 2025; Arroyo et al., 2022). For more than a century, Arrhenius-type formulations have described an approximately exponential rise over moderate temperatures, but they are empirical and often deviate on the warm side (Arrhenius, 1889; Medlyn et al., 2002; van't Hoff, 1884). In leaf physiology, Arrhenius models have been widely applied to dark respiration and the biochemical parameters of photosynthesis, V_{cmax} and J_{max} (Atkin & Tjoelker, 2003; Kumarathunge et al., 2019; Medlyn et al., 2002). In practice, Arrhenius fits are often adequate around moderate temperatures but become less accurate near the warm side where the temperature dependence of many enzymatic and membrane-associated processes deviate from simple exponential behaviour (Carter et al., 2025; Smith & Keenan, 2020). The peaked Arrhenius variant equations partly accommodates this by allowing a decline beyond an optimum temperature, but it remains empirical and does not directly expose the underlying thermodynamic quantities that control curvature and sensitivity (Medlyn et al., 2002).

2.7.2 Macromolecular Rate Theory (MMRT): a thermodynamic alternative

MMRT extends transition-state theory to enzymes by allowing the heat capacity of activation to vary with temperature. This single addition yields a mechanistic explanation for the characteristic concave-down curvature of many biological rate-temperature curves and provides parameters that allow a physical interpretation (Arcus et al., 2016; Liang et al., 2018). In MMRT, the key descriptors are:

- The optimum temperature (T_{opt}), where the rate would reach a theoretical maximum.
- The inflection temperature (T_{inf}), where temperature sensitivity is greatest; and
- The change in activation heat capacity ($\Delta C_p^{\ddagger}$), typically negative for enzymes, which sets the degree of warm-side deceleration.

These descriptors link curvature to enzyme thermodynamics rather than fitting an empirical peak. Because $\Delta C_p^{\ddagger}$ governs how the activation enthalpy and entropy evolve with temperature, MMRT naturally predicts progressively smaller marginal gains in rates as leaf temperature increases. This can account for the observed departures from exponential behaviour in both mitochondrial respiration and photosynthetic processes (Arcus & Mulholland, 2025; Liang et al., 2018). This thermodynamic framing is useful when comparing treatments, species or organs because it links curvature in the temperature response directly to enzyme level properties rather than relying on purely empirical peaks.

At the leaf scale, MMRT has been applied successfully to dark respiration, often capturing a conserved shape up to moderate temperatures and explaining the common deceleration at higher temperatures without assuming generalised protein denaturation at unrealistically low limits (Liang et al., 2018; M. Xu et al., 2021). For photosynthesis, V_{cmax} and J_{max} show distinct temperature responses: V_{cmax} is largely governed by Rubisco catalysis and activation state, whereas J_{max} reflects the performance of thylakoid electron

transport (Cheah & Teh, 2020; Crous et al., 2022). Empirically, J_{max} tends to exhibit a lower warm-side tolerance than V_{cmax}, consistent with the greater thermal sensitivity of membrane-embedded electron transfer steps and associated coupling processes (Carter et al., 2025; Medlyn et al., 2002; Smith & Keenan, 2020). MMRT accommodates these differences by allowing process specific $\Delta C_p^{\ddagger}$ values and thereby different T_{opt} and T_{inf}, offering a unified language to compare carboxylation and electron transport limitations across species and environments (Arcus & Mulholland, 2025; Liang et al., 2018).

Both respiration and photosynthetic capacities acclimate to growth temperature, shifting T_{opt} and altering apparent temperature sensitivity over days to weeks (Atkin & Tjoelker, 2003; Kumarathunge et al., 2019; Zhu et al., 2021). Across species and climates, substantial variability is observed in the shapes of the A_{net}-T, V_{cmax}-T and J_{max}-T curves, reflecting genetic differences, biochemical regulation and membrane properties. It is therefore advantageous to have a thermodynamic parametrisation that remains interpretable across these contexts. By providing $\Delta C_p^{\ddagger}$, T_{opt} and T_{inf}, MMRT enables direct comparisons across traits and across species, and often outperforms empirical Arrhenius-type fits when projecting responses to warming or when harmonising datasets for model validation. These matter for land-surface and terrestrial biosphere models, in which leaf level temperature responses of photosynthesis and respiration propagate to canopy carbon balance and climate feedback estimates (Oliver et al., 2022).

2.8 Knowledge gaps and expected contributions

2.8.1 Estimation of Γ* and D_L with the Laisk method.

There is no agreed, physiologically consistent procedure for estimating Γ* and D_L that explicitly accounts for the intrinsic curvature of the A_{net}-C_c relationship and the influence of the chosen CO_2 bracket in Laisk-type protocols. Many studies still assume local linearity over a too broad CO_2 window, particularly at low temperature, which introduces systematic bias and can produce physiologically implausible estimates.

Addressing the lack of a physiologically consistent Laisk procedure, this thesis offers a photosynthetic theory-grounded reanalysis in the A_{net}-C_c domain that avoids linearisation, uses temperature-aware CO_2 ranges, to yield accurate and physiologically plausible estimates of Γ* and D_L, comparable across temperatures.

2.8.2 Transient and steady components of dark respiration with distinct temperature dependencies

The literature lacks an operational and consistent awareness that, after lights off, leaf CO_2 flux comprises components with different identities and time scales. PIB and LEDR constitute a non-steady phase that precedes the dark steady state, and each displays its own magnitude, duration, and temperature dependence. Although studies describe PIB or LEDR in isolation, in methodological practice dark respiration is still treated as a single entity, so these transient signals are often not reported separately from the dark steady state. This introduces bias in thermal inference, because temperature metrics calculated in time windows that include PIB or LEDR reflect oxidation of pools and repartitioning of fluxes after light, not the intrinsic behaviour of the dark steady state.

This conceptual gap directly affects how the thermal sensitivities of dark respiration are estimated and compared. If PIB, LEDR, and the R_{dark} are not distinguished explicitly, R_{dark} is overestimated, and metrics such as constant-Q_{10}, Arrhenius activation energy, or MMRT descriptors are distorted, since the non-steady phase shortens or lengthens with temperature and changes shape with recent light history. Consequently, datasets that do not separate these phases confound temperature responses of transient processes driven by light-built pools with the thermodynamic properties of the mitochondrial steady state. Recognising and reporting explicitly the PIB, LEDR and R_{dark}, with their temporal and thermal metrics, is therefore essential for interpreting dark respiration comparably across treatments and studies. In this thesis, the expected contribution is a component resolved characterisation of PIB, LEDR and the R_{dark} across temperatures, reporting their distinct

temporal and thermodynamic descriptors so that comparisons target the intended physiological state.

2.8.3 Empirical temperature functions lack mechanistic interpretability

Across the literature, temperature responses of leaf gas exchange traits such as V_{cmax}, J_{max}, A_{net}, D_L and R_{dark} are most often summarised with empirical functions including Q_{10} and Arrhenius or peaked Arrhenius formulations. These representations are convenient and often fit a limited temperature range, but they do not provide mechanistic parameters, and their warm side behaviour is sensitive to the chosen fitting window. As a result, the same dataset can yield different apparent sensitivities depending on range and scaling, and cross study comparisons become difficult to interpret beyond the immediate empirical fit.

It is important to generate a thermodynamic characterisation that connects the shape of the temperature response to physical quantities of the catalytic system. Macromolecular Rate Theory supplies that link by allowing the heat capacity of activation to vary with temperature, yielding $\Delta C_P^{\ddagger}$, T_{opt}, and T_{inf}, together with local sensitivities at a reference temperature. These descriptors are process interpretable, stable to extrapolation within biological limits, and support comparisons across traits, treatments and species. Framing leaf gas exchange traits within MMRT therefore complements empirical summaries with mechanistic insight, improving inference under warming and enabling harmonisation of datasets for model evaluation.

3 Estimating Γ* and D_L using the Laisk method combined with photosynthetic theory

3.1 Introduction

Plants assimilate carbon from the atmosphere through photosynthesis. This physiological process can be described using mathematical models, among which the model developed by Farquhar, von Caemmerer, and Berry (FvCB model) in 1980 is the most widely used for understanding and quantifying carbon fixation in terrestrial C_3 plants (Farquhar et al., 1980; Walker & Ort, 2015; Herrmann et al., 2020; Machino et al., 2021). The FvCB model includes key biochemical parameters that are essential for predicting plant responses to environmental changes (Farquhar et al., 1980; Ubierna et al., 2019) and plays a crucial role in assessing carbon balances from individual leaves to global ecosystems (Kitao et al., 2021; Sun et al., 2014; Walker et al., 2017). Within the FvCB model, two important parameters are the photorespiratory CO_2 compensation point (Γ*) and the rate of decarboxylation in the light (D_L), also known as the rate of light respiration (R_L) or day respiration (R_{day}) (Berghuijs et al., 2019; Gong et al., 2018; Schmiege et al., 2023; Walker & Cousins, 2013). Here, I refer to D_L as the total CO_2 release under light to capture the CO_2 contributions of respiratory processes and decarboxylation processes following the terminology used in Tcherkez et al. (2024), excluding CO_2 released by photorespiratory decarboxylation.

Accurate estimation of D_L is critical for understanding carbon dynamics from individual leaves to ecosystem scale, and for assessing global carbon budgets (Heskel, 2018; Needham et al., 2025; Ranathunga et al., 2025). However, quantifying D_L remains an experimental challenge (Kroner & Way, 2016; Way et al., 2019), because D_L cannot be measured directly using gas exchange techniques. It must be estimated, with the method developed by Laisk (1977) as described by Brooks & Farquhar (1985), being one of the

most widely applied approaches (Berghuijs et al., 2019; Gong et al., 2018). In addition, other approaches such as the Kok and Yin methods are widely discussed alternatives (Yin et al., 2011; Farquhar & Bush, 2017; Tcherkez et al., 2017). However, these methods are used exclusively to estimate D_L and cannot be applied to determine Γ*. Several studies have reported that D_L is consistently underestimated when using the Kok method, especially under photorespiratory conditions (Yin & Amthor, 2024) when the inevitable changes in intercellular CO_2 concentrations under changing light levels are ignored (Kirschbaum & Farquhar, 1987).

The Laisk method involves estimating Γ* and D_L by plotting measurements of photosynthesis (A_{net}) against low CO_2 partial pressure, measured under different levels of photosynthetic photon flux density (PPFD) (Berghuijs et al., 2019; Laisk, 1977; Walker & Cousins, 2013). Linear regressions are then applied to subsets of these points, and the intersection of the resulting lines is used to infer Γ* and D_L. However, according to the theory outlined in the equations of the FvCB model, the response of photosynthesis to CO_2 is inherently curvilinear (Farquhar et al., 1980; Walker & Ort, 2015), meaning that the linear approximation introduces systematic errors in the estimation of both parameters.

Strategies have therefore been proposed to minimise the biases associated with this linear approximation. One such strategy is the slope–intercept regression method, a refinement of the common intercept approach that does not directly address the physiological non-linearity, but instead reduces bias caused by similar slopes between neighbouring lines. This method assigns greater weight to intersections where the slopes differ more markedly, thereby improving the robustness of the linear fit (Walker & Ort, 2015). Alternatively, some studies have applied polynomial regressions to capture the curvature more explicitly (Tholen et al., 2012; Walker & Ort, 2015). However, polynomials have no theoretical or physiological basis for describing photosynthesis, and their use can lead to unrealistic values for Γ* and D_L if any extrapolation is needed, or even at the extreme points of the available observations.

More recently, Yin and Amthor (2024) proposed an alternative to the linear Laisk approach by applying a non-rectangular hyperbolic model to simultaneously estimate D_L and mesophyll conductance (g_m). Their method incorporates chlorophyll fluorescence to account for the variation of electron transport with light intensity and explicitly corrects for the CO_2 reassimilation that occurs during measurements at low CO_2 (Yin and Amthor, 2024). Use of the non-rectangular hyperbolic model leads to D_L estimates that are approximately 25% higher than those obtained with the traditional Laisk method, highlighting the importance of incorporating non-linear analysis into the method.

Estimating Γ* and D_L under low-temperature conditions using the Laisk method can be problematic and may lead to erroneous results, particularly if equipment constraints prevent the use of CO_2 partial pressures close to the expected Γ* (Γ^*_{exp}) (Atkin et al., 2000; Tcherkez & Atkin, 2021). In that case, the linear regression approach may yield erroneous values of D_L, as shown in the intersection of the regression lines for 300 and 150 µmol photons m^{-2} s^{-1} (Figure 3.1). These findings highlight the limitations of the Laisk method in accurately estimating Γ* and D_L, especially at low temperatures (Atkin et al., 2000; Way et al., 2019).

Way et al. (2019) attributed the occurrence of erroneous negative D_L values to factors such as low-temperature effects on chloroplast CO_2 partial pressure, cuvette leaks, and anaplerotic CO_2 fixation. However, the primary cause of these inaccuracies could also arise from the non-linear nature of A_{net}-C_c curves. When this non-linearity varies with the selection of a CO_2 partial pressure range that does not include a Γ^*_{exp} value, it can lead to physiologically impossible values of D_L, particularly at low temperatures. This highlights the need for an approach capable of estimating accurate and physiologically meaningful D_L, in order to produce high quality data that can support robust interpretations of carbon gains and losses in plants, and improve the representation of plant carbon balance under light conditions in ecosystem and global models.

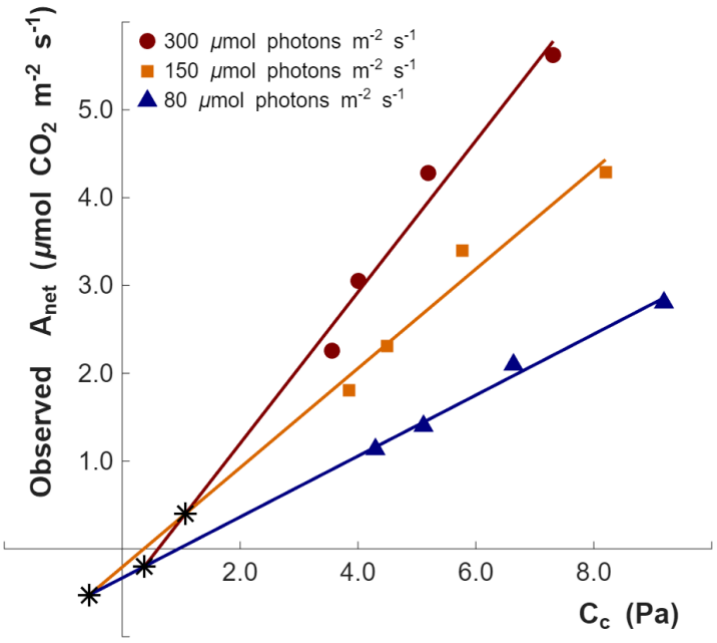

FIGURE 3.1. Observed net photosynthetic rate (A_{net}) as a function of chloroplastic CO_2 partial pressure (C_c), measured at 6°C under three light intensities: 300, 150, and 80 µmol photons m^{-2} s^{-1} (shown in dark red, orange and blue, respectively). The CO_2 partial pressure ranged from 3.6 to 9.2 Pa. Experimental data points are shown individually, with linear regressions fitted for each light level (solid lines). The intersections of the regression lines are marked with black asterisks.

In this chapter, I test the hypothesis that the range of CO_2 partial pressure used in the Laisk method significantly affects the estimation of Γ* and D_L due to the underlying non-linear nature of the A_{net}-C_c relationship. Using both simulated and experimental data, I quantify the biases introduced by applying linear regressions, comparing the results to theoretical expectations based on photosynthetic theory. I further examine how the choice of CO_2 range influences the accuracy of these estimates across temperatures. Based on these findings, I propose a refined methodology that improves the accuracy of photosynthetic carbon dynamic predictions across varying environmental conditions by applying the FvCB model to experimental datasets.

3.2 Materials and Methods

3.2.1 Growth Conditions and Experimental Data Collection

Sunflower (*Helianthus annuus* "Russian Giant") plants were grown from seed in 1.5 L plastic pots and cultivated in a plant growth unit. Throughout the experiment, plants were well-watered and fertilised regularly. Day/night temperature and relative humidity were 24/19 °C and 40/65 %, respectively. Photoperiod was 14 h with a light intensity of 400 µmol photons m^{-2} s^{-1} at the leaf level. Fully expanded leaves from the upper canopy were selected for CO_2 assimilation measurements. These measurements were performed using a GFS-3000 portable gas-exchange and fluorescence system (Heinz Walz GmbH, Effeltrich, Germany), equipped with a 4 cm^2 leaf chamber and a red-blue LED light source (10 % blue, 90 % red).

Prior to determining assimilation rates at each light intensity and CO_2 partial pressure, the leaves were given a 30-minute metabolic adjustment period at 6 °C, under a CO_2 partial pressure of 40 Pa and 300 µmol photons m^{-2} s^{-1}. This period ensured that photosynthesis had reached a steady state. Similarly, following each change in light intensity, the CO_2 partial pressure was set to 40 Pa to ensure full Rubisco activation.

Measurements were taken at a range of CO_2 partial pressures (1.2 to 9.2 Pa) under three photon flux densities: 300, 150, and 80 µmol photons m^{-2} s^{-1}. For subsequent analysis, the dataset was divided into four subsets, based on the inclusion or exclusion of Γ^*_{exp}, estimated at 1.54 Pa at 6 °C (Brooks & Farquhar, 1985). For subsets where Γ^*_{exp} was included, the CO_2 ranges were 1.2–3.6 Pa (narrow) and 1.2–6.6 Pa (wide). For those excluding Γ^*_{exp}, the narrow range was 3.6–6.6 Pa and the wide range was 3.6–9.2 Pa.

3.2.2 Definitions of Γ used in this chapter*

In this chapter, I deal with the empirical derivation of Γ* from gas-exchange measurements. I outline theoretical problems that arise from the derivation of Γ* from gas exchange data and how they relate to the range of CO_2 partial pressures available for analysis. For that, I needed to distinguish between Γ* with three possible meanings. To avoid confusion in the following text, they are briefly outlined here:

- **Γ*** (Estimated Γ*): The actual value estimated directly from available experimental data. That is the value one aims to refine through additional measurements.

- **Γ^*_{ref}** (Reference Γ*): The value used in the illustrative modelling to highlight problems that arise from using different approaches to derived Γ* at different temperatures and over different ranges of CO_2 partial pressures.

- **Γ^*_{exp}** (Expected Γ*): The value of Γ* broadly expected at specific temperatures. It is the value that can typically be used in experimental work to define an appropriate CO_2 range for measurements so that Γ* falls within, or, at least, close to the range of measurements.

Γ^*_{ref} and Γ^*_{exp} are values obtained either from established empirical equations in the literature (e.g. Brooks & Farquhar, 1985) or calculated from the partial pressure of oxygen and the specificity of Rubisco.

3.2.3 Estimation of Γ* and D_L Using the Laisk Method

Γ* and D_L were estimated using the traditional Laisk method, which involves determining the intersection points between pairs of linear regressions fitted to data obtained at different light intensities. When more than two light levels are available, multiple pairwise intersections are calculated, and the final estimates of Γ* and D_L are obtained by averaging the *x*- and *y*-coordinates of all intersection points.

The *x*-coordinate of each pairwise intersection point, representing an individual Γ* estimate, was calculated as:

$$\Gamma^*_{ij} = \frac{b_i - b_j}{m_j - m_i} \tag{3.1}$$

where m_i and m_j are the slopes, and b_i and b_j are the *y*-intercepts, of the regression lines corresponding to light levels *i* and *j*. Similarly, the corresponding *y*-coordinate for each intersection, representing an individual D_L estimate, was calculated as:

$$D_{L\,ij} = m_i\,\Gamma^*_{ij} + b_i \tag{3.2}$$

The final values of Γ* and D_L were then determined by averaging all pairwise estimates:

$$\Gamma^* = \frac{1}{n}\sum_{(i,j)}\Gamma^*_{ij} \tag{3.3}$$

$$D_L = \frac{1}{n}\sum_{(i,j)} D_{L\,ij} \tag{3.4}$$

Where *n* is the total number of pairwise intersections.

3.2.4 Common Considerations in Laisk Analyses: Environmental Dependence of g_m and D_L

An important methodological consideration in applying the Farquhar model is that the estimation of Γ* and D_L must be based on chloroplastic CO_2 partial pressure (C_c), rather than intercellular CO_2 partial pressure (C_i). The Laisk method was originally developed under the implicit assumption of infinite g_m, implying $C_i = C_c$. However, it is now well established that g_m is smaller than originally assumed and typically small enough to

require an important additional diffusion gradient between the intercellular air spaces and the chloroplastic sites of photosynthesis.

The mesophyll conductance is sensitive to multiple environmental factors (Bernacchi et al., 2002; Flexas et al., 2007; Li et al., 2020). In this context, g_m functions as a dynamic variable, co-varying with other photosynthetic traits in response to light, temperature, and CO_2 regimes (Shrestha et al., 2019). The question then arises whether variability and uncertainty in g_m can lead to significant errors in Γ* and D_L estimates. To explore this, and to test the robustness of Γ* and D_L estimates with respect to g_m, I conducted a comprehensive sensitivity analysis (Figure 3.2). I varied g_m from 0.5 to 10.0 µmol m^{-2} s^{-1} Pa^{-1} at 25°C. By spanning this extensive range, the analysis captures the potential variability in g_m across different plant functional types and environmental contexts.

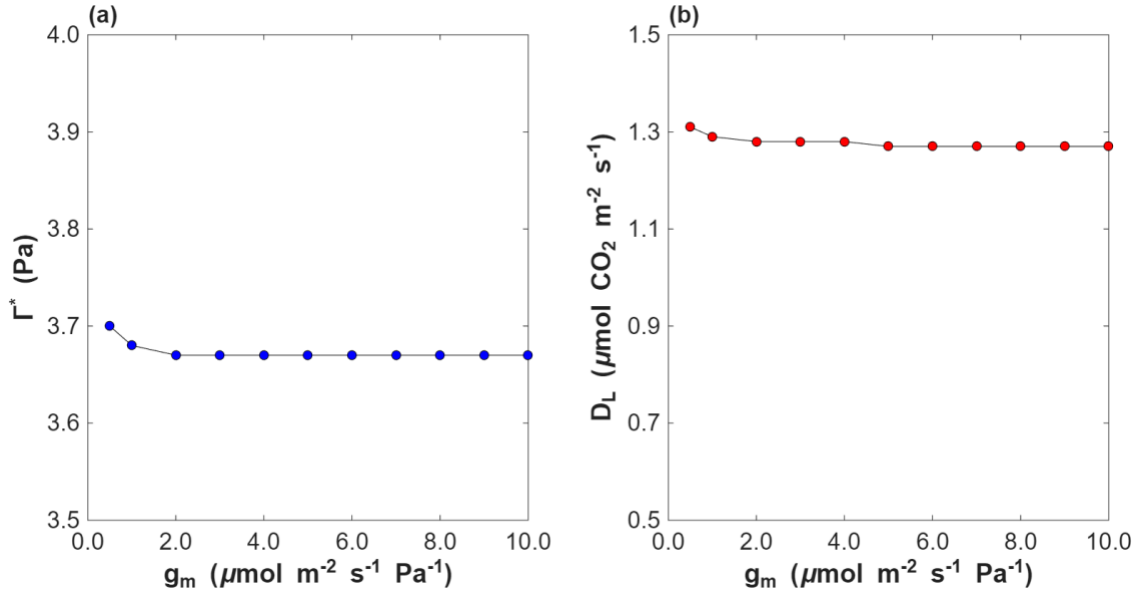

FIGURE 3.2. Sensitivity of parameter estimation to mesophyll conductance (g_m) in sunflower (*Helianthus annuus* "Russian giant"). Estimated values of Γ* (a) and D_L (b) are shown as a function of g_m. The simulations were conducted at 25°C using the Farquhar model implemented in the Excel-based fitting tool developed for this study, with all other parameters held constant.

The results of this sensitivity analysis showed that both Γ* and D_L estimates remained remarkably stable across this range, particularly within the 2–10 μmol m^{-2} s^{-1} Pa^{-1} interval, where Γ* was 3.67 Pa and D_L was 1.27 μmol CO_2 m^{-2} s^{-1}. Even at the lowest conductance (0.5 μmol m^{-2} s^{-1} Pa^{-1}), where variation was most pronounced, Γ* increased by only 0.82% (from 3.67 to 3.70 Pa) and D_L by only 3.1% (from 1.27 to 1.31 μmol m^{-2} s^{-1}). This outcome highlights the robustness of the method even when g_m is variable or uncertain, because measurements made near Γ* involve very low net CO_2 assimilation rates. In that regime, A_{net} is close to zero, so the liquid-phase diffusion from C_i to C_c described by A_{net}= g_m (C_i - C_c) implies a very small gradient between intercellular air spaces and chloroplasts, making estimates comparatively insensitive to uncertainty in g_m (Walker & Ort, 2015; Busch et al., 2024). In addition, since the Laisk method derives Γ* and D_L from the intercept of multiple A_{net}-C_c regressions, systematic variations in CO_2 drawdown across treatments are largely compensated in the intercept calculation. Even at slightly higher CO_2 partial pressures and A_{net} rates, the chloroplastic CO_2 drawdown required to overcome mesophyll diffusion limitations is proportional to CO_2 uptake, so its effect cancels when the intercepts of multiple lines are used to derive Γ* and D_L, because the intercept reflects a condition where A_{net} approaches zero.

On the other hand, in the classical Laisk method it is commonly assumed that D_L remains constant across changes in irradiance and CO_2 during the experiment. From a methodological standpoint, reports of CO_2 dependent changes in leaf respiration may partly reflect gas exchange artefacts rather than metabolic regulation, which cautions against over-interpreting CO_2 effects on D_L within the conditions (Amthor et al., 2001; Yin and Amthor, 2024). However, consideration of possible artefactual explanations do not preclude the possibility that there may also be genuine metabolic variability. Recent metabolomic and isotopic evidence has shown that CO_2 release in the light draws on multiple carbon sources, including stored substrates that could lead to short term dependence on recent CO_2 and irradiance (Abadie et al., 2024). Over the moderate to high irradiance range typically employed for gas-exchange step measurements in the classical

Laisk protocol, the fraction of dark respiration that persists in the light has been shown to be largely insensitive to irradiance (Kirschbaum & Farquhar, 1987; Peisker & Apel, 2001). Accordingly, I treat D_L as invariant in the present analyses, while noting that any potential dependence on CO_2 and low irradiance should be tested explicitly in future work.

3.2.5 Simulations for Quantifying the Bias of Laisk Method

To quantify the bias of the estimated Γ* and D_L using the Laisk method across different temperatures, I simulated net assimilation rates (A_{net}) using the FvCB model, as described in section 1.1, across a temperature range from 5 to 40 °C and under three light intensities (300, 150, and 80 µmol photons m^{-2} s^{-1}). Parameters used in the simulation are detailed in the Table 3.1. V_{cmax} and J_{max} were derived from experimental measurements at 25 °C and their temperature dependence was modelled using the MMRT function (Equations 3.5). α and θ were kept constant across all temperatures.

$$\ln(k) = \ln\left(\frac{k_B T}{h}\right) - \frac{\Delta H^{\ddagger}_{T_0+}\Delta C_p^{\ddagger}(T - T_0)}{RT} + \frac{\Delta S^{\ddagger}_{T_0+}\Delta C_p^{\ddagger}(\ln T - lnT_0)}{R} \tag{3.5}$$

where k is the catalytic rate, k_B is Boltzmann's constant, h is Planck's constant, R is the universal gas constant, $\Delta H^{\ddagger}_{T0}$ is the change in enthalpy at a reference temperature T_0, $\Delta S^{\ddagger}_{T0}$ is the change in entropy at T_0 and, $\Delta C_p^{\ddagger}$ is the change in heat capacity between the ground and transition states.

For V_{cmax}, an additional adjustment was made to incorporate thermal deactivation at high temperatures using the denaturation function based on Peterson et al (2004). This function models the reversible equilibrium between active (E_{act}) and inactive (E_{inact}) enzyme forms (K_{eq}) and its temperature dependence is described as:

$$\ln(K_{eq}) = \frac{\Delta H_{eq}}{R}\left(\frac{1}{T_{eq}} - \frac{1}{T}\right) \tag{3.6}$$

where ΔH_{eq} is the enthalpy change associated with the active-inactive enzyme transition and T_{eq} is the temperature at which the concentration of E_{act} and E_{inact} are equal. MMRT with deactivation fits five free parameters: the three MMRT parameters $\Delta H^{\ddagger}T_0$, $\Delta S^{\ddagger}T_0$ and $\Delta Cp^{\ddagger}$, and the two deactivation parameters ΔH_{eq} and T_{eq}. Physical constants (kB, h, R) are fixed. All five free parameters were estimated by non-linear least squares fits to V_{cmax}(T) data.

For each light level, I simulated A_{net} under three C_c levels that vary under different temperatures and are defined relative to Γ^*_{ref} (the reference value of Γ^*): Γ^*_{ref} + 2.1 Pa, Γ^*_{ref} + 4.6 Pa, and Γ^*_{ref} + 7.2 Pa. Γ^*_{ref} was calculated following the equation described by Brooks and Farquhar (1985). By varying the C_c level under different temperatures that correspond to Γ^*_{ref}, I avoided any potential bias from mismatches between Γ^* and the CO_2 range to better quantify the effectiveness of the Laisk method on estimating Γ^* and D_L. At every temperature under the selected light levels, i.e., 300, 150, and 80 μmol photons m^{-2} s^{-1}, I constructed three A_{net}-C_c curves that intersected in a unique point, which is the prescribed Γ^* in the simulation (Γ^*_{ref}). Based on the simulated A_{net} at each temperature, I applied the Laisk method to estimate the Γ^* and D_L using the linear regression outlined above. The differences between the derived Γ^* and Γ^*_{ref} under temperatures from 5 to 40°C denoted the bias in estimating Γ^* using the Laisk method as $\epsilon(\Gamma^*)$. A bias estimate for DL $\epsilon(D_L)$, was derived similarly.

TABLE 3.1. List of parameters and their values used in the simulations on the FvCB model.

Parameter (unit)	Value	Meaning and source.
e (-)	0.1	Empirical factor which transforms the function of Vc into a smooth hyperbola. Kirschbaum and Farquhar (1984).

$E_{a(Kc)}$ **(*k*J mol^{-1})**	59.4	Activation energy for Kc. Sharkey et al. (2007).
$E_{a(Ko)}$ **(*k*J mol^{-1})**	35.9	Activation energy for Ko. Sharkey et al. (2007).
K_a **(Pa)**	1.0	Michaelis-Menten constant for activation of Rubisco by CO_2 at a given Mg^{2+} concentration and pH. Kirschbaum and Farquhar (1984).
K_c **25°C (Pa)**	36.9	Michaelis-Menten constant for CO_2. von Caemmerer and Quick (2000). Jordan and Ogren (1984).
K_o **25°C (*k*Pa)**	35.1	Michaelis-Menten constant for O_2. von Caemmerer and Quick (2000). Jordan and Ogren (1984).
O_2 **(*k*Pa)**	21.0	Partial pressure of oxygen.

P **(*k*Pa)**	102.1	Average pressure in the gas exchange chamber.
R **(J mol^{-1} K^{-1})**	8.314	Ideal gas constant.
α (mol e- mol photons^{-1})	0.25	Quantum yield of electron transport. The literature reports values between 0.01 - 0.5 moles e- mol photons^{-1}.
θ (-)	0.30	Describes the curvature of photosynthesis.The literature reports values between 0.01 - 10

To better understand the effect of different ranges of C_c on the estimation of Γ* and D_L, I conducted a sensitivity analysis by extending the simulations using two distinct C_c ranges: inclusion of Γ^*_{ref} and exclusion of Γ^*_{ref} within the selected C_c ranges. Both scenarios, in which Γ^*_{ref} was either included or excluded from the selected C_c range, were evaluated across the temperatures ranging from 5 to 40°C. When Γ^*_{ref} was included, each C_c range began 0.5 Pa below Γ^*_{ref} with the initial range extending to 0.5 Pa above it. The upper limit of each subsequent range was extended by 0.5 Pa, up to a maximum of 10 Pa. In contrast, when Γ^*_{ref} was excluded, the C_c range began at 3.0 Pa above Γ^*_{ref}. The first range extended 1.0 Pa above that starting point, and, similarly, the upper limits of subsequent ranges were increased by 0.5 Pa until a maximum of 10.5 Pa was reached.

3.2.6 Simulations of Modelled Intercepts for Linear Regressions and FvCB Model

Except for bias introduced by the Laisk method, measurement errors from infrared gas analysers (IRGAs) can also contribute to errors in estimating Γ* and D_L. Based on experimental data collected under varying conditions of temperature, light, and CO_2 partial pressure, I determined a standard deviation of 0.07 µmol CO_2 $m^{-2}s^{-1}$ in the net assimilation rates (A_{net}) of the gas-exchange systems (own observations).

To incorporate this uncertainty, I implemented a Monte Carlo approach, generating ten thousand A_{net} simulated values per treatment. Each treatment corresponds to a specific combination of CO_2 range (narrow or wide) and inclusion or exclusion of Γ^*_{ref} in the analysed C_c interval. Simulated A_{net} values (A_{sim}) were produced using the Box–Muller transformation (Scott, 2011), which converts two uniformly distributed random numbers (u_1, u_2) into a normally distributed variable (z) with a mean of 0 and a standard deviation of 1, according to the following equation:

$$z = \sqrt{-2Ln\,(u_2)} * \cos(2\pi * u_1) \tag{3.7}$$

For each dataset, the A_{sim} was computed using the equation:

$$A_{Sim} = A_{obs} + z(i) * error \tag{3.8}$$

where z(i) represents the i-th value generated through the Box-Muller method, A_{obs} is the observed value of A, and *error* denotes the standard deviation of the measurements, i.e. 0.07 µmol CO_2 $m^{-2}s^{-1}$. This approach allowed incorporation of measurement uncertainty and evaluation of its effect on the estimation of Γ* and D_L using both linear regression and the FvCB model.

3.2.7 Application of the Photosynthetic Model to Experimental Data

I applied the photosynthetic model to the experimental data collected during the first phase of the study. The fitting process involved optimising the parameters V_{cmax}, J, α, and θ, as

well as estimating Γ* and D_L, using the parameter values listed in Table 3.1. Parameter optimisation was performed in MATLAB R2025b using the *fminsearch* function to minimise the negative log-likelihood between observed and modelled net assimilation rates. Through iterative adjustment of the model parameters, this procedure yielded the best-fitting values for each treatment, resulting in a unique intersection point among the three A_{net}-C_c curves.

3.3 Results

3.3.1 Bias in Determining Γ* and D_L Using Linear Regressions from 5 to 40 °C.

Figure 3.1 illustrates the erroneous estimates of Γ* and D_L based on the A_{net}-C_c curve at 6°C using the Laisk method with linear regressions, where the Γ^*_{exp} from the linear regression locates beyond the measured range of CO_2 partial pressures. The simulations across temperatures from 5 to 40°C (Figure 3.3) demonstrated that the estimates obtained via linear regression are highly inaccurate at low temperatures, for example at 5 and 10 °C (Figures 3.3a and 3.3b). Under these lower temperatures, the regression lines often intersect with positive net assimilation rates that would imply erroneous negative values for D_L. Moreover, the intersections from different regression pairs are scattered and diverge from the Γ^*_{ref} and D_L values used in the simulations. At higher temperatures, estimates of D_L based on the Laisk method became physiologically meaningful. At 15°C (Figure 3.3c), the regression lines intersected with negative net assimilation rates, although the intersecting points still occurred at C_c well below the Γ^*_{ref} values used in the simulations. At 20, 30, and 40°C (Figures 3.3d-f), the regression lines intersected at distinct single points with corresponding meaningful estimates of D_L. However, the inferred estimates of Γ* remained underestimates from Γ^*_{ref}.

Notably, at higher temperatures, the Γ* values tended to converge more closely with Γ^*_{ref}, suggesting that the limitations of the Laisk method become markedly more pronounced under moderate and low temperatures. This bias at lower temperatures could be linked to

the lower CO_2 partial pressure values corresponding to Γ^*_{exp}, and the pronounced curvature in the A_{net}-C_c relationship.

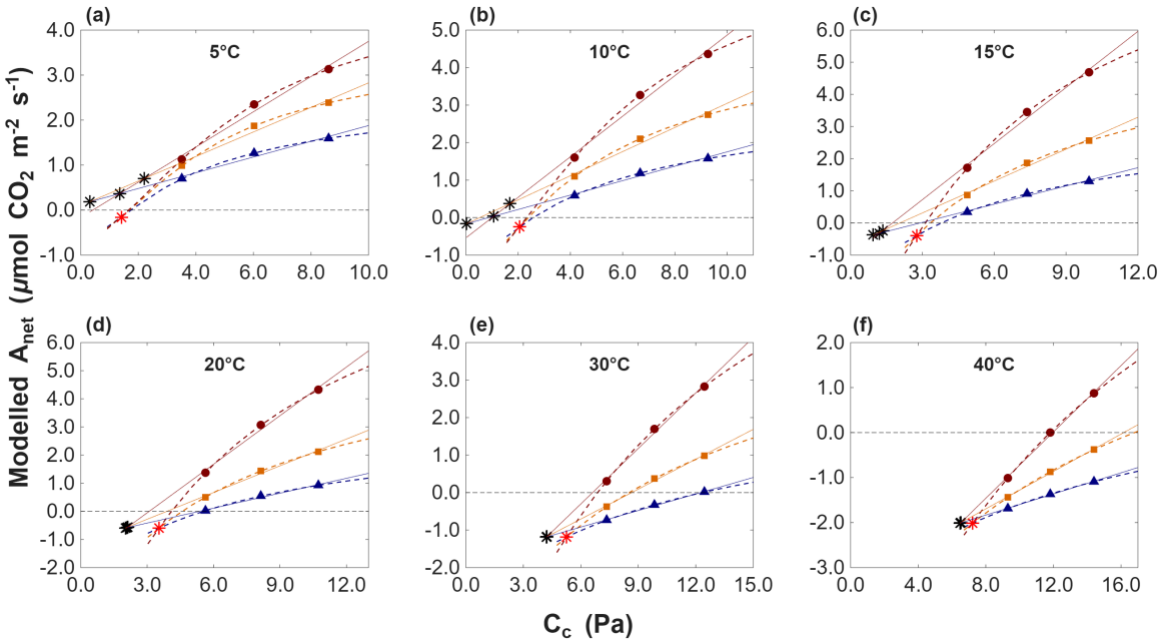

FIGURE 3.3. Modelled net assimilation rate as a function of chloroplastic CO_2 partial pressure (C_c). Dashed lines represent simulations from the FvCB model, with corresponding solid symbols. Solid lines show linear regressions fitted to these modelled data points. The three light intensities used (300, 150, and 80 μmol photons m^{-2} s^{-1}) are indicated by dark red, orange, and blue, respectively. Simulations are shown for six temperatures (5, 10, 15, 20, 30, and 40°C). Black asterisks indicate the intersections of the linear regressions, while the red asterisk marks the prescribed intersection used to simulate the reference values of Γ* and D_L at each temperature.

Figure 3.4 summarises the values of Γ* and D_L estimated using linear regressions (black), in comparison with the reference values used in the simulation based on the FvCB model (red), across a temperature range from 5 to 40 °C. These results are based on the modelled data shown in Figure 3.3 and reflect the outcomes of applying linear relationships to estimate Γ* and D_L from the simulated A_{net}-C_c curves. Overall, Γ* values obtained from the linear regressions were underestimated compared to Γ^*_{ref} at all temperatures except 5 °C (Figure 4a), where Γ* was overestimated. This deviation is explained by the position

of the line intersections at 5 °C (Figure 3a). The magnitude of these errors was notable. At 15°C, Γ* was underestimated by 1.43 Pa, and even at 40 °C, where the issue is less pronounced, the underestimation remained at 0.69 Pa. Regarding D_L (Figure 4b), the estimates closely matched the modelled values at temperatures of 20 °C and above. However, D_L was strongly underestimated below 20 °C, producing physiologically meaningless values at 5 and 10 °C.

At this point, it is necessary to also draw attention to one of the complications of finding generic patterns. In applying the Laisk method, one typically uses three low-light intensities that generate different levels of RuBP regeneration and allow the identification of their cross-over points that define both Γ* and D_L. If rates are controlled by RuBP regeneration, fitting linear relationships to inherently curved responses consistently leads to mathematical errors, essentially affecting the estimation of Γ*, while D_L can still be estimated correctly. This is the pattern seen at higher temperatures in Figure 3.4.

However, depending on the light levels used and the rates of Rubisco activity at different temperatures, the readings at highest light levels may or may not be limited by Rubisco activity instead of RuBP regeneration. This does not invalidate the use of the Laisk method, but it alters the pattern of errors. In the simulations, as temperature was decreased, Rubisco activity eventually became low enough to become the rate-limiting step at the highest used light level of 300 μmol photons m^{-2} s^{-1}. With my specific parameterisation, this limitation occurred at temperatures of 15°C and below, causing the error introduced by linear relationships to shift from affecting Γ* estimates to affecting D_L estimates. These are still equally important estimation errors, but they simply manifest themselves in different ways (Figure 3.4).

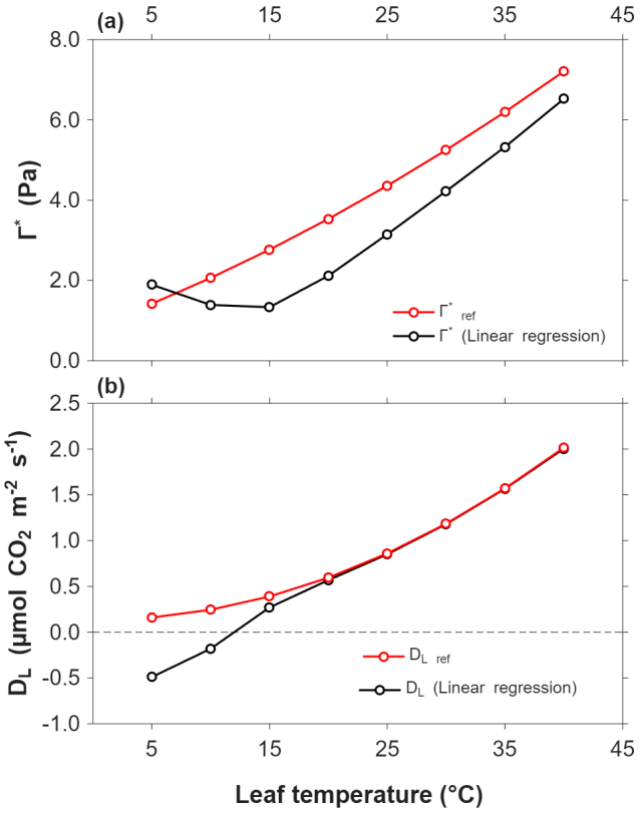

FIGURE 3.4. Temperature-dependent variations in Γ* and D_L from 5 to 40°C. (a) Comparison between the Γ^*_{ref} values (solid red line) used in the FvCB model and the Γ* estimates derived from the linear regression intercepts (solid black line). (b) Comparison between the modelled $D_{L\text{-}ref}$ values (solid red line) and the D_L estimates from the linear regression intercepts (solid black line).

My results highlighted the challenge in accurately estimating Γ* and D_L using the Laisk method, particularly at low temperatures (Tcherkez & Atkin, 2021; Way et al., 2019). This difficulty arises because linear regressions fitted to data at different light intensities do not adequately capture the curvature inherent in the A_{net}-C_c relationship (Figure 3.3). As a result, this can lead to erroneous estimates of D_L, often resulting in physiologically meaningless values (Atkin et al., 2000a; Way et al., 2019a). This methodological flaw can be amplified when the measured C_c range does not include the Γ^*_{exp}. At 6°C, Γ* was around 1.54 Pa (Brooks & Farquhar, 1985), which was significantly lower than the starting point of 3.6 Pa in the measured C_c range. Moreover, considering the wide measured C_c

range of about 5.6 Pa, i.e. from Γ^*_{exp} +2.1 Pa to Γ^*_{exp} +7.2 Pa with varying Γ^*_{exp} under different temperatures in Figure 3.1, substantial errors in the estimation of Γ* and D_L are expected by using linear regressions in the Laisk method due to the non-linear nature of the A_{net}-C_c curve based on the FvCB model, especially under lower temperatures (Figures 3.3a and 3.3b).

3.3.2 Sensitivity Analysis of Γ* and D_L Across Different C_c Range from 5 to 40 °C.

Figures 3.3 and 3.4 illustrate the disparities in estimating Γ* and D_L using the Laisk method within a C_c range from Γ^*_{exp} +2.1 Pa to Γ^*_{exp} +7.2 Pa, thus excluding the Γ^*_{exp} from the CO_2 measurement range. As the measured C_c range spans from narrow to wide, either including or excluding the Γ^*_{exp}, the curvature of the A_{net}-C_c curve becomes apparent, consequently resulting in higher errors in the estimates of Γ* and D_L. The simulation (Figure 3.5) quantifies the estimation errors for Γ*, i.e. $\epsilon(\Gamma^*)$, and D_L, i.e. $\epsilon(D_L)$, across CO_2 measurement spans from 1 to 10.5 Pa.

When Γ^*_{exp} was included in the C_c range, $\epsilon(\Gamma^*)$ remained close to zero for data spanning up to approximately 3 Pa across all temperatures (Figure 3.5a). Beyond 3 Pa, $\epsilon(\Gamma^*)$ increased at lower temperatures, with errors reaching 0.92 Pa at 5 °C and 0.45 Pa at 10 °C under the widest C_c range tested (10.5 Pa). In contrast, at higher temperatures (30 and 40 °C), Γ* was slightly underestimated, with errors not exceeding −0.5 Pa. Similarly, $\epsilon(D_L)$ remained approximately zero below the C_c range of 3 Pa (Figure 3.5c) and after 3 Pa, D_L was consistently underestimated, i.e. $\epsilon(D_L)<0$, as the C_c range increased across all temperatures. The absolute $\epsilon(D_L)$ was less than 0.5 μmol CO_2 m^{-2} s^{-1} for all temperatures up to a C_c range of 7 Pa. At 5 °C, underestimation in D_L became more pronounced with increasing C_c range, reaching −0.7 under the widest range tested. In contrast, at higher temperatures, such as 30 °C and 40 °C, the underestimation was minimal and remained close to zero throughout.

Substantial overestimations of Γ* were observed at low and moderate temperatures when Γ^*_{exp} was excluded from the C_c range (Figure 3.5b), with $\epsilon(\Gamma^*)$ reaching nearly 2 Pa at 5 °C under a C_c range of 3 Pa. As the C_c range increased, the overestimation diminished and eventually turned into underestimation at higher temperatures. For instance, at 40 °C, the error dropped from 0.3 Pa at the lowest C_c range to −2.5 Pa at the widest C_c range (Figure 3.5b). Figure 3.5d depicted substantial underestimation of D_L at low and moderate temperatures, with the largest discrepancies for $\epsilon(D_L)$ observed under the widest C_c range. At higher temperatures such as 30 °C and 40 °C, the underestimation remained minimal across the entire C_c range.

These results suggest that, to minimise estimation errors using linear regressions in the Laisk method, it is not feasible to rely on C_c ranges that exclude Γ^*_{exp}, as large errors are present even under narrow CO_2 spans. The absence of Γ^*_{exp} leads to systematic bias from the outset, particularly at lower temperatures. When Γ^*_{exp} is included, a C_c range of up to 3 Pa around it appears to minimise both $\epsilon(\Gamma^*)$ and $\epsilon(D_L)$, across temperatures. Including Γ^*_{exp} in this range proved essential, particularly at low temperatures, where the risk of over- or underestimation was highest. Beyond 3 Pa, errors increased markedly, especially for D_L at 5 °C.

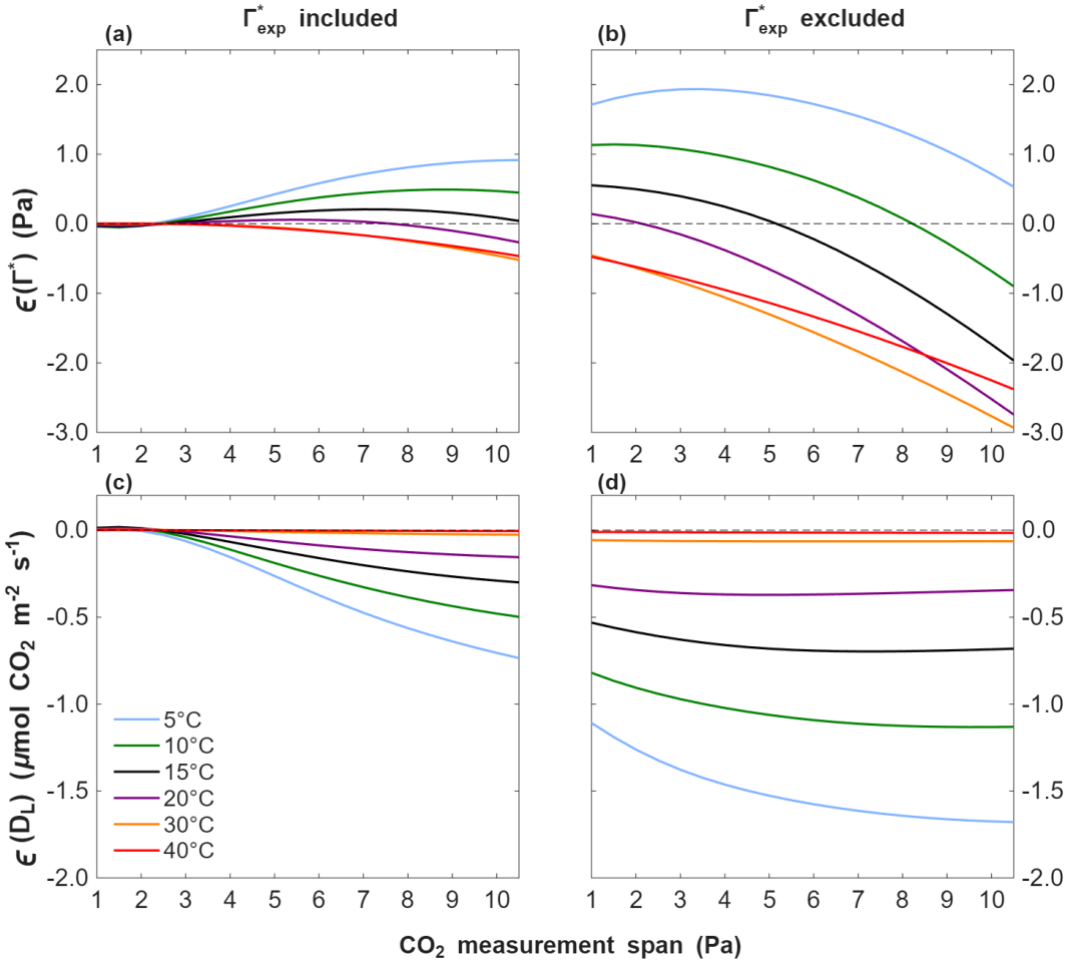

FIGURE 3.5. The pattern of $\epsilon(\Gamma^*)$ and $\epsilon(D_L)$ over the evaluated C_c range across temperatures from 5 to 40 °C. Panels a and b show $\epsilon(\Gamma^*)$ and panels c and d show $\epsilon(D_L)$. Panels a and c correspond to simulations in which Γ^*_{exp} was included within the C_c range, beginning from 0.5 Pa below Γ^*_{exp} with the narrowest range extending to 0.5 Pa above Γ^*_{exp}. Panels b and d correspond to simulations in which Γ^*_{exp} was excluded, with the C_c range that began from 3.0 Pa above Γ^*_{exp}. In both cases, the upper limit of each subsequent range was increased in 0.5 Pa increments, up to a maximum of 10.5 Pa.

3.3.3 Estimates of Γ* and D_L from Monte Carlo Simulations Using Linear Regressions and the FvCB Model

I assessed how IRGA measurement errors would affect the estimates of Γ* and D_L. Figure 3.5 illustrated that theoretically, better estimates of these parameters could be obtained if one used a narrow CO_2 measurement range, preferably including the value of Γ^*_{exp} when using linear regressions. In practice, that approach would be curtailed by inevitable experimental error in gas-exchange measurements that require a wider measurement range to partly negate the influence of random measurement errors. Therefore, I conducted a Monte Carlo approach using both the linear regression and FvCB model, across narrow and wide CO_2 ranges, and with or without inclusion of Γ^*_{exp}. For that analysis, I calculated expected data points from simulations of the FvCB model and then randomly modified each point to emulate the presence of experimental error. The results are summarised in Table 3.2 and visualised in Figure 3.6.

When applying the FvCB model, the estimated values for Γ* and D_L were consistent and tightly clustered, regardless of whether Γ^*_{exp} was included, or whether the CO_2 range was narrow or wide. In contrast, estimates obtained from linear regression diverged substantially depending on the inclusion of Γ^*_{exp}. When Γ^*_{exp} was included, D_L estimates remained close to the true values: 1.06 μmol CO_2 m^{-2} s^{-1} for the narrow range and 0.98 ± 0.07 μmol CO_2 m^{-2} s^{-1} for the wide range. However, Γ* was still underestimated in both cases. When Γ^*_{exp} was excluded, the estimates became highly inaccurate, particularly under wide CO_2 ranges, where Γ* dropped to 0.24 Pa and D_L to 0.14 μmol CO_2 m^{-2} s^{-1} (Table 3.2).

Figure 3.6 illustrates the distribution of intersection points derived from the simulated experiments using the Monte Carlo method. When the FvCB model was integrated into the Laisk method, the resulting estimates formed a compact and consistent cluster across all treatments, demonstrating high robustness to input data variability. Similarly, linear regressions that include Γ^*_{exp} yielded distributions more closely aligned with those obtained from the FvCB model, particularly under narrow CO_2 ranges (Figure 3.6a). This suggests that, under such conditions, the choice of analysis methods would have little impact on the inferred values of Γ* and D_L. However, even the use of a wide CO_2 range resulted in a slight underestimation of Γ* (Figure 3.6b).

Problems with the use of linear regressions for analysis became much worse when the available data did not include Γ^*_{exp}, and the linear regression approach produced a broader and more dispersed distribution of intersection points. Under these conditions, the linear regression approach was likely to produce erroneous estimates, in extreme cases even including negative values for both Γ* and D_L (Figures 3.6c and 3.6d). These conceptual flaws invalidate the derivation of any Γ* and D_L estimates with linear analysis if they do not include CO_2 partial pressures that include Γ*.

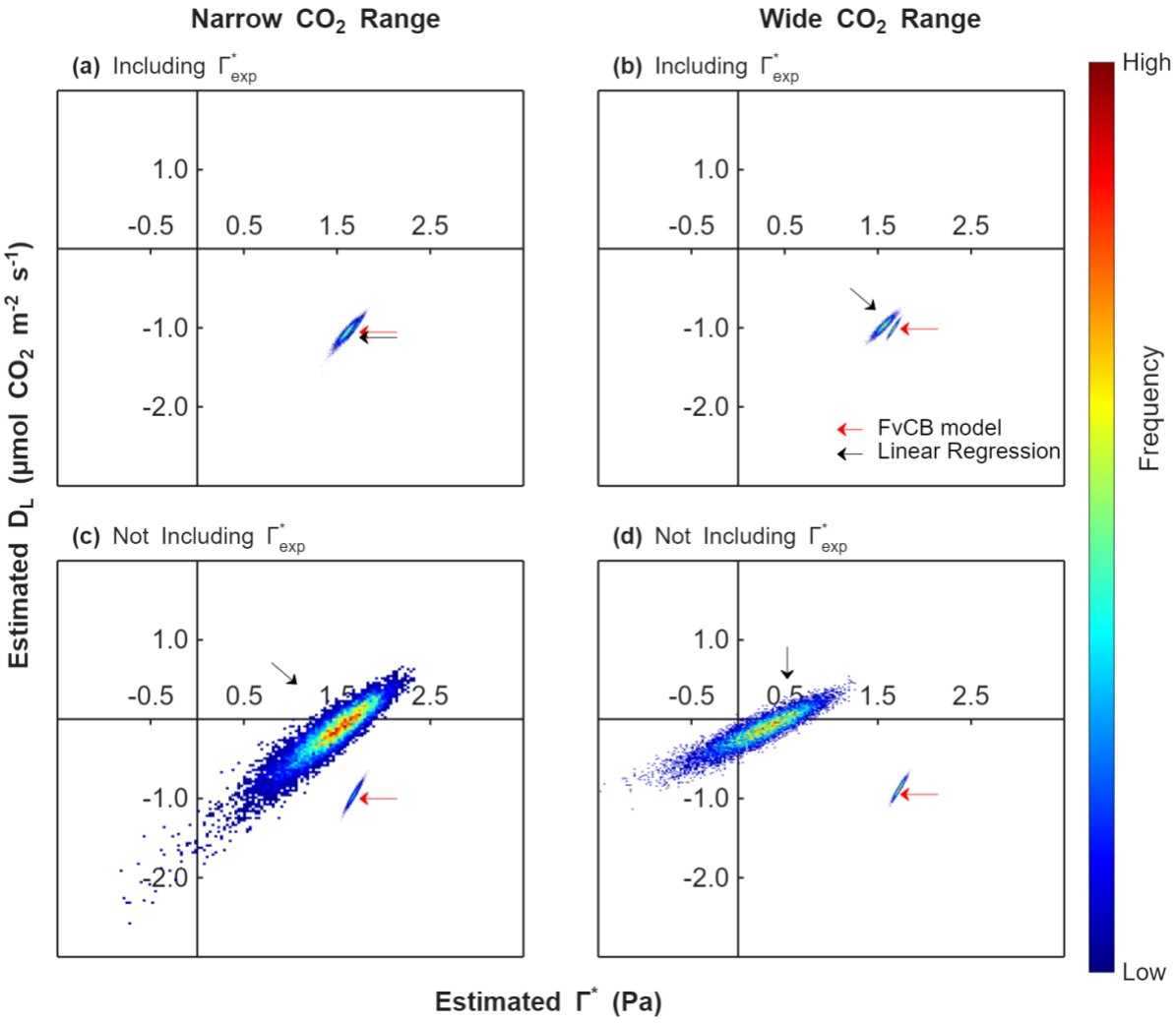

FIGURE 3.6. Distribution of intersection points for estimated Γ* and D_L from ten thousand Monte Carlo simulations at 6 °C. Each panel compares the performance of the FvCB model with Linear Regressions. Panels (a) and (b) refer to analyses that included Γ^*_{exp}, with panel (a) using a narrow CO_2 range and panel (b) using a wide CO_2 range. In contrast, the analyses illustrated in panels (c) and (d) did not include Γ^*_{exp}, with panel (c) employing a narrow and panel (d) a wider CO_2 range. Heat maps display the density of intersection points: warmer colours indicate higher concentrations of points, while cooler colours represent lower densities. Black arrows indicate the dispersion of intersection points obtained using linear regressions, while red arrows represent those obtained using the FvCB model.

TABLE 3.2. Estimates of Γ* and D_L based on ten thousand simulations with varying ranges of CO_2 partial pressures and two estimation methods. For simulations including Γ^*_{exp} in the dataset, the CO_2 ranges were either narrow (1.2–3.6 Pa) or wide (1.2–6.6 Pa). For simulations excluding Γ^*_{exp}, the narrow range was 3.6–6.6 Pa and the wide range was 3.6–9.2 Pa. Values are presented as mean ± standard deviation. Simulations were conducted for a leaf temperature of 6 °C and with assumed true values of 1.67 Pa for Γ* and 1.0 µmol CO_2 m^{-2} s^{-1} for D_L.

Method	**Γ^*_{ref}**	**CO_2 range**	**Γ*** **(Pa)**	**D_L** **(µmol CO_2 m^{-2} s^{-1})**
FvCB model	Included	Narrow	1.70±0.04	0.98±0.07
		Wide	1.67±0.03	1.01±0.05
	Excluded	Narrow	1.68±0.04	0.96±0.09
		Wide	1.73±0.04	0.87±0.07
Linear regression	Included	Narrow	1.60±0.06	1.06±0.09
		Wide	1.56±0.06	0.98±0.07
	Excluded	Narrow	1.44±0.36	0.18±0.34
		Wide	0.24±0.37	0.14±0.21

3.3.4 Estimation of Γ* and D_L Using the FvCB Model and Linear Regressions Applied to Experimental Data

Figure 3.7 revisits the same experimental dataset presented earlier in Figure 3.1, now reanalysed using both linear regressions and the FvCB model at 6 °C. In panel (a), fits were performed over a narrow CO_2 range (1.2–3.6 Pa) that included Γ^*_{exp}. Under these conditions, the intersection points derived from linear regressions (black asterisks) were consistent across light intensities and closely aligned with the intersection point generated by the FvCB model (red asterisk). This alignment highlights the importance of including Γ^*_{exp} when applying the linear regressions in the Laisk method, as it reduces bias and provides physiologically plausible estimates of both Γ* and D_L.

In contrast, panel (b) shows the same dataset fitted using a broader CO_2 range (3.6–9.2 Pa) from which Γ^*_{exp} was excluded. Here, the intersection points from linear regressions (black asterisks) diverged substantially and led to implausible estimates, including negative values for respiration and unrealistic Γ*. Meanwhile, the FvCB model continued to produce a physiologically consistent fit, with the modelled intersection point remaining robust despite the absence of Γ^*_{exp} in the data range. Together, these results reinforce the problematic use of linear regressions for analysis when Γ^*_{exp} is excluded. By contrast, use of the FvCB model demonstrates greater robustness and reliability, offering consistent and biologically meaningful estimates even when Γ^*_{exp} is not included in the CO_2 measurement range.

Panel (c) pools the data from panels a and b to compare both approaches across the full C_c range (1.2–9.2 Pa). At the main scale the linear regressions and the FvCB fit look similar, yet the inset in the upper right shows a consistent leftward and downward shift of the linear regression intersection relative to the modelled intersection. This shift indicates systematic underestimation of Γ* and D_L by the linear regressions compared with the FvCB model.

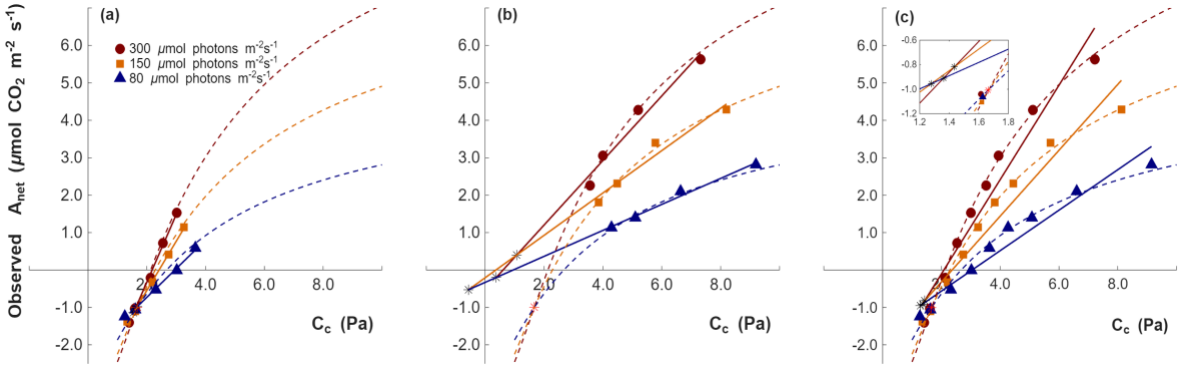

FIGURE 3.7. Observed net photosynthetic rate (A_{net}) as a function of chloroplastic CO_2 partial pressure (C_c) measured at a leaf temperature of 6 °C under three light intensities: 300 (dark red), 150 (orange), and 80 (blue) µmol photons m^{-2} s^{-1}. Experimental data are shown as individual points. Solid lines represent linear regressions, while dotted lines indicate theoretical fits based on the FvCB model. Panel (a) corresponds to fits derived from the data obtained over a narrow CO_2 range (1.2–3.6 Pa) that included Γ^*_{exp}, while panel (b) shows fits from the data obtained over a wider CO_2 range (3.6–9.2 Pa) that did not include Γ^*_{exp}. Panel (c) displays fits derived from the entire experimental CO_2 range (1.2–9.2 Pa). The inset in panel (c) provides a magnified view of the region where the regression lines and modelled curves intersect, highlighting the differences between the intersection points generated by the linear regressions and the intersection obtained with the Farquhar model. The red asterisk marks the intersection point of the three A_{net}-C_c curves, while black asterisks indicate the intersections of the three linear regressions at each light intensity.

3.4 Discussion

3.4.1 Methodological Limitation of the Classical Laisk Approach

The parameters Γ* and D_L are key to describing photosynthetic CO_2 responses, and the Laisk method has long been used to estimate them (Berghuijs et al., 2019; Gong et al., 2018). However, my findings show a fundamental methodological limitation inherent in this approach, because it implicitly assumes linearity in the A_{net}–C_c relationship, despite strong theoretical and empirical evidence that photosynthesis exhibits a non-linear response to CO_2 (Farquhar et al., 1980; Onoda et al., 2005; Zhang, 2010). This linearity assumption introduces systematic bias, especially when wide CO_2 ranges are used, as the deviation between linear and non-linear models increases with the span of CO_2 partial

presures used (Figure 3.5). Consequently, use of linear relationships may result in implausible and physiologically unrealistic estimates, such as negative values for Γ* or D_L (Figures 3.1, 3.7).

3.4.2 Effects of CO_2 Range and Inclusion of the Expected Γ*

Negative D_L estimates have also been reported in other studies of C_3 species when linear regressions were applied across wide CO_2 ranges (Atkin et al., 2000; Kroner & Way, 2016; Way et al., 2019). For example, Way et al. (2019) used C_i values ranging from 4.0 to 15.0 Pa, a wide range which did not include the Γ^*_{exp} for the tested temperature. As a result, they obtained negative D_L values, indicating positive net CO_2 uptake, which most likely reflected methodological artefacts caused by not including the Γ^*_{exp} and the use of wide CO_2 ranges.

The theoretical analysis indicated that excluding the Γ^*_{exp} introduces systematic errors, while its inclusion markedly improves the reliability of estimates obtained through linear regression, as shown in Figure 3.5. Although Way et al. (2019) did not explicitly aim to test for the effect of inclusion of Γ^*_{exp} in their research, when it fell within their measurement range, their estimated D_L values were positive. However, even when the Γ^*_{exp} is included, using wide CO_2 ranges can still introduce substantial error, as shown in the simulations (Figures 3.5a and 3.5c). For example, Way et al. (2019) reported measurements at 4.0 and 15.0 Pa, hence over a measurement span of 11.0 Pa. Over that range, the FvCB model predicts considerable deviation from linearity in the A_{net}-C_c response. Narrower CO_2 ranges reduce that problem by sampling a more localised and nearly linear segment of the curve, while broader ranges encompass greater curvature, increasing the risk of inaccurate estimates. Implicitly assuming linearity across wide CO_2 ranges is misleading and results in notable errors in the estimation of both Γ* and D_L.

These errors are further exacerbated when the selected CO_2 range does not include the Γ^*_{exp}, as the regression may require extrapolation beyond the measured data. This issue is especially pronounced at low temperatures where Γ* is lower, the curvature of the A_{net}–C_c

response is more prominent and where due to instrument limitations, the CO_2 partial pressures used often lie above the Γ^*_{exp}.

3.4.3 Influence of Temperature and Published Discrepancies

A literature review by Walker & Ort (2015), reported variability in the intercellular CO_2 photocompensation point at 25°C, with values ranging from 3.1 to 4.9 Pa, representing a spread of 1.8 Pa at a single temperature. As shown in Figure 3.4, the modelled estimate of Γ* using linear regressions can lead to an underestimate Γ*, with the extent of underestimates depending on the range of partial pressures used and whether it includes or excludes the Γ^*_{exp} (Figure 3.5). This could account for the range of values reported by Walker & Ort (2015).

This variability in the estimates obtained using the Laisk method often arises from the use of CO_2 ranges that do not include the region around Γ*, especially at lower temperatures where Γ* is significantly lower than at higher temperatures. This then requires extrapolation outside the range of measurement CO_2 partial pressures and amplifies the problem of non-capture of the existing curvature in the A_{net}-C_c curve. While this may sometimes reflect instrumental constraints, it may also indicate limited awareness about the importance of selecting a range of CO_2 partial pressures that include the Γ^*_{exp} to ensure accurate estimation of both parameters.

3.4.4 Uncertainty Analysis via Monte Carlo Simulations

The Monte Carlo simulations provided additional evidence of the inherent uncertainty in estimating Γ* and D_L using linear regression or the FvCB model. I found that even small measurement errors in net CO_2 assimilation rates that are within the precision range of modern gas exchange analysers can lead to substantial variability in the estimated intersection points of linear regressions (Figure 3.6). This effect is particularly pronounced when the selected CO_2 range does not include the Γ^*_{exp}, resulting in a wide spread of

possible outcomes and, in some cases, physiologically implausible estimates such as negative values for Γ* and D_L (Figure 3.6).

Even when the Γ^*_{exp} is included within the measurement range, applying linear regressions across a wide CO_2 range still leads to a slight underestimation of Γ* (Table 3.2, Figure 3.6b). In contrast, when a narrow CO_2 range is used, the intersection points obtained through both linear regression and the FvCB model converge to nearly identical values (Figure 3.6a). This suggests that under these specific conditions, both methods can yield comparable estimates of Γ* and D_L. The problem of estimating the non-linear A_{net}-C_c curve with linear relationships could, in principle, be ameliorated by using a narrow range of CO_2 partial pressures. A limited range of C_c may locally approximate linearity within the A_{net}–C_c curve, which would improve the validity of using linear regression in such cases.

When both approaches were tested under the same level of experimental error, the Monte Carlo analysis showed that the variation in Γ* and D_L estimates was markedly lower when using the FvCB model. Considering the physiological and technical constraints discussed above, as well as the findings presented in Figure 3.6 and Table 3.2, implementing the FvCB model in the Laisk Method offers a practical and robust approach for estimating Γ* and D_L across a range of temperatures. The FvCB model performs reliably across both wide and narrow CO_2 ranges and effectively avoids the systematic errors associated with fitting linear regressions and consistently outperforms it, even when the expected Γ^*_{exp} is not included in the CO_2 measurement range.

3.4.5 Advantages of Integrating the FvCB Model into the Laisk Method

To demonstrate the use and application of my methodological proposal to incorporate photosynthetic theory into the Laisk method, I analysed the A_{net}-C_i dataset reported by Yin et al. (2011) and used again in the study by Yin and Amthor (2024). In their article, Yin and Amthor (2024) calculated the apparent Γ* (C_i*) from oxygen partial pressure and Rubisco specificity, resulting in 35 μmol mol^{-1}, and then fixed this value to determine the

apparent D_L. However, the original Laisk method allows both parameters to be estimated from the intersection of at least three linear regressions constructed from A_{net}-C_i curves measured at three sub-saturating light intensities under low CO_2. Fixing C_i* in the Laisk method can introduce methodological error because it constrains the intersection to a value of C_i* set *a priori* rather than letting the data determine it, affecting the estimation of D_L.

This is inconsistent with the Laisk method and can bias D_L, especially when the analysed C_i range is wide or not close to Γ^*_{exp}. Yin and Amthor (2024) reported a D_L value of 0.97 µmol m^{-2} s^{-1} using the linear method, and 1.21 µmol m^{-2} s^{-1} using the non-rectangular hyperbolic equation they proposed, based on chlorophyll *a* fluorescence data. However, when I digitised their data and replotted it, the linear regressions produced different outcomes, yielding three intersections in markedly different locations and therefore widely divergent estimates of C_i* and D_L, as shown in Figure 3.8. This divergence arose because I allowed the data to determine the intersection points rather than imposing a fixed C_i*. The intersections were so widely separated that averaging them to estimate C_i* and D_L was inappropriate.

I then analysed the same data with my proposed approach (Figure 3.8b). I used the J_{max} and θ values reported by Yin and Amthor (2024), requiring only three parameters to be fitted in the model: C_i*, D_L and V_{cmax}. This yielded estimated values of C_i*= 41.6 µmol mol^{-1} and D_L= 0.57 µmol m^{-2} s^{-1}, which were substantially different from those reported by Yin and Amthor (2024).

When I restricted the analysis to a narrower CO_2 range, as recommended in my methodology for more reliable linear regression estimates (Figure 3.8c), the three intersections from the linear regressions lay closer together, yielding a C_i* much nearer to that from my model. Running the model on the same narrow range (dotted line Figure 3.8) gave values that were very close to those from the wide range (Figure 3.8b). C_i* changes from 41.6 to 42.0 µmol mol^{-1} and D_L from 0.57 to 0.64 µmol m^{-2} s^{-1}.

Despite the apparent proximity of the intersections between the linear regressions and the FvCB model when a narrower CO_2 range was used (Figure 3.8c), C_i* was still underestimated by 5.7% and D_L by 23.4%. It showed that even at moderate temperatures, where the issue is less pronounced than at low temperatures, linear regressions can still yield misleading estimates unless a narrow CO_2 range is used that includes or closely brackets Γ^*_{exp} (Figure 3.8a). Therefore, I recommend using the approach based on the FvCB model to obtain more accurate estimates of Γ* and D_L.

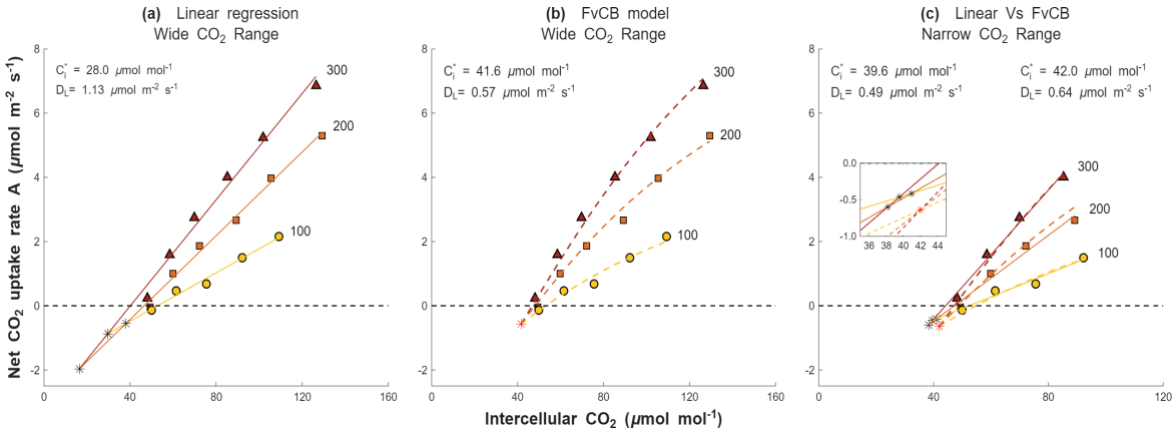

FIGURE 3.8. Linear and non-linear Laisk analyses from wheat leaves at 25 °C. Redrawn using the wheat leaf dataset at 25 °C originally reported by Yin et al. (2011), following the re-plotting and interpretative framework of Yin & Amthor (2024). Net CO_2 assimilation (A, μmol m^{-2} s^{-1}) is plotted against intercellular CO_2 mole fraction (C_i, μmol mol^{-1}). Three light intensities are shown, 100, 200, and 300 μmol photons m^{-2} s^{-1}, encoded as yellow circles, orange squares, and dark-red triangles, respectively. The dotted horizontal line marks A = 0. D_L is reported as a positive magnitude (D_L = R_d). The symbol C_i* denotes the apparent Γ* inferred using C_i. (a) Linear regression using a wide CO_2 range. Straight line fits of A_{net}–C_i for each PPFD. Pairwise intersections of the regressions (black asterisks) are averaged to obtain estimates of C_i* and D_L. (b) FvCB model using the wide CO_2 range. The same data fitted with the full FvCB model. The red asterisk marks the model-based intersection (C_i*, D_L). (c) Comparison between linear and FvCB using a narrower CO_2 range. Black asterisks show linear-method intersections, and the red asterisk shows the FvCB intersection.

3.5 Conclusion

My study shows that the classical Laisk method, when applied across wide CO_2 ranges or without bracketing the Γ^*_{exp}, can yield biased or physiologically implausible estimates of Γ^* and D_L. Integrating the Farquhar, von Caemmerer, and Berry (FvCB) photosynthesis model into the Laisk method:

- Reduces systematic bias by capturing the inherent curvature of the A_{net}–C_c relationship.
- Maintains accuracy across a wide spectrum of temperatures and CO_2 partial pressures.
- Lowers the variance of the estimates under realistic measurement noise, as shown by Monte Carlo.

Refining the Laisk approach with a mechanistic framework not only improves parameter estimation in C_3 plants but also enhances the reliability of carbon-flux models used to predict plant responses to climate change.

4 Temperature dependence of Γ* and D_L

4.1 Introduction

Accurate estimation of CO_2 release by plants in the light is essential for understanding plant carbon balance, predicting photosynthetic rates across temperatures, and scaling physiological processes to canopies and ecosystems (Burgess, 2023; Heskel et al., 2016; Sharkey, 2016). Reliable quantification of leaf CO_2 exchange in the light requires separating gross photosynthesis from concurrent CO_2 losses due to photorespiration and other decarboxylation processes (Busch et al., 2024). This separation becomes possible once Γ* and D_L are estimated from gas-exchange measurements, typically using the Laisk method (Burgess, 2023; Gong et al., 2018; Moreno-Echeverry et al., 2026; Yin & Amthor, 2024).

Γ* is the CO_2 compensation point in the absence of D_L, which allows calculation of the balance between Rubisco carboxylation and oxygenation and thus determines the photorespiratory cost of photosynthesis (Zhang et al., 2024). This parameter is a mechanistic quantity that depends on Rubisco specificity for CO_2 relative to O_2 and on the chloroplast partial pressure of O_2, and on the metabolic integration of metabolites in the photorespiratory pathway (Busch et al. 2018). As temperature rises, Rubisco specificity declines, oxygenation increases relative to carboxylation, and for that reason Γ* increases (Hermida-Carrera et al., 2016; Viil et al., 2012). This shift moves CO_2 compensation points to higher C_c, depresses apparent photosynthetic efficiency at low CO_2, and alters the partitioning between carboxylation limited and electron transport limited regimes (Busch & Sage, 2017; Dusenge et al., 2019). D_L also increases with temperature, and both the magnitude and the curvature of the D_L-Temperature response depend on irradiance, substrate supply, leaf nitrogen, and acclimation state (Atkin et al., 2000; Bernacchi et al., 2001; Cai et al., 2018).

Here, I define D_L as the rate of CO_2 release in the light, arising from mitochondrial respiration together with light-linked anabolic decarboxylation that are tightly coupled to photosynthetic metabolism (Tcherkez et al., 2017; Zheng et al., 2024). These fluxes are coordinated by the malate valve and associated organic acid shuttles, which balance cellular energy and redox status across organelles (Igamberdiev & Bykova, 2023). The malate valve exports reducing power from chloroplasts via the malate oxaloacetate shuttle and helps sustain glycine decarboxylase activity in photorespiration. The citrate valve promotes citrate efflux to support NADPH formation and to supply 2-OG (2-oxoglutarate) for amino-acid and 2-ODD (2-oxoglutarate dependent dioxygenase) biosynthesis (Igamberdiev & Bykova, 2023).

In illuminated leaves, mitochondria shift from acting primarily as ATP factories to functioning as thermodynamic buffers that stabilise ATP/ADP and NAD(P)H/NAD(P)$^+$ ratios across compartments by operating the TCA cycle in an open (hemicycle) mode and engaging non-coupled electron-transport pathways (Igamberdiev & Bykova, 2023). In this context, D_L reflects a composite flux, the sum of mitochondrial TCA activity and anabolic decarboxylation, rather than dark-type respiration alone.

Capturing the temperature dependence of Γ* and D_L is critical because together these parameters set the intercepts and affect the slope of A_{net}–C_c relationships (Busch et al., 2024; Walker & Ort, 2015). Imprecisely parameterised Γ*(T) or D_L(T) directly propagate to inferred values of V_{cmax} and J_{max}, obtained from A_{net}–C_c curves, such that variation in Γ*(T) or D_L(T) can be mistaken for genuine changes in carboxylation or electron transport capacity (Bernacchi et al., 2001; Busch et al., 2024; Sharkey et al., 2007).

Reliable estimates of Γ*(T) and D_L(T) improve the mechanistic understanding of variability in photosynthetic parameters between species and environments and increase confidence in measurement systems by grounding inference in biochemistry rather than in instrumental or methodological artefacts. Reduced parameter uncertainty also enable mechanistic coupling of photosynthesis to energy budgets and metabolite pools,

improving the interpretation of post-illumination CO_2 fluxes and the early dynamics of light–dark transitions.

Here, I extend my previous integration of the Laisk framework with photosynthetic theory to quantify how Γ* and D_L vary with temperature. My objective is to estimate Γ*(T) and D_L(T) from A_{net}–C_i curves. For Γ*, I evaluate the simple Arrhenius and constant-Q_{10} models. I did not fit MMRT to Γ*(T) because MMRT describes temperature effects on catalytic rates via transition state thermodynamics, whereas Γ* is a derived concentration determined by Rubisco specificity and gas solubilities; the theory and my data therefore support near-exponential behaviour over the range. For D_L, I test simple Arrhenius, constant-Q_{10}, and MMRT functions. Model choice prioritises parsimony while capturing observed curvature. For each model, I report parameter estimates with confidence intervals, the local temperature sensitivity s(T) and implied Q_{10}(T), as well as standard goodness of fit metrics.

4.2 Materials and Methods

4.2.1 Plant Growth Conditions and Gas Exchange Measurements

Sunflower (*Helianthus annuus* "Russian Giant") plants were grown in a plant growth unit. Plants were watered daily to field capacity and fertilised weekly with a balanced nutrient solution. The photoperiod was 14 h, day/night air temperatures were 24/19 °C, and relative humidity was around 40 % during the day and approximately 65 % at night. Incident PPFD at the leaf surface during growth was 400 µmol photons m^{-2} s^{-1}.

Gas exchange was measured on fully expanded, upper-canopy leaves using a LI-6400XT portable photosynthesis system (LI-COR Biosciences, Lincoln, NE, USA). Before each temperature curve, the leaf was acclimated for 20 min at the target leaf temperature with chamber relative humidity near 60 %, 40 Pa of CO_2, ambient O_2, 500 µmol photons m^{-2} s^{-1} and recorded atmospheric pressure. Leaf temperatures ranged from 3.9 to 42 °C during the measurements.

4.2.2 Determination of Γ* and D_L

At each target leaf temperature, Γ* and D_L were estimated with the modified Laisk approach as described by Moreno-Echeverry et al. (2026). For every temperature, I measured three A_{net}–C_c curves at low CO_2 partial pressure and under three sub-saturating PPFD levels, while holding leaf temperature constant. Each curve consisted of six to eight measurement points across the low CO_2 range. Each modified Laisk estimate was based on the intersection of three linear regressions fitted, resulting in a total of 56 independent Laisk determinations across all temperatures. The three light levels were analysed jointly in a Laisk-type, low-C_i framework linked to the FvCB model. PPFD was treated as a driver of the initial slope, whereas Γ* and D_L were constrained to be identical across the three curves at that temperature. Under these constraints, the fitted A_{net}–C_c curves shared a single common intersection in (C_c, A_{net}) coordinates, from which Γ* was taken as the x-intercept and D_L as the y-intercept (reported as a positive rate corresponding to a negative A_{net}-intercept). I worked in C_c space through:

$$C_c = C_i - \frac{A_{net}}{g_m} \tag{4.1}$$

where g_m was estimated within a constrained, multi-stage fitting procedure using the full A–C_i dataset across light levels, rather than being inferred from the C_i–C_c relationship alone.". Thus, C_c and g_m were jointly constrained by the model during curve fitting, ensuring internally consistent estimates of V_{cmax}, J_{max}, Γ* and D_L.

To stabilise the common intersection across light levels at each temperature, fitting proceeded in stages for each leaf and temperature, using all A_{net}-C_i data from the three light intensities simultaneously at every stage:

1. **Stage 1**. All parameters free (V_{cmax}, J_{max}, α, θ, D_L, Γ* and g_m), using the combined dataset for that leaf at that temperature across the three light levels.

2. **Stage 2**. Refitting while holding V_{cmax}, J_{max}, α and θ at their first stage estimates and updating Γ*, D_L and g_m. This step allows the common intersection to stabilise while holding the capacity and curvature terms constant.
3. **Stage 3**. final refit of Γ* and D_L with g_m held fixed.

All parameters were estimated with the Excel fitting template developed in my chapter 1, using Solver (GRG Nonlinear) to minimise the sum of squared residuals, under biologically informed bounds.

4.2.3 Temperature-response models for Γ* and D_L

To characterise the temperature dependence of Γ* and D_L, I fitted standard thermal-response functions. For both, I used the constant-Q_{10} and simple Arrhenius models, for D_L, I additionally fitted MMRT. The reference temperature was T_{25} = 298.15 K (25 °C).

Arrhenius/MMRT use absolute temperature T (Kelvin) and the constant-Q_{10} exponent is written per °C. Parameters are reported relative to the value at 25 °C.

Literature benchmark for Γ* and D_L

To provide independent literature benchmarks derived with the Laisk method, I included the in vivo Arrhenius formulations of Bernacchi et al., 2001 for both Γ*(T) and D_L (R_d in their paper). In their parametrisation,

$$\Gamma^*(T)[mmol\ mol^{-1}] = exp\left(c_{\Gamma^*} - \frac{\Delta H_{a,\Gamma^*}}{RT}\right), \quad (4.2)$$

$$R_{day}(T)(normalised) = exp\left(c_{R_{day}} - \frac{\Delta H_{a,R_{day}}}{RT}\right), \ \ R_{day}(25\ ℃) = 1 \quad (4.3)$$

The parameters used were c = 19.02 and ΔH_a = 37.8 kJ mol^{-1}, R is the gas constant and T is in Kelvin. Γ* was converted to Pa using Γ* (Pa) = $\Gamma^*_{\text{mmol mol-1}}$ x P/10^6 with P= 101.000 Pa. Because R_{day} (T) in Bernacchi (2001) is normalised (unitless, equal to 1 at 25 °C), for comparison with my D_L data (µmol CO_2 m^2 s^{-1}) I anchored its magnitude by multiplying the normalised curve by the Arrhenius-estimate $D_{L,25}$.

$$D_L^{Bern}(T) = D_{L,25}^{Arr} \, x \, R_{day}(T). \tag{4.4}$$

Both benchmarks' curves are plotted alongside the fitted models but are excluded from model ranking (AICc) because their coefficients are fixed and not estimated from my data.

Constant-Q_{10} model

$$X(T_c) = X_{25} Q_{10}^{\frac{T_c - 25}{10}}, \tag{4.5}$$

where X is Γ* (Pa) or D_L (µmol CO_2 m^2 s^{-1}), T_c is the leaf temperature in °C, X_{25} is the value at 25 °C, and Q_{10} is the fold-change per 10 °C.

Arrhenius model

$$X(T) = X_{25} \, exp\left[\frac{E_a}{R}\left(\frac{1}{T_{25}} - \frac{1}{T}\right)\right], \tag{4.6}$$

with activation energy E_a (J mol^{-1}), gas constant R = 8.314 Jmol^{-1}K^{-1}, and T in Kelvin. This form preserves $X(T_{25}) = X_{25}$.

MMRT model

$$\ln X(T) = ln\left(\frac{k_B T}{h}\right) + \frac{\Delta S^{\ddagger}}{R} - \frac{\Delta H^{\ddagger}}{RT} + \frac{\Delta C_p^{\ddagger}}{R}\left[1 - \frac{T}{T_{ref}} + ln\left(\frac{T}{T_{ref}}\right)\right], \tag{4.7}$$

where X is D_L, T_{ref} = 298.15 K, k_B is Boltzmann's constant and h is Planck's constant. $\Delta H^{\ddagger}$, $\Delta S^{\ddagger}$ and $\Delta C_p^{\ddagger}$ are fitted activation enthalpy, entropy and heat-capacity change,

respectively. For estimation, I used the algebraically equivalent, numerically stable centred log-linear form according with Liang (2018):

$$\ln X(T) = a + b\left(\frac{1}{T} - \frac{1}{T_{ref}}\right) + c\ln\left(\frac{T}{T_{ref}}\right) + d\,(T - T_{ref}) \qquad (4.8)$$

This parameterisation keeps T in Kelvin, reduces collinearity by centring at T_{ref}, and yields stable robust fits (bisquare weights).

Interpretation of the compact coefficients in the thermodynamic form:

$$\boldsymbol{a} = ln\left(\frac{k_B T_{ref}}{h}\right) + \frac{\Delta S^{\ddagger}}{R} - \frac{\Delta H^{\ddagger}}{RT_{ref}}, \qquad (4.9)$$

$$\boldsymbol{b} = -\frac{\Delta H^{\ddagger}}{R}, \qquad \boldsymbol{c} = 1 + \frac{\Delta C_p^{\ddagger}}{R}, \qquad \boldsymbol{d} = -\frac{\Delta C_p^{\ddagger}}{RT_{ref}}. \qquad (4.10, 4.11, 4.12)$$

I used the compact coefficients *a, b, c*, *d* solely for estimation and did not treat them as directly interpretable thermochemical quantities.

4.2.4 Apparent parameters for cross-model comparison (E_a* and Q_{10}*)

To compare models on a common scale, I fitted ln X(T) by robust non-linear least squares (bisquare weights) with T in Kelvin, and then computed the local log-slope:

$$s(T) = \frac{d\ln X}{dT} \quad [K^{-1}], \qquad (4.13)$$

evaluating at T_{25} = 298.15 K gives the apparent quantities

$$\boldsymbol{E_a^*(T)} = RT^2\, s(T), \qquad \boldsymbol{Q_{10}^*(T)} = \exp[10\, s(T)]. \qquad (4.14, 4.15)$$

For each model the implied X_{25}, s(T), E_a*(T) y Q_{10}*(T) are:

Q_{10} model:

$$\boldsymbol{s(T)} = \frac{ln\ Q_{10}}{10}, \qquad \boldsymbol{E_a^*(T)} = RT^2\frac{\ln Q_{10}}{10}, \qquad \boldsymbol{Q_{10}^*(T)} = Q_{10} \qquad (4.16, 4.17, 4.18)$$

Arrhenius model:

$$\boldsymbol{s(T)} = \frac{E_a}{RT^2}, \qquad \boldsymbol{E_a^*(T)} = E_a, \qquad \boldsymbol{Q_{10}^*(T)} = exp\left[\frac{10E_a}{RT^2}\right]. \quad (4.19, 4.20, 4.21)$$

MMRT model:

$$\boldsymbol{s(T)} = -\frac{b}{T^2} + \frac{c}{T} + d, \qquad (4.22)$$

$$\boldsymbol{E_a^*(T)} = R(-b + cT + dT^2), \qquad \boldsymbol{Q_{10}^*(T)} = exp\left[10\left(-\frac{b}{T^2} + \frac{c}{T} + d\right)\right] \quad (4.23, 4.24)$$

$$At\ T = T_{ref}, \quad \boldsymbol{X_{25}} = \exp(a)$$

Coefficients to describe the thermal response of Γ* and D_L are fixed from Bernacchi et al., 2001. Apparent local sensitivity and implied Q_{10} at 25 °C follow directly from the published activation energies:

$$\boldsymbol{s_{25}} = 100\ \frac{\Delta H_a}{R} T_{25}^{-2} \quad [\%\ °C^{-1}], \qquad (4.25)$$

$$\boldsymbol{E_a^*(T_{25})} = \Delta H_a, \qquad (4.26)$$

$$\boldsymbol{Q_{10,25}^*} = exp\left(10\frac{\Delta H_a}{R}\ T_{25}^{-2}\right). \qquad (4.27)$$

I report Γ^*_{25} in Pa and D_{L25} in μmol m^{-2} s^{-1}. Confidence intervals are not provided because these benchmarks are not fitted to my data.

4.2.5 Arrhenius-coordinate diagnostic

I examined temperature responses in Arrhenius coordinates by plotting ln X against 1000/T (with T in Kelvin), where X denotes either Γ* (Pa) or D_L (μmol CO_2 m^2 s^{-1}). For each parameter, I fitted the linear model [ln(X) = α+βx], x=1000/T, using robust least squares with bisquare weights. The fitted slope β provided a diagnostic of the apparent activation energy via:

$$\boldsymbol{E_a^*} = -1000R\,\beta \tag{4.28}$$

I also report the local temperature sensitivity, *s*(T) and the corresponding Q_{10}* at 25 °C.

$$\boldsymbol{s_{25}} = \frac{100E_a^*}{RT_{25}^2}, \qquad \boldsymbol{Q_{10}^*} = exp\left(\frac{10E_a^*}{RT_{25}^2}\right) \tag{4.29, 4.30}$$

4.2.6 Statistical analysis

Fitting approach and domains

All thermal response models were fitted by nonlinear least squares in MATLAB R2025b. Goodness of fit and parsimony metrics were always computed on the same domain used for fitting 3.9 to 42 °C.

Goodness of fit and parsimony

For observation i, y_i is the observed rate and $\hat{y}_i$ the model prediction; *n* is the sample size in the fitting domain and *k* the number of free parameters.

$$SSE = \sum_{i=1}^{n}(y_i - \hat{y_i})^2, \qquad RMSE = \sqrt{\frac{1}{n}\sum_{i=1}^{n}(y_i - \hat{y_i})^2}. \tag{4.31, 4.32}$$

Model ranking used the small sample corrected Akaike Information Criterion,

$$AIC_c = n \ln\left(\frac{SSE}{n}\right) + 2k + \frac{2k(k+1)}{n-k-1} \tag{4.33}$$

Within each comparison set, I report,

$$\Delta AICc_j = AICc_j - \min_{m \in M} AICc_m, \tag{4.34}$$

And the corresponding Akaike weight,

$$p_j = \frac{\exp\left(-\frac{1}{2}\Delta AIC_{c,j}\right)}{\sum_{m \in M} exp\left(-\frac{1}{2}\Delta AIC_{c,m}\right)} \tag{4.35}$$

Here, M denotes the set of candidate models in the comparison. The ΔAICc values quantify distance to the best model (0 the best). Interpretation follows common thresholds: ΔAICc < 2 (essentially equivalent), 4–7 (some support for the lower-AICc model), >10 (strong support for the lower-AICc model). The weights p_j provide the relative support for each model (summing to 1 across M). For the Bernacchi benchmark curves, I report SSE, RMSE and R^2 against the observations over the same fitting domain for Γ* and D_L but excluded these benchmarks from AICc computation and model ranking because no parameters are fitted to my data. The benchmarks therefore provide an external reference for absolute and local performance while preserving the fairness of the model selection framework.

4.3 Results

Across the 56 Laisk datasets, Γ* rose smoothly with leaf temperature over the measured range (3.9-42.0 °C), showing the gently accelerating increase expected for an exponential-type response (Figure 4.1). In panel (a) I compare the two most widely used Γ* temperature functions: Brooks & Farquhar (1985), derived in vivo from gas-exchange,

and Jordan & Ogren (1984), determined in vitro. The first one was made only between 15 and 30 °C, whereas the second one used data spanning 5 to 40 °C. As a result, extrapolation outside the original calibration windows, especially of the polynomials, is not reliable and, as seen in Figure 4.1, can introduce visible deviation at the extremes. Panel (b) shows that both the simple Arrhenius and the constant-Q_{10} models reproduce the overall trend with comparable fidelity. Discrepancies are small and emerge chiefly near the limits of the temperature range.

The Bernacchi et al (2001) benchmark aligns closely through the mid-temperature range but sits below the observations at cooler temperatures and increases above them towards the warm end, indicating a steeper warm-side sensitivity than observed here. Overall, for Γ*, either empirical formulation (Arrhenius or constant-Q_{10}) provided an adequate description over the experimental span, with the Bernacchi curve serving as an external check.

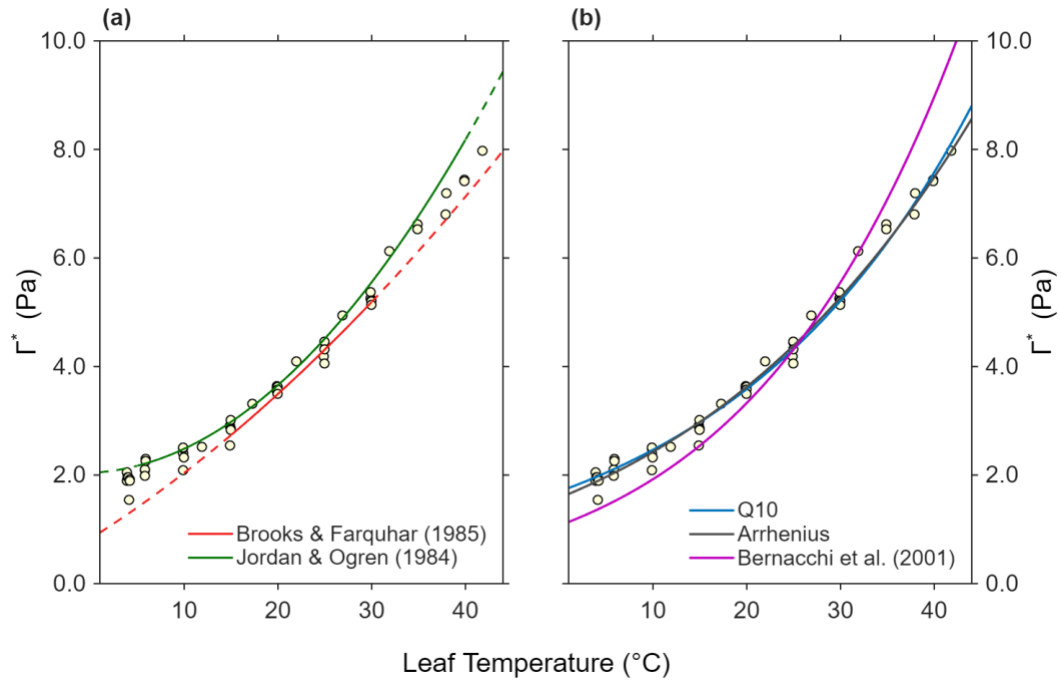

Figure 4.1. Temperature dependence of Γ* (Pa). (a) Comparison of the Brooks and Farquhar, 1985 and Jordan and Ogren, 1984 parameterisations. Solid segments indicate the author's reported

temperature ranges, dashed lines are extrapolations. (b) Fits of simple Arrhenius and constant-Q_{10} models to my data, with the fixed in-vivo benchmark of Bernacchi et al. (2001) overlaid. Symbols are observations; lines denote model predictions/benchmark.

Table 4.1. Parameter estimates for the temperature dependence of Γ* under two alternative models. $\Gamma^*_{(25)}$ is Γ* at 25 °C in pascals. For the constant-Q_{10} model the fitted parameter is Q_{10}; an apparent activation energy E_a* is reported. For the Arrhenius model, the fitted parameters were $\Gamma^*_{(25)}$ and the activation energy E_a. An apparent Q_{10}* is also reported. Red asterisks denote parameters not fitted in that model but computed to aid cross-model comparability, they should be interpreted as apparent values conditional on the assumed model form. Confidence intervals for derived quantities were obtained by propagation of uncertainty from the fitted parameters.

Parameter	Model	Estimate	95% CI
Γ^*_{25} (Pa)	Constant-Q_{10}	4.36	[4.31, 4.40]
	Arrhenius	4.39	[4.34, 4.44]
E_a (kJ mol^{-1})	Constant-Q_{10}	28.47*	[27.74, 29.19]
	Arrhenius	27.62	[26.83, 28.41]
Q_{10}	Constant-Q_{10}	1.47	[1.46, 1.48]
	Arrhenius	1.44*	[1.42, 1.47]
s_{25} (% °C^{-1})	Constant-Q_{10}	3.85	[3.77, 3.94]
	Arrhenius	3.74	[3.65, 3.82]

Parameter estimates for Γ* at 25 °C were virtually identical across models (Table 4.1): Γ^*_{25} was 4.36 Pa under the constant-Q_{10} fit and 4.39 Pa under Arrhenius, with narrow, overlapping 95% CIs. The two models also yielded similar temperature sensitivities at 25 °C (s_{25}= 3.7-3.9 % °C^{-1}). As expected, the models express that sensitivity with different primary coefficients. The constant-Q_{10} fit gave Q_{10} = 1.47, while the Arrhenius fit estimated E_a = 27.62 kJ mol^{-1}. When expressed on the common apparent scale, the Q_{10}-derived E_a* (28.47 kJ mol^{-1}) and the Arrhenius-derived Q_{10}* (1.44) closely match their counterparts, reinforcing that both formulations describe a moderate thermal dependence of Γ*. The fixed Bernacchi (2001) benchmark converted to 4.31 Pa at 25°C with ΔH_a = 37.83kJ mol^{-1}, implying s_{25}=5.12 % °C^{-1} and $Q^*_{10\ 25}$=1.64, consistent with species/protocol differences and the fact that these coefficients are not fitted to the dataset.

Goodness of fit metrics were similarly high for both models, with a R^2 = 0.99 in each case (Table 4.2). The constant-Q_{10} model achieved slightly lower SSE and RMSE, and the best AICc (-204.7), giving ΔAICc=0 for Q_{10} and ΔAICc = 7.20 for Arrhenius. By conventional thresholds, this constitutes strong support for the constant-Q_{10} model over Arrhenius for Γ* across the temperature range, while acknowledging that the differences were small for practical purposes. For context, the fixed Bernacchi (2001) benchmark, yielded SSE = 19.735, RMSE = 0.578 and R^2 = 0.88 against the observations over the same temperature domain, reflecting expected offsets for a literature curve not fitted to these data.

Table 4.2. Goodness of fit and information criteria for the models in Figure 4.1b. Reported metrics are R^2 (coefficient of determination), SSE (the sum of squared residuals), RMSE (root-mean-squared error, same scale as the response), AICc (small-sample corrected Akaike Information Criterion) and ΔAICc (difference from the best model within each trait). Lower SSE, RMSE and AICc indicate better fit. Model selection was based on the native fitted parameters only; the apparent quantities marked with red asterisks in Table 4.1 were provided solely for interpretability and do not influence these metrics.

Model	R^2	SSE	RMSE	AICc	ΔAICc
Q_{10}	0.989	1.343	0.155	-204.7	0
Arrhenius	0.990	1.528	0.165	-197.5	7.2
Bernacchi	0.879	18.735	0.578	-	-

D_L increased smoothly across the measured range and accelerates toward the warm end. The constant-Q_{10} and Arrhenius curves remained essentially exponential throughout, at 45 °C the Q_{10} prediction was higher than the Arrhenius prediction. The MMRT curve followed the same rise at cool-moderate temperatures but showed a subtle change in curvature at the hottest end, bending slightly rightwards and thus departing from a pure exponential. Consequently, near 45 °C, the Q_{10} and MMRT predictions were very close, with Q_{10} giving marginally higher values, while Arrhenius gave the lowest. Overall, model separation remained modest and remained confined to the warmest temperatures (Figure 4.2).

In the MMRT fit, the curvature coefficient *d* was not significantly different from zero (its 95% CI included 0), consistent with $\Delta C_p^{\ddagger} \approx 0$ over the experimental range. The coefficient *c* was also poorly constrained (ill-conditioned). Taken together, and given the parameter non-identifiability, there was no statistical evidence for a non-zero $\Delta C_p^{\ddagger}$ within the temperature span.

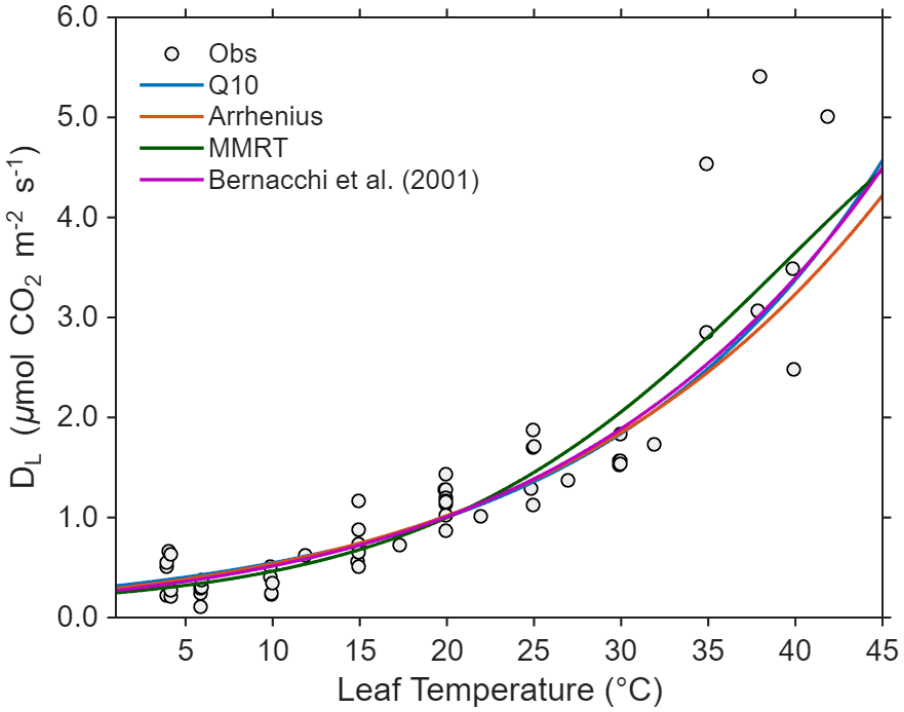

Figure 4.2. Observed rates of D_L (μmol CO_2 m^{-2} s^{-1}) are plotted against leaf temperature, together with model predictions from three alternatives: a constant-Q_{10} model, a simple Arrhenius model, and an Eyring-based MMRT. Fits were obtained by non-linear least squares. The magenta line shows the Bernacchi et al (2001) day-respiration benchmark, normalised in the original study and here scaled to my $D_{L,25}$ (Arrhenius) to place it in absolute units; it is provided for reference only. Lines show the fitted curves evaluated over the plotted temperature range, and symbols show the data.

Across the three models, the 25 °C rate clustered tightly at $D_{L,25}$ around 1.36-1.45 μmol CO_2 m^{-2} s^{-1}, with overlapping 95% CIs (Q_{10}: 1.36 [1.19, 1.53]; Arrhenius: 1.38 [1.20, 1.56]; MMRT: 1.45 [1.27, 1.66]). Thermal sensitivity differed modestly by model (Table 4.3). The MMRT fit implied the strongest response at 25 °C, with s_{25}= 7.26% C^{-1} and an effective Q_{10}* = 2.07. The Arrhenius and constant-Q_{10} fits were slightly lower and similar to each other: s_{25}= 5.97% C^{-1} (Arrhenius) and 6.06% C^{-1} (Q_{10}), corresponding to Q_{10}* = 1.78 and Q_{10} = 1.83, respectively.

Table 4.3. Parameter estimates for the temperature dependence of D_L under three alternative models. $D_{L,25}$ is the rate at 25 °C in μmol CO_2 $m^{-2}s^{-1}$. In the constant-Q_{10} model, $D_{L,25}$ and Q_{10} were fitted, and the local temperature sensitivity at 25 °C and the apparent activation energy are reported. In the Arrhenius model, $D_{L,25}$ and E_a were fitted, with the s_{25} and the apparent Q_{10}* reported for comparison. For MMRT $D_{L,25}$, s_{25}, and the apparent quantities E_a* and Q_{10}* at 25 °C are reported. Red asterisks mark parameters that were not fitted within that model but calculated to aid cross model comparability. Confidence intervals for derived quantities were obtained by propagation of uncertainty from the fitted parameters.

Parameter	Model	Estimate	95% CI
$D_{L,25}$ (μmol m^2 s^{-1})	MMRT	1.45	[1.27, 1.66]
	Arrhenius	1.38	[1.20, 1.56]
	Q_{10}	1.36	[1.19, 1.53]
E_a (kJ mol^{-1})	MMRT	53.67*	[45.49, 61.86]
	Arrhenius	44.11	[35.35, 52.88]
	Q_{10}	44.82*	[40.45, 49.19]
Q_{10}	MMRT	2.07*	[1.85, 2.31]
	Arrhenius	1.78*	[1.68, 1.89]
	Q_{10}	1.83	[1.63, 2.04]
s_{25} (% $°C^{-1}$)	MMRT	7.26	[6.16, 8.37]
	Arrhenius	5.97	[5.35, 6.59]
	Q_{10}	6.06	[5.47, 6.66]

On the apparent scale, the three models yielded activation energies in the range 44-54 kJ mol^{-1} and Q_{10} (or Q_{10}*) values of 1.78-2.07. This combination indicates a strong thermal sensitivity of D_L around 25 °C. It falls squarely within the widely cited range for enzyme-mediated respiratory processes in leaves ($Q_{10} \approx 2$; $E_a \approx$ 45-60 kJ mol^{-1}) across species and biomes (Atkin & Tjoelker, 2003; Cai et al., 2018; Heskel et al., 2016). As an external reference, the Bernacchi et al. (2001) day-respiration curve (normalised in the original study) was scaled by my Arrhenius $D_{L,25}$ to place it in absolute units. Over the same domain it gave $D_{L,25}$ = 1.379 μmol CO_2 m^{-2} s^{-1}, s_{25} = 6.277 % C^{-1} (implied $Q_{10,25}$ = 1.836).

Model-fit metrics were high and had similar R^2 values (0.78-0.82). Residual scatter (RMSE) was small for all models (0.49-0.54 on the response scale). AICc nonetheless differentiated them: MMRT had the lowest value (-71.38) and the highest Akaike weight (0.74), Q_{10} was competitive (AICc -68.91; weight 0.22), and Arrhenius received the least support with AICc -65.60 and 0.04 of weight (Table 4.4). The Bernacchi et al. (2001) benchmark, assessed over the same domain but not fitted, yielded R^2 = 0.798, SSE = 14.795 and RMSE = 0.514.

In Arrhenius space, both traits show clear, near-linear trends across the sampled range. For Γ* (Figure 4.3a) the observations, expressed as ln(Γ*), fall tightly on a straight line and the two model curves are practically coincident, with only negligible spread at the warm end. For D_L (Figure 4.3b), ln (D_L) decreases almost perfectly linearly with 1000/T. MMRT predicts the highest values compared with the other models at the warm end, with the spacing widening slightly toward the cold end.

In summary, all three models describe D_L(T) well. MMRT captures a slightly stronger curvature/temperature sensitivity and is favoured by information criteria, while the constant-Q_{10} gives a comparably good empirical description. Arrhenius performs marginally worse over the full temperature range.

Table 4.4. Goodness of fit and information criteria for the three fitted models MMRT, Arrhenius and constant-Q_{10}. The Bernacchi et al. (2001) day-respiration benchmark is included for reference only. Reported metrics are R^2 (coefficient of determination), SSE (the sum of squared residuals), RMSE (root-mean-squared error, same scale as the response), AICc (small-sample corrected Akaike Information Criterion) and Akaike weight. Model selection is based on the native fitted parameters only; the apparent quantities marked with red asterisks in Table 4.3 are provided solely for interpretability and do not influence these metrics.

Model	R^2	SSE	RMSE	AICc	Weight
MMRT	0.817	13.38	0.488	-71.378	0.74
Arrhenius	0.780	16.09	0.536	-65.602	0.04
Q_{10}	0.793	15.17	0.520	-68.914	0.22
Bernacchi	0.798	14.79	0.514	-	-

For Γ*, the apparent activation energy from the linear fit [ln X = α + β (1000/T)] was 27.42 kJ mol^{-1}, indicating a moderate thermal dependence (Figure 4.3a). The local temperature sensitivity at 25 °C was 3.71 % $°C^{-1}$, implying that Γ* increases by 3.7 % per °C around this temperature. Consistent with this, the Q_{10}* was 1.45, meaning a 10 °C rise multiplies Γ* by 1.45. For D_L, the E_a* was 51.15 kJ mol^{-1}, consistent with s_{25} = 6.92% $°C^{-1}$ and Q_{10}*=1.99 (a doubling per 10 °C; Figure 4.3b).

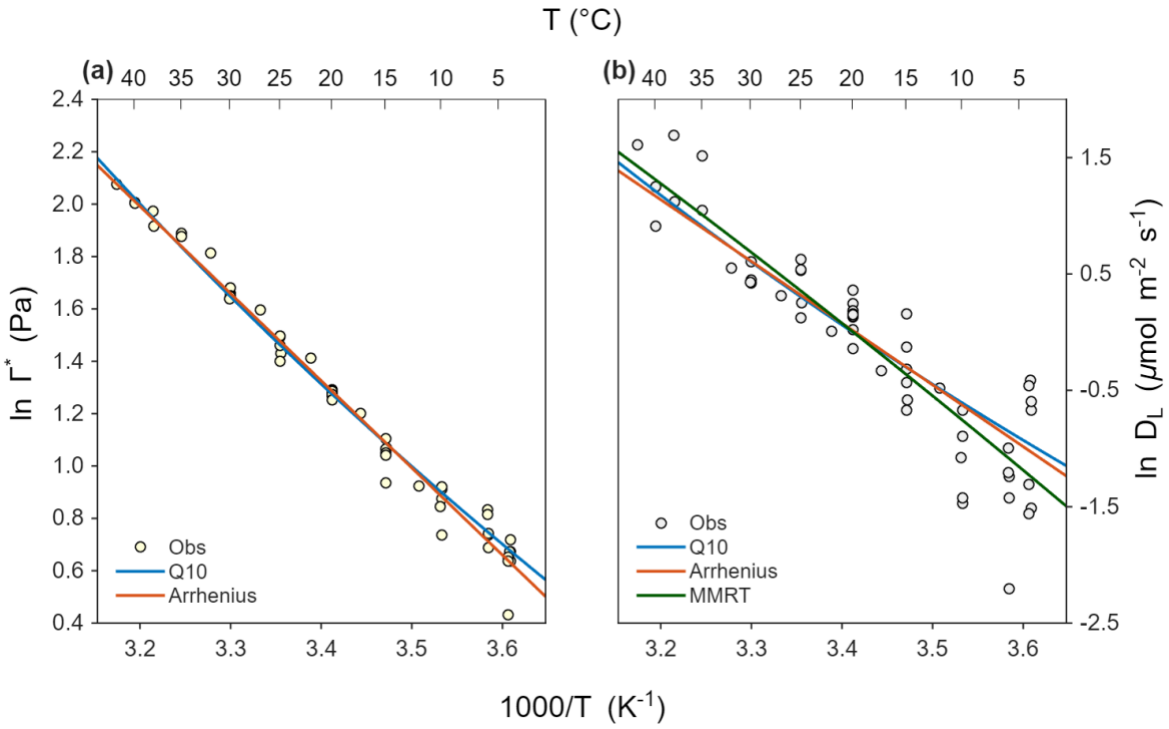

Figure 4.3. Arrhenius plots for the temperature responses of Γ* and D_L. (a) ln of Γ* vs 1000/T (K^{-1}). (b) ln of D_L vs 1000/T (K^{-1}). Symbols show the observations; solid lines are model predictions (Q_{10} in blue, Arrhenius in orange, and MMRT in green). Fits were obtained by non-linear least squares. The upper x-axis gives the corresponding temperature in °C; y-axes are natural-log scales with units indicated.

4.4 Discussion

4.4.1 Interpreting the temperature dependence of Γ*

The temperature dependence of Γ* arises from Rubisco biochemistry. In the FvCB model, Γ* = O/(2$S_{c/o}$), so it reflects the balance between Rubisco carboxylation and oxygenation and is proportional to oxygen partial pressure (Galmés et al., 2016). With warming, Γ* increases primarily because the CO_2:O_2 specificity factor ($S_{c/o}$) declines as the oxygenation transition state becomes relatively favoured (Bernacchi et al., 2001).

The apparent activation energy for Γ* in sunflower in this study (E_a* ≈ 27-28 kJ mol^{-1}) lies at the upper edge of the interspecific range reported from Rubisco-specificity analyses in C_3 plants ≈ 19.8-26.5 kJ mol^{-1}; *Glycine max* at 26.5 kJ mol^{-1} (Hermida-Carrera et al., 2016). By contrast, Bernacchi et al. (2001) reported a higher value for *Nicotiana tabacum* (E_a ≈ 37.8 kJ mol^{-1}), plausibly reflecting differences in species, growth conditions and estimation methodology.

Physiologically, a 3.7% °C^{-1} rise in Γ* has tangible consequences. Because Γ* sets the photorespiratory load at low C_c, warming shifts the A_{net}-C_c curve rightwards and increases the CO_2 compensation point in the absence of D_L, thereby depressing A_{net} unless carboxylation capacity or g_m increase in parallel (Busch & Sage, 2017). This helps to explain why cooler conditions often favour C_3 photosynthesis at ambient CO_2, whereas hot, low-CO_2 environments accentuate photorespiration.

The fixed in-vivo benchmark of Bernacchi et al., (2001) yields a Γ*$_{25}$ very close to mine (≈ 4.32 Pa vs 4.36-4.39 Pa), but a steeper local sensitivity at 25 °C (s_{25} ≈ 5.1 % °C^{-1}, Q*$_{10,25}$ ≈ 1.64) than my fitted values (≈ 3.7-3.9 % °C^{-1}). This difference is consistent with species/protocol effects and with the explicit O_2-dependence of Γ*. In my measurements O_2 was held constant and Γ*(T) was estimated from the improved Laisk method (Moreno-Echeverry et al., 2026), producing a near-exponential response across the sampled range that falls well within published interspecific ranges.

4.4.2 Interpreting the temperature dependence of D_L

D_L is not synonymous with dark-type mitochondrial respiration alone. In the light, CO_2 release also arises from anabolic decarboxylation tightly coupled to biosynthetic demand (Araújo et al., 2014; Tcherkez et al., 2024). For example, plastidial pyruvate dehydrogenase supplies acetyl-CoA for fatty-acid synthesis, releasing CO_2 from pyruvate; the oxidative pentose-phosphate pathway (OPPP) decarboxylates 6-phosphogluconate to ribulose-5-phosphate, providing reducing power and ribose precursors for sucrose and nucleotide formation, and isocitrate dehydrogenase decarboxylates isocitrate to 2-

oxoglutarate (2-OG), a key carbon skeleton for amino-acid biosynthesis (Araújo et al., 2014; Galili et al., 2014; Lin & Oliver, 2008; Tcherkez et al., 2024; Tcherkez & Atkin, 2021).

Each step is enzyme-catalysed and therefore temperature-responsive. Taken together with TCA-linked fluxes, these routes can amplify the apparent E_a* and Q_{10}* of D_L as biosynthetic demand rises. This view is consistent with illuminated mitochondria acting as thermodynamic buffers that coordinate ATP/ADP and redox balance across compartments via malate and citrate valves (Igamberdiev & Bykova, 2023), thereby tightening the coupling between photosynthetic metabolism and light-linked CO_2 release.

Mechanistically, photorespiratory NADH elevates the mitochondrial reduction state in the light, activating the alternative oxidase (AOX) and internal dehydrogenases and biasing the TCA towards an open hemicycle (Igamberdiev & Bykova, 2023). Citrate efflux to the cytosol supports NADPH generation and 2-oxoglutarate production via the citrate valve, thereby sustaining amino-acid biosynthesis and other 2-oxoglutarate-dependent reactions (Igamberdiev & Bykova, 2023). Within this redox-buffering framework, D_L is expected to show a non-linear temperature response, increasing more steeply per degree Celsius at higher temperatures as enzymatic rates in mitochondrial metabolism accelerate. This provides a mechanistic basis for why D_L should not be considered equivalent to dark respiration. Consistent with this interpretation, the thermal sensitivity of D_L observed here is stronger than that typically reported for dark respiration, supporting a dominant role of mitochondrial control of CO_2 release in the light. Enzyme-limited reactions in the TCA cycle and the mitochondrial electron-transport chain commonly exhibit activation energies of approximately 45–60 kJ mol^{-1} (Atkin & Tjoelker, 2003; Bernacchi et al., 2001; Cai et al., 2018; Heskel et al., 2016), and the E_a* estimated for D_L in this study falls within this physiological range.

At moderate temperatures, respiratory fluxes are strongly temperature-sensitive; however, the apparent sensitivity (e.g. Q_{10}, s_{25}) depends on the measurement temperature and the

model used. For dark respiration, reported Q_{10} values cluster around 2.0, but commonly span 1.3–2.5 as irradiance, substrate supply, leaf nitrogen and thermal acclimation vary (Covey-Crump et al., 2002; Heskel et al., 2016; Tjoelker et al., 2001). Moreover, Q_{10} typically declines with measurement temperature as control shifts from enzyme limited capacity (i.e. the maximal catalytic/transport potential of the pathway) to resource limitation (restricted by available substrates and adenylate/phosphate balance) (Atkin & Tjoelker, 2003; Covey-Crump et al., 2002). Consequently, both the magnitude and curvature of $D_L(T)$ can vary across species and measurement protocols. Within the physiological leaf-temperature range, many datasets are well described without imposing a warm-side deactivation term for D_L (Bernacchi et al., 2001; Cai et al., 2018). Short-term regulatory adjustments and long-term changes in respiratory machinery both moderate the temperature response (Atkin & Tjoelker, 2003).

The biosynthetic demand for membrane lipids, stromal protein turnover and sucrose export often increases as leaf temperatures increase (Fan et al., 2024; Mathieu et al., 2018; Saidi et al., 2010). This means that chloroplastic and cytosolic decarboxylation fluxes must also scale with temperature, shifting the partitioning of D_L away from strictly mitochondrial origins. Conversely, under sink limitation (e.g., restricted export/phloem loading or phosphate shortage) these anabolic decarboxylation routes may down-regulate, reducing D_L without a change in core mitochondrial capacity (Buckley & Adams, 2011; Paul & Foyer, 2001).

Bernacchi's $R_{day}(T)$ is a normalised Arrhenius function (equal to 1 at 25 °C) derived via Laisk method in tobacco plants. To compare with my D_L (μmol CO_2 m^{-2} s^{-1}), I scaled that fixed-shape curve by my $D_{L,25}$ (from the Arrhenius fit) to place it on an absolute scale. Across the same temperature range, it tracked the mid-range values of D_L reasonably but diverged at the extremes, indicating a steeper warm-side sensitivity here. Such differences are plausible given species and protocol contrasts, and growth and acclimation histories. Because its coefficients are fixed a priori and not estimated from my data, I treat the

Bernacchi function as an external reference rather than including it in model ranking; it is useful for context, but not for AICc comparison.

4.5 Conclusion

The temperature dependence of Γ* and D_L can be captured with simple equations that are both empirically robust over my measurement range. For Γ*, a constant-Q_{10} model provides the strongest statistical support and offers a parsimonious empirical description, whereas for D_L, the MMRT model was favoured and better reflected the slight warm-end curvature observed. Importantly, practical differences between models were small across most temperatures, so model selection should prioritise parsimony, biological plausibility, and the intended use of the parameters.

Viewing D_L as a light-linked composite flux, rather than as an approximate measure of dark respiration, provides a useful framework for interpreting its temperature dependence. Likewise, estimating both traits from common Laisk intersections in C_c space reduces methodological artefacts and improves transferability to V_{cmax} and J_{max} fitting, and to crop and land surface models.

5 Temperature dependence of V_{cmax} and J_{max}

5.1 Introduction

Plants play a key role as carbon sinks through photosynthesis, capturing atmospheric CO_2 and storing it temporarily. This process supports plant growth and development, underpins terrestrial primary production, and is strongly modulated by environmental factors (Chen et al., 2024; Liao et al., 2023). Among environmental factors, temperature exerts a dominant control on photosynthesis because it directly regulates the rates of the underlying biochemical reactions (Crous et al., 2022; Moore et al., 2021). Most of these reactions are enzyme mediated, and both catalytic rates and structural stability vary markedly with temperature.

Photosynthetic parameters, such as the maximum rate of carboxylation by Rubisco (V_{cmax}) and the maximum rate of electron transport (J_{max}), show pronounced temperature dependence (Kumarathunge et al., 2019). Their thermal optima are not universal but vary with species, environmental conditions, and the physiological state of the plant (Machino et al., 2021; Yamaguchi et al., 2016). However, at temperatures above the thermal optimum, photosynthesis can be impaired by multiple mechanisms. These include irreversible processes such as protein denaturation and loss of membrane integrity (Lee et al., 2024; Yanhui et al., 2020), and partially reversible processes such as elevated production of reactive oxygen species (ROS), which can be neutralised by antioxidant systems (Devireddy et al., 2021; Khorobrykh et al., 2020).

Rubisco activation declines with increasing leaf temperature, and this pattern is better explained by regulation through Rubisco activase (Rca) than by changes in Rubisco content (Perdomo et al., 2017; Scafaro et al., 2018). Rubisco activase is an ATP-dependent

chaperone that removes inhibitory sugar phosphates from Rubisco active sites. The thermal behaviour of Rca depends on isoform composition, sensitivity to the ADP to ATP balance, redox state and post translational modifications, leading to genotype and environment specific temperature responses of Rubisco activation (Amaral et al., 2024; Crafts-Brandner & Law, 2000; Perdomo et al., 2017; Salvucci & Crafts-Brandner, 2004; Scafaro et al., 2019). Increasing leaf temperature alters the stromal environment and can increase thylakoid proton leak, which constrains Rubisco activase and lowers the fraction of active Rubisco (Crafts-Brandner & Law, 2000; Filaček et al., 2022; Salvucci & Crafts-Brandner, 2004).

From a thermodynamic perspective, enzyme temperature responses can be interpreted with transition state theory (Arcus et al., 2016). The rate constant depends on the activation free energy ($\Delta G^{\ddagger}$), which is set by the enthalpy of activation ($\Delta H^{\ddagger}$), and the entropy of activation ($\Delta S^{\ddagger}$), such that $\Delta G^{\ddagger} = \Delta H^{\ddagger} - T\Delta S^{\ddagger}$. When the heat capacity change on activation ($\Delta C\mathrm{p}^{\ddagger}$) is negative, both $\Delta H^{\ddagger}$ and $\Delta S^{\ddagger}$ vary with temperature, which produces the characteristic curvature and a thermal optimum (Arcus et al., 2016; Liang et al., 2018). At temperatures above this optimum, increases in $\Delta H^{\ddagger}$ together with shifts in $\Delta C_{\mathrm{p}}^{\ddagger}$ raise $\Delta G^{\ddagger}$, reducing catalytic rates and causing reversible thermodynamic deactivation (Arcus et al., 2016). This provides a quantitative rationale for the reversible loss of Rubisco activation when heat limits Rubisco activase and activity is restored on cooling.

The characterisation of thermal responses in biological processes has traditionally relied on empirical and semi mechanistic equations. The Arrhenius equation is widely used as a parsimonious description of temperature dependence and for tis practical value in model parameterisation (Galmés et al., 2016a; Tikhonov & Vershubskii, 2020). In its original form, the Arrhenius equation assumes a constant activation energy and predicts an exponential increase in rate with temperature.

At the intact leaf level, net CO_2 assimilation rate reflects interacting components that respond differently to temperature: V_{cmax}, J_{max} and triose phosphate utilisation, and is

further constrained by CO_2 diffusion through stomata and mesophyll to the chloroplasts (Evans, 2021; Farquhar et al., 1980; Flexas et al., 2012; Warren & Dreyer, 2006). As temperature rises, Rubisco's specificity for CO_2 relative to O_2 declines and the photorespiratory CO_2 compensation point (Γ^*) increases. This shifts the net balance towards oxygenation, so net assimilation can peak and then decline even if the underlying capacities for V_{cmax} and J_{max} continue to increase with temperature (Brooks & Farquhar, 1985; Jordan & Ogren, 1984). However, at the leaf level these interacting components often produce curvature in log rate versus temperature, and clear thermal optima that the original formulation cannot capture (Bauerle et al., 2012; Crous et al., 2022; Kositsup et al., 2009; Slot & Winter, 2017). To address these limitations, extensions have been proposed, including the peaked Arrhenius with high temperature deactivation for V_{cmax} and J_{max}, which captures both the initial rise and the decline above the thermal optimum and has been applied in field and controlled studies (Benomar et al., 2019; Bermudez et al., 2021; Fürstenau Togashi et al., 2018; Kumarathunge et al., 2019). Empirical fits have also been used to describe curvature, including non-mechanistic equations fitted to A_{net} as a function of temperature, although extrapolations require caution (Bauerle et al., 2012; Kositsup et al., 2009).

Although useful, these approaches do not impose thermodynamic constraints or represent how $\Delta H^{\ddagger}$ and $\Delta S^{\ddagger}$ vary with temperature, nor do they account for variation in $\Delta C_p^{\ddagger}$ (Arcus et al., 2016; Hobbs et al., 2013; Liang et al., 2018). Macromolecular rate theory (MMRT) explicitly incorporates $\Delta C_p^{\ddagger}$, reproducing both the rise and the decline beyond the thermal optimum and yielding thermodynamically interpretable parameters, $\Delta H^{\ddagger}$, $\Delta S^{\ddagger}$ and $\Delta C_p^{\ddagger}$, from which the optimal temperature (T_{opt}) and the inflection temperature (T_{inf}) can be derived (Liang et al., 2018).

In leaf respiration, MMRT has been shown to outperform Arrhenius models and to perform comparably to flexible log-polynomial formulations when evaluated at the global scale (Alster et al., 2022; Duffy et al., 2021; Liang et al., 2018; Numa et al., 2021; Schipper et al., 2019). Beyond leaves, MMRT has also been applied to soil microbial and total soil respiration, providing a unifying framework for describing temperature responses across biological scales (Numa et al., 2021; Schipper et al., 2019). Across these systems, the heat-capacity term $\Delta C_p^{\ddagger}$ behaves as a conserved thermal trait across biomes and functional groups, whereas the pre-exponential factor a and the reference rate $k(T_0)$ vary systematically with acclimation and environmental history (Alster et al., 2022; Duffy et al., 2021).

Despite these advances, direct applications of MMRT to photosynthesis, and specifically to V_{cmax} and J_{max}, remain unexplored. To address this gap, I characterised the temperature dependence of photosynthesis in sunflower by evaluating V_{cmax} and J_{max} through a comparative analysis of the peaked Arrhenius model and MMRT. This approach allows determination of the extent to which MMRT changes the representation of the full shape of the temperature response curve and the estimation of key thermal parameters relative to simpler models.

5.2 Materials and Methods

5.2.1 Plant Growth Conditions and Gas Exchange Measurements

Sunflower (*Helianthus annuus* "Russian Giant") plants were grown inside a plant growth unit. Plants were watered daily to field capacity and fertilised weekly with a balanced nutrient solution. Day/night air temperature was 24/19 °C, with relative humidity at approximately 40 % during the day and 65 % at night. A 14 h photoperiod was supplied, providing a photosynthetic photon flux density (PPFD) of 400 μmol photons m^{-2} s^{-1} at the leaf surface. Gas-exchange measurements were conducted on fully expanded upper-

canopy leaves using a LI-6400XT portable photosynthesis system (LI-COR Biosciences, Lincoln, NE, USA).

Before each measurement, the selected leaf was acclimated for 20 min at the target leaf temperature under chamber conditions set to approximately 60 % relative humidity, a PPFD of 2000 μmol m^{-2} s^{-1}, and a CO_2 partial pressure of 40 Pa. A_{net}–C_i curves were generated by varying the chambrer inlet CO_2 from 200 to 5 Pa, with leaf temperatures ranging from 5.4 to 44.3 °C.

5.2.2 Estimation of V_{cmax} and J_{max} from A_{net}–C_i Curves

V_{cmax} and J were estimated from A_{net}–C_i response curves using the Farquhar, von Caemmerer and Berry model of C_3 photosynthesis (Farquhar et al., 1980), incorporating modifications of Kirschbaum & Farquhar (1984) and Ubierna et al. (2019). Full equations and temperature functions are provided in Chapter 2, Section 2.4. Ambient pressure was 101.6 kPa and oxygen was 21 %. The Michaelis Menten constants at 25 °C were K_c (25) = 0.037 kPa and K_o (25) = 35.1 kPa (Jordan & Ogren, 1984; von Caemmerer & Quick, 2000). Activation energies were E_a (K_c) = 59.4 kJ mol^{-1} and E_a (K_o) = 35.9 kJ mol^{-1} (Sharkey et al., 2007), and the gas constant was R = 8.314 J mol^{-1} K^{-1}. The photorespiratory compensation point was computed as $\Gamma^* = 42.7 + 1.68(T - 25) + 0.012(T - 25)^2$ where T is leaf temperature in °C (Brooks & Farquhar, 1985). Fits were obtained using nonlinear least squares in MATLAB R2025b.

5.2.3 Temperature dependence modelling of V_{cmax} and J_{max}

The temperature dependencies of normalised V_{cmax} and J_{max} were characterised as a function of leaf temperature using two alternative models: Macromolecular Rate Theory (MMRT) and the peaked Arrhenius function.

First, to anchor the response around the observed rise to the empirical optimum, I fitted a cubic polynomial to the normalised trait over the ascending limb of the response. For a

polynomial $y(T) = aT^3 + bT^2 + cT + d$ (with T in °C), the inflection temperature (T_{inf}) was defined as the real root of the second derivate, $y''(T) = 6aT + 2b$, hence:

$$T_{inf} = -\frac{b}{3a}, \quad yT_{inf} = y(T_{inf}) \tag{5.1}$$

These anchors were then converted to Kelvin for model evaluation and used as reference points in MMRT by setting $T_0 = T_{inf}$ and enforcing a pass through $[T_{inf}, y(T_{inf})]$. Next, I implemented MMRT in its T_{inf} anchored form (the formulation used for fitting). Let $x = T/T_{inf}$ with T in Kelvin and $R = 8.314$ J mol^{-1} K^{-1}. The anchored MMRT writes the rate relative to the anchor as:

$$ln\left[\frac{k(T)}{k_{inf}}\right] = 1 + \sqrt{\frac{-\Delta C_P^{\ddagger}}{R}}(x-1) + \frac{\Delta C_P^{\ddagger}}{2R}(x-1)^2 \tag{5.2}$$

I fixed T_{inf} and kT_{inf} (= yT_{inf} for normalised traits) from the polynomial step and estimated only $\Delta C_p^{\ddagger}$ by nonlinear least squares on the ascending limb data (for V_{cmax}: 5-35 °C; for J_{max}: 5-31 °C), evaluating temperature in Kelvin. I enforced the physically motivated constraint $\Delta C_p^{\ddagger} < 0$ (bounds [-4000, -10^{-3}] J mol^{-1} K^{-1}; initial value -1000 J mol^{-1} K^{-1}). Full range predictions were reconstructed as:

$$k\,(T) = k_{inf} * exp + \left(1 + \sqrt{\frac{-\Delta C_P^{\ddagger}}{R}}(x-1) + \frac{\Delta C_P^{\ddagger}}{2R}(x-1)^2\right) \tag{5.3}$$

with $x = T/T_{inf}$ and R = 8.314 J mol^{-1} K^{-1}. The baseline optimum followed from d ln k/dT = 0, with

$$a_{lin} = 1 + \sqrt{\frac{-\Delta C_p^{\ddagger}}{R}}, \qquad b_{quad} = \frac{\Delta C_P^{\ddagger}}{2R}, \qquad x_{opt} = \frac{-a_{lin}}{2b_{quad}} \tag{5.4, 5.5, 5.6}$$

and,

$$T_{opt} = T_{inf}\left(1 + x_{opt}\right) \tag{5.7}$$

Finally, where a clear downturn above the optimum was evident, I multiplied the anchored MMRT term by a reversible Medlyn type deactivation factor,

$$f_{deact}(T) = \frac{1 + \exp\left(\frac{T_{ref}\Delta S - H_d}{RT_{ref}}\right)}{1 + \exp\left(\frac{T\Delta S - H_d}{RT}\right)}, \quad T_{ref} = 298.15K \tag{5.8}$$

and estimated H_d (J mol^{-1}) and ΔS (J mol^{-1} K^{-1}) on the full temperature range while keeping T_{inf}, kT$_{inf}$ and the fitted $\Delta C_p^{\ddagger}$ fixed (bounds: Hd ∈ [5 X 10^4, 5 X 10^5] J mol^{-1}; ΔS ∈ [100, 1200] J mol^{-1} K^{-1}; initials H_d= 2 x 10^5 Jmol-1, ΔS = 650 Jmol^{-1}K^{-1}).

For comparison, I fitted the peaked simple and peaked Arrhenius response across the full temperature range, estimating E_a, H_d, and ΔS by nonlinear least squares.

$$k(T) = k_{ref} \exp\left[\left(\frac{E_a}{R}\right)\left(\frac{\left(T - T_{ref}\right)}{T\,T_{ref}}\right)\right], \; T_{ref} = 298.15K \tag{5.9}$$

$$k(T) = k_{ref} \exp\left[\left(\frac{E_a}{R}\right)\left(\frac{\left(T - T_{ref}\right)}{T\,T_{ref}}\right)\right]\left[\frac{1 + \exp\left(\frac{T_0\Delta S - H_d}{RT_0}\right)}{1 + \exp\left(\frac{T\Delta S - H_d}{RT}\right)}\right], T_{ref} = 298.15K$$

(5.10)

5.2.4 Linearity diagnostic in Arrhenius coordinates

To identify the temperature sub-range on the ascending limb where the Arrhenius transform is approximately linear, I analysed ln(y) versus 1000/T (K). Starting from the lowest temperature, I ran a forward range-scan, fitting a linear model [ln(y) = α + β x] and testing a quadratic extension [ln(y) = α + β x + γ x^2] at each step. I extended the upper bound until the quadratic term became significant at two sided p < 0.05 and reduced AIC

by more than two units. The largest range that did not breach this criterion was designated the linear window.

5.2.5 Statistical analysis

Fit domains and parameter counts.

All thermal response models were fitted by nonlinear least squares in MATLAB R2025a (*lsqnonlin*). Goodness of fit and parsimony metrics were always computed on the same domain used for fitting: the basal window for Arrhenius and MMRT stage-2, and the full 5–43 °C span for MMRT × Deact and Peaked Arrhenius. The basal window was 5–35 °C for V_{cmax} and 5–31 °C for J_{max}. That is, from the minimum temperature to the T_{opt} of each one. Parameter counts were k = 1 for Arrhenius (E_a) and MMRT stage-2 ($\Delta C_p^{\ddagger}$), k = 2 for MMRT × Deact (H_d, ΔS), and k = 3 for Peaked Arrhenius (E_a, H_d, ΔS). In MMRT stage-2, the curve was anchored at (T_{inf}, $y(T_{inf})$) and only $\Delta C_p^{\ddagger}$ was fitted on the basal window; MMRT × Deact then fitted (H_d, ΔS) in the full temperature range with that anchor fixed.

Metrics and model ranking

For observation i, y_i is the observed normalised rate and $\hat{y}_i$ the model prediction; n denotes the sample size in the fitting domain and k the number of free parameters.

$$SSE = \sum_{i=1}^{n} (y_i - \hat{y}_i)^2, \qquad RMSE = \sqrt{\frac{1}{n}\sum_{i=1}^{n} (y_i - \hat{y}_i)^2} \tag{5.11, 5.12}$$

Model ranking used the small sample corrected Akaike Information Criterion:

$$AIC_c = n \ln\left(\frac{SSE}{n}\right) + 2k + \frac{2k(k+1)}{n-k-1} \tag{5.13}$$

Within each comparison set (basal models; global models), I report ΔAICc = AICc − min (AICc), so the best model in that set has ΔAICc = 0. Interpretation follows the usual

thresholds: ΔAICc < 2 (essentially equivalent), 4–7 (some support for the lower-AICc model), >10 (strong support for the lower-AICc model). I also report the apparent temperature optimum (T_{opt}) from the fitted curves. R^2 is shown only for the basal linearity diagnostics described next; for bell shaped global fits I rely on SSE/RMSE and AICc (and rank by ΔAICc).

5.3 Results

In this chapter, I analysed 85 A_{net}-C_i curves from sunflower leaves spanning 5.4 to 44.3 °C. Figure 5.1 shows representative curves at 10, 20, 30, and 40 °C. Across temperatures, net CO_2 assimilation rate (A_{net}) increased with intercellular CO_2 partial pressure (C_i), with both magnitude and curvature varying systematically with temperature. From cold to warm conditions, A_{net} rose across the C_i range, peaked at mid to high temperatures, and declined at the hottest measurements, indicating high temperature deactivation. Limitation partitioning behaved as expected: Rubisco limitation (A_c) dominated at low C_i, RuBP-regeneration limitation (A_j) prevailed at higher C_i, and the A_c-A_j crossover shifted to higher C_i with increasing temperature.

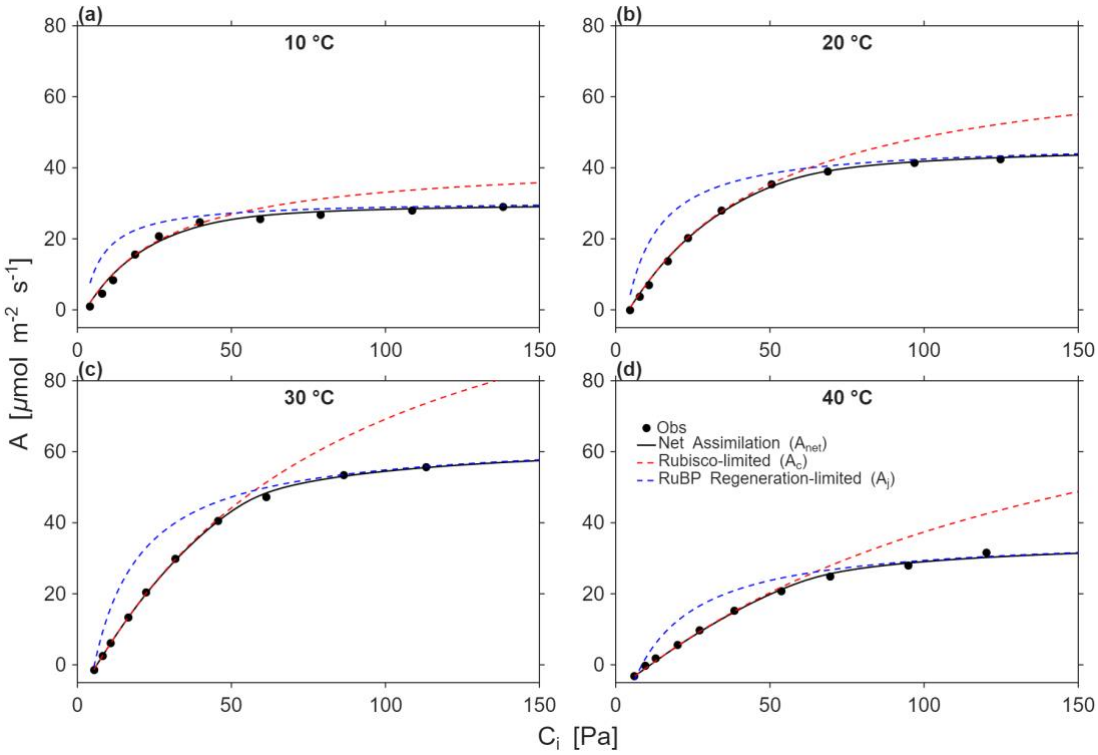

FIGURE 5.1. Representative A_{net}–C_i response curves across four leaf temperatures (A_{net}: µmol m^{-2} s^{-1}; C_i: Pa). Panels (a–d) correspond to 10, 20, 30 and 40 °C, respectively. Filled circles are observations; the solid black line is the FvCB fit; dashed red and blue lines indicate the Rubisco-limited rate (A_c) and the RuBP regeneration-limited rate (A_j). Measurements were made at a saturating photon flux density of 2000 µmol photons m^{-2} s^{-1}.

Figure 5.2 connects the qualitative patterns to the curve features that inform parameter estimates. For a representative leaf, the fitted FvCB components are overlaid to show how V_{cmax} and J_{max} are identified. In panel (a), the A_{net}–C_i responses separate cleanly by temperature (10, 15, 25, 35, 40 °C). At low C_i, the 10 and 15 °C curves almost coincide and have the shallowest initial slope. Warming to 25 °C makes the initial slope steeper, and the steepest initial slope occurs at 35 °C. At 40 °C the initial rise is less steep than at 35 °C, signalling the onset of high-temperature impairment. With warming, the point where curvature increases and the curve bends toward its ceiling shifts leftwards (saturation is reached at lower C_i at 25–35 °C than at 10–15 °C). The high C_i asymptote climbs from 10 °C to 25 °C and to 35 °C and then drops at 40 °C, ending near the cool

temperature levels. Thus, 35 °C attains the highest A_{net} across the range, 25 °C is slightly lower, and 10, 15 and 40 °C converge to similar upper rates despite their different starts, an overall warm side optimum with a downturn at 40 °C.

Comparing panel (a) with panel (b), the Rubisco limited rate (A_c) closely tracks net assimilation at low to moderate C_i. At each temperature the curves are nearly coincident over the low and moderate C_i range (10 and 15 °C are very similar; 25 and 35 °C are steeper but preserve the ordering). The key divergence appears at high C_i: in panel (a) A_{net} bends to a temperature dependent plateau (highest near 35 °C), whereas in panel (b) the Rubisco-limited rate (A_c) continues to rise without a clear ceiling over the plotted C_i range. That separation marks the onset of regeneration limitation: A_{net} saturates not because Rubisco has reached a ceiling, but because the regeneration side becomes limiting at high C_i. At 40 °C, both panels are depressed relative to 25–35 °C, consistent with warm side impairment.

Panel (c) shows the RuBP regeneration-limited rate (A_j), which behaves quite differently at the start of the curves: the initial slope is much steeper than in (a) or (b), and the response reaches a plateau at substantially lower C_i. The level of that plateau follows the same temperature pattern as A_{net} is highest near 35 °C, slightly lower at 25 °C, and reduced at 40 °C; 10 °C remains lowest. Thus, A_j in panel (c) sets the high C_i ceiling seen for A_{net} in panel (a). At the fixed irradiance used, this ceiling reflects the available electron-transport capacity (J) and downstream regeneration steps.

With V_{cmax} and J_{max} derived from the A_{net}–C_i curves spanning 5.4 – 44.3 °C, each leaf's series was normalised to its 25 °C value so that differences in scale did not interfere with thermal patterns. Using these normalised series, the temperature dependence of both parameters was then evaluated and compared using the MMRT and Arrhenius models.

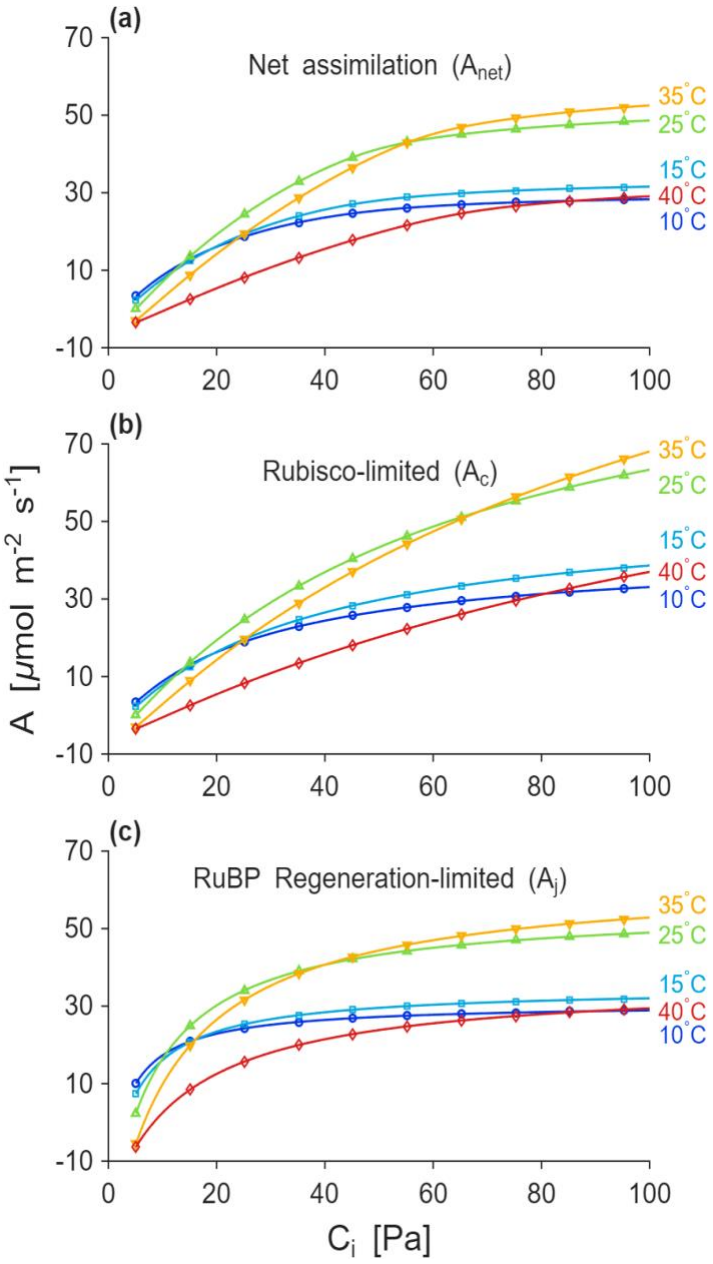

FIGURE 5.2. Responses of net assimilation (A_{net}), Rubisco-limited rate (A_c) and RuBP regeneration-limited rate (A_j) across intercellular CO_2 partial pressure (C_i) for one representative leaf at several temperatures. Curves are fits of the FvCB model.

MMRT was implemented as a three-stage fitting procedure. First, a cubic polynomial was fitted to the basal segment of each normalised temperature series (V_{cmax}: 5–35 °C; J_{max}: 5–31 °C) to locate the T_{inf} and its ordinate $y(T_{inf})$. The fitted polynomials were:

$$V_{cmax} \rightarrow y(T) = -5.70\ x\ 10^{-5}T^3 + 4.40\ x\ 10^{-3}T^2 - 5.10\ x\ 10^{-2}T + 0.410$$

$$J_{max} \rightarrow y(T) = -5.40\ x\ 10^{-5}T^3 + 2.90\ x\ 10^{-3}T^2 - 7.40\ x\ 10^{-3}T + 0.240$$

Estimates of T_{inf} and $y(T_{inf})$ derived from these fits are shown in Figure 5.3 and listed in Table 5.1.

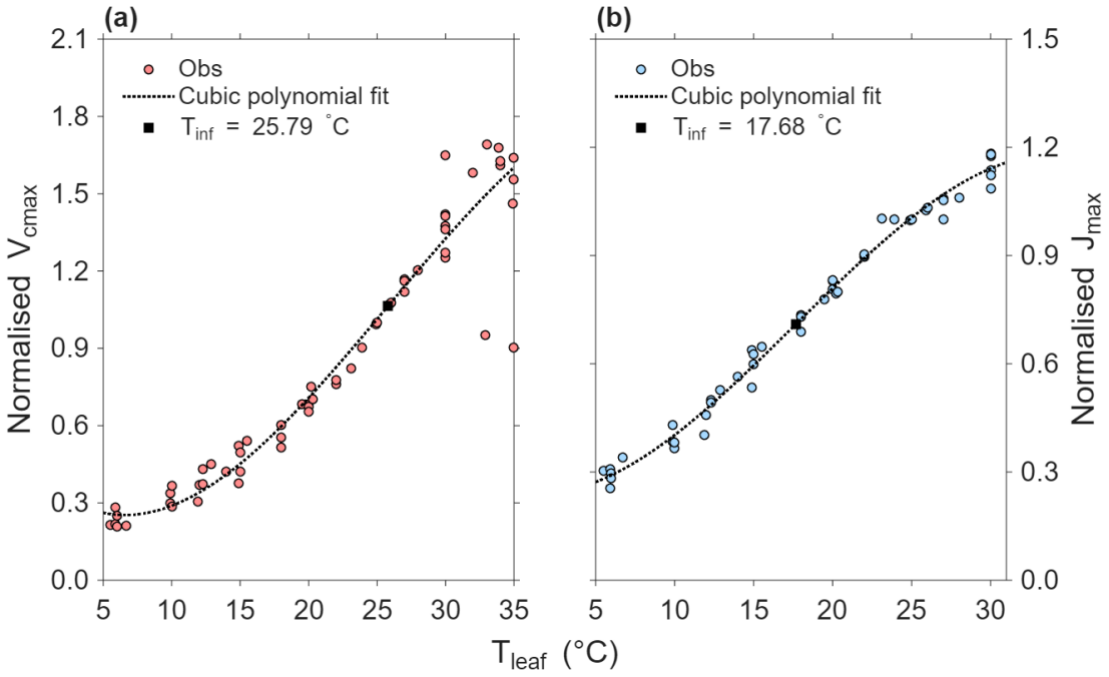

FIGURE 5.3. Normalised V_{cmax} and J_{max} versus temperature, with cubic polynomial fits used to locate T_{inf} and $y(T_{inf})$. Open circles are the observations (red for V_{cmax} and blue for J_{max}); the dashed line is the cubic fit; the filled square marks T_{inf} (with ordinate $y(T_{inf})$). (a) V_{cmax} (fit over 5–35 °C); (b) J_{max} (fit over 5–31 °C).

Second, using T_{inf} and $y(T_{inf})$ as anchors, the MMRT stage-2 form was fitted on the same basal window to estimate the curvature parameter $\Delta C_p^{\ddagger}$ (Equation 5.3). Third, with T_{inf} and $\Delta C_p^{\ddagger}$ held fixed, the deactivation parameters (Hd, ΔS) were fitted over the full range of temperature (Equation 5.8). Parameter estimates for V_{cmax} and J_{max} from these MMRT fits are reported in Table 5.1. MMRT yielded very similar apparent $\Delta C_p^{\ddagger}$ values for the normalised fits (−2.26 and −2.11 kJ mol^{-1} K^{-1} for V_{cmax} and J_{max}, respectively), with T_{inf} of 25.79 °C (V_{cmax}) and 17.68 °C (J_{max}). Using the same basal window but fitting the rates in original units (unnormalized rates) with T_{inf} and y(T_{inf}) held fixed, $\Delta C_p^{\ddagger}$ was -1.43 and -2.79 kJ mol^{-1} K^{-1} for V_{cmax} and J_{max}, respectively, and T_{inf} was 27.62 °C and 15.70 °C. Thus, while the qualitative ordering is unchanged (J_{max} has a lower T_{inf}), the anchored fits indicate stronger basal curvature for J_{max} (more negative $\Delta C_p^{\ddagger}$). The deactivation parameters were H_d 237 and 239, and ΔS 750 and 763 for V_{cmax} and J_{max} respectively.

T_{inf} was estimated prior to $\Delta C_p^{\ddagger}$ to minimise parameter collinearity and to ensure that basal curvature was quantified relative to a well-defined inflection point, rather than allowing $\Delta C_p^{\ddagger}$ to absorb uncertainty in T_{inf}.

In parallel, I fitted Arrhenius type models to the same normalised series. Over the basal window, the simple Arrhenius fit estimates only E_a. Across the full 5–44 °C span, the Peaked Arrhenius allows for deactivation and estimates E_a together with H_d and ΔS. Parameter values for V_{cmax} and J_{max} from these Arrhenius fits are summarised in Table 5.2. The Arrhenius activation energy is higher for V_{cmax} than for J_{max} in the basal window, (E_a = 41.8 vs 35.9 kJ mol^{-1}) and over the full temperature span and using the Peaked Arrhenius (E_a = 58.3 vs 42.4 kJ mol^{-1}). The deactivation constants are H_d = 195–208 kJ mol^{-1} and ΔS = 627–672 J mol^{-1} K^{-1} for V_{cmax} and J_{max} respectively.

TABLE 5.1. MMRT fitting workflow and parameter estimates for V_{cmax} and J_{max}. Stage 1 fits a cubic polynomial to the basal temperature window to obtain the anchor point T_{inf} and its ordinate $y(T_{inf})$. Stage 2 fits the MMRT on the same basal window, with T_{inf} and $y(T_{inf})$ held fixed, to estimate the curvature parameter $\Delta C_p^{\ddagger}$. Stage 3 fits the deactivation form over the full range temperature, with T_{inf} and apparent $\Delta C_p^{\ddagger}$ fixed, to estimate H_d and ΔS. The Fit domain column gives the temperature range used at each stage in °C; Anchors held fixed lists parameters constrained from the preceding stage. Units: T_{inf} (°C); $y(T_{inf})$ (dimensionless); $\Delta C_p^{\ddagger}$ (kJ mol^{-1} K^{-1}); H_d (kJ mol^{-1}) and ΔS (J mol^{-1} K^{-1}).

	Trait	Stage	Fit domain	Anchors held fixed	Fitted parameters
MMRT	V_{cmax}	1	5-35	None (polynomial fit)	$\mathbf{T_{inf}}$ = 25.79; $\boldsymbol{y(T_{inf})}$ = 1.06
		2	5-35	$\mathbf{T_{inf}}$ = 25.79; $\boldsymbol{y(T_{inf})}$ = 1.06	**Apparent** $\mathbf{\Delta C_p^{\ddagger}}$ = −2.26
		3	5-44	$\mathbf{T_{inf}}$ = 25.79; $\mathbf{\Delta C_p^{\ddagger}}$ = −2.26	$\mathbf{H_d}$ = 237; $\mathbf{\Delta S}$ = 750
	J_{max}	1	5-31	None (polynomial fit)	$\mathbf{T_{inf}}$=17.68; $\boldsymbol{y(T_{inf})}$=0.71
		2	5-31	$\mathbf{T_{inf}}$ = 17.68; $\boldsymbol{y(T_{inf})}$ = 0.71	**Apparent** $\mathbf{\Delta C_p^{\ddagger}}$ = −2.11
		3	5-44	$\mathbf{T_{inf}}$ = 17.68; $\mathbf{\Delta C_p^{\ddagger}}$ = −2.11	$\mathbf{H_d}$ = 239; $\mathbf{\Delta S}$ = 763

TABLE 5.2. Arrhenius and Peaked Arrhenius parameter estimates for V_{cmax} and J_{max}. Basal fits are restricted to the ascending-temperature window (V_{cmax}: 5–35 °C; J_{max}: 5–31 °C) and fitting only the activation energy (E_a). Peaked fits use the full range (5–44 °C) and estimate E_a together with the high-temperature deactivation terms (H_d and ΔS). The Fit domain column lists the temperature interval used for each fit in °C. Units: E_a and H_d in kJ mol^{-1}; ΔS in J mol^{-1} K^{-1}.

	Trait	Model	Fit domain	Fitted parameters
Arrhenius	V_{cmax}	Basal	5-35	$\mathbf{E_a}$ = 41.8
		Peaked	5-44	$\mathbf{E_a}$ = 58.3; $\mathbf{H_d}$ = 195; $\mathbf{\Delta S}$ = 627
	J_{max}	Basal	5-31	$\mathbf{E_a}$ = 35.9
		Peaked	5-44	$\mathbf{E_a}$ = 42.4 $\mathbf{H_d}$ = 208; $\mathbf{\Delta S}$ = 672

Figure 5.4 summarises the temperature response of normalised V_{cmax}, separating the basal window (5–35 °C) from the full temperature range. Within the basal window (panel a), both the simple Arrhenius and the basal MMRT capture the rise, but MMRT fits better: R^2 improves from 0.88 (Arrhenius) to 0.90 (MMRT), SSE falls from 1.82 to 1.48, RMSE from 0.17 to 0.15, and AICc from −230.2 to −243.8 (ΔAICc = 13.6 in favour of MMRT; Table 5.3). Over the full range of temperature (panel b), MMRT with an explicit high-temperature deactivation term and the peaked Arrhenius produce nearly identical curves through the rise and peak. Their errors are very similar (SSE 5.99 vs 5.94; RMSE 0.267 vs 0.266), and AICc differs by only 1.41 units (−217.65 vs −216.24), favouring MMRT + deactivation; both recover a warm-side optimum near 35 °C (35.0 vs 34.2 °C; Table 5.4).

For panel (b), V_{cmax} is well described by both forms, with a small but consistent information criterion edge for MMRT with deactivation. However, the residual warm side departures suggest that additional damage or regulatory terms may still be required to reproduce the observed pattern.

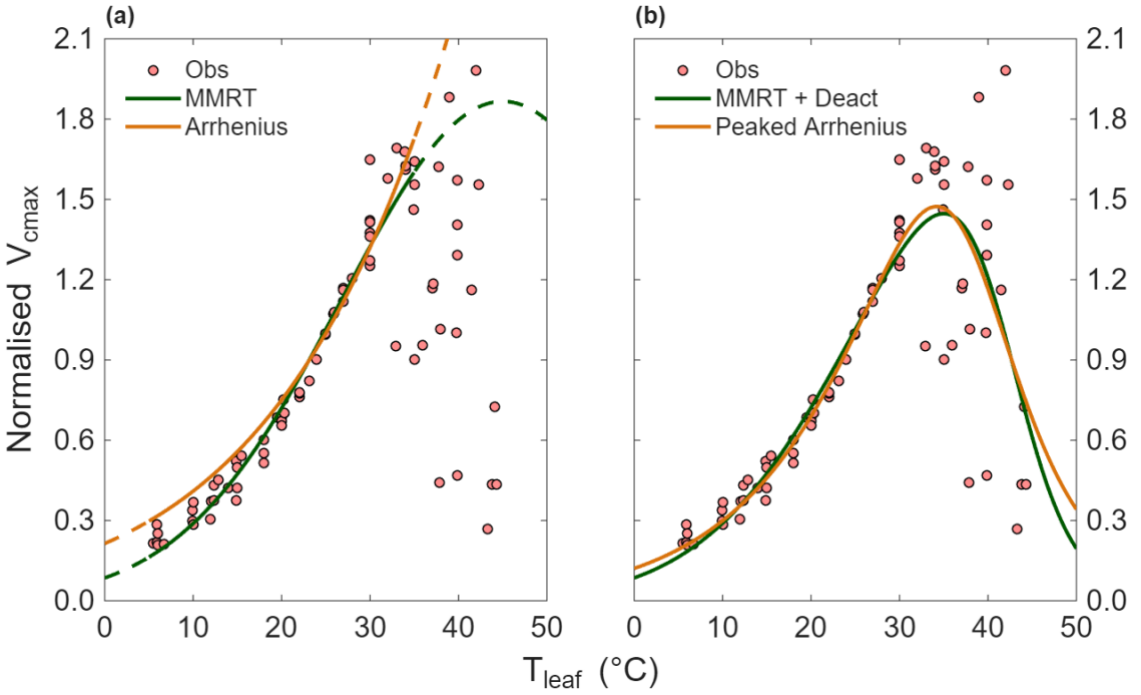

FIGURE 5.4. Temperature dependence of normalised V_{cmax}. (a) Basal fits (5–35 °C): MMRT versus Arrhenius. (b) Full range of temperature: MMRT with high-temperature deactivation versus Peaked Arrhenius. Symbols are V_{cmax} estimates derived from A_{net}–C_i curves; green solid lines show MMRT (with or without deactivation), and orange dashed lines show Arrhenius (simple or peaked).

Figure 5.5 presents the corresponding analysis for normalised J_{max}, again distinguishing the basal window (5–31 °C) from the full temperature range. In panel (a) the separation is clearer: MMRT substantially outperforms the simple Arrhenius equation within the basal window (R^2 0.99 vs 0.95; SSE 0.05 vs 0.24; RMSE 0.03 vs 0.07) and MMRT is decisively preferred by AICc (−375.8 vs −290.3; ΔAICc = 85.6; Table 5.3). In panel (b) MMRT + deactivation again has the lower error (SSE 1.81 vs 1.88; RMSE 0.417 vs 0.418) and the better AICc (−317.99 vs −314.63; ΔAICc = 3.36), with essentially the same T_{opt} (30.8 vs

30.7 °C; Table 5.4). Overall, J_{max} shows pronounced curvature that the MMRT captures more effectively both in the basal domain and over the full thermal range.

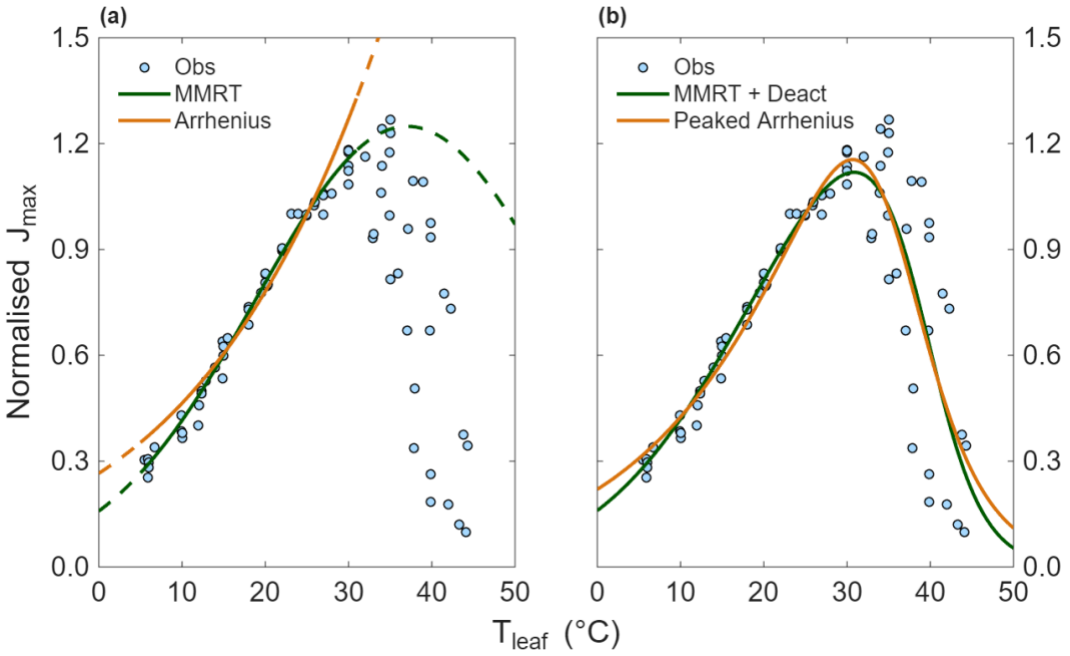

FIGURE 5.5. Temperature dependence of normalised J_{max}. (a) Basal fits (5–31 °C): MMRT versus Arrhenius. (b) Full range of temperature: MMRT with high-temperature deactivation versus Peaked Arrhenius. Symbols are J_{max} estimates derived from A_{net}–C_i curves; green solid lines show MMRT (with or without deactivation), and orange dashed lines show Arrhenius (simple or peaked).

TABLE 5.3. Basal-window fits for normalised V_{cmax} (5–35 °C) and normalised J_{max} (5–31 °C). Two models are compared: a basal MMRT form and simple Arrhenius. Columns report R^2 (coefficient of determination), SSE (sum of squared errors, normalised scale), RMSE (root-mean-squared error, same scale as the response), AICc (small-sample corrected Akaike Information Criterion), and ΔAICc (difference from the best model within each trait). Lower SSE, RMSE and AICc indicate better fit; higher R^2 indicates more variance explained. All metrics are unitless because the responses are normalised.

Trait	Model	R^2	SSE	RMSE	AICc	ΔAICc
V_{cmax}	MMRT	0.90	1.48	0.15	-243.8	13.6
	Arrhenius	0.88	1.82	0.17	-230.2	
J_{max}	MMRT	0.99	0.05	0.03	-375.8	85.6
	Arrhenius	0.95	0.24	0.07	-290.3	

TABLE 5.4. Full-range fits for normalised V_{cmax} and J_{max}. Two model structures are compared: MMRT + deact (MMRT with an explicit high-temperature deactivation term) and Peaked Arrhenius. Columns report T_{opt} (temperature of the fitted maximum, °C), SSE (sum of squared errors, normalised scale), RMSE (root-mean-squared error, same scale as the response), AICc (small-sample corrected Akaike Information Criterion), and ΔAICc (difference from the best model within each trait). Lower SSE, RMSE and AICc indicate better fit. T_{opt} is derived from the fitted curve. All metrics except T_{opt} are unitless because the responses are normalised. Fits were performed over the full temperature span shown in Figures 5.4b and 5.5b.

Trait	Model	T_{opt}	SSE	RMSE	AICc	△AICc
V_{cmax}	MMRT + deact	35.0	5.99	0.267	-217.65	1.41
	Peaked Arrhenius	34.2	5.94	0.266	-216.24	
J_{max}	MMRT + deact	30.8	1.81	0.147	-317.99	3.36
	Peaked Arrhenius	30.7	1.84	0.148	-314.63	

On Arrhenius coordinates, both V_{cmax} and J_{max} display an approximately linear segment at low to mid temperatures that defines the basal window. Using only this temperature range, I compared MMRT with Arrhenius. In the same coordinates, the MMRT overlay follows the curvature evident in the observations, whereas Arrhenius remains a straight line for both V_{cmax} and J_{max} (Figure 5.6a, b).

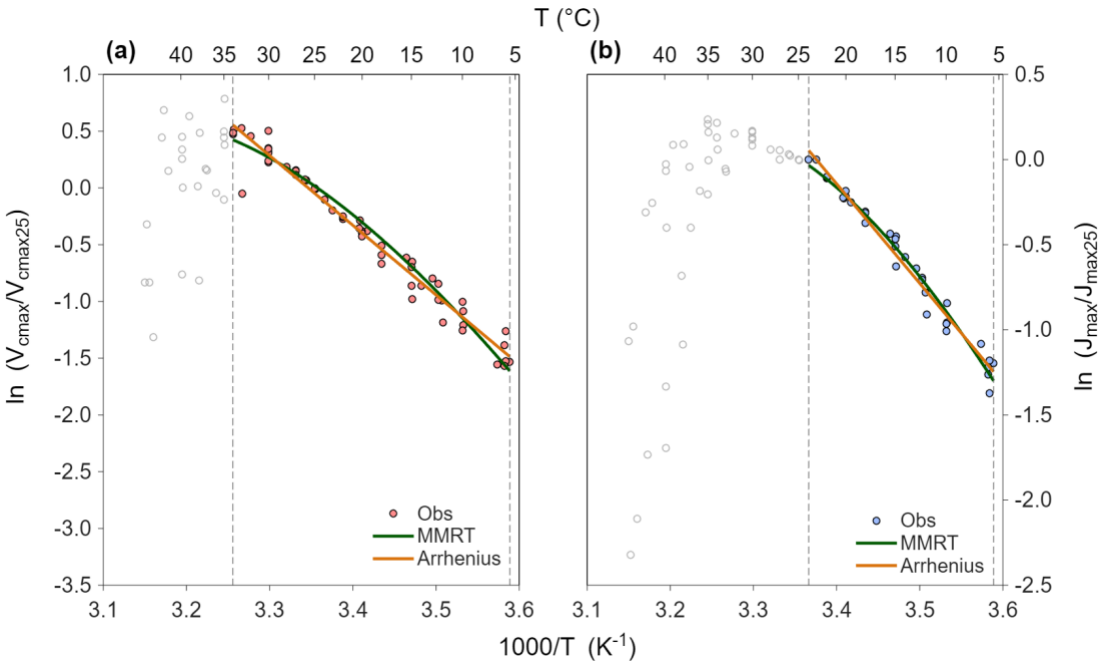

FIGURE 5.6. Arrhenius plots for V_{cmax} (a) and J_{max} (b). Data are plotted as ln (normalised rate) versus 1000/T (K^{-1}). Lines are Arrhenius (orange) and MMRT (green) models fitted only to points within the linear Arrhenius region, symbols are observations. Vertical dashed lines mark the basal window; the upper x-axis shows T (°C).

5.4 Discussion

My data resolve the temperature dependence of the two biochemical determinants of C_3 photosynthesis, V_{cmax} and J_{max}, and reveal both the shape and mechanistic origin of their thermal responses. Three results stand out. First, on the ascending limb, the observations on Arrhenius coordinates show a consistent departure from strict linearity within the basal window for both traits (Figure 5.6). Second, using only this window, MMRT reproduces that bend and fits better than a simple Arrhenius line; the presence of curvature on ln(rate) versus 1000/T (K^{-1}) implies $\Delta C_p^{\ddagger} \neq 0$, meaning that $\Delta H^{\ddagger}$ and $\Delta S^{\ddagger}$ vary with temperature, whereas the Arrhenius form assumes $\Delta C_p^{\ddagger} = 0$ and therefore linearity in this space. Third, once the decline above the thermal optimum is included, MMRT with an explicit

deactivation term and the peaked Arrhenius recover essentially the same T_{opt} for each trait with V_{cmax} ≈ 35 °C and J_{max} ≈ 31 °C (Table 5.4), which explains why the full-range performance is statistically similar despite the models differing in interpretation.

5.4.1 Thermodynamic and physiological interpretation

In MMRT, negative heat capacity change of activation ($\Delta C_p^{\ddagger}$) causes both $\Delta H^{\ddagger}$ and $\Delta S^{\ddagger}$ to decrease with warming, bending Arrhenius plots and naturally producing a finite optimum without invoking ad hoc breakpoints. Using normalised data, the apparent $\Delta C_p^{\ddagger}$ for V_{cmax} and J_{max} were similar (≈ −2.2 kJ mol^{-1} K^{-1}), consistent with enzyme catalysed processes where transition states are more ordered than ground states (Arcus et al., 2016; Walker et al., 2024). I used normalised fits to place leaves on a common scale so that model fit statistics reflect the form of the temperature response rather than differences in magnitude. These magnitudes sit within the range reported for other biological rates (≈ −1 to −12 kJ mol^{-1} K^{-1}), supporting the view that curvature is an intrinsic thermodynamic property (Arcus et al., 2016; Van Der Kamp et al., 2018; Xu et al., 2021). To interpret $\Delta C_p^{\ddagger}$ in original units I also fitted MMRT to unnormalized rates over the same basal window with T_{inf} and y(T_{inf}) held fixed, which gave $\Delta C_p^{\ddagger}$ of -1.43 for V_{cmax} and -2.79 kJ mol^{-1} K^{-1} for J_{max}. These raw anchored values indicate stronger basal curvature in J_{max} and are consistent with RuBP regeneration and stromal environment being more heat sensitive than Rubisco carboxylation, while the conclusions from the normalised model comparison remain unchanged.

When $\Delta C_p^{\ddagger} \neq 0$, because $\Delta H^{\ddagger}$ and $\Delta S^{\ddagger}$ vary with temperature, the activation barrier, $\Delta G^{\ddagger}$, rises at temperatures above the optimum even without structural damage (Arcus et al., 2016). Catalytic rates could decline in a reversible manner (Crafts-Brandner & Law, 2000; Salvucci & Crafts-Brandner, 2004). This explains why the activation state of Rubisco falls when heat limits Rubisco activase, and why activation could be restored on cooling (Qu et al., 2021). The same thermodynamic driver is expected to influence electron transport capacity, consistent with early changes in chlorophyll fluorescence that occur before

membranes or reaction centres are compromised (Filaček et al., 2022; Maxwell & Johnson, 2000). Together, these lines of evidence support the suggestions that the basal curvature reflects $\Delta C_p^{\ddagger} \neq 0$ and reversible thermodynamic deactivation of stromal enzymes, with Rubisco activase acting as an early heat sensitive control on Rubisco activation, while thylakoid complexes show an efficiency loss that is detectable before visible damage (Qu et al., 2021).

With $\Delta C_p^{\ddagger} < 0$, T_{opt} lies above T_{inf} by an offset governed by the balance of $\Delta H^{\ddagger}$ and $\Delta C_p^{\ddagger}$ (Hobbs et al., 2013; Liang et al., 2018). In my data, T_{inf} for J_{max} is about 8 °C lower than for V_{cmax} and T_{opt} is also cooler for J_{max} (≈ 30.7–30.8 °C) than for V_{cmax} (≈ 34.2–35.0 °C). Physiologically, this ordering indicates that RuBP regeneration becomes thermodynamically disadvantaged earlier than Rubisco carboxylation as the leaf warms, consistent with an earlier decline in electron transport capacity and with the sensitivity of Calvin–Benson regeneration steps (Crous et al., 2022; Scafaro et al., 2023). In MMRT terms, the two traits have similar apparent $\Delta C_p^{\ddagger}$ (≈ −2.2 kJ mol^{-1} K^{-1}), however, raw fits indicate a more negative $\Delta C_p^{\ddagger}$ for J_{max} than for V_{cmax} (-2.79 vs -1.43 kJ mol^{-1} K^{-1}), consistent with stronger basal curvature. In both cases, the cooler anchor for J_{max} (lower T_{inf}) shifts its response leftwards, yielding an earlier peak and earlier downturn. This pattern accords with comparative studies where J_{max} often peaks at cooler temperatures than V_{cmax} and begins to decline sooner, though field conditions and species identity can reduce or mask this separation (Dreyer et al., 2001; Hernández et al., 2021; Slot et al., 2021).

Although J_{max} is often interpreted as reflecting electron-transport-limited RuBP regeneration, it is a pathway level property that integrates thylakoid electron transport, control at the cytochrome b_6f complex, ATP synthase coupling and downstream Calvin-Benson cycle steps such as sedoheptulose-1,7-bisphosphatase (SBPase) and phosphoribulokinase (PRK) (Harrison et al., 2001; Johnson & Berry, 2021a; Ruban, 2016; Scafaro et al., 2016). Accordingly, warming can reduce J_{max} through multiple factors: shifts in proton-motive force partitioning ($\Delta pH/\Delta\Psi$) and membrane ion conductance,

acceleration of non-photochemical quenching and state transitions, and temperature-dependent constraints on regeneration enzymes (Avenson et al., 2005; Lefebvre et al., 2005; Salvucci et al., 2006; Takizawa et al., 2007; Tikkanen & Aro, 2012; Weston et al., 2007).

By contrast, V_{cmax} reflects Rubisco catalytic competence at saturating RuBP and CO_2, buffered by Rubisco activase, carbamylation state and Mg^{2+} availability (Scafaro et al., 2016; Weston et al., 2007). At higher temperatures, Rubisco activase becomes heat-labile, and its function is further curtailed by elevated ADP:ATP ratios and changes in stromal pH. In parallel, warming promotes decarbamylation of Rubisco's active site and can weaken Mg^{2+} coordination, lowering the proportion of catalytically competent enzymes. In this framework, those effects reduce the active fraction before the onset of irreversible damage, and are therefore captured phenomenologically by the deactivation factor, which reproduces the reversible warm-side downturn in the thermal response (Qu et al., 2021; Salvucci et al., 2006; Scafaro et al., 2016).

5.4.2 Deactivation dynamics at high temperature (Hd, ΔS) and their interpretation

Across the full temperature range, the high-temperature deactivation term ($H_d \approx 237–239$ kJ mol^{-1}; $\Delta S \approx 750–763$ J mol^{-1} K^{-1}) captures the reversible warm-side downturn before irreversible injury is evident (Kattge & Knorr, 2007; Medlyn et al., 2002). A comparatively high, positive ΔS is consistent with greater configurational disorder in the inactive ensemble (for example, local unfolding, altered oligomeric state or weakened cofactor binding), in line with reversible enzyme-inactivation frameworks prior to denaturation (Hobbs et al., 2013; Peterson et al., 2007). Thus, T_{opt} is jointly determined by the anchored MMRT rise ($\Delta C_p^{\ddagger}$, T_{inf}) and the warm-side deactivation (H_d, ΔS). The near-identical T_{opt} recovered by the two model structures, MMRT × deactivation versus the peaked Arrhenius, suggests that both models capture the same catalytic efficiency increases to a warm optimum and then a decline in a largely reversible manner (Kattge & Knorr, 2007; Kumarathunge et al., 2019). As is well recognised, when warm-side coverage is limited,

the deactivation parameters can be weakly identified and strongly co-vary, which is why many analyses fix H_d to a canonical value (≈200 kJ mol^{-1}) unless the data clearly support otherwise (Medlyn et al., 2002; Kattge & Knorr, 2007). Conceptually, the deactivation factor is phenomenological: it captures the warm side shape as a reversible shift in the active-inactive ensemble and does not, by itself, diagnose irreversible denaturation (Peterson et al., 2007; Hobbs et al., 2013). I did not directly measure protein denaturation, but leaves remained viable at the temperatures and exposure durations used, with no visible heat injury. Accordingly, I interpret the warm side downturn as regulation dominated, consistent with enzyme activation control and stromal environment discussed above, while not excluding a possible contribution from denaturation at the upper end of the temperature range.

5.4.4 Model evidence and selection.

Within the basal windows (5–35 °C for V_{cmax}; 5–31 °C for J_{max}), Arrhenius lines under-fit the warm side of the rise, whereas MMRT follows the slight negative curvature, yielding lower SSE/RMSE and much better AICc (notably for J_{max}: ΔAICc ≈ 86 in favour of MMRT). This reflects a thermodynamic signal: the single extra parameter ($\Delta C_p^{\ddagger}$) replaces the assumption of constant activation energy with a physically grounded curvature term. Once the downturn is included, however, both MMRT × deactivation and the peaked Arrhenius have sufficient flexibility to capture the bell-shaped response, explaining the small AICc differences in Table 5.4. However, agreement over the full range of temperature does not diminish the thermodynamic gain observed in the basal window.

For inference on thermal trait shape, MMRT-derived quantities, $\Delta C_p^{\ddagger}$, T_{inf} and T_{opt}, should be preferred, as they provide interpretable axes that apparent activation energies cannot. When data are confined to the basal window, MMRT without a deactivation term is appropriate. Where the dataset spans high temperatures, an MMRT baseline coupled to a high-temperature deactivation function is recommended for mechanistic interpretation. However, in any model that includes a warm-side deactivation function whether MMRT

with deactivation or the peaked Arrhenius, parameter identifiability warrants caution: with limited warm-side coverage the deactivation parameters (H_d, ΔS) are often weakly constrained and strongly co-vary. In such cases, it may be preferred to confine inference to the MMRT rise or fix H_d to a canonical value if a downturn must be represented.

5.5. Conclusion

In sunflower leaves, the temperature responses of both V_{cmax} and J_{max} depart from linearity in Arrhenius coordinates over the rising (sub-optimal) range. An MMRT formulation with $\Delta C_p^{\ddagger} < 0$ captures this basal curvature and improves fit quality, particularly for J_{max}. Over the full temperature range, the position of the optimum and the warm-side downturn are recovered equally well by the composite MMRT with deactivation and by a peaked Arrhenius.

Thermodynamically, the fitted $\Delta C_p^{\ddagger}$ values for the two parameters are similar, indicating comparable ordering at the transition state, yet J_{max} displays lower T_{inf} and T_{opt} than V_{cmax}, consistent with RuBP-regeneration processes being more heat-sensitive than Rubisco-carboxylation. Methodologically, MMRT provides thermodynamically interpretable trait axes, $\Delta C_p^{\ddagger}$, T_{inf} and T_{opt} that a simple Arrhenius cannot. Within the basal window, MMRT should therefore be preferred for inference on shape and for comparing traits across contexts. Where the data span temperatures above the optimum, an MMRT baseline coupled to a reversible deactivation function affords a mechanistic account of both the rise and the downturn. The peaked Arrhenius remains adequate for descriptive purposes.

6 Temperature dependence of the components of leaf CO_2 release in the dark.

6.1 Introduction

Production of CO_2 by darkened leaves, commonly described as leaf dark respiration (R_{dark}), reflects the combined activity of many biochemical processes that oxidise carbohydrates, organic acids or amino acids. These processes support cellular energy and redox balances, recycle cofactors, and provide carbon skeletons for growth, repair and defence (Geigenberger & Fernie, 2014; Igamberdiev & Bykova, 2023; Le & Millar, 2023; O'Leary et al., 2019; Tcherkez et al., 2024). This CO_2 efflux is supplied mainly by glycolysis (pyruvate decarboxylation) and the tricarboxylic-acid (TCA) cycle (Fernie et al., 2004). Electrons from NADH and $FADH_2$ reduce molecular oxygen to water via the mitochondrial electron transport chain (involving cytochrome *c* oxidase, complex IV) or the alternative oxidase (AOX). Proton pumping across the inner membrane drives oxidative phosphorylation to form adenosine triphosphate (ATP) (Schertl & Braun, 2014). Only a small amount of ATP is produced within the TCA cycle itself via succinyl-CoA ligase (Zhang & Fernie, 2023).

The carbon that fuels respiratory metabolism in leaves is derived from multiple interconnected sources that collectively sustain R_{dark}. Sugars and starch are catabolised through glycolysis and pyruvate dehydrogenase to acetyl-CoA, which enters the TCA cycle (Fernie et al., 2004). Amino acids contribute to carbon skeletons by transamination and deamination, for example alanine to pyruvate and glutamate to 2-oxoglutarate (Hildebrandt et al., 2015). In addition, preexisting pools of malate, citrate and oxaloacetate are dynamically mobilised and replenished according to metabolic demand (Araújo et al., 2012).

These intermediates are not confined to energy production but are continuously withdrawn from the TCA cycle to support biosynthesis and cellular maintenance (Nunes-Nesi et al., 2013). 2-oxoglutarate plays a central role in amino-acid turnover and nitrogen assimilation, while oxaloacetate and aspartate contribute to nucleotide and amino-acid biosynthesis (Azevedo et al., 2006; Han et al., 2021; Hodges, 2002; Huergo & Dixon, 2015). Glutamate further serves as the precursor for tetrapyrrole synthesis required for haem and chlorophyll formation via the plastidial C5/delta-aminolevulimnate acid pathway (Brzezowski et al., 2015). Citrate exported to the cytosol provides acetyl-CoA for lipid remodelling and membrane repair and supplies carbon skeletons for nitrogen assimilation during subsequent light periods (Abadie et al., 2024; Fatland et al., 2002).

Viewed in this context, R_{dark} represents a CO_2 efflux that supports net photosynthetic carbon gain at the whole-plant scale by maintaining metabolic flexibility, redox balance and the capacity for repair and acclimation. By sustaining these processes within a viable operating range, R_{dark} contributes not only to carbon balance but also to leaf energy homeostasis and long-term physiological performance (Atkin & Tjoelker, 2003; Z. Xu et al., 2015).

Immediately after leaf transition from light to darkness, two phenomena that produce CO_2 are linked to previous light conditions: the post-illumination burst (PIB) and the light-enhanced dark respiration (LEDR) (Atkin et al., 1998; Raghavendra & Padmasree, 2003). PIB is a brief transient increase in net CO_2 release dominated by decarboxylation of photorespiratory intermediates as light-maintained pools and gradients collapse (Gregory et al., 2024; Hoefnagel et al., 1998). A prominent contributor is glycine that accumulates during photorespiration and is oxidised by the mitochondrial glycine decarboxylase complex (Fu et al., 2023; Vines et al., 1983). The term “burst” comes from how infrared gas analysers register a peak in net CO_2 release when photosynthetic uptake stops abruptly while decarboxylation continues, so the measured trace shows a spike before relaxing towards as lower baseline in the dark. Mechanistically, this is a pool-depletion driven efflux rather than the activation of a new source or new enzymatic activity, consistent with

a transient mismatch between the fall in CO_2 uptake and the persistence of decarboxylation from light-maintained pools (Fu et al., 2023; Hoefnagel et al., 1998; Parys & Romanowska, 2000). The magnitude and apparent temperature sensitivity of the PIB may in part reflect the size and turnover of the photorespiratory glycine pool and the activity of the glycine decarboxylase complex, while also depending on irradiance, oxygen availability and temperature (Fu et al., 2023; Parys & Romanowska, 2000; Peterson, 1983; Sharkey & Xu, 2025).

LEDR is a more prolonged elevation of respiratory CO_2 release measured in darkness after illumination before decreasing to an eventual steady baseline respiration rate in the dark (Atkin et al., 2000; Barbour et al., 2007; Lehmann et al., 2016). This release of CO_2 is believed to reflect the continued oxidation of metabolites accumulated in the light together with rebalancing of ATP and redox states across organelles (Fan et al., 2024; Gessler et al., 2009; Lehmann et al., 2015, 2016; Raghavendra & Padmasree, 2003; Scheibe, 2004). Malate is often reported as a key contributor to LEDR, acting through the malate valve and as an anaplerotic substrate that accumulates in the light and can support part of the excess respiration after illumination (Atkin et al., 1998; Lehmann et al., 2016; Scheibe, 2004). This is consistent with malate and oxaloacetate cycling that transfers reducing power between chloroplast, peroxisomes and mitochondria, often termed the malate valve (Lehmann et al., 2016; Raghavendra & Padmasree, 2003; Scheibe, 2004).

When light is turned off, these pools are oxidised and decarboxylated, increasing the respiratory flux above rates in the light, until a new equilibrium in pools sizes and fluxes are established (Atkin et al., 2000; Barbour et al., 2007; Pinelli & Loreto, 2003; Sharkey & Xu, 2025). The size of the organic acid pools and the strength of respiratory coupling therefore influence both the amplitude and the duration of LEDR, and both scale with light intensity and with the balance between photochemical supply, photorespiratory demand and anabolic sinks (Gessler et al., 2009, 2017; Igamberdiev & Eprintsev, 2016; Reddy et al., 1991).

Previous work has shown that temperature strongly modulates R_{dark} and LEDR (Gessler et al., 2017; Zheng et al., 2024). It alters enzyme kinetics, protein stability, membrane viscosity, and proton conductance elements that set the degree of respiratory coupling, substrate supply and cofactor availability (Atkin & Tjoelker, 2003; Hazel et al., 1991; Nicholls, 2021). At moderate temperature, respiratory rates usually increases with temperature. At higher temperatures, curvature and apparent optima arise as thermodynamic limits and structural constraints raise the free energy of activation and promote uncoupling or alternative electron transport pathways (Arcus et al., 2016; Atkin & Tjoelker, 2003; Vanlerberghe, 2013).

Despite extensive work on leaf dark respiration, there is no consensus on the dark acclimation time used before measurement. Protocols range from a few minutes to one hour after lights off, which risks confounding LEDR with the steady state dark respiration rate and may bias measurements of both the rate and temperature dependence of R_{dark} (Bruhn et al., 2025; Schmiege et al., 2023). Furthermore, R_{dark} is not a single process, but the aggregate of components with distinct pool dynamics and thermal responses, but the temperature dependence of these components and their shifting timing and amplitude after leaf darkening have not been quantified on a comparable basis. Here I address these gaps by resolving the post illumination trajectory, separating LEDR from steady state R_{dark} across a wide thermal range, and comparing parsimonious thermal models. I also test whether the status of metabolite pools before and after darkening explains variation in LEDR magnitude and duration. The post illumination burst is described qualitatively but excluded from modelling, because analyser response time and chamber mixing distort the earliest seconds after darkening and would bias parameter estimates.

6.2 Materials and Methods

6.2.1 Plant Growth Conditions and Gas Exchange Measurements

Sunflower (*Helianthus annuus* "Russian Giant") plants were cultivated in a plant growth unit. They were watered daily to field capacity and fertilised weekly with a balanced nutrition solution. The photoperiod was 14 h, with day and night air temperatures of 24 and 19 °C respectively. Relative humidity was approximately 40% during the day and 65% at night. Photosynthetic photon flux density at the leaf surface during growth was 400 µmol photons m^{-2} s^{-1}. Gas exchange was measured on fully expanded upper canopy leaves using a GFS-3000 portable gas-exchange and fluorescence system (Heinz Walz GmbH, Effeltrich, Germany).

6.2.2 Partitioning of dark respiration components

Leaves were exposed to 2000 µmol photons m^{-2} s^{-1} at different measurement temperatures for one hour and then measured for one hour in darkness. Leaf temperature spanned 8.4 to 41 °C. Quantitative analysis focused on basal R_{dark} and on LEDR. Basal R_{dark} was taken as the mean of the last five minutes of the dark period, and net CO_2 exchange in darkness was expressed as a negative flux (Figure 6.1).

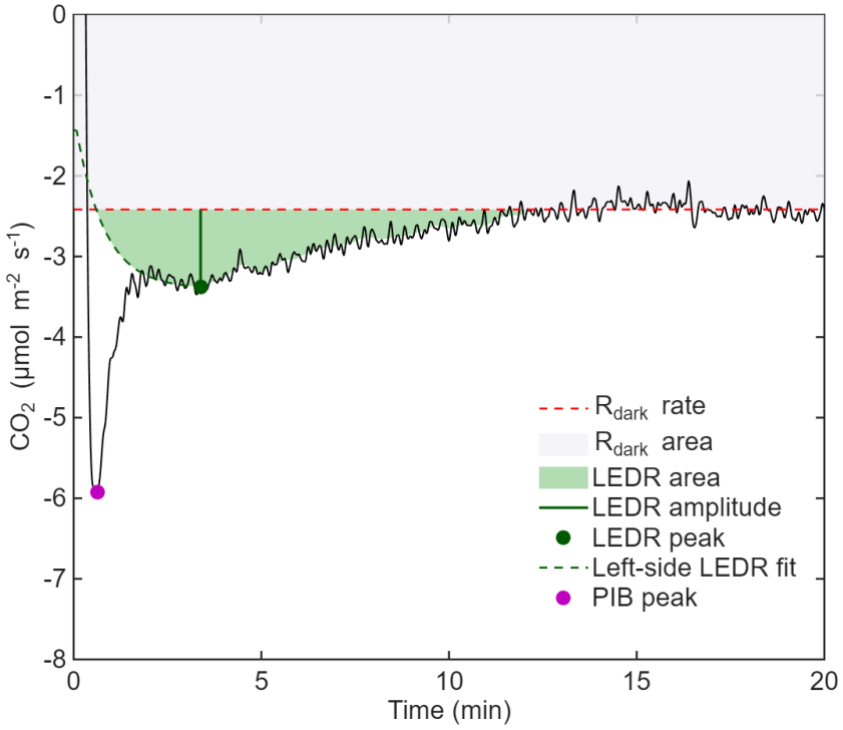

FIGURE 6.1. Schematic of the partitioning of dark respiration components. The black trace shows the observed CO_2 exchange after lights-off. The red dashed line marks R_{dark}. Grey shading indicates the R_{dark} area. Green shading denotes the LEDR (excess above R_{dark}), separated into the left-side LEDR fit (green dashed line) and the post-peak decay. The green vertical line marks the LEDR amplitude, and the green dot marks the LEDR peak. The magenta dot shows the PIB peak in the first seconds after darkness begins.

6.2.3 LEDR modelling and area calculation

LEDR amplitude, denoted as $LEDR_{amp}$, was modelled as a rise to a peak followed by a decay toward R_{dark}. The observed net CO_2 exchange after lights-off is $R(t)$ in µmol m^{-2} s^{-1}, with $R(t) \leq 0$ in darkness and R_{dark} is the steady dark respiration baseline. The excess respiratory flux above the baseline rate was calculated as:

$$\Delta R(t) = R_{dark} - R(t) \geq 0. \quad (6.1)$$

Note that this procedure calculates the integrated excess respiration flux as a positive integral. The LEDR peak was located by fitting a fourth-order polynomial to the data segment around the maximum of $\Delta R(t)$ and taking the minimum of the fitted $R(t)$. The peak time was recorded as t_{peak}. The $LEDR_{amp}$ was calculated as the excess above the R_{dark} baseline, also expressed as a positive quantity:

$$LEDR_{amp} = R_{dark} - R(t_{peak}) > 0. \tag{6.2}$$

The rising limb (left side) was modelled as a normalised exponential that approaches the fitted peak from an unknown baseline R_{base} with $R_{dark} \leq R_{base} \leq 0$. In excess form:

$$\Delta R(t) = \Delta R_{base} + \left(LEDR_{amp} - \Delta R_{base}\right) \frac{1 - exp\left(\frac{-t}{\tau_{rise}}\right)}{1 - exp\left(\frac{-t_{peak}}{\tau_{rise}}\right)}, \quad 0 \leq t \leq t_{peak.} \tag{6.3}$$

Where $\Delta R_{base} = R_{dark} - R_{base}$. The rise time constant (τ_{rise}) and R_{base} were estimated by least squares on the pre-peak segment, with the fit constrained to lie between R_{dark} and zero.

Post-peak data were smoothed with locally weighted regression and then fitted by least squares to a single exponential in excess form:

$$\Delta R(t) = LEDR_{amp}\, exp\left(-\frac{t - t_{peak}}{\tau_{decay}}\right), \quad t \geq t_{peak.} \tag{6.4}$$

Areas were computed as excess relative to the R_{dark} baseline. The time t_{95} was defined as the first time at which the smoothed trace satisfies $\Delta R(t) \leq 0.05\ LEDR_{amp}$. The left hand LEDR area was

$$A_{LEDR,\ left} = \int_0^{t_{peak}} max\{0, R_{dark} - R_{left}(t)\}\, dt, \tag{6.5}$$

where $R_{left}(t)$ is the fitted rising limb. The right hand LEDR area was

$$A_{LEDR,\ right} = \int_{t_{peak}}^{t_{end}} max\{0, R_{dark} - R_{right}(t)\}\, dt, \tag{6.6}$$

where R_{right} (t) is the smoothed decay and t_{end} = min (t95, t_{last}), with t_{last} the final available time point in the record. The total LEDR was A_{LEDR} = $A_{LEDR,\ left}$ + $A_{LEDR,\ right}$. Integrals were calculated numerically with the trapezoidal rule on the native time grid, converting minutes to seconds to report areas in μmol m^{-2}.

At or below 10 °C, no identifiable LEDR peak was observed within 60 min and there was no clear approach to a stable dark rate. Consequently, amplitude and integral were not identifiable, and the records were excluded from curve fitting and summary statistics.

6.2.4 Temperature dependence modelling of R_{dark} and LEDR

Rates were normalised to their value at 25 °C and modelled as a function of leaf temperature over the observed range. Throughout, T denotes absolute temperature (K), T_{25} = 298.15 K and y(T) is the normalised rate with $y(T_{25}) = 1$.

Constant-Q_{10} model

$$y(T_c) = Q_{10}^{\frac{T_c - 25}{10}}, \tag{6.7}$$

where T_c is the leaf temperature in °C and Q_{10} is the fold-change per 10 °C.

Arrhenius model

$$y(T) = \ exp\left[\frac{E_a}{R}\left(\frac{1}{T_{25}} - \frac{1}{T}\right)\right], \tag{6.8}$$

with activation energy E_a (J mol^{-1}), and the universal gas constant R = 8.314 J mol^{-1} K^{-1}. This form preserves $y(T_{25}) = 1$.

Peaked Arrhenius

$$y(T) = \exp\left[\left(\frac{E_a}{R}\right)\left(\frac{1}{T_{25}} - \frac{1}{T}\right)\right] \left[\frac{1 + \exp\left(\frac{T_{25}\Delta S - H_d}{RT_{25}}\right)}{1 + \exp\left(\frac{T\Delta S - H_d}{RT}\right)}\right], \quad (6.9)$$

with deactivation enthalpy H_d (J mol^{-1}) and entropy ΔS (J mol^{-1} K^{-1}).

MMRT anchored at the empirical inflection point

A cubic polynomial was fitted to the ascending limb of the normalised trait y versus T_c (°C). For y(T)= aT^3 + bT^2 + cT + d, the inflection temperature (T_{inf}) satisfies y''(T) = 6aT + 2b, hence:

$$T_{inf} = -\frac{b}{3a}, \quad yT_{inf} = y(T_{inf}) \quad (6.10)$$

These anchors were converted to Kelvin and used in MMRT by fixing T_{inf} and $y(T_{inf})$. The anchored MMRT describes the response relative to the anchor as:

$$ln\left[\frac{y(T)}{y_{inf}}\right] = 1 + \sqrt{\frac{-\Delta C_P^{\ddagger}}{R}}(x-1) + \frac{\Delta C_P^{\ddagger}}{2R}(x-1)^2, \quad (6.11)$$

With the single fitted parameter $\Delta C_p^{\ddagger}<0$ estimated by non-linear least squares on the ascending limb. Full-range predictions follow as

$$y(T) = y_{inf}\ exp\left(1 + \sqrt{\frac{-\Delta C_P^{\ddagger}}{R}}(x-1) + \frac{\Delta C_P^{\ddagger}}{2R}(x-1)^2\right) \quad (6.12)$$

The baseline optimum satisfies d ln y/dT = 0, with

$$a_{lin} = 1 + \sqrt{\frac{-\Delta C_p^{\ddagger}}{R}}, \qquad b_{quad} = \frac{\Delta C_P^{\ddagger}}{2R}, \qquad x_{opt} = \frac{-a_{lin}}{2b_{quad}} \qquad (6.13, 6.14, 6.15)$$

and,

$$T_{opt} = T_{inf}\left(1 + x_{opt}\right) \qquad (6.16)$$

6.2.5 Linearity diagnostic in Arrhenius coordinates

To assess Arrhenius linearity, rates were plotted as ln y(T) against x = 1000/T (K^{-1}), with a synchronised top axis in °C. A straight trend in these coordinates indicates simple Arrhenius behaviour, whereas systematic curvature signals temperature-dependent deviations. Observations and the four fitted curves were overlaid in the same coordinates to permit a direct visual diagnostic of linearity versus curvature within the measurement temperature range.

6.2.6 Metabolite time courses and sampling

This set of measurements was designed to test how the concentration of key soluble metabolites changes immediately after lights off, and whether I could detect a metabolic time course, and if so, whether it depended on temperature. I focused on major compounds that are expected to contribute to respiration in darkness and to the early light-dark transients, which include low molecular weight sugars and organic acids. Metabolic analyses were carried out using NMR, which is the best method to quantify metabolites directly (i.e. unlike mass spectrometry which requires calibration curves and isotopic internal standards, NMR provide direct quantification). NMR analyses generated spectra showing the intensity of chemical groups of metabolites as a function of the chemical shift (magnetic resonance frequency expressed relative to the international standard, in part per million). Chemical shifts are intrinsic properties of molecules and thus allow metabolite identification. The NMR analyses were carried out at the French National Research

Institute for Agriculture, Food and Environment (INRAE), using the NMR facility of Moltech Anjou (University of Angers, France).

Two metabolite time courses were conducted to characterise temperature-dependent metabolite dynamics during the first hour of darkness: the first one (referred to as 'short-term') focused on the first 90 seconds, and the second one (referred to as 'mid-term') corresponded to samples collected over the first hour after the light was turned off. Proton nuclear magnetic resonance (^{1}H-NMR) was used to analyse samples from the short-term time series. Carbon-13 nuclear magnetic resonance (^{13}C-NMR) was used to analyse samples from the mid-term series. This difference in NMR analysis was due to sample size, short-term series samples being much smaller (10 mg dry weight) than long-term series samples (100 mg dry weight). This analytical strategy was a compromise to account for the fact that (*i*) ^{1}H analysis is more sensitive and thus adapted to small samples, despite a lower resolution for individual sugar peaks; (*ii*) ^{13}C analysis is less sensitive and so adapted to large samples but provides a better resolution for sugar individual peaks (and the malate peak associated with the C-2 carbon atom position). In other words, the main constrain were the trade-off between sensitivity and spectral resolution and the need for different sample sizes for the two series. ^{1}H-NMR provided higher sensitivity but some overlap among individual sugar peaks. ^{13}C-NMR reduced peak overlap and resolved the malate C-2 signal but required larger samples and longer acquisition times. These choices reflect a design to capture both rapid early transients and subsequent changes over the first hour in darkness.

Plants were maintained at 5, 25 or 35 °C for one hour under 700 µmol photons m^{-2} s^{-1} and then for one hour in darkness. The experiment started every day at 09:00 am. Plant growth conditions are described in the section 'Plant Growth Conditions and Gas Exchange Measurements'. For each temperature, there were four biological replicates and six time points. The first time point was taken in the light two minutes before light was turned off. In the rapid ^{1}H-NMR series (short term) the remaining five samples were collected within the first 60 – 90 seconds of darkness. In the ^{13}C-NMR series (mid-term), the remaining

time points in darkness were at 1, 4, 10, 30 and 60 minutes. At each time point, samples were excised and immediately quenched in liquid nitrogen to stop enzymatic activity. All material was lyophilised to preserve metabolite profiles and allow normalisation on a dry mass basis.

6.2.7 Extraction for metabolic analysis

Lyophilised tissue was pulverised to a fine powder using a bead mill with stainless steel beads (SPEX SamplePrep, Geno/Grinder). For ^{1}H-NMR, 10 mg dry matter was extracted with 80:20 (v/v) methanol-d_4: water (CD_3OD: H_2O), vortexed and centrifuged for 15 minutes at 10,000 revolutions per minute (rpm) and 4°C. The supernatant was transferred and dried in a vacuum concentrator (miVac Quattro, Genevac; speed vac) for 18 hours, then resuspended in 540 µL phosphate buffer with 10 µL TMSPS (sodium 3-(trimethylsilyl)propionate-2,2,3,3-*d*$_4$ 0.05% w:w in D_2O; quantification and chemical shift reference) and 50 µL D_2O (deuterium oxide), vortexed and transferred to the NMR tube. For ^{13}C-NMR, 100 mg dry matter was extracted with 80:20 (v/v) methanol: water plus 0.2 mL 2,3-$^{13}C_2$-maleic acid solution at 6.25 mM (internal ^{13}C reference for quantification), vortexed and centrifuged for 30 minutes at 10,000 rpm and 4°C. The supernatant was transferred and dried in a vacuum concentrator for 18 hours, then resuspended in 550 µL phosphate buffer with 50 µL D_2O, vortexed and transferred to NMR tubes.

6.2.8 NMR analysis

All NMR analyses were performed using a 600 MHz Bruker Ascend NMR spectrometer (Bruker BioSpin) with automated sample handling and He-cryoprobe. Acquisitions were completed using deuterium as the lock and 298 K as sample temperature. ^{1}H-analyses were carried out using excitation sculpting for water suppression (pulse program zgesgp), 1 s acquisition time, 1 s inter-scan delay, 9.5 µs pulse power (90° pulse) over 256 scans (about 12 min per sample). ^{13}C analyses were carried out using an inverse-gated pulse program (zgig) with 1 s acquisition time, 1 s inter-scan delay, 10 µs pulse power (90°

pulse) and H-decoupling via the Waltz64 sequence, over 16,200 scans (about 9 h per sample).

6.2.9 Quantification and unit conversion for malate

Leaf mass per area (LMA) was used to convert malate from a dry-mass basis to an area-normalised amount. LMA was calibrated for this sunflower cultivar under the same growth conditions, using leaves from the upper canopy third that matched the sampling position for the NMR material. A biological triplicate was harvested for this calibration. For each leaf *i*, dry mass DW_i (g) and area A_i (cm^2) were recorded, and LMA was computed as:

$$LMA_i \ [g\ m^{-2}] = \frac{DW_i}{A_i} x\ 10^4. \quad (6.17)$$

The factor 10^4 converts cm^2 to m^2. The calibration value used for all conversions was the triplicate mean:

$$\overline{LMA} = 32.52\ gm^{-2}$$

NMR provided malate concentration on a dry-mass basis, denoted here as c_{DW} (µmol mg^{-1} DW). To express malate per leaf area (µmol m^{-2}), values were converted as:

$$Malate\ [\mu mol\ m^{-2}] = c_{DW}[\mu mol\ mg^{-1}]\ x\ 1000\ [mg\ g^{-1}]\ x\ \overline{LMA}\ [g\ m^{-2}] \quad (6.18)$$

Here, the factor 1000 converts µmol mg^{-1} to µmol g^{-1}.

6.2.10 Statistical analysis

Fitting approach and domains

All thermal-response models were fitted using non-linear least squares in MATLAB R2025b. For this chapter, goodness of fit and parsimony metrics were always computed on the same domain used for fitting.

Metrics and model ranking

For observation i, y_i is the observed rate and $\hat{y}_i$ the model prediction; *n* is the sample size in the fitting domain and *k* the number of free parameters.

$$SSE = \sum_{i=1}^{n} (y_i - \hat{y}_i)^2, \qquad RMSE = \sqrt{\frac{1}{n}\sum_{i=1}^{n} (y_i - \hat{y}_i)^2}. \tag{6.19, 6.20}$$

Model ranking used the small sample corrected Akaike Information Criterion,

$$AIC_c = n \ln\left(\frac{SSE}{n}\right) + 2k + \frac{2k(k+1)}{n-k-1} \tag{6.21}$$

within each comparison set, I report,

$$\Delta AICc_j = AICc_j - \min_{m \in M} AICc_m, \tag{6.22}$$

and the corresponding Akaike weight,

$$p_j = \frac{\exp\left(-\frac{1}{2}\Delta AIC_{c,j}\right)}{\sum_{m \in M} exp\left(-\frac{1}{2}\Delta AIC_{c,m}\right)} \tag{6.23}$$

where p_j are Akaike weights (sum to 1) indicating the relative support. Interpretation follows the usual thresholds: ΔAICc < 2 (essentially equivalent), 4–7 (some support for the lower-AICc model), >10 (strong support for the lower-AICc model).

Spectra from NMR were segmented into 166 manually delimited integrals for ^{1}H and 200 integrals for ^{13}C, with automatic integration run with Topspin®. Each integral then represented a metabolic feature that could be used for statistical analyses. Features were assigned to metabolites by chemical shift and multiplicity, and the resulting peak areas

were taken forward for statistical analysis. Univariate analyses used a two-way ANOVA with temperature, time and their interaction across six discretised sampling points. Complementary analyses treated time as a continuous variable, within each individual temperature, and tested for the significance of the linear regression (F-test). In addition, multivariate analysis by orthogonal partial least squares (OPLS) was performed to assess temperature- or time-driven structure in the data. The results of the OPLS are not shown here since the time effect was not significant ($P > 0.05$) in the multivariate analysis.

6.3 Results

6.3.1 Thermal responses of the CO_2 flux in the dark

I recorded 57 light-to-dark transitions across temperatures ranging from 8.4 to 41 °C; one hour at 2000 µmol photons m^{-2} s^{-1} was followed by one hour in darkness. Dark respiration was partitioned into three observable features as outlined in Figure 6.1. A post illumination burst during the first seconds in darkness (PIB), a sustained light enhanced dark respiration above the darkness baseline (LEDR), and a steady state that defines basal R_{dark}.

6.3.2 Temperature dependence of PIB

Figure 6.2 shows representative time courses at five temperatures. Very shortly after lights-off, the net CO_2 exchange became negative, produced a transient peak consistent with the PIB that was visible at 17, 25 and 37 °C, but could not be identified at 7 and 41 °C. Superimposed on this response, there was a clear period of light enhanced dark respiration, with amplitude and duration that varied with leaf temperature. Warmer leaves typically reached the dark baseline more quickly, whereas cooler leaves maintained an elevated excess for longer. The steady state rate taken from the last five minutes defined basal R_{dark} for each trace.

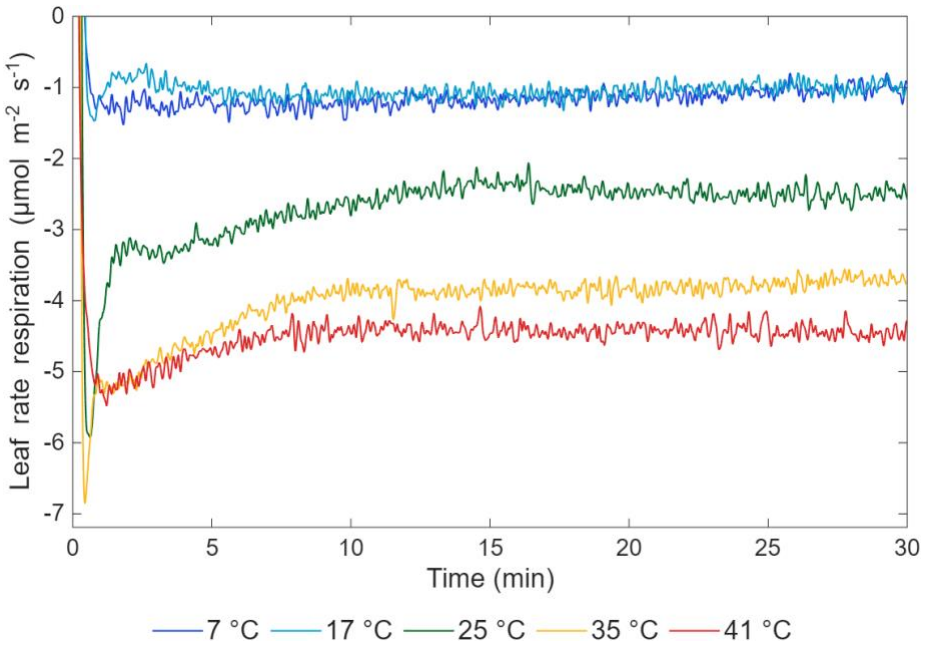

FIGURE 6.2. Example time-courses of leaf dark respiration after lights-off at five leaf temperatures (7, 17, 25, 35 and 41 °C), with each temperature in a distinct colour as indicated in the legend. Traces show an immediate post-darkness dip (the PIB, whose prominence varies with temperature), followed by a transient LEDR response that relaxes towards a steady state R_{dark}.

With the three components derived from the light-to-dark transition measurements, each leaf's series was normalised to its own 25 °C value so that differences in scale did not interfere with thermal patterns. At lights-off, photosynthetic CO_2 fixation stops almost immediately, the accumulated photorespiratory intermediates are metabolised (glycine is rapidly decarboxylated), the TCA cycle becomes fully engaged, and organic acids accumulated in the light begin to be oxidised (Fu et al., 2023; Lehmann et al., 2016). The gas analyser therefore registers a composite signal in the first seconds that mixes the cessation of photosynthetic CO_2 uptake with the release of CO_2 in the dark, while instrument response delay and chamber mixing accentuate a peak shaped signal.

Rather than a discrete physiological spike as often portrayed in the literature, the PIB is better understood as the combined effect of a physiological feature of post-illumination CO_2 release together with an instrument-level visual artefact that at the operational level

led to an apparent overshoot. Nevertheless, the PIB provides a partial indicator of the underlying glycine oxidation that follows lights-off (Fu et al., 2023; Rawsthorne & Hylton, 1991), even though it does not capture that process in full because of gas mixing in the chamber and tubing. For that reason, the PIB was treated here only qualitatively and excluded from statistical and modelling analyses. The magnitude of its peak was recorded by the IRGA being consistently detectable within an intermediate thermal window of about 15 to 35 °C and its value increased with temperature (R^2= 0.93) (Figure 6.3).

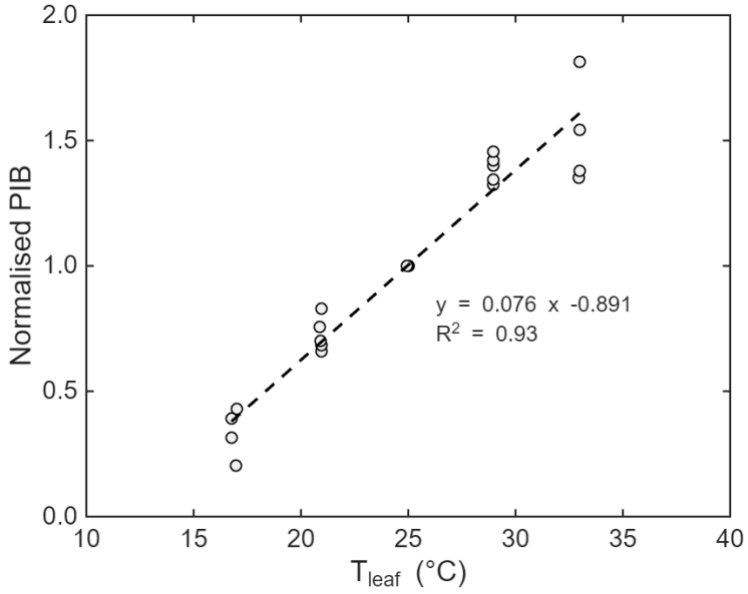

FIGURE 6.3. Post-illumination burst (PIB) as a function of leaf temperature, with values normalised within each leaf to its 25 °C value. Points show the normalised PIB in the first seconds after lights-off. The black dashed line is a linear regression fitted over the data range.

6.3.3 Temperature dependence of basal respiration R_{dark}

Across the 8.4 - 41.0 °C span, normalised R_{dark} rose monotonically over the measured temperature range (Figure 6.4). Comparing the models on the normalised data, constant-Q_{10} and simple Arrhenius captured the cool to moderate rise but systematically overshot at the warm end, where the observations start to curve. By contrast, the peaked Arrhenius and MMRT followed this warm data while preserving the mid-range slope, which gave

visibly closer agreement across the full temperature range (Figure 6.5a). The Arrhenius diagnostic in log space reinforced this view. As temperature increased, clear departures from linearity emerged above 33 °C, consistent with temperature-dependent deactivation of respiratory enzymes and changes in mitochondrial control of electron transport. In this domain, the constant-Q_{10} and simple Arrhenius representations diverged from the observations, whereas MMRT captured the systematic downturn in basal R_{dark} (Figure 6.5b).

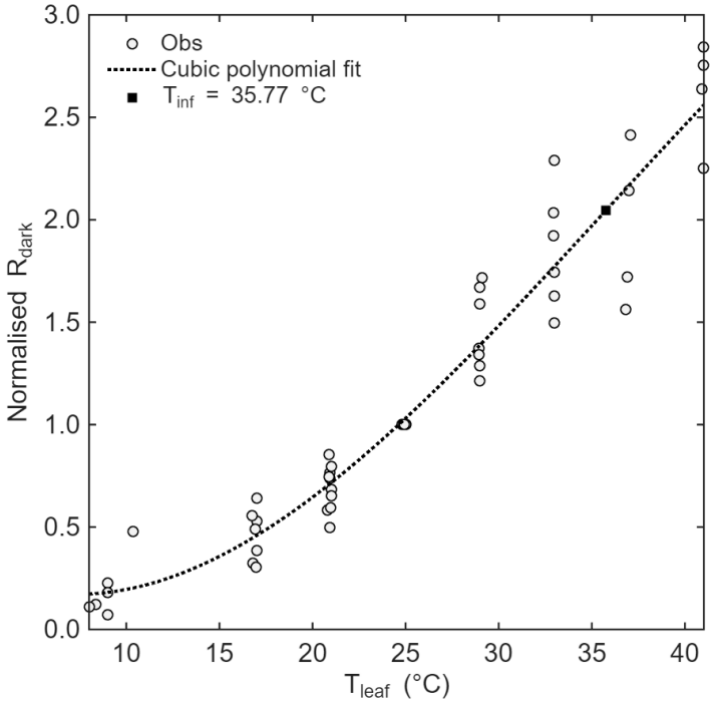

FIGURE 6.4. Normalised R_{dark} versus temperature, with cubic polynomial fits used to locate T_{inf} and y(T_{inf}). Grey open circles are the observations, and the dashed line is the cubic fit over 8.4–41.0 °C. The filled square marks T_{inf} (with ordinate y(T_{inf})).

The MMRT workflow used two stages with explicit anchors that stabilised the fit on the normalised response (Table 6.1). First, a cubic polynomial was fitted over the measured range to locate the inflection and its ordinate y(T_{inf}) (Figure 6.4). The fitted polynomial was:

$$y(T) = -4.10\ x\ 10^{-5}T^3 + 4.40\ x\ 10^{-3}T^2 - 5.82\ x\ 10^{-2}T + 0.379 \qquad (6.24)$$

which placed the inflection point at 35.8 °C, with ordinate y(T_{inf}) = 2.05. Below the inflection, the rise was approximately exponential, and above it, the rate increased more slowly, anticipating high-temperature deactivation. Holding these anchors fixed, the stage two MMRT fit estimated the curvature parameter, giving $\Delta C_p^{\ddagger}$ = -2.18 kJ mol^{-1} K^{-1}. Only MMRT delivered an optimum, with T_{opt} = 56.0 °C, a feature that the constant-Q_{10} and simple Arrhenius models cannot generate and that the peaked Arrhenius did not realise for these data.

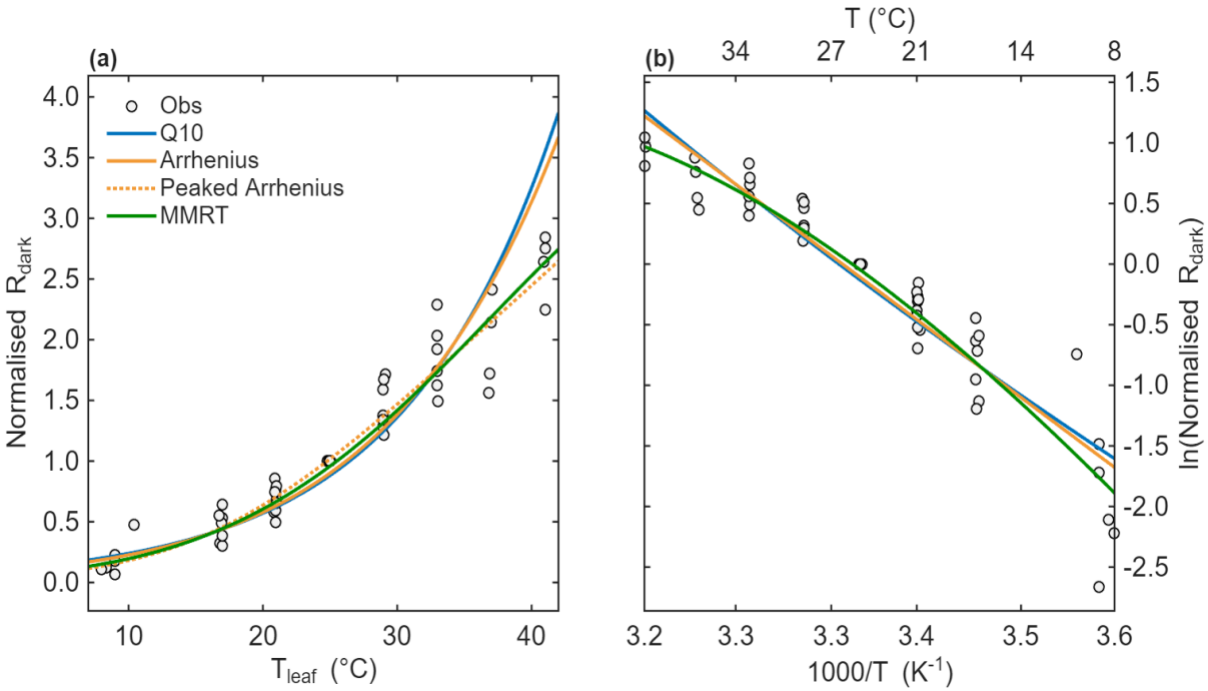

FIGURE 6.5. Temperature dependence of normalised R_{dark}. (a) Observations (open circles) with fits from four thermal models: constant-Q_{10}, simple Arrhenius, peaked Arrhenius and MMRT. (b) Arrhenius plot of ln (normalised R_{dark}) against 1000/T (K^{-1}). The lines in (b) match the fits shown in (a). Curves were normalised within leaf to that leaf's value at 25 °C. For scale, the across-leaf mean R_{dark} at 25 °C was 2.07 ± 1.18 µmol m^{-2} s^{-1} (mean ± SD).

Parameter estimates from the simple Arrhenius and constant-Q_{10} formulations are not presented because these models provide an inadequate description over the observed temperature range. By contrast, the peaked Arrhenius improved curvature relative to the simple form and returned E_a = 110.9 kJ mol^{-1}, H_d = 88.8 kJ mol^{-1} and ΔS = 299.7 J mol^{-1} K^{-1}. However, this set is not physiologically interpretable because $H_d < E_a$. In the deactivation form an interior maximum requires $H_d \geq E_a$ so that activation dominates at cooler temperatures and deactivation dominates at warmer temperatures. When $H_d < E_a$ the response remains monotonic, and any apparent maximum occurs at the boundary of the data. In this fit, the empirical maximum falls at the upper limit of the observed window.

TABLE 6.1. MMRT fitting workflow and parameter estimates for R_{dark}. Stage 1 fits a cubic polynomial to obtain the anchor point T_{inf} and its ordinate y(T_{inf}). Stage 2 fits the MMRT with T_{inf} and y(T_{inf}) held fixed, to estimate the curvature parameter $\Delta C_p^{\ddagger}$. Units: T_{inf} (°C); y(T_{inf}) (dimensionless); $\Delta C_p^{\ddagger}$ (kJ mol^{-1} K^{-1}).

Model	Stage	Anchors held fixed	Fitted parameters
MMRT	1	None (polynomial fit)	$\boldsymbol{T_{inf}}$ = 35.8; $\boldsymbol{y(T_{inf})}$ = 2.05
	2	$\boldsymbol{T_{inf}}$ = 35.8; $\boldsymbol{y(T_{inf})}$ = 2.05	$\boldsymbol{\Delta C_p^{\ddagger}}$ = −2.18

Goodness of fit and information criteria supported these visual patterns (Table 6.2). MMRT had the strongest support once parsimony was accounted for, with AICc = -188.07 and an Akaike weight of 0.684. The peaked Arrhenius also fitted well with ΔAICc = 1.54 and a weight of 0.316, which indicates secondary, but not trivial, support relative to MMRT. The simple Arrhenius and constant-Q_{10} models were clearly inferior, with much

larger ΔAICc values. All reported metrics are dimensionless because responses were normalised. Overall, the figures show that MMRT captures the warm end curvature while preserving mid-range slopes, and the information criteria confirm MMRT as the preferred description of the thermal response of R_{dark}.

TABLE 6.2. Goodness of fit and information criteria for the MMRT, simple Arrhenius, peaked Arrhenius, and constant-Q_{10} models fitted to normalised R_{dark}. Reported metrics are SSE (the sum of squared residuals), RMSE (root-mean-squared error, same scale as the response), AICc (Akaike Information Criterion with small sample correction), and ΔAICc (difference from the best model in this table). Smaller SSE, RMSE and AICc indicate better fit. All metrics are dimensionless because the responses were normalised.

Model	SSE	RMSE	AICc	△AICc
MMRT	2.03	0.19	-188.1	0
Simple Arrhenius	5.33	0.31	-130.8	57.3
Peaked Arrhenius	1.85	0.18	-186.5	1.5
Constant-Q_{10}	6.66	0.34	-118.1	69.9

6.3.4 Temperature dependence of LEDR

At or below 10 °C, a LEDR peak could not be identified within 60 min and there was no clear approach to a stable dark rate. Traces showed a near plateau with only a very small decline, so the amplitude and the integral were not identifiable. A representative low temperature curve is provided in figure 6.6.

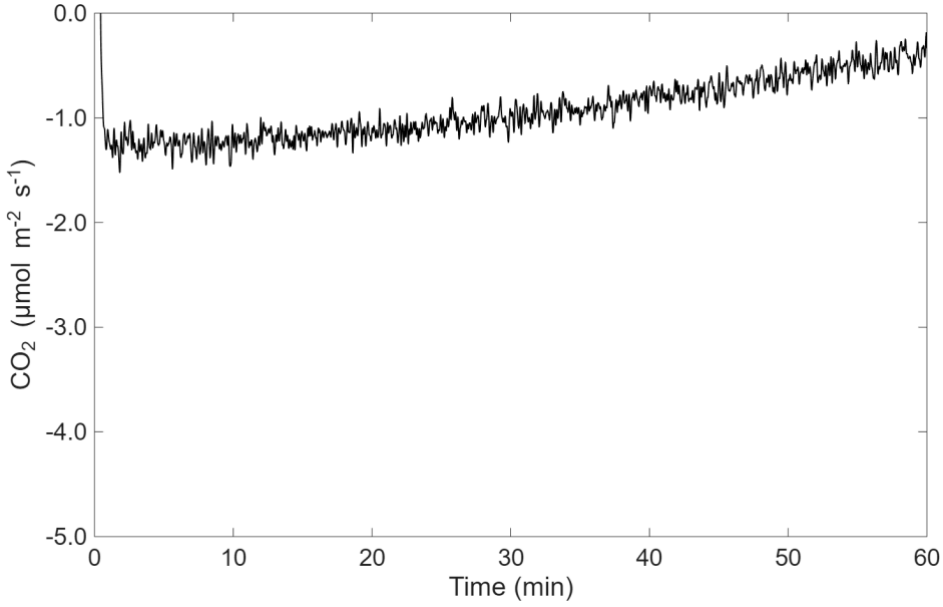

FIGURE 6.6. CO_2 release after lights off at 7 °C. The trace shows a monotonic decline without an identifiable LEDR peak or a clear approach to a dark steady state within 60 min, so amplitude and area were not defined, and these temperatures were excluded from LEDR analyses.

The normalised LEDR increased with temperature, but the increase became progressively less steep at higher temperatures, indicating reduced temperature sensitivity rather than a decline in amplitude (Figure 6.7a). To anchor the MMRT workflow, I first fitted a cubic polynomial to the observations. The cubic provided smooth trends across the measurement range and could be used to locate the inflection temperature T_{inf} = 23.2 °C, together with its ordinate y(T_{inf}) = 0.85. The fitted polynomial was:

$$y(T) = -6.15\ x\ 10^{-5}T^3 + 4.28\ x\ 10^{-3}T^2 - 0.019\ T - 0.247 \qquad (6.25)$$

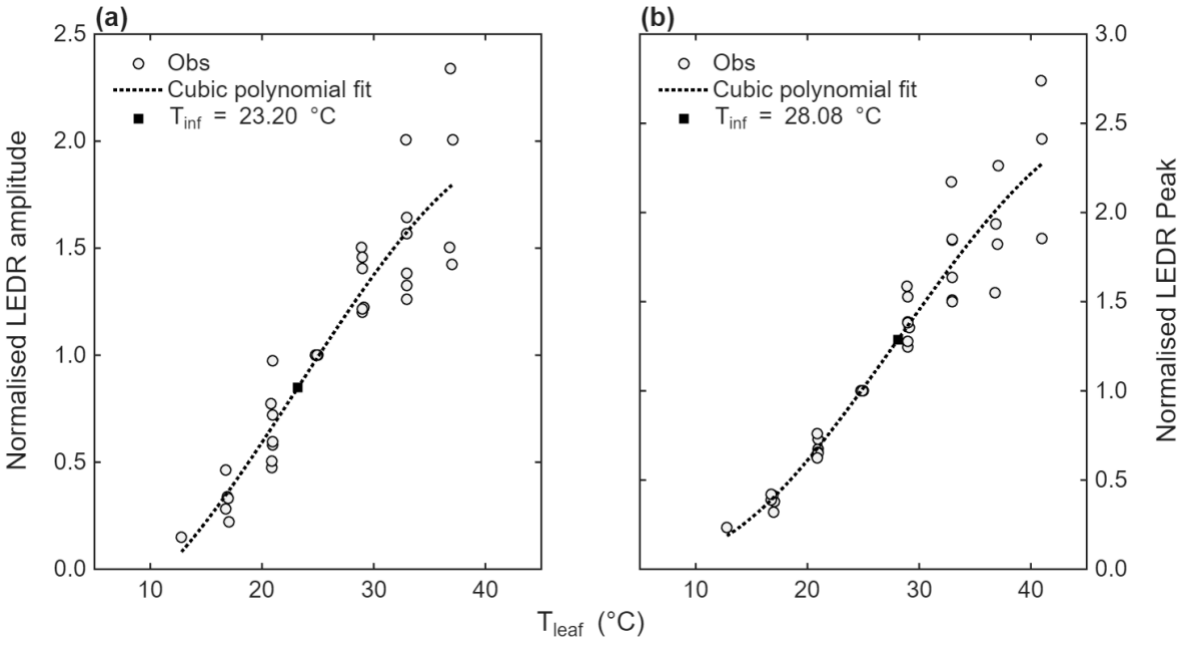

FIGURE 6.7. Normalised LEDR amplitude (a) and Normalised LEDR peak (b) versus temperature, with cubic polynomial fits used to locate T_{inf} and y(T_{inf}). Grey open circles are the observations, and the dashed line is the cubic fit over 13.0–38.0 °C for LEDR and 13.0–41.0 °C for LEDR peak. The filled squares marks T_{inf} (with ordinate y(T_{inf})).

Using those anchors, I fitted the MMRT models in two (Figure 6.8a) and three stages (Figure 6.8b), as summarised in Table 6.3. Stage 2 held $T_{inf,}$ and y(T_{inf}) fixed, as calculated in stage 1, and estimated the parameter $\Delta C_p^{\ddagger}$, which was -4.00 kJ mol^{-1} K^{-1}. Stage 3 then fitted the deactivation form over the full temperature range with T_{inf} and $\Delta C_p^{\ddagger}$ fixed and returned H_d equal to 251 kJ mol^{-1} and ΔS equal to 637 J mol^{-1} K^{-1}. These anchored stages ensured that the curvature around the basal window and the high temperature decline were constrained by a common physical reference.

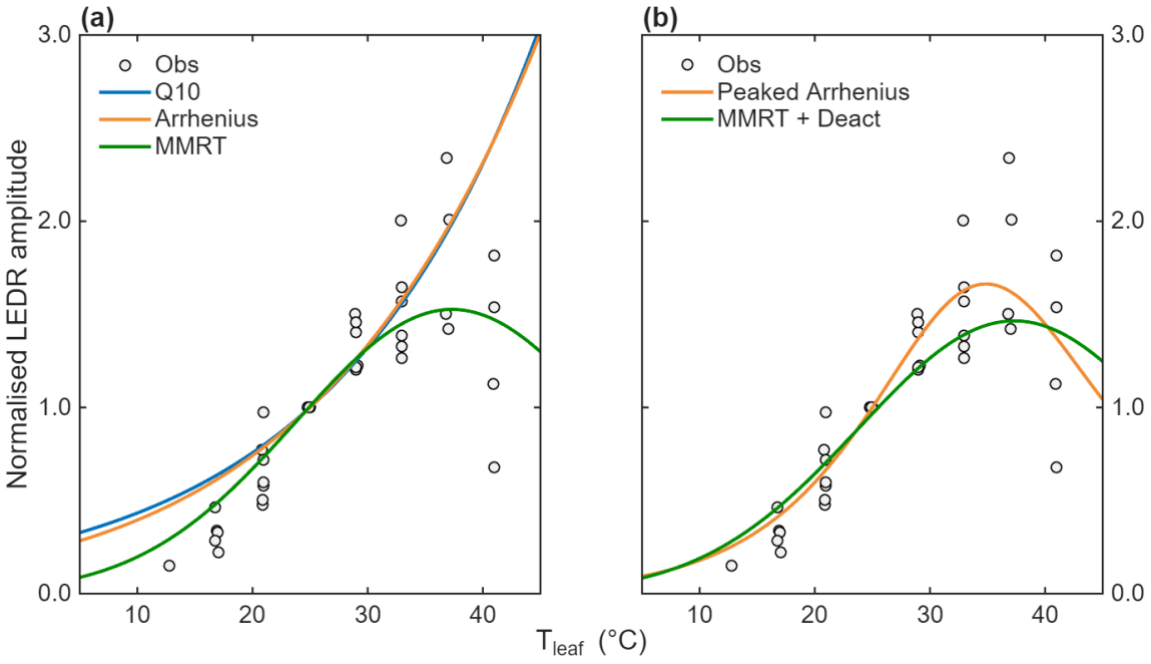

FIGURE 6.8. Temperature dependence of normalised LEDR amplitude. (a) MMRT 2-stage, simple Arrhenius and constant-Q_{10}. (b) MMRT 3-stage (with high-temperature deactivation) versus Peaked Arrhenius. Symbols are observations; green solid lines show MMRT (with or without deactivation function), the blue solid line shows constant-Q_{10}, and orange lines show Arrhenius (simple or peaked). For scale, the across-leaf mean $LEDR_{amp}$ at 25 °C was 1.08 ± 0.24 μmol m^{-2} s^{-1} (mean ± SD).

I then compared alternative thermal response models using the normalised LEDR data. Figure 6.8a overlays simple Arrhenius and constant-Q_{10} against the MMRT 2-stage curve. The simple Arrhenius and constant-Q_{10} fail to describe the warm end behaviour, so parameter estimates for these formulations are not reported. Figure 6.8b contrast the MMRT with high temperature deactivation (3-stage) against the peaked Arrhenius model. The peaked Arrhenius fit returned E_a equal to 85.6 kJ mol^{-1}, and deactivation terms H_d equal to 168.8 kJ mol^{-1} and ΔS equal to 548.2 J mol^{-1} K^{-1}.

TABLE 6.3. MMRT fitting workflow and parameter estimates for LEDR amplitude. Stage 1 fits a cubic polynomial to obtain the anchor point T_{inf} and its ordinate y(T_{inf}). Stage 2 fits the MMRT with T_{inf} and y(T_{inf}) held fixed to estimate the curvature parameter $\Delta C_p^{\ddagger}$. Stage 3 fits the deactivation form over the full range temperature, with T_{inf} and $\Delta C_p^{\ddagger}$ fixed to estimate H_d and ΔS. "Anchors held fixed" lists parameters constrained from the preceding stage. Units: T_{inf} (°C); y(T_{inf}) (dimensionless); $\Delta C_p^{\ddagger}$ (kJ mol^{-1} K^{-1}), H_d (kJ mol^{-1}) and ΔS (J mol^{-1} K^{-1}).

Model	Stage	Anchors held fixed	Fitted parameters
MMRT	1	None (polynomial fit)	$\boldsymbol{T_{inf}}$ = 23.2; $\boldsymbol{y(T_{inf})}$ = 0.85
	2	$\boldsymbol{T_{inf}}$ = 23.2; $\boldsymbol{y(T_{inf})}$ = 0.85	$\boldsymbol{\Delta C_p^{\ddagger}}$ = −4.00
	3	$\boldsymbol{T_{inf}}$ = 23.2; $\boldsymbol{\Delta C_p^{\ddagger}}$ = −4.00	$\boldsymbol{H_d}$ = 251; $\boldsymbol{\Delta S}$ = 637

Goodness of fit and information criteria are given in Table 6.4. The peaked Arrhenius model gave the smallest SSE and RMSE and the lowest AICc, so it ranked first with ΔAICc equal to 0. MMRT 2-stage (without explicit deactivation) ranked second with AICc equal to -127.9 and ΔAICc equal to 2.9. A ΔAICc of about 3 implies only modest evidence for the best model over the runner up, and SSE and RMSE were very similar for these two models. MMRT with deactivation was close in RMSE but had higher AICc and ΔAICc equal to 10.4. Simple Arrhenius and constant-Q_{10} had much larger errors and much higher AICc values, which indicates poor statistical support once the temperature peak is considered.

Given the small AICc gap between the top two models, I use the 2-stage MMRT for mechanistic inference, because its single free parameter $\Delta C_p^{\ddagger}$ quantifies the heat capacity change of activation and therefore the intrinsic curvature of the temperature response. This parameter is interpretable, dimensionally consistent, and comparable across treatment and species because T_{inf} and y(T_{inf}) standardise the scale. Consistent with those rankings,

estimated optima were well defined for the peaked models. Importantly, this choice does not imply that the peaked Arrhenius is inferior in a predictive sense, but rather reflects the different aims of empirical description versus mechanistic interpretation. The peaked Arrhenius returned T_{opt} equal to 34.9 °C, while the MMRT returned T_{opt} equal to 37.3 °C whether the deactivation term was enabled in the final stage, or not.

TABLE 6.4. Goodness of fit and information criteria for the MMRT, Arrhenius and constant-Q_{10} models fitted to normalised LEDR amplitude. Reported metrics are SSE (the sum of squared residuals), RMSE (root-mean-squared error, same scale as the response), AICc (Akaike Information Criterion with small sample correction), and ΔAICc (difference from the best model in this table). Smaller SSE, RMSE and AICc indicate better fit. All metrics are dimensionless because the responses were normalised.

Model	SSE	RMSE	AICc	△AICc
MMRT 2-Stage	2.72	0.24	-127.9	2.9
MMRT 3-Stage	2.91	0.25	-120.5	10.4
Simple Arrhenius	8.01	0.42	-78.3	52.6
Peaked Arrhenius	2.32	0.22	-130.9	0
Constant-Q_{10}	8.12	0.42	-77.7	53.2

Results for the normalised magnitude of the LEDR peak are presented in Figure 6.9. Cubic polynomial provided the anchors used to standardise the peak analysis. In Figure 6.7b the cubic fit identified the inflection temperature and its ordinate for the LEDR peak, which I then used as fixed anchor in the MMRT workflow. Table 6.5 summarises this workflow. The fitted polynomial was:

$$y(T) = -6.97\ x\ 10^{-5}T^3 + 5.87\ x\ 10^{-3}T^2 - 0.077\ T + 0.354 \quad (6.26)$$

Stage 1 fitted the cubic to obtain T_{inf} = 28.1 °C and y(T_{inf}) = 1.28 for the LEDR peak. Stage 2 then fitted the anchored MMRT to estimate the single curvature parameter, returning $\Delta C_p^{\ddagger}$ = -3.63 kJ mol^{-1} K^{-1}. I next compared thermal response models for the magnitude of the LEDR peak (Figure 6.9a). The peaked Arrhenius returned E_a = 128.1 kJ mol^{-1} and ΔS = 386.3 J mol^{-1} k^{-1}. Because $H_d < E_a$, this fit does not exhibit a finite thermal optimum within the observed ranged, so H_d and ΔS are not physiologically interpretable.

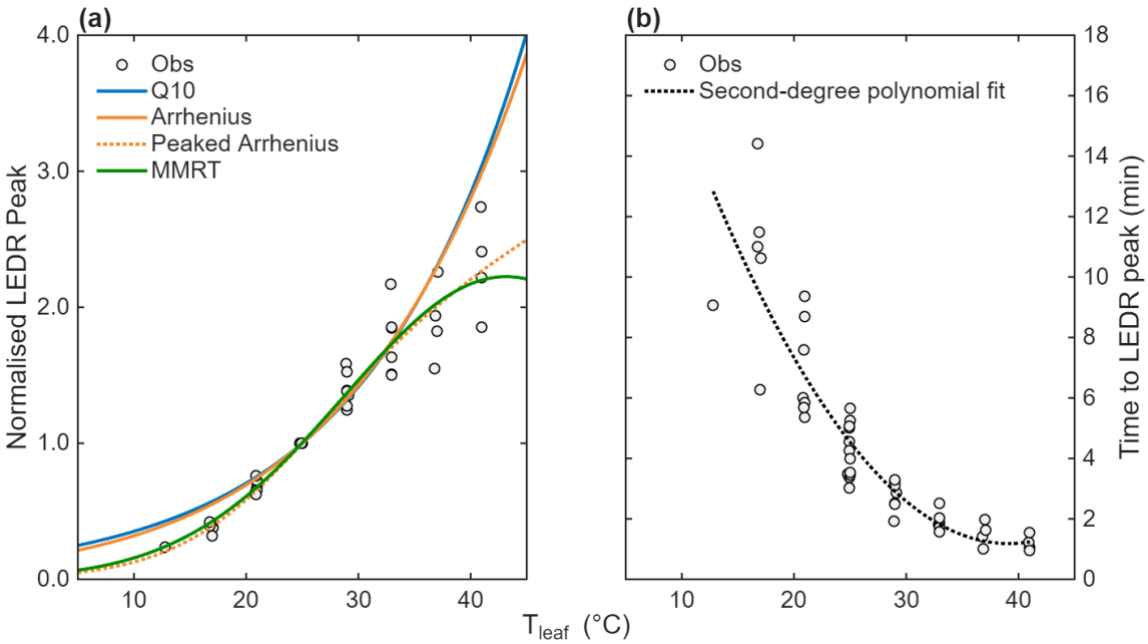

FIGURE 6.9. Temperature dependence on LEDR peak magnitude and timing. (a) Normalised LEDR peak versus leaf temperature. Open circles are observations; curves show constant-Q_{10} (blue), simple Arrhenius (orange), peaked Arrhenius (orange dashed), and MMRT (green) fits. (b) Time to the LEDR peak versus leaf temperature with a second-degree polynomial fit (dashed). For scale, the across-leaf mean LEDR peak at 25 °C was 3.14 ± 1.18 µmol m^{-2} s^{-1} ^{1} (mean ± SD).

TABLE 6.5. MMRT fitting workflow and parameter estimates for normalised LEDR peak. Stage 1 fits a cubic polynomial to obtain the anchor point T_{inf} and its ordinate y(T_{inf}). Stage 2 fits the MMRT with T_{inf} and y(T_{inf}) held fixed, to estimate the curvature parameter $\Delta C_p^{\ddagger}$. Units: T_{inf} (°C); y(T_{inf}) (dimensionless); $\Delta C_p^{\ddagger}$ (kJ mol^{-1} K^{-1}).

Model	Stage	Anchors held fixed	Fitted parameters
MMRT	1	None (polynomial fit)	$\boldsymbol{T_{inf}}$ = 28.1; $\boldsymbol{y(T_{inf})}$ = 1.28
	2	**Tinf =** 28.1**; y(Tinf) =** 1.28	$\boldsymbol{\Delta C_p^{\ddagger}}$ = −3.63

Goodness of fit and information criteria for models fitted to normalised LEDR peak are shown in Table 6.6. MMRT two stage had the smallest SSE and RMSE and the lowest AICc. The peaked Arrhenius model was second, with ΔAICc = 2.7, indicating that the two models are statistically competitive, with only modest evidence favouring MMRT. Simple Arrhenius and constant-Q_{10} showed much larger errors and much higher AICc values, indicating weak statistical support.

The temperature that maximises the LEDR peak from the anchored MMRT was T_{opt} = 43.2 °C (Figure 6.9a). Finally, the timing for the peak shortened markedly with temperature (Figure 6.9b). A second-degree polynomial captured a monotonic decline in the time to peak as leaves warmed (R^2 = 0.74), consistent with faster approach to the peak at higher temperatures.

TABLE 6.6. Goodness of fit and information criteria for the MMRT, simple Arrhenius, peaked Arrhenius, and constant-Q_{10} models fitted to normalised LEDR peak. Reported metrics are SSE (the sum of squared residuals), RMSE (root-mean-squared error, same scale as the response), AICc (Akaike Information Criterion with small sample correction), and ΔAICc (difference from the best model in this table). Smaller SSE, RMSE and AICc indicate better fit. All metrics are dimensionless because the responses were normalised.

Model	SSE	RMSE	AICc	△AICc
MMRT	1.25	0.17	-163.9	0
Simple Arrhenius	3.81	0.29	-112.5	51.4
Peaked Arrhenius	1.20	0.16	-161.1	2.7
Constant-Q_{10}	4.20	0.30	-108.1	55.8

Figure 6.10 shows the data and model fits in Arrhenius coordinates to emphasise shape. Figure 6.10a shows that the ln normalised LEDR amplitude declines approximately linearly with clear curvature at the coolest and warmest ends. MMRT tracks this curvature and stays close to the observations over the full span because it allows a non-zero $\Delta C_p^{\ddagger}$, so the activation enthalpy and entropy vary with temperature, and the Arrhenius plot bends accordingly. Simple Arrhenius fixes E_a and therefore gives a straight line, which appears to poorly match the apparent curvature in the observations. In Figure 6.9b, MMRT again follows the data best across the full range, while simple Arrhenius and constant-Q_{10} show the largest systematic departures.

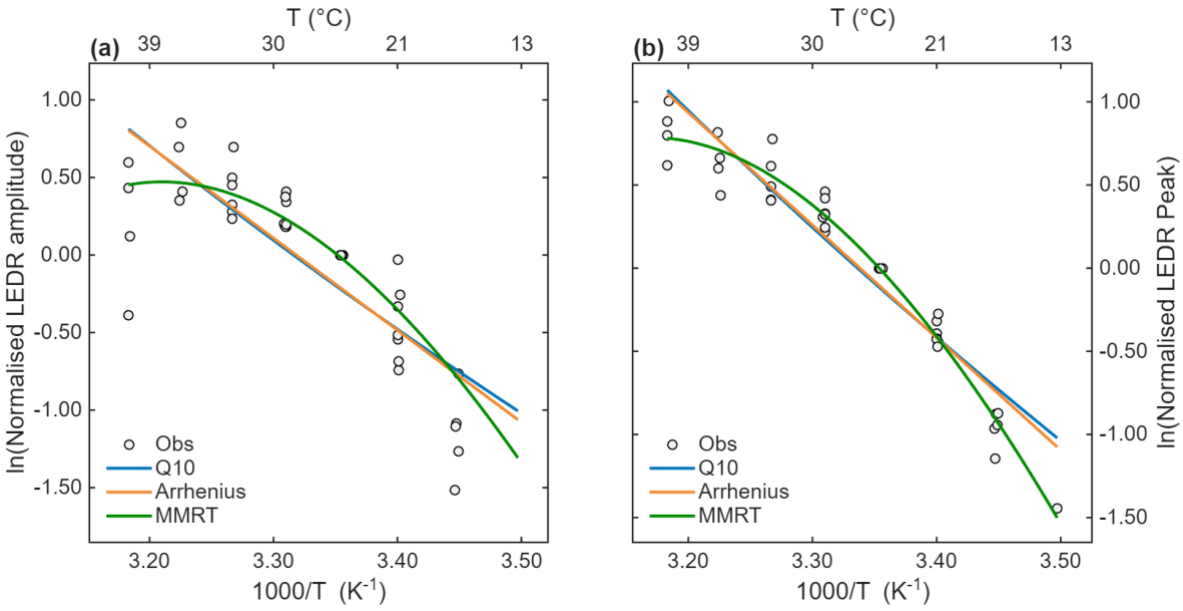

FIGURE 6.10. Temperature dependence of normalised LEDR amplitude and its normalised peak in Arrhenius coordinates (ln rate versus 1000/T). (a) Normalised LEDR amplitude. (b) Normalised LEDR peak. Open circles: observations; lines: fits from three thermal models (constant-Q_{10}, simple Arrhenius, and MMRT). The lower axis shows 1000/T(K^{-1}) and the upper axis leaf temperature (°C). Curves are the models fits to the data in each panel. Rates were normalised within leaf to that leaf's value at 25 °C.

Normalised LEDR area integrated above R_{dark} during the first hour after lights-off are plotted against leaf temperature (Figure 6.11). Figure 6.11a (Total area) integrates the excess of CO_2 released from lights-off to 60 min. Figure 6.11b (Left area) integrates from the LEDR peak back to the onset, and Figure 6.11c (Right area) integrates from the peak forward to the R_{dark} baseline. Parameter estimates are summarised in Table 6.7. For MMRT, the curvature was governed by negative $\Delta C_p^{\ddagger}$ values in all panels (−6.76 to −9.17 kJ mol^{-1} K^{-1}), consistent with the concave thermal shape, while $\Delta H_0^{\ddagger}$ varied in sign and magnitude across panels, giving analytic optima at 27.7 °C (Total), 24.5 °C (Left), and 28.8 °C (Right). The peaked Arrhenius returned activation energies between 113.6 and 117.6 kJ mol^{-1}, high-temperature deactivation enthalpies between 166.2 and 207.9 kJ mol^{-1}, and entropies between 559 and 702 J mol^{-1} K^{-1}. Its analytic optima were lower than MMRT in every panel, at 20.1 °C (Total), 22.4 °C (Left), and 20.7 °C (Right).

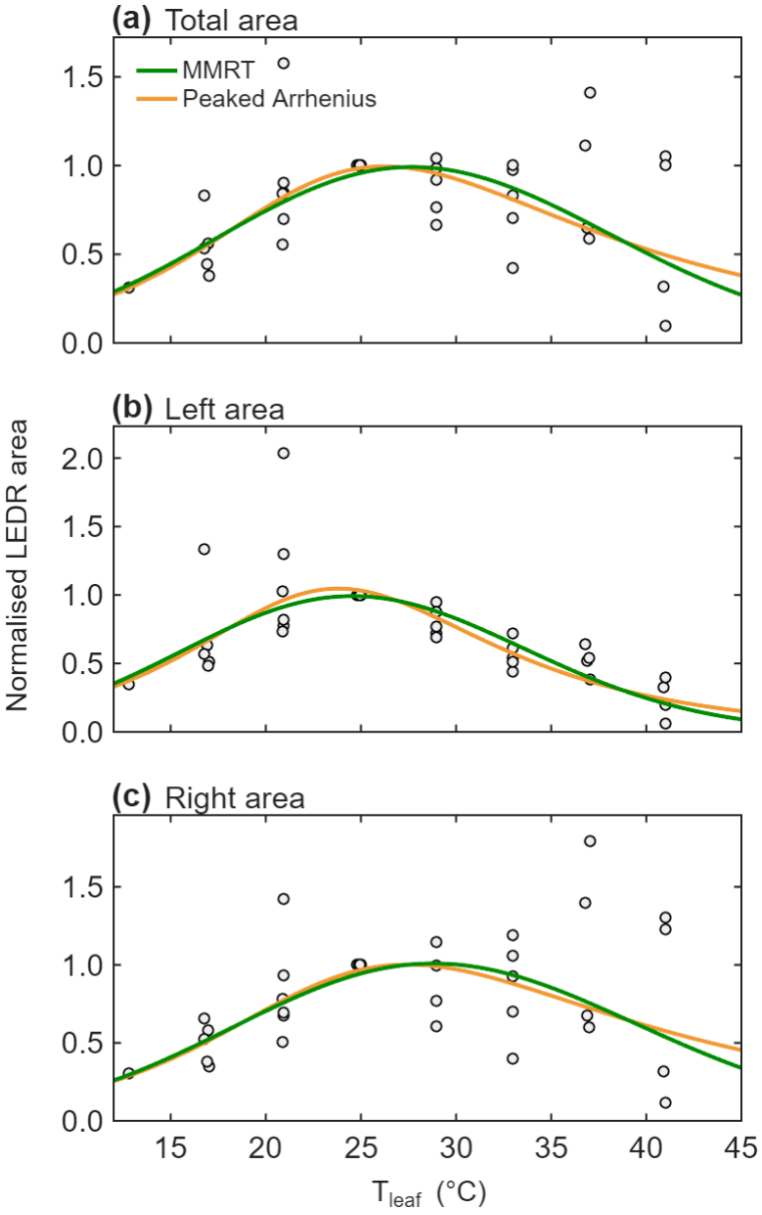

FIGURE 6.11. Normalised LEDR area versus leaf temperature. Panel (a) shows the total normalised LEDR area integrated over one hour after lights off. Panel (b) shows the left area, defined as the integral from lights-off up to the LEDR peak. Panel (c) shows the right area, defined as the integral from the LEDR peak back to the R_{dark} baseline. Symbols are normalised observations. Solid curves are model fits from MMRT (green) and the peaked Arrhenius (orange).

TABLE 6.7. Thermal response parameters estimated for the normalised LEDR area. Rows show fits of the MMRT and the peaked Arrhenius model to the total, left and right areas, where left area is the area from the LEDR peak back to onset and right is from the LEDR peak forward to the R_{dark} baseline. Reported parameters for MMRT, $\Delta C_p^{\ddagger}$ (kJ mol^{-1} K^{-1}) and $\Delta H_0^{\ddagger}$ (kJ mol^{-1}); for peaked Arrhenius, E_a (kJ mol^{-1}), H_d (kJ mol^{-1}) and ΔS (J mol^{-1} K^{-1}). T_{opt} (°C) is the analytic optimum from each model's parameters. The scale terms (log A for MMRT and A for peaked Arrhenius) were fitted but were omitted here for brevity. All LEDR areas were normalised at 25 °C before fitting.

Model	Area	Fitted parameters	T_{opt}
MMRT	Total	$\boldsymbol{\Delta C_p^{\ddagger}}$**= -7.04;** $\boldsymbol{\Delta H_0^{\ddagger}}$**=** 16.5	27.7
	Left	$\boldsymbol{\Delta C_p^{\ddagger}}$**= -9.17;** $\boldsymbol{\Delta H_0^{\ddagger}}$**= -6.74**	24.5
	Right	$\boldsymbol{\Delta C_p^{\ddagger}}$**= -6.76;** $\boldsymbol{\Delta H_0^{\ddagger}}$**=** 23.3	28.8
Peaked Arrhenius	Total	$\boldsymbol{E_a}$ **=** 117.6**;** $\boldsymbol{H_d}$ **=** 174.4**;** $\boldsymbol{\Delta S}$ **=** 588.6	20.1
	Left	$\boldsymbol{E_a}$ **=** 114.2; $\boldsymbol{H_d}$ **=** 207.9; $\boldsymbol{\Delta S}$ **=** 701.7	22.4
	Right	$\boldsymbol{E_a}$ **=** 113.6**;** $\boldsymbol{H_d}$ **=** 166.2**;** $\boldsymbol{\Delta S}$ **=** 559.3	20.7

Goodness of fit and parsimony metrics are showed in Table 6.8. Across panels, SSE was 2.72–4.13 and RMSE 0.23–0.31. MMRT received the higher Akaike weight for the Total area (0.64); ΔAICc = 1.13 for peaked Arrhenius and for the Right area (Akaike weight = 0.73; ΔAICc = 1.97), indicating slightly stronger support after accounting for parameter count. For the Left area the evidence was essentially similar (Akaike weight = 0.52 for MMRT and 0.48 for peaked Arrhenius; ΔAICc = 0.17). The results indicate that MMRT provides a marginally better description of the temperature pattern of normalised LEDR

area, particularly for the Total and Right windows, while the peaked Arrhenius yields similar accuracy with lower estimated optima.

TABLE 6.8. Goodness of fit and parsimony metrics for thermal response models fitted to the normalised LEDR areas. For each area (Total, left and right) I report the residual sum of squares (SSE), RMSE (root-mean-squared error, same scale as the response), AICc (Akaike Information Criterion with small sample correction), ΔAICc (difference from the best model in this table) and the Akaike weight. Smaller SSE, RMSE and AICc indicate better fit. All metrics are dimensionless because the responses were normalised. The parameter counts were k = 3 for MMRT and k = 4 for the peaked Arrhenius function.

Model	Area	SSE	RMSE	AICc	△AICc	Akaike Weight
MMRT	Total	2.80	0.26	-107.0	0.00	0.64
	Left	2.31	0.23	-115.1	0.00	0.52
	Right	4.13	0.31	-90.8	0.00	0.73
Peaked Arrhenius	Total	2.72	0.25	-105.9	1.13	0.36
	Left	2.19	0.23	-114.9	0.17	0.48
	Right	4.08	0.31	-88.8	1.97	0.27

6.3.5 Metabolic analysis during PIB and LEDR

6.3.5.1 Overview of metabolic profiles

After characterising thermal responses with different models, I examined how metabolites changed during a dark period following illumination. Representative ^{1}H-NMR and ^{13}C-NMR spectra of leaf extracts were segmented into 166 and 200 integrals respectively, used as quantitative features (Figure 6.12). The results were analysed using a two-way ANOVA to find metabolites that were associated with a time effect, a temperature effect and an interaction time x temperature effect. Using the ANOVA and hierarchical clustering (Pearson correlation) of significant features, the spectra were visualised as metabolic profiles across six discretised sampling instants and three temperatures. The NMR data are represented here as heatmaps, showing significant NMR signals (using a colour scale to show relative intensity) listed in rows (referenced with the chemical shift on the right hand side) in samples (in columns). Column (sample) labels are encoded as *T-t-i* to track each replicate and its temporal sequence (Figure 6.13). NMR signals were organised via hierarchical clustering (visible on the left hand side).

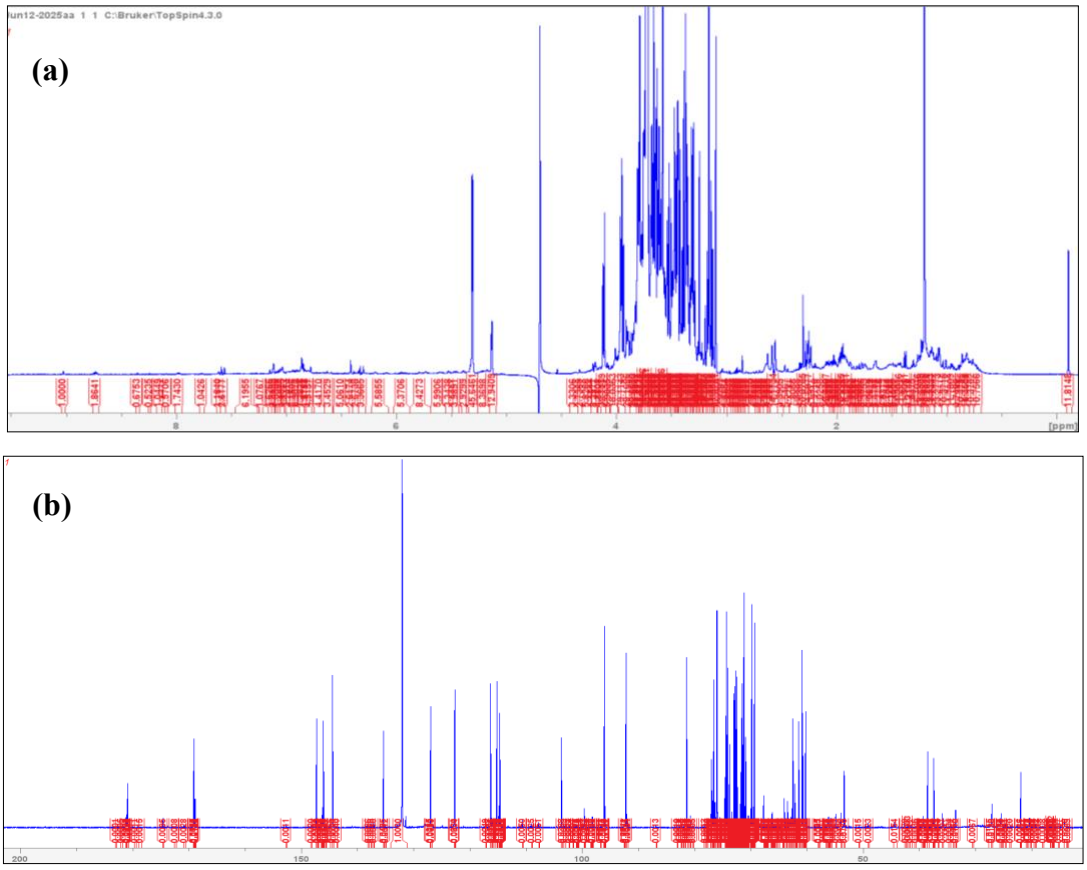

FIGURE 6.12. Representative ^{1}H-NMR (a) and ^{13}C-NMR (b) spectra of sunflower leaf extracts. The x-axis shows chemical shift in parts per million (δ, ppm). The y axis shows signal intensity. In panel (a), the blue trace is the proton spectrum, and blue peaks (either as singlets or multiplets) correspond to protons (non-exchangeable H-atoms) in different metabolites. In panel (b), peaks correspond to distinct carbon atoms (singlets only). Red regions mark the manually delimited integration windows (buckets) used as quantitative features, with n= 166 for ^{1}H and n= 200 for ^{13}C; the red numbers are the corresponding areas.

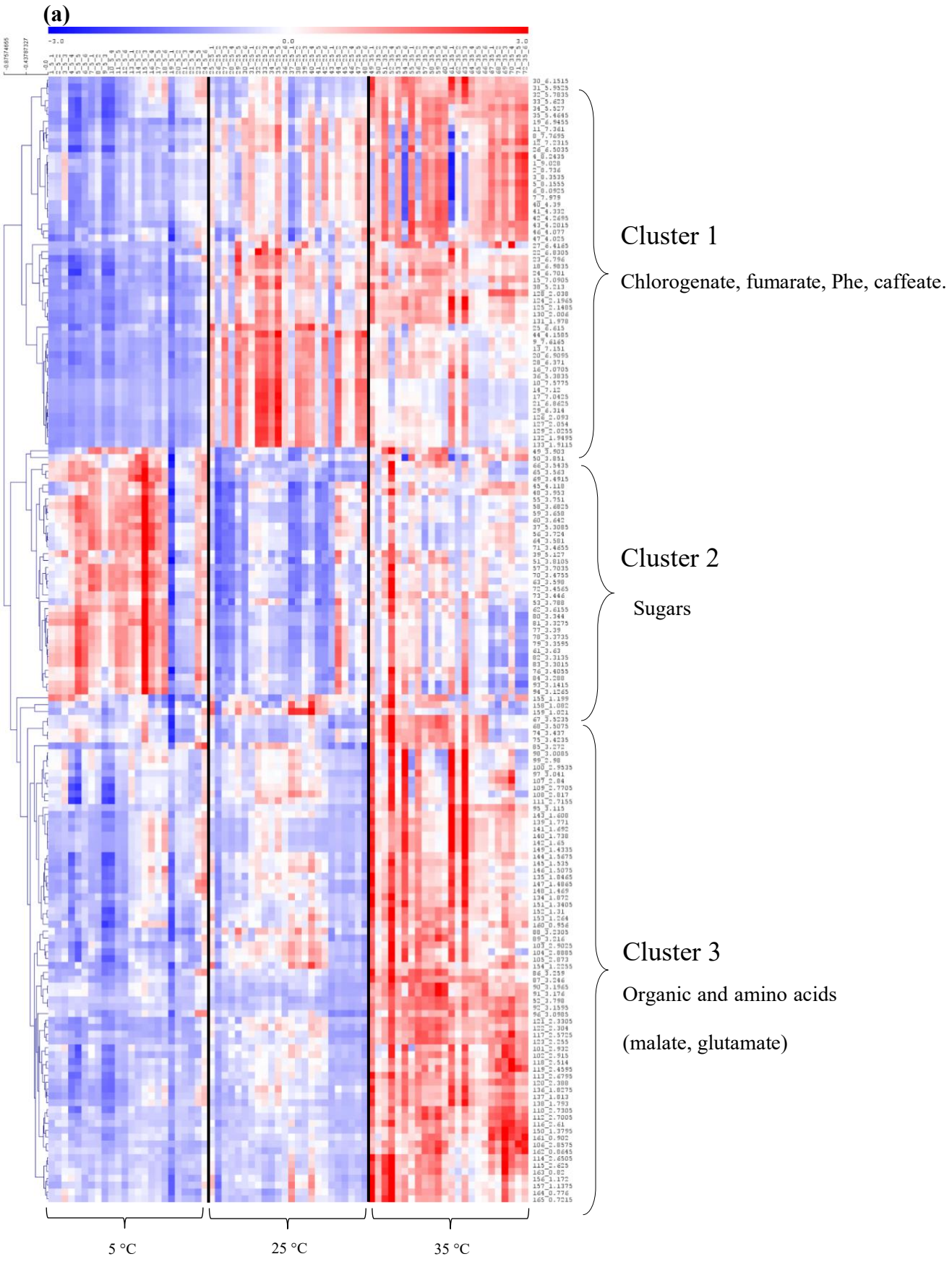
(a)
Cluster 1
Chlorogenate, fumarate, Phe, caffeate.
Cluster 2
Sugars
Cluster 3
Organic and amino acids
(malate, glutamate)
5 °C
25 °C
35 °C

(b)

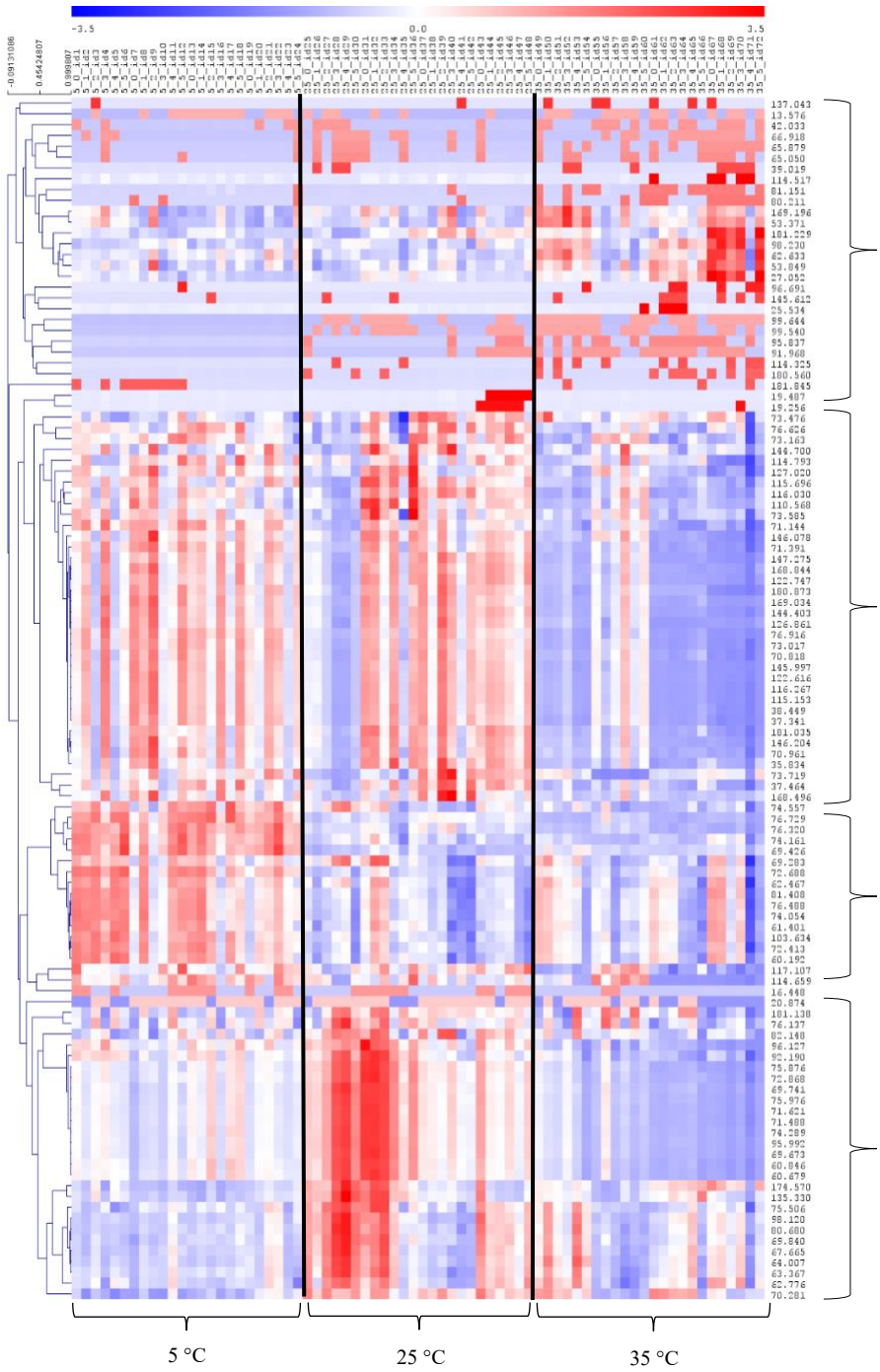
Cluster 1
(Phospho)choline, organic acid
(isocitrate)
Cluster 2
(Glycerate, chlorogenate)
Cluster 3
(Sucrose)
Cluster 4
(Glucose and galactose)
5 °C
25 °C
35 °C

FIGURE 6.13. Heatmap of NMR features associated with a significant temperature effect. (a) ^{1}H-NMR with166 features; (b) ^{13}C-NMR with 200 features. Rows are the integrated spectral features identified by their chemical shift in ppm shown at right. Columns are individual samples, labelled in the header as *T*-*t*-*i* where *T* is temperature in °C (5, 25 or 35), *t* is the discretised time point from 0 to 5 within each biological replicate and *i* is the sample number from 1 to 72. For each temperature, there are four biological replicates, each sampled at six time points. Colours represent row wise z scores (standardised within each feature): blue indicates values below the feature mean, and red above the mean. The left dendrogram shows hierarchical clustering of features with similar profiles across samples (Pearson correlation) and allows the visualisation of clusters of covarying metabolites. All features passed the two-way ANOVA for a temperature effect across the six discretised sampling points. On the right hand side, most important metabolites in each cluster are indicated.

In both the ^{1}H and ^{13}C heatmaps, temperature was the dominant source of variation. ^{1}H-NMR revealed the groups enriched at 35 °C. That included aromatic and organic acid signals such as chlorogenate, fumarate and phenylalanine (cluster 1), whereas a block of sugars declined after the light was turned off and remained lower under warm conditions (cluster 2). A third group (cluster 3), composed mainly of organic and amino acids (including malate and glutamate), increased later during the dark period. The ^{13}C data showed a consistent picture. At 35 °C, signals assigned to phosphocholine and the organic-acid region around 181 ppm increased, and isocitrate was also detected. In contrast, glycerate and chlorogenate were lower at 35 °C. Sucrose was more abundant at 5 °C, while glucose and galactose were higher at 25 °C and 35 °C. For both nuclei (^{1}H, ^{13}C), almost all features passed the two-way ANOVA threshold for the temperature effect across the six sampling times. Time itself had a much smaller influence than temperature, simply because a subset of features showed trajectories that differed with temperature (i.e. temperature-dependent time effect) within the early part of the dark period and thereafter, the change with time was proportionally smaller than that of temperature and therefore, was more impacted by leaf-to-leaf variability. For ^{1}H-NMR, no feature was associated with a significant time effect while some features were associated with a time x temperature interaction effect. These included: fumarate, chlorogenate and glutamate/glutamine, with early changes at 35 °C that were not found at 5°C (Figure 6.14a). In ^{13}C-NMR, more features were found to be associated with a time effect (Figure

6.14b), but only two had a significant time x temperature interaction effect: isocitrate (at 39.17 ppm) and probable methyl maleic acid (137.04 ppm) displayed transient responses that differed between 5, 25 and 35 °C over the six sampling instants.

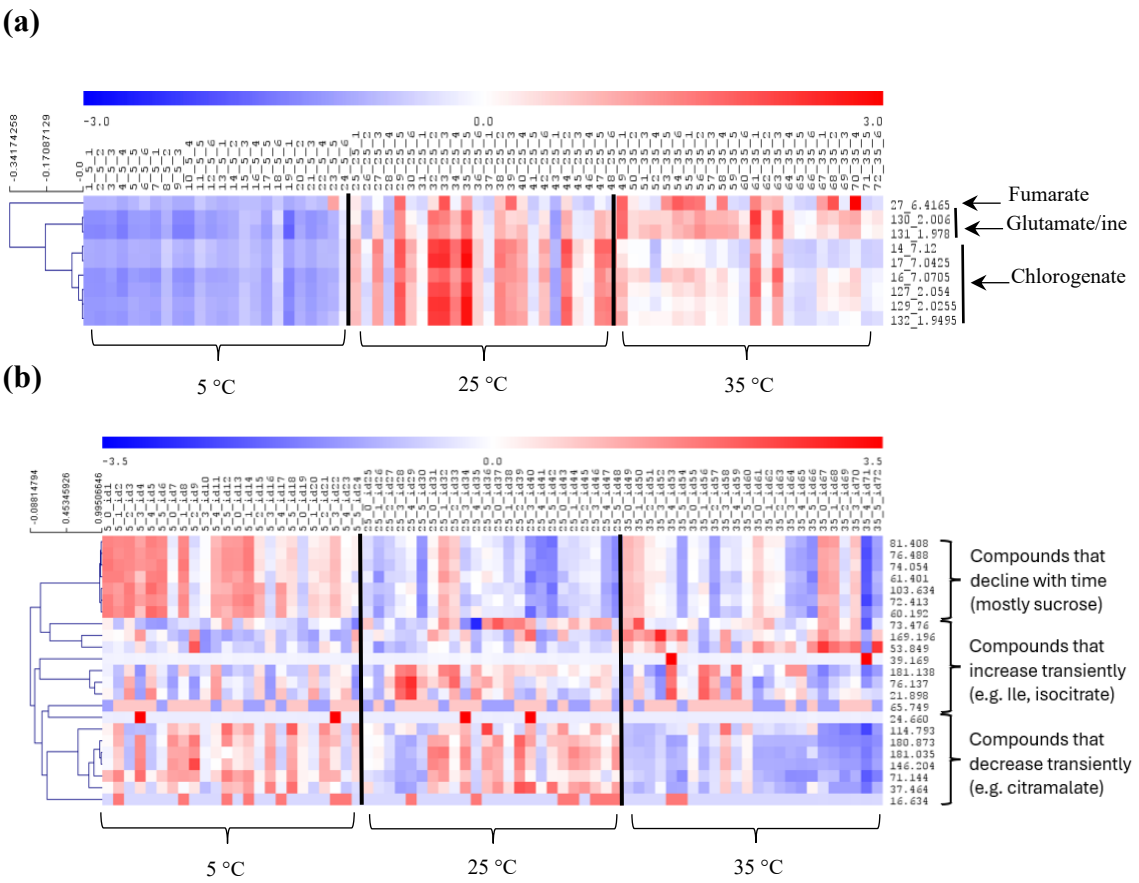

FIGURE 6.14. Heatmap of NMR features showing a significant time x temperature interaction effect or time effect. Panel (a) shows ^{1}H-NMR features with a time x temperature effect, and panel (b) shows ^{13}C-NMR features with a time effect. Rows are the integrated spectral features identified by their chemical shift in ppm shown at right. Columns are individual samples, labelled in the header as *T*-*t*-*i* where *i* is the sample number from 1 to 72, *T* is temperature in °C (5, 25 or 35), and *t* is the discretised time point from 1 to 6 within each biological replicate. For each temperature there are four biological replicates, each sampled at six time points. Colours represent row wise z scores (standardised within each feature): blue indicates values below that feature's mean, and red above the mean. The left dendrogram shows clustering of features with similar profiles across samples. Features displayed met $p < 0.05$ in a two-way ANOVA across the six sampling points.

6.3.5.2 Effect of time and temperature on malate content

At this stage, it is interesting to focus on malate, since it has been suggested to be a key actor of LEDR (Atkin et al., 1998; Fan et al., 2024; Lehmann et al., 2015, 2016). Absolute malate concentrations were calculated from NMR signals and expressed in μmol m^{-2} (Figure 6.15). It could be seen that (i) there was an apparent tendency of the average content to decline with time at 25 and 35°C (but not at 5°C); (ii) the malate content differed significantly between temperature treatments. However, despite the apparent tendency to change with time after lights-off, this change was not statistically significant ($P > 0.05$). At 25 °C, the malate pool was largest throughout, starting at 1035 ± 260 μmol m^{-2} and dipping within 1 min, then returning to its initial level by 4 min and remaining near 830 ± 260 μmol m^{-2} at 60 min. At 35 °C, the malate pool was consistently lower than at 25 °C and declined steadily from 927 to 576 μmol m^{-2} by 30 min before a slight recovery to 614 ± 195 μmol m^{-2} at 60 min. In contrast, at 5 °C the malate concentration was smallest (298 ± 97 μmol m^{-2}), rose transiently to 426 μmol m^{-2} at 4 min, then declined, ending at 273 ± 163 μmol m^{-2}.

Over the first hour in darkness, LEDR at 5 °C was indistinct, respiration rates were close to the detection limit, and malate concentration remained nearly constant. I therefore did not quantify the LEDR-malate relationship at this temperature and focused on 25 and 35 °C. The integrated LEDR area increased from 775 μmol m^{-2} at 25 °C to 919 μmol m^{-2} at 35 °C, while malate decrease from its concentration in the light to the lowest value reached within the first hour of darkness (Δmalate) by 260 μmol m^{-2} at 25 °C and 351 μmol m^{-2} at 35 °C. Expressed as the fraction of LEDR potentially supplied by malate loss (f = Δmalate/LEDR), the contributions were $f = 0.33$ at 25 °C and $f = 0.38$ at 35 °C. These patterns indicate that malate turnover scales with the magnitude of LEDR and could potentially account for about a third of the CO_2 release during LEDR at moderate to warm temperatures.

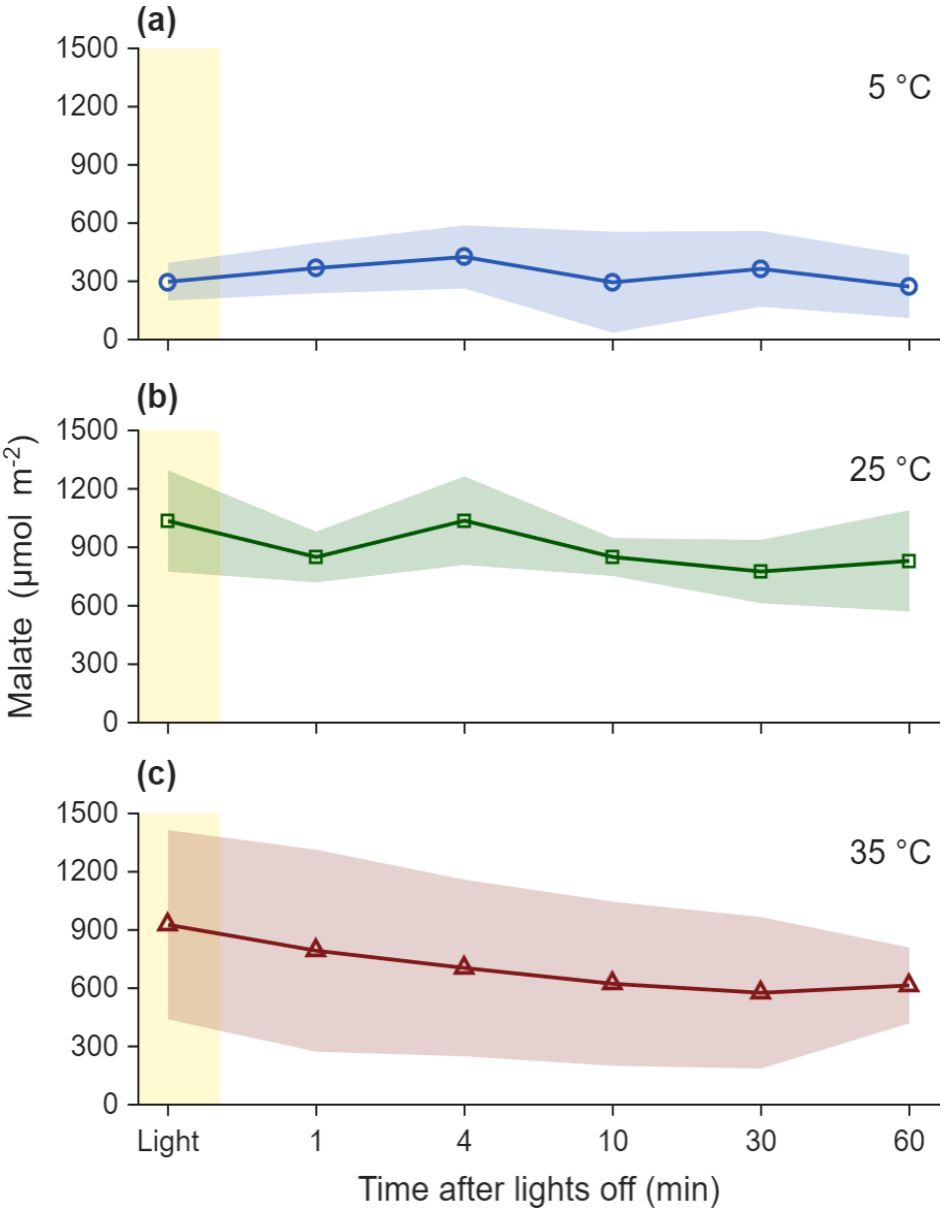

FIGURE 6.15. Temporal changes in malate concentration following lights-off at three temperatures. Panels show 5 °C (a), 25 °C (b) and 35 °C (c). Symbols show temperature-specific means with connecting lines and shaded bands show the standard deviation across replicates. The "light" point is the sample taken two minutes before lights-off. Subsequent samples were taken at 1, 4, 10, 30 and 60 min. Malate concentration per leaf area is expressed in µmol m^{-2}.

6.4 Discussion

6.4.1 Scope and modelling framework

This chapter addresses how temperature shapes two observable facets of leaf respiration in darkness: the basal steady state R_{dark} and the transient light enhanced dark respiration (LEDR). The experimental design separates the immediate post-illumination burst (PIB) from LEDR and treats PIB qualitatively, given known response-time distortions in the first seconds after darkening (Bulley & Tregunna, 1970; Jud et al., 2016; Reddy et al., 1991). Data obtained at different temperatures on the same leaves were normalised to 25 °C to reduce data variability that stemmed from differences in leaves' photosynthetic capacity and allowed better focused inference on responses to different temperatures (Heskel et al., 2016; Medlyn et al., 2002). Within this framework, anchored MMRT captured the temperature response and warm-side curvature in Arrhenius coordinates for R_{dark} and LEDR metrics, and it provided an interpretable parameter through the heat capacity change of activation $\Delta C_p^{\ddagger}$. The peaked Arrhenius served as a flexible descriptive comparator while the simple Arrhenius and constant-Q_{10} functions could not adequately describe the high-temperature down-turn in enzyme activities (Arcus & Mulholland, 2025; Atkin & Tjoelker, 2003; Heskel et al., 2016; Liang et al., 2018; Warren & Dreyer, 2006).

6.4.2 R_{dark}: monotonic warming with warm side curvature

Normalised R_{dark} increased monotonically across the measured range and showed warm-side downward curvature in Arrhenius space above about 33 °C, consistent with global analyses that report a declining temperature sensitivity of leaf respiration as leaves warm (Crous et al., 2022; Heskel et al., 2016; Zheng et al., 2024). MMRT captured this curvature in the normalised data (Liang et al., 2018). Thermodynamically, a negative $\Delta C_p^{\ddagger}$ makes the apparent activation enthalpy and entropy vary with temperature, which bends the Arrhenius plots as temperature rises (Arcus et al., 2016; Arcus & Mulholland, 2025).

Physically, warming redistributes the proportion of functionally distinct conformational sub ensembles in the catalytic and transport machinery, thereby shifting the effective activation barrier with temperature (Arcus et al., 2016; Bunzel et al., 2021). Across studies, Q_{10} for leaf respiration is not fixed and usually falls as temperature rises, matching the observed warm side curvature in R_{dark} (Atkin & Tjoelker, 2003; Crous et al., 2022).

The peaked Arrhenius equation failed to yield an interior maximum over the observed range for R_{dark} because $H_d < E_a$, so parameter values were not physiologically interpretable for these data. By contrast, MMRT required only $\Delta C_p^{\ddagger}$ once T_{inf} and $y(T_{inf})$ were anchored and explained the curvature through a single, dimensionally consistent quantity. MMRT estimated a T_{opt} near 56 °C for R_{dark}, above the measured window, which should be read as a model implied optimum rather than an observed maximum.

6.4.3 LEDR as a light conditioned response

Amplitude

$LEDR_{amp}$ rose with temperature up to an intermediate range and then declined at warmer temperatures. Anchored MMRT returned a T_{opt} of about 37 °C, which was within the physiological operating range for sunflower leaves and coincides with the observed peak of the response.

$LEDR_{amp}$ differs from R_{dark} because its substrates and redox constraints were set in the preceding light (Lehmann et al., 2016; Tcherkez et al., 2017). High light builds organic acid pools like malate and fumarate and primes chloroplastic NADP-malate dehydrogenase through thioredoxin, with greater engagement of cytosolic and mitochondrial dehydrogenases (Scheibe, 2004; Selinski & Scheibe, 2019; Yokochi et al., 2021). On darkening, these pools are oxidised and decarboxylated, producing a transient excess above the R_{dark} baseline that depends on prior light metabolism and available respiratory substrates (Lehmann et al., 2015, 2016; Parys & Romanowska, 2000; Tcherkez et al., 2005; Vines et al., 1983).

A negative $\Delta C_p^{\ddagger}$ for $LEDR_{amp}$ indicates that the ensemble of steps governing the transient inherits temperature dependent curvature, consistent with MMRT and with experimental demonstrations of negative activation heat capacity in enzymes systems (Arcus et al., 2016; Arcus & Mulholland, 2025; Bunzel et al., 2021; Liang et al., 2018). At cold to moderate temperatures, $LEDR_{amp}$ often increases with warming because metabolic steps involved in decarboxylation are sensitive to temperature and use substrate pools built in the light. A temperature dependent limit then appears as reflected by curvature and due to substrate pools exhaustion. As a result, warming speeds the effective steps on the rising part of LEDR and can raise the amplitude, before any "warm side" limit appears (Lehmann et al., 2016; Parys & Romanowska, 2000; Vines et al., 1983).

Peak magnitude and timing

The LEDR peak is the instantaneous net CO_2 flux rate at t_{peak} and equals R_{dark} plus $LEDR_{amp}$ (please see Fig. 6.1 for further clarification). Because it combines baseline and LEDR-driven excess, its temperature pattern reflects both components. In my data, R_{dark} shows a strong, smooth temperature dependence that the models capture well, whereas $LEDR_{amp}$ is more scattered. Consequently, the LEDR peak inherits the clear temperature signal from R_{dark} and tracks the model fits more closely than $LEDR_{amp}$ alone. The time to peak shortened with temperature, consistent with a faster approach to the maximum as effective rate constants increase.

LEDR areas: rise and decay with time

The total normalised LEDR area integrates the transient above R_{dark}, while the left and right areas isolate the rise and the decay, respectively. The left area quantifies how quickly the system moves from lights-off to the peak and depends on the rapid remobilisation of substrates inherited from the light phase, thus (i) exerting a strong reductant pressure immediately after darkening, and (ii) a transient adenylate imbalance that initially

constrains phosphorylation with cytosolic ADP becoming limiting, such metabolic conditions have long been recognised during light-dark transitions (Geigenberger & Fernie, 2014; Hampp et al., 1982; Santarius et al., 1964; Urlrich et al., 1992). Rapid engagement of non-phosphorylating routes relieves redox backpressure when ADP is limiting, allowing electron flow without immediate ATP formation and stabilising redox poise, for example through AOX (Igamberdiev & Bykova, 2023; Igamberdiev & Eprintsev, 2016). These routes help keep the TCA cycle turning and maintain NAD to NADH ratios while adenylates equilibrate via adenylate kinase and related reactions (Geigenberger & Fernie, 2014; Igamberdiev & Kleczkowski, 2006). At lights-off, several reduced pools are primed for oxidation, including malate, isocitrate, pyruvate, glycolate, and other carbon skeletons (Lehmann et al., 2015, 2016; Rawsthorne & Hylton, 1991; Selinski & Scheibe, 2019). Consistent with the idea of a rapid metabolic process (redox and adenylate readjustment), the left area tends to covary with $LEDR_{amp}$ and peak timing.

The right hand area captures how quickly the system returns to R_{dark} and is governed by the degree of proton-ATP coupling in the mitochondrial electron transport chain as well as any high-temperature loss of catalytic efficiency. Uncoupling (i.e. proton "leak" across the inner mitochondrial membrane, so that protons return to the matrix without ATP generation by the ATP synthase) reduces respiratory efficiency and accelerates dissipation of the proton-motive force (Divakaruni & Brand, 2011; Igamberdiev & Kleczkowski, 2006; Jastroch et al., 2010; Sweetlove et al., 2006).

Because temperature can influence the rise and decay of LEDR through partly distinct mechanisms, the left and right areas showed different thermal patterns even when the total area of LEDR appeared only weakly temperature dependent. After normalisation, residual differences in redox "history" (i.e. inherited from the light period), light interception and sink demand remain, but these are mostly present as shifts in timing and symmetry rather than as change in magnitude in my data.

6.4.4 PIB: a qualitative window on residual photorespiratory flux

The PIB was most visible within a mid-temperature window and was weak or absent at the cold and hot extremes. This pattern may be consistent with the combined effects of photorespiratory glycine pool size in the light and analyser response on darkening. In C_3 leaves, a substantial glycine pool accumulates in the light and declines rapidly after lights-off as glycine decarboxylase drives a post-darkening CO_2 pulse. The IRGA registers an apparent overshoot because photosynthetic uptake ceases almost immediately while decarboxylation persists and increases as mixing within the gas exchange chamber equilibrates gas concentrations. Although the instrument-related overshoot component is an artefact, the temperature window where the PIB is clearly resolved still encodes useful information about situations in which light history and photorespiratory process build sufficient glycine to produce a measurable pulse (Fu et al., 2023; Rawsthorne & Hylton, 1991). For this reason, the PIB was treated qualitatively and excluded from model fitting.

6.4.5 Mechanistic integration

Three features provide a unified explanation for the observed warm side bend and for the decline of $LEDR_{amp}$ beyond the intermediate peak. First, increasing proton conductance across the inner mitochondrial membrane increases proton leakage, dissipating the proton motive force more rapidly than at lower temperatures, which lower effective phosphorylation efficiency. For a given electron flux less ATP is formed per unit oxygen reduced, so additional heating yields progressively smaller gains in respiratory throughput (Divakaruni & Brand, 2011; Jastroch et al., 2010; Macherel et al., 2021). Second, temperature shifts the partitioning of electron flow between tightly coupled pathways and alternative routes that bypass ATP formation, for example engagement of the alternative oxidase. Such bypass flow lowers the ATP yield per O_2 and attenuates the marginal benefit of further warming (Sluse & Jarmuszkiewicz, 1998; Vanlerberghe, 2013; Vanlerberghe et al., 2020). Third, temperature sensitive protein stability reduces catalytic competence. Unfolding, active-site reorganisation and cofactor lability depress catalytic turnover. In

MMRT terms, this appears as negative $\Delta C_p^{\ddagger}$, which implies temperature dependent activation thermodynamics in the ensemble of the enzymes that set the respiratory CO_2 flux (Arcus et al., 2016; Arcus & Mulholland, 2025; Bunzel et al., 2021; McLeod et al., 2025). Together these processes reduce the incremental return of extra thermal energy on catalytic performance, producing the non-Arrhenius curvature in R_{dark} and shaping the rise and decay of LEDR.

6.4.6 Metabolic evidence against a single organic acid mechanism in LEDR

The metabolite survey using NMR supports the view that the post-illumination dark period is not fuelled by a single substrate pool but reflect a broader temperature conditioned reallocation/utilisation of carbon (Abadie et al., 2018; Lehmann et al., 2016; Xu et al., 2025). Heatmaps for ^{1}H and ^{13}C show a strong temperature effect across the sampling window (all metabolites were associated with a temperature effect in ^{1}H data), which aligns with the kinetic evidence that, under my experimental condition, temperature is the primary driver of respiratory behaviour. The time course of malate is consistent with this view because absolute concentrations are relatively small and the changes after lights-off are modest.

A progressive utilisation of the malate pool formed in the light cannot account quantitatively for the time course or the temperature response of respiration. Across the hour in darkness malate pools ranged around 300 to 1000 μmol m^{-2} and shifted only modestly, with the largest net decline about 350 μmol m^{-2} at 35 °C, and a brief early rise at 5 °C. Expressed against the integrated LEDR signal, f = Δmalate/LEDR was 0.13 at 5 °C, 0.33 at 25 °C and 0.38 at 35 °C, so malate loss could at most account for about one third of LEDR at warm temperatures and only a small fraction at 5 °C. The remainder must arise from other substrates and processes operating in parallel.

Consistent with this, NMR spectra show temperature-structure changes across several organic-acid and aromatic regions, together with increases in hexose-rich zones, while cold conditions show a considerable increase in leaf sucrose content (Adler et al., 2025;

Kaplan et al., 2004; Kitashova et al., 2023). This combination suggests that lights-off triggers a broad re orchestration of storage and transport metabolites towards substrates that feed central carbon metabolism and redox balancing, with the exact balance set by temperature (Guy et al., 2008; Lehmann et al., 2016; Obata & Fernie, 2012).

Only a small set of features showed a significant time x temperature interaction. In the proton data, fumarate, chlorogenate and glutamate (or glutamine) changed early at 35 °C but not at 5 °C. In the carbon data, isocitrate vary with both factors. These results suggest that specific pathways are affected by time in a temperature-dependent manner, while many metabolites are primarily affected by temperature and then change only modestly over one hour. This is consistent with a picture where a limited number of specific control points respond rapidly at lights-off, while most metabolite pools follow the thermal context set by the preceding light period and by mitochondrial function in darkness.

At 35°C the pattern is compatible with higher anaplerotic flux via PEPC supplying oxaloacetate and malate to the TCA cycle, together with shifts in ATP and NAD(P)H coupling that suggest increased AOX activity and partial uncoupling (Sweetlove et al., 2010; Vanlerberghe et al., 2020; Zhang et al., 2023). Higher levels in organic-acid regions and selected amino acids are consistent with the flux through the TCA cycle and related pathways (which generate carbon skeletons and feed organic acid pools) that generate CO_2 without necessarily producing ATP at the same efficiency as under cooler conditions (Abadie et al., 2024; Boex-Fontvieille et al., 2013). The decline in sucrose and the relative rise of hexose-rich regions at warm temperature likely reflects an increased investment of carbohydrate into respiratory routes as well as export (Lafta & Lorenzen, 1995; Nicholls, 2021).

This study used NMR base metabolic profiling to obtain an overview of temperature effects on metabolites around the light to dark transition. A full mass balance and comparison with CO_2 loss would require absolute contents for all relevant metabolites, calculations that combine them, and targeted approaches such as high-resolution gas

chromatography coupled to mass spectrometry (HR-GC/MS), isotope labelling and enzyme assays, which are beyond the scope of this thesis.

6.5 Conclusions

- Anchored MMRT has been statistically demonstrated to be the preferred framework for mechanistic comparison of dark respiration components. Once T_{inf} and y(T_{inf}) are fixed from the polynomial stage, a single parameter $\Delta C_p^{\ddagger}$ captures the curvature, with parsimony and clear meaning. This parameter is comparable across traits and treatments, and links directly to how the apparent activation energy varies with temperature. Anchoring at the empirical inflection reduces leverage from the warm tail and avoids over fitting with multiple deactivation terms. The same negative $\Delta C_p^{\ddagger}$ that explains warm curvature in R_{dark} is consistent with the higher $LEDR_{amp}$ and the shorter time to LEDR peak at warmer temperatures. Peaked Arrhenius remains a useful descriptive comparator, whereas simple Arrhenius and constant-Q_{10} are adequate only within a basal window.
- Metabolically, LEDR is not a single pool phenomenon. The NMR profiles and the mass balance against CO_2 loss indicate that malate can contribute but alone cannot account for the full transient, especially at low temperature. Instead, several pathways participate, including organic acid turnover, amino acid metabolism and carbohydrate remobilisation, with temperature shaping both coupling and substrate use.
- Altogether, these results support a thermodynamic view in which warming reduces the marginal ATP yield per electron through increasing proton leakage and altered partitioning, while the enzymatic machinery shifts towards states with higher activation free energy. Anchored MMRT therefore offers a coherent basis for inference and comparison. These results motivate future work that pair absolute metabolite quantification with gas exchange and determines whether $\Delta C_p^{\ddagger}$ and inferred coupling changes scale from leaf to canopy.

7 Conclusions and perspectives

This thesis shows that the classical Laisk method, when applied across wide CO_2 ranges or without bracketing the Γ^*_{exp}, can yield biased or physiologically implausible estimates of Γ^* and D_L. Integrating the Farquhar, von Caemmerer, and Berry (FvCB) photosynthesis model into the Laisk method: (i) reduces systematic bias by capturing the inherent curvature of the A_{net}–C_c relationship, (ii) maintains accuracy across a wide spectrum of temperatures and CO_2 partial pressures and (iii) lowers the variance of the estimates under realistic measurement noise, as shown by Monte Carlo.

The temperature dependence of Γ^* and D_L can be captured with simple equations that are both empirically robust over my measurement range. For Γ^*, a constant-Q_{10} model provides the strongest statistical support and offers a parsimonious empirical description, whereas for D_L, the MMRT model was favoured and better reflected the slight warm-end curvature observed. Importantly, practical differences between models were small across most temperatures, so model selection should prioritise parsimony, biological plausibility, and the intended use of the parameters.

The temperature responses of V_{cmax} and J_{max} depart from linearity in Arrhenius coordinates over the rising (sub-optimal) range. An MMRT formulation with $\Delta C_p^{\ddagger} < 0$ captures this basal curvature and improves fit quality, particularly for J_{max}. Over the full temperature range, the position of the optimum and the warm-side downturn are recovered equally well by the composite MMRT with deactivation and by a peaked Arrhenius.

Anchored MMRT has been statistically demonstrated to be the preferred framework for mechanistic comparison of dark respiration components. Once T_{inf} and $y(T_{inf})$ are fixed from the polynomial stage, a single parameter $\Delta C_p^{\ddagger}$ captures the curvature, with

parsimony and clear meaning. This parameter is comparable across traits and treatments, and links directly to how the apparent activation energy varies with temperature. Anchoring at the empirical inflection reduces leverage from the warm tail and avoids over fitting with multiple deactivation terms. The same negative $\Delta C_p^{\ddagger}$ that explains warm curvature in R_{dark} is consistent with the higher $LEDR_{amp}$ and the shorter time to LEDR peak at warmer temperatures. Peaked Arrhenius remains a useful descriptive comparator, whereas simple Arrhenius and constant-Q_{10} are adequate only within a basal window.

Macromolecular Rate Theory provided the best description of temperature dependence across most analysed traits (Table 7.1). MMRT captured the intrinsic curvature on a log-rate scale, yielded interpretable parameters including an effective change in heat capacity of activation ($\Delta C_p^{\ddagger}$), the inflection temperature at which temperature sensitivity is greatest (T_{inf}) and the optimum temperature at which the predicted rate is maximal (T_{opt}), and reproduced warm-side downturns in its baseline form. Here, $\Delta C_p^{\ddagger}$ should be understood as an emergent property of the integrated biochemical network underlying each trait, rather than as a parameter attributable to any single enzyme or reaction.

TABLE 7.1. Summary of thermal responses for gas-exchange traits. Entries report the inflection temperature (T_{inf}), the optimum temperature (T_{opt}), the heat-capacity change on activation ($\Delta C_p^{\ddagger}$) and whether a high temperature deactivation term was included. "Not estimated" indicates the quantity was not fitted by design; "not applicable" indicates the metric does not apply to the trait or model; "not in range" indicates the model optimum lies outside the observed temperature window; 'non-negative' indicates $\Delta C_p^{\ddagger}$ was estimated ≥ 0, so no internal optimum exists within the measurement range.

Trait	Best model	T_{inf} (°C)	T_{opt} (°C)	$\Delta C_p^{\ddagger}$ (kJ mol^{-1} K^{-1})	Deactivation term
Γ*	Q_{10}	not applicable	not applicable	not applicable	not applicable
D_L	MMRT	not estimated	not in range	non-negative	No
V_{cmax}	MMRT	25.8	35.0	-2.3	Yes
J_{max}	MMRT	17.7	30.8	-2.1	Yes
R_{dark}	MMRT	35.8	not in range	-2.2	No
LEDR$_{amp}$	Peaked Arrhenius	23.2	37.3	-4.0	No
LEDR$_{peak}$	MMRT	28.1	43.2	-3.6	No
LEDR$_{area}$	MMRT	not estimated	27.7	-7.0	No

7.1 Guidelines to resolve the metabolic origin of LEDR

NMR profiling supports a multi-substrate origin for LEDR rather than a single organic-acid mechanism. Malate changes after lights-off explain only a fraction of the integrated LEDR at warm temperature and very little at low temperatures, while temperature-dependent shifts in organic-acids, aromatic and hexose regions, together with a low-temperature induced sucrose rise, indicate a broader reallocation of storage and transport metabolites towards central carbon metabolism and redox balance as temperature changes.

Future work should close the carbon mass balance of LEDR by pairing MMRT-based gas exchange with absolute metabolite quantification across the light-dark transition (targeted organic acids, amino acids and sugars). Also, to solve the origin of the LEDR, future studies are warranted to:

- use stable-isotope tracing and high-resolution mass spectrometry to resolve substrate routing and identify the specific metabolic nodes (rate-limiting enzymes, branch points or shuttles such as the malate valve) that show time and temperature sensitivity

- quantify how $\Delta C_p^{\ddagger}$, T_{inf} and T_{opt} shift with acclimatisation, time of day and species, and test whether inferred coupling changes scale from leaf to canopy

- exploit genetic resources to explore LEDR: for example, it would be very useful to monitor LEDR in respiratory mutants such as mitochondrial complex I mutants (Lothier et al., 2019). In effect, they are viable and have higher basal respiration and lower O_2/ATP coupling efficiency (with higher AOX activity and involvement of alternative NAD(P)H dehydrogenases). Therefore, they would be instrumental to test the hypothesis of low mitochondrial efficiency in LEDR.

- assess the chloroplast contribution by examining whether a transient burst of plastidial pyruvate dehydrogenase activity consumes residual triose-phosphates immediately after lights-off before starch degradation becomes dominant.

Finally, it would be interesting to incorporate LEDR area and LEDR amplitude parameterisations into photosynthesis and respiration submodels so that simulations can account for the temperature sensitive coupling between light period carbon processing and dark fluxes. Together with MMRT based descriptions of V_{cmax} and J_{max} and a constant-Q_{10} for Γ*, this provides a coherent and implementable set of temperature response functions that can improve predictions under variable thermal regimes.

References

- Abadie, C., Bathellier, C. and Tcherkez, G. (2018). Carbon allocation to major metabolites in illuminated leaves is not just proportional to photosynthesis when gaseous conditions (CO_2 and O_2) vary. New Phytologist 218(1), 94–106. https://doi.org/10.1111/nph.14984
- Abadie, C., Lalande, J., Dourmap, C., Limami, A. and Tcherkez, G. (2024). Leaf day respiration involves multiple carbon sources and depends on previous dark metabolism. Plant, Cell & Environment 47, 2146–2162.
- Adler, S. O., Kitashova, A., Bulović, A., Nägele, T. and Klipp, E. (2025). Plant cold acclimation and its impact on sensitivity of carbohydrate metabolism. Systems Biology and Applications 11(1). https://doi.org/10.1038/s41540-025-00505-1
- Alster, C. J., Robinson, J. M., Arcus, V. L. and Schipper, L. A. (2022). Assessing thermal acclimation of soil microbial respiration using macromolecular rate theory. Biogeochemistry 158(1), 131–141. https://doi.org/10.1007/s10533-021-00885-6
- Amaral, J., Lobo, A. K. M. and Carmo-Silva, E. (2024). Regulation of Rubisco activity in crops. New Phytologist 241(1), 35–51. https://doi.org/10.1111/nph.19369
- Amthor, J., Koch, G., Willms, J. and Layzell, D. (2001). Leaf O_2 uptake in the dark is independent of coincident CO_2 partial pressure. Journal of Experimental Botany 52, 2235–2238.
- Amthor, J. S. (2025). After photosynthesis, what then: Importance of respiration to crop growth and yield. Field Crops Research 321. https://doi.org/10.1016/j.fcr.2024.109638
- Araújo, W. L., Nunes-Nesi, A., Nikoloski, Z., Sweetlove, L. J. and Fernie, A. R. (2012). Metabolic control and regulation of the tricarboxylic acid cycle in photosynthetic and heterotrophic plant tissues. Plant, Cell and Environment 35(1), 1–21. https://doi.org/10.1111/j.1365-3040.2011.02332

- Araújo, W. L., Martins, A. O., Fernie, A. R. and Tohge, T. (2014). 2-Oxoglutarate: Linking TCA cycle function with amino acid, glucosinolate, flavonoid, alkaloid, and gibberellin biosynthesis. Frontiers in Plant Science 5(OCT). https://doi.org/10.3389/fpls.2014.00552
- Arcus, V. L. and Mulholland, A. J. (2025). Temperature, dynamics, and enzyme-catalysed reaction rates. Annual Review of Biophysics 28, 32. https://doi.org/10.1146/annurev-biophys-121219
- Arcus, V. L., Prentice, E. J., Hobbs, J. K., Mulholland, A. J., van der Kamp, M. W., Pudney, C. R., Parker, E. J. and Schipper, L. A. (2016). On the temperature dependence of enzyme-catalysed rates. Biochemistry 55(12), 1681–1688. https://doi.org/10.1021/acs.biochem.5b01094
- Arrhenius, S. (1889). Über die Reaktionsgeschwindigkeit bei der Inversion von Rohrzucker durch Säuren. Z. Phys. Chem. 4, 226–248.
- Arroyo, J. I., Díez, B., Kempes, C. P., West, G. B. and Marquet, P. A. (2022). A general theory for temperature dependence in biology. Proceedings of the National Academy of Sciences 119(30), 1–7. https://doi.org/10.1073/pnas
- Arshad, R., Saccon, F., Bag, P., Biswas, A., Calvaruso, C., Bhatti, A. F., Grebe, S., Mascoli, V., Mahbub, M., Muzzopappa, F., Polyzois, A., Schiphorst, C., Sorrentino, M., Streckaitė, S., van Amerongen, H., Aro, E. M., Bassi, R., Boekema, E. J., Croce, R., … Büchel, C. (2022). A kaleidoscope of photosynthetic antenna proteins and their emerging roles. Plant Physiology 189(3), 1204–1219. https://doi.org/10.1093/plphys/kiac175
- Atkin, O. K., Evans, J. R. and Siebke, K. (1998). Relationship between the inhibition of leaf respiration by light and enhancement of leaf dark respiration following light treatment. Australian Journal of Plant Physiology 25(4), 437–443. https://doi.org/10.1071/PP97159
- Atkin, O. K., Evans, J. R., Ball, M. C., Lambers, H. and Pons, T. L. (2000). Leaf respiration of snow gum in the light and dark: Interactions between temperature and irradiance. Plant Physiology 122, 915–923.

- Atkin, O. K. and Tjoelker, M. G. (3). Thermal acclimation and the dynamic response of plant respiration to temperature. Trends in Plant Science 8(7), 343–351. https://doi.org/10.1016/S1360-1385(03)00136-5
- Avenson, T. J., Kanazawa, A., Cruz, J. A., Takizawa, K., Ettinger, W. E. and Kramer, D. M. (2005). Integrating the proton circuit into photosynthesis: Progress and challenges. Plant, Cell and Environment 28(1), 97–109. https://doi.org/10.1111/j.1365-3040.2005.01294.x
- Azevedo, R. A., Lancien, M. and Lea, P. J. (2006). The aspartic acid metabolic pathway, an exciting and essential pathway in plants. Amino Acids 30(2), 143–162. https://doi.org/10.1007/s00726-005-0245-2
- Badger, M. R. and Price, G. D. (1994). The role of carbonic anhydrase in photosynthesis. Annual Review of Plant Physiology and Plant Molecular Biology 45(1), 369–392. https://doi.org/10.1146/annurev.pp.45.060194.002101
- Baldocchi, D. (2014). Measuring fluxes of trace gases and energy between ecosystems and the atmosphere: The state and future of the eddy covariance method. Global Change Biology 20(12), 3600–3619. https://doi.org/10.1111/gcb.12649
- Baldocchi, D. (2020). How eddy covariance flux measurements have contributed to our understanding of global change biology. Global Change Biology 26(1), 242–260. https://doi.org/10.1111/gcb.14807
- Barbour, M. M. (2017). Understanding regulation of leaf internal carbon and water transport using online stable isotope techniques. New Phytologist 213(1), 83–88. https://doi.org/10.1111/nph.14171
- Barbour, M. M., Evans, J. R., Simonin, K. A. and von Caemmerer, S. (2016). Online CO_2 and H_2O oxygen isotope fractionation allows estimation of mesophyll conductance in C_4 plants and reveals that mesophyll conductance decreases as leaves age in both C_4 and C_3 plants. New Phytologist 210(3), 875–889. https://doi.org/10.1111/nph.13830

- Barbour, M. M., McDowell, N. G., Tcherkez, G., Bickford, C. P. and Hanson, D. T. (2007). A new measurement technique reveals rapid post-illumination changes in the carbon isotope composition of leaf-respired CO_2. Plant, Cell and Environment 30(4), 469–482. https://doi.org/10.1111/j.1365-3040.2007.01634.x
- Barbour, M. M., Warren, C. R., Farquhar, G. D., Forrester, G. and Brown, H. (2010). Variability in mesophyll conductance between barley genotypes, and effects on transpiration efficiency and carbon isotope discrimination. Plant, Cell and Environment 33(7), 1176–1185. https://doi.org/10.1111/j.1365-3040.2010.02138.x
- Barreto, P., Koltun, A., Nonato, J., Yassitepe, J., Maia, I. de G. and Arruda, P. (2022). Metabolism and signalling of plant mitochondria in adaptation to environmental stresses. International Journal of Molecular Sciences 23(19). https://doi.org/10.3390/ijms231911176
- Bathe, U., Leong, B. J., Van Gelder, K., Barbier, G. G., Henry, C. S., Amthor, J. S. and Hanson, A. D. (2023). Respiratory energy demands and scope for demand expansion and destruction. Plant Physiology 191(4), 2093–2103. https://doi.org/10.1093/plphys/kiac493
- Bauerle, W. L., Oren, R., Way, D. A., Qian, S. S., Stoy, P. C., Thornton, P. E., Bowden, J. D., Hoffman, F. M. and Reynolds, R. F. (2012). Photoperiodic regulation of the seasonal pattern of photosynthetic capacity and the implications for carbon cycling. Proceedings of the National Academy of Sciences of the United States of America 109(22), 8612–8617. https://doi.org/10.1073/pnas.1119131109
- Bauwe, H., Hagemann, M. and Fernie, A. R. (2010). Photorespiration: Players, partners and origin. Trends in Plant Science 15(6), 330–336. https://doi.org/10.1016/j.tplants.2010.03.006
- Beer, C., Reichstein, M., Tomelleri, E., Ciais, P., Jung, M., Carvalhais, N., Rodenbeck, C., Arain, M., Baldocchi, D., Bonan, G., Bondeau, A., Cescatti, A., Lasslop, G., Lindroth, A., Lomas, M., Luyssaert, S., Margolis, H., Oleson, K., Roupsard, O., … Papale, D. (2010). Terrestrial gross carbon dioxide uptake: Global distribution and

covariation with climate. Science 329(5993), 834–848. https://doi.org/10.1126/science.1192033

- Benomar, L., Moutaoufik, M. T., Elferjani, R., Isabel, N., DesRochers, A., Guellab, A. El, Khlifa, R. and Hassania, L. A. I. (2019). Thermal acclimation of photosynthetic activity and RuBisCO content in two hybrid poplar clones. PLoS ONE 14(2). https://doi.org/10.1371/journal.pone.0206021
- Berghuijs, H. N. C., Yin, X., Ho, Q. T., Retta, M. A., Nicolaï, B. M. and Struik, P. C. (2019). Using a reaction–diffusion model to estimate day respiration and reassimilation of (photo)respired CO_2 in leaves. New Phytologist 223(2), 619–631. https://doi.org/10.1111/nph.15857
- Bermudez, R., Stefanski, A., Montgomery, R. A. and Reich, P. B. (2021). Short- and long-term responses of photosynthetic capacity to temperature in four boreal tree species in a free-air warming and rainfall manipulation experiment. Tree Physiology 41(1), 89–102. https://doi.org/10.1093/treephys/tpaa115
- Bernacchi, C. J., Portis, A. R., Nakano, H., von Caemmerer, S. and Long, S. P. (2002). Temperature response of mesophyll conductance: Implications for the determination of Rubisco enzyme kinetics and for limitations to photosynthesis in vivo. Plant Physiology 130, 1992–1998.
- Bernacchi, C. J., Singsaas, E. L., Pimentel, C., Portis, A. R. and Long, S. P. (2001). Improved temperature response functions for models of Rubisco-limited photosynthesis. Global Change Biology 21(3), 253–259. https://doi.org/10.1111/J.1365-3040.2001.00668.X
- Boex-Fontvieille, E. R. A., Gauthier, P. P. G., Gilard, F., Hodges, M. and Tcherkez, G. G. B. (2013). A new anaplerotic respiratory pathway involving lysine biosynthesis in isocitrate dehydrogenase-deficient Arabidopsis mutants. New Phytologist 199(3), 673–682. https://doi.org/10.1111/nph.12319
- Bräutigam, A. and Gowik, U. (2016). Photorespiration connects C_3 and C_4 photosynthesis. Journal of Experimental Botany 67(10), 2953–2962. https://doi.org/10.1093/jxb/erw056

- Brooks, A. and Farquhar, G. D. (1985). Effect of temperature on the CO_2/O_2 specificity of ribulose-1,5-bisphosphate carboxylase/oxygenase and the rate of respiration in the light: Estimates from gas-exchange measurements on spinach. Planta 165, 397–406.
- Bruhn, D., Griffin, K. L. and Møller, I. M. (2025). Importance of timing of dark acclimation for estimating light inhibition of leaf respiratory CO_2 efflux. Plant, Cell and Environment 48(5), 3151–3158. https://doi.org/10.1111/pce.15335
- Brzezowski, P., Richter, A. S. and Grimm, B. (2015). Regulation and function of tetrapyrrole biosynthesis in plants and algae. Biochimica et Biophysica Acta – Bioenergetics 1847(9), 968–985. https://doi.org/10.1016/j.bbabio.2015.05.007
- Buckley, T. N. and Farquhar, G. D. (2004). A new analytical model for whole-leaf potential electron transport rate. Plant, Cell & Environment 27, 1487–1502.
- Buckley, T. N. and Adams, M. A. (2011). An analytical model of non-photorespiratory CO_2 release in the light and dark in leaves of C_3 species based on stoichiometric flux balance. Plant, Cell and Environment 34(1), 89–112. https://doi.org/10.1111/j.1365-3040.2010.02228.x
- Buckley, T. N., Vice, H. and Adams, M. A. (2017). The Kok effect in Vicia faba cannot be explained solely by changes in chloroplastic CO_2 concentration. New Phytologist 216(4), 1064–1071. https://doi.org/10.1111/nph.14775
- Bulley, N. R. and Tregunna, E. B. (1970). Photorespiration and the post-illumination CO_2 burst. Canadian Journal of Botany 49, 1277–1284.
- Bunzel, H. A., Anderson, J. L. R., Hilvert, D., Arcus, V. L., van der Kamp, M. W. and Mulholland, A. J. (2021). Evolution of dynamical networks enhances catalysis in a designer enzyme. Nature Chemistry 13(10), 1017–1022.
- Burgess, A. J. (2023). Breath of green life: Reduction in plant day and night respiration under elevated CO_2. Plant Physiology 192(1), 31–33. https://doi.org/10.1093/plphys/kiad087

- Burnett, A. C., Davidson, K. J., Serbin, S. P. and Rogers, A. (2019). The "one-point method" for estimating maximum carboxylation capacity of photosynthesis: A cautionary tale. Plant, Cell and Environment 42(8), 2472–2481. https://doi.org/10.1111/pce.13574
- Busch, F. A. (2020). Photorespiration in the context of Rubisco biochemistry, CO_2 diffusion and metabolism. The Plant Journal 101(4), 919–939. https://doi.org/10.1111/tpj.14674
- Busch, F. A., Ainsworth, E. A., Amtmann, A., Cavanagh, A. P., Driever, S. M., Ferguson, J. N., Kromdijk, J., Lawson, T., Leakey, A. D. B., Matthews, J. S. A., Meacham-Hensold, K., Vath, R. L., Vialet-Chabrand, S., Walker, B. J. and Papanatsiou, M. (2024). A guide to photosynthetic gas-exchange measurements: Fundamental principles, best practice and potential pitfalls. Plant, Cell and Environment 47(9), 3344–3364. https://doi.org/10.1111/pce.14815
- Busch, F. A. and Sage, R. F. (2017). The sensitivity of photosynthesis to O_2 and CO_2 concentration identifies strong Rubisco control above the thermal optimum. New Phytologist 213(3), 1036–1051. https://doi.org/10.1111/nph.14258
- Busch, F.A., Sage, R.F., Farquhar, G.D. (2018) Plants increase CO_2 uptake by assimilating nitrogen via the photorespiratory pathway. Nature Plants 4, 46-4. https://doi.org/10.1038/s41477-017-0065-x
- Cai, C., Li, G., Yang, H., Yang, J., Liu, H., Struik, P. C., Luo, W., Yin, X., Di, L., Guo, X., Jiang, W., Si, C., Pan, G. and Zhu, J. (2018). Do all leaf photosynthesis parameters of rice acclimate to elevated CO_2, elevated temperature, and their combination, in FACE environments? Global Change Biology 24(4), 1685–1707. https://doi.org/10.1111/gcb.13961
- Canadell, J., Monteiro, P., Costa, M., Cotrim, L., Cox, P., Eliseev, S., Ishii, M., Jaccard, S., Koven, C., Lohila, A., Patra, P., Piao, S., Rogel, J., Syampungani, S., Zaehle, S. and Zickfeld, K. (2021). Global carbon and other biogeochemical cycles and feedbacks. In V. Masson-Delmotte, P. Zhai, A. Pirani, S. Connors, C. Péan, S. Berger, N. Claud, Y. Chen, L. Goldfarb, M. Gomis, M. Huang, K. Leitzell, E. Lonnoy, J. Matthews,

T. Maycock, T. Waterfield, O. Yelekçi, Y. Yu and B. Zhou (eds), Climate Change 2021: The Physical Science Basis (pp. 673–816). Cambridge University Press, Cambridge, UK and New York, NY, USA. https://doi.org/10.1017/9781009157896.007

- Cao, P., Su, X., Pan, X., Liu, Z., Chang, W. and Li, M. (2018). Structure, assembly and energy transfer of plant photosystem II supercomplex. Biochimica et Biophysica Acta – Bioenergetics 1859(9), 633–644. https://doi.org/10.1016/j.bbabio.2018.03.007

- Carter, K. R., Cavaleri, M. A., Atkin, O. K., Bahar, N. H. A., Cheesman, A. W., Choury, Z., Crous, K. Y., Doughty, C. E., Dusenge, M. E., Ely, K. S., Evans, J. R., Silva, J. F., Mau, A. C., Medlyn, B. E., Meir, P., Norby, R. J., Read, J., Reed, S. C., Reich, P. B., … Wu, J. (2025). Photosynthetic responses to temperature across the tropics: A meta-analytic approach. Annals of Botany 135(7), 1293–1310. https://doi.org/10.1093/aob/mcae206

- Chadee, A., Alber, N. A., Dahal, K. and Vanlerberghe, G. C. (2021). The complementary roles of chloroplast cyclic electron transport and mitochondrial alternative oxidase to ensure photosynthetic performance. Frontiers in Plant Science 12. https://doi.org/10.3389/fpls.2021.748204

- Cheah, S. S. and Teh, C. B. S. (2020). Parameterisation of the Farquhar–von Caemmerer–Berry C_3 photosynthesis model for oil palm. Photosynthetica 58(3), 769–779. https://doi.org/10.32615/ps.2020.020

- Chen, J., Wang, P., Mi, H. L., Chen, G. Y. and Xu, D. Q. (2010). Reversible association of ribulose-1,5-bisphosphate carboxylase/oxygenase activase with the thylakoid membrane depends upon the ATP level and pH in rice without heat stress. Journal of Experimental Botany 61(11), 2939–2950. https://doi.org/10.1093/jxb/erq122

- Chen, Y., Zhu, Z., Zhao, W., Li, M., Cao, S., Zheng, Y., Tian, F. and Myneni, R. B. (2024). The direct and indirect effects of environmental factors on global terrestrial gross primary productivity over the past four decades. Environmental Research Letters 19(1). https://doi.org/10.1088/1748-9326/ad107f

- Covey-Crump, E. M., Attwood, R. G. and Atkin, O. K. (2002). Regulation of root respiration in two species of Plantago that differ in relative growth rate: The effect of short- and long-term changes in temperature. Plant, Cell and Environment 25(11), 1501–1513. https://doi.org/10.1046/j.1365-3040.2002.00932.x
- Cox, A. J. F., Hartley, I. P., Meir, P., Sitch, S., Dusenge, M. E., Restrepo, Z., González-Caro, S., Villegas, J. C., Uddling, J. and Mercado, L. M. (2023). Acclimation of photosynthetic capacity and foliar respiration in Andean tree species to temperature change. New Phytologist 238(6), 2329–2344. https://doi.org/10.1111/nph.18900
- Crafts-Brandner, S. J. and Law, R. D. (2000). Effect of heat stress on the inhibition and recovery of the ribulose-1,5-bisphosphate carboxylase/oxygenase activation state. Planta 212, 67–74.
- Crous, K. Y., Uddling, J. and De Kauwe, M. G. (2022). Temperature responses of photosynthesis and respiration in evergreen trees from boreal to tropical latitudes. New Phytologist 234(2), 353–374. https://doi.org/10.1111/nph.17951
- Dao, O., Kuhnert, F., Weber, A. P. M., Peltier, G. and Li-Beisson, Y. (2022). Physiological functions of malate shuttles in plants and algae. Trends in Plant Science 27(5), 488–501. https://doi.org/10.1016/j.tplants.2021.11.007
- Davis, G. A. and Kramer, D. M. (2020). Optimization of ATP synthase c-rings for oxygenic photosynthesis. Frontiers in Plant Science 10. https://doi.org/10.3389/fpls.2019.01778
- De Causmaecker, S., Douglass, J. S., Fantuzzi, A., Nitschke, W. and Rutherford, A. W. (2019). Energetics of the exchangeable quinone, Q_B, in photosystem II. Proceedings of the National Academy of Sciences of the United States of America 116(39), 19458–19463. https://doi.org/10.1073/pnas.1910675116
- de Souza, V. F., Gonçalves, J. F. C., Rasulov, B., Talts, E., Morfopoulos, C., Junior, S. D., Albuquerque, P. M. and Niinemets, Ü. (2025). Photosynthetic temperature tolerance threshold determines how isoprene emission is affected by elevated CO_2 concentration at high temperatures. Plant–Environment Interactions 6(3). https://doi.org/10.1002/pei3.70053

- Degen, G. E. and Johnson, M. P. (2024). Photosynthetic control at the cytochrome b_6f complex. The Plant Cell 36(10), 4065–4079. https://doi.org/10.1093/plcell/koae133
- Degen, G. E., Orr, D. J. and Carmo-Silva, E. (2021). Heat-induced changes in the abundance of wheat Rubisco activase isoforms. New Phytologist 229(3), 1298–1311. https://doi.org/10.1111/nph.16937
- Dellero, Y., Jossier, M., Schmitz, J., Maurino, V. G. and Hodges, M. (2016). Photorespiratory glycolate–glyoxylate metabolism. Journal of Experimental Botany 67(10), 3041–3052. https://doi.org/10.1093/jxb/erw090
- Devireddy, A. R., Tschaplinski, T. J., Tuskan, G. A., Muchero, W. and Chen, J. G. (2021). Role of reactive oxygen species and hormones in plant responses to temperature changes. International Journal of Molecular Sciences 22(16). https://doi.org/10.3390/ijms22168843
- Divakaruni, A. S. and Brand, M. D. (2011). The regulation and physiology of mitochondrial proton leak. Physiology (Bethesda) 26(3), 192–205. https://doi.org/10.1152/physiol.00046.2010
- Douthe, C., Dreyer, E., Epron, D. and Warren, C. R. (2011). Mesophyll conductance to CO_2, assessed from online TDL-AS records of $^{13}CO_2$ discrimination, displays small but significant short-term responses to CO_2 and irradiance in Eucalyptus seedlings. Journal of Experimental Botany 62(15), 5335–5346. https://doi.org/10.1093/jxb/err141
- Dreyer, E., Le Roux, X., Montpied, P., Daudet, F. and Masson, F. (2001). Temperature response of leaf photosynthetic capacity in seedlings from seven temperate tree species. Tree Physiology 21, 223–232.
- Duffy, K. A., Schwalm, C. R., Arcus, V. L., Koch, G. W., Liang, L. L. and Schipper, L. A. (2021). How close are we to the temperature tipping point of the terrestrial biosphere? Science. https://www.science.org

- Dusenge, M. E., Duarte, A. G. and Way, D. A. (2019). Plant carbon metabolism and climate change: Elevated CO_2 and temperature impacts on photosynthesis, photorespiration and respiration. New Phytologist 221(1), 32–49. https://doi.org/10.1111/nph.15283
- Elferjani, R., Benomar, L., Momayyezi, M., Tognetti, R., Niinemets, Ü., Soolanayakanahally, R. Y., Théroux-Rancourt, G., Tosens, T., Ripullone, F., Bilodeau-Gauthier, S., Lamhamedi, M. S., Calfapietra, C. and Lamara, M. (2021). A meta-analysis of mesophyll conductance to CO_2 in relation to major abiotic stresses in poplar species. Journal of Experimental Botany 72(12), 4384–4400. https://doi.org/10.1093/jxb/erab127
- Carmo-Silva, E. and Salvucci, M. E. (2013). The regulatory properties of Rubisco activase differ among species and affect photosynthetic induction during light transitions. Plant Physiology 161(4), 1645–1655. https://doi.org/10.1104/pp.112.213348
- Emrich-Mills, T. Z., Proctor, M. S., Degen, G. E., Jackson, P. J., Richardson, K. H., Hawkings, F. R., Buchert, F., Hitchcock, A., Hunter, C. N., Mackinder, L. C. M., Hippler, M. and Johnson, M. P. (2025). Tethering ferredoxin–$NADP^+$ reductase to photosystem I promotes photosynthetic cyclic electron transfer. The Plant Cell 37(3). https://doi.org/10.1093/plcell/koaf042
- Evans, J. R. (2021). Mesophyll conductance: Walls, membranes and spatial complexity. New Phytologist 229(4), 1864–1876. https://doi.org/10.1111/nph.16968
- Evans, J. R., Kaldenhoff, R., Genty, B. and Terashima, I. (2009). Resistances along the CO_2 diffusion pathway inside leaves. Journal of Experimental Botany 60(8), 2235–2248. https://doi.org/10.1093/jxb/erp117
- Evans, J. R. and von Caemmerer, S. (1996). Carbon dioxide diffusion inside leaves. Plant Physiology 110(2), 339–346. https://doi.org/10.1104/pp.110.2.339
- Fan, K. T., Xu, Y. and Hegeman, A. D. (2024). Elevated temperature effects on protein turnover dynamics in Arabidopsis thaliana seedlings revealed by ^{15}N-stable isotope labelling and ProteinTurnover algorithm. International Journal of Molecular Sciences 25(11). https://doi.org/10.3390/ijms25115882

- Fan, Y., Tcherkez, G., Scafaro, A. P., Taylor, N. L., Furbank, R. T., von Caemmerer, S. and Atkin, O. K. (2024). Variation in leaf dark respiration among C_3 and C_4 grasses is associated with use of different substrates. Plant Physiology 195(2), 1475–1490. https://doi.org/10.1093/plphys/kiae064
- Farquhar, G. D. and Busch, F. A. (2017). Changes in the chloroplastic CO_2 concentration explain much of the observed Kok effect: A model. New Phytologist 214(2), 570–584. https://doi.org/10.1111/nph.14512
- Farquhar, G. D., von Caemmerer, S. and Berry, J. A. (1980). A biochemical model of photosynthetic CO_2 assimilation in leaves of C_3 species. Planta 149(1), 78–90. https://doi.org/10.1007/BF00386231
- Fatland, B. L., Ke, J., Anderson, M. D., Mentzen, W. I., Li, W. C., Allred, C. C., Johnston, J. L., Nikolau, B. J. and Wurtele, E. S. (2002). Molecular characterization of a heteromeric ATP-citrate lyase that generates cytosolic acetyl-coenzyme A in Arabidopsis. Plant Physiology 130(2), 740–756. https://doi.org/10.1104/pp.008110
- Fernie, A. R., Carrari, F. and Sweetlove, L. J. (2004). Respiratory metabolism: Glycolysis, the TCA cycle and mitochondrial electron transport. Current Opinion in Plant Biology 7(3), 254–261. https://doi.org/10.1016/j.pbi.2004.03.007
- Filaček, A., Živčák, M., Ferroni, L., Barboričová, M., Gašparovič, K., Yang, X., Landi, M. and Brestič, M. (2022). Pre-acclimation to elevated temperature stabilises the activity of photosystem I in wheat plants exposed to an episode of severe heat stress. Plants 11(5). https://doi.org/10.3390/plants11050616
- Flamholz, A. I., Prywes, N., Moran, U., Davidi, D., Bar-On, Y. M., Oltrogge, L. M., Alves, R., Savage, D. and Milo, R. (2019). Revisiting trade-offs between Rubisco kinetic parameters. Biochemistry 58(31), 3365–3376. https://doi.org/10.1021/acs.biochem.9b00237
- Flexas, J., Díaz-Espejo, A., Galmés, J., Kaldenhoff, R., Medrano, H. and Ribas-Carbó, M. (2007). Rapid variations of mesophyll conductance in response to changes in CO_2 concentration around leaves. Plant, Cell & Environment 30, 1284–1298.

- Flexas, J., Barbour, M. M., Brendel, O., Cabrera, H. M., Carriquí, M., Díaz-Espejo, A., Douthe, C., Dreyer, E., Ferrio, J. P., Gago, J., Gallé, A., Galmés, J., Kodama, N., Medrano, H., Niinemets, Ü., Peguero-Pina, J. J., Pou, A., Ribas-Carbó, M., Tomás, M., … Warren, C. R. (2012). Mesophyll diffusion conductance to CO_2: An unappreciated central player in photosynthesis. Plant Science 193–194, 70–84. https://doi.org/10.1016/j.plantsci.2012.05.009
- Flexas, J., Ribas-Carbó, M., Díaz-Espejo, A., Galmés, J. and Medrano, H. (2008). Mesophyll conductance to CO_2: Current knowledge and future prospects. Plant, Cell and Environment 31(5), 602–621. https://doi.org/10.1111/j.1365-3040.2007.01757.x
- Foyer, C. H., Neukermans, J., Queval, G., Noctor, G. and Harbinson, J. (2012). Photosynthetic control of electron transport and the regulation of gene expression. Journal of Experimental Botany 63(4), 1637–1661. https://doi.org/10.1093/jxb/ers013
- Fu, X., Gregory, L. M., Weise, S. E. and Walker, B. J. (2023). Integrated flux and pool size analysis in plant central metabolism reveals unique roles of glycine and serine during photorespiration. Nature Plants 9(1), 169–178. https://doi.org/10.1038/s41477-022-01294-9
- Fürstenau Togashi, H., Colin Prentice, I., Atkin, O. K., Macfarlane, C., Prober, S. M., Bloomfield, K. J. and Evans, B. J. (2018). Thermal acclimation of leaf photosynthetic traits in an evergreen woodland, consistent with the coordination hypothesis. Biogeosciences 15(11), 3461–3474. https://doi.org/10.5194/bg-15-3461-2018
- Friedlingstein, P., O'Sullivan, M., Jones, M. W., Andrew, R. M., Hauck, J., Landschützer, P., Le Quéré, C., Li, H., Luijkx, I. T., Olsen, A., Peters, G. P., Peters, W., Pongratz, J., Schwingshackl, C., Sitch, S., Canadell, J. G., Ciais, P., Jackson, R. B., Alin, S. R., … Zeng, J. (2025). Global Carbon Budget 2024. Earth System Science Data 17(3), 965–1039. https://doi.org/10.5194/essd-17-965-2025
- Galili, G., Avin-Wittenberg, T., Angelovici, R. and Fernie, A. R. (2014). The role of photosynthesis and amino acid metabolism in the energy status during seed development. Frontiers in Plant Science 5. https://doi.org/10.3389/fpls.2014.00447

- Galmés, J., Hermida-Carrera, C., Laanisto, L., & Niinemets, Ü. (2016). A compendium of temperature responses of Rubisco kinetic traits: variability among and within photosynthetic groups and impacts on photosynthesis modelling. Journal of Experimental Botany, 67(17), 5067–5091. https://doi.org/10.1093/jxb/erw267
- Gauthier, P. P. G., Saenz, N., Griffin, K. L., Way, D., & Tcherkez, G. (2020). Is the Kok effect a respiratory phenomenon? Metabolic insight using 13C labelling in Helianthus annuus leaves. New Phytologist, 228(4), 1243–1255. https://doi.org/10.1111/nph.16756
- Geigenberger, P., & Fernie, A. R. (2014). Metabolic control of redox and redox control of metabolism in plants. Antioxidants and Redox Signalling, 21(9), 1389–1421. https://doi.org/10.1089/ars.2014.6018
- Gessler, A., Roy, J., Kayler, Z., Ferrio, J. P., Alday, J. G., Bahn, M., del Castillo, J., Devidal, S., García-Muñoz, S., Landais, D., Martín-Gomez, P., Milcu, A., Piel, C., Pirhofer-Walzl, K., Galiano, L., Schaub, M., Haeni, M., Ravel, O., Salekin, S., … Resco de Dios, V. (2017). Night and day. Circadian regulation of night-time dark respiration and light-enhanced dark respiration in plant leaves and canopies. Environmental and Experimental Botany, 137, 14–25. https://doi.org/10.1016/j.envexpbot.2017.01.014
- Gessler, A., Tcherkez, G., Karyanto, O., Keitel, C., Ferrio, J. P., Ghashghaie, J., Kreuzwieser, J., & Farquhar, G. D. (2009). On the metabolic origin of the carbon isotope composition of CO2 evolved from darkened light-acclimated leaves in Ricinus communis. New Phytologist, 181(2), 374–386. https://doi.org/10.1111/j.1469-8137.2008.02672.x
- Ghashghaie, J., & Badeck, F. W. (2014). Opposite carbon isotope discrimination during dark respiration in leaves versus roots. A review. New Phytologist, 201(3), 751–769. https://doi.org/10.1111/nph.12563
- Ghifari, A. S., Saha, S., & Murcha, M. W. (2023). The biogenesis and regulation of the plant oxidative phosphorylation system. Plant Physiology, 192(2), 728–747. https://doi.org/10.1093/plphys/kiad108

- Gjindali, A., Page, R., Ashton, C. J., Robertson, I., Page, M. T., Bloemers, D., Gould, P. D., Worrall, D., Orr, D. J., & Carmo-Silva, E. (2025). Two cowpea Rubisco activase isoforms for crop thermotolerance. New Phytologist, 247(3), 1199–1217. https://doi.org/10.1111/nph.70271
- Gong, X. Y., Tcherkez, G., Wenig, J., Schäufele, R., & Schnyder, H. (2018). Determination of leaf respiration in the light. Comparison between an isotopic disequilibrium method and the Laisk method. New Phytologist, 218(4), 1371–1382. https://doi.org/10.1111/nph.15126
- Guy, C., Kaplan, F., Kopka, J., Selbig, J., & Hincha, D. K. (2008). Metabolomics of temperature stress. Physiologia Plantarum, 132(2), 220–235. https://doi.org/10.1111/j.1399-3054.2007.00999.x
- Gregory, L. M., Tejera-Nieves, M., & Walker, B. J. (2024). Measuring and quantifying characteristics of the post-illumination burst. In B. J. Walker (Ed.), Photorespiration. Methods in Molecular Biology (Vol. 2792). Humana, New York, NY.
- Gregory, L. M., McClain, A. M., Kramer, D. M., Pardo, J. D., Smith, K. E., Tessmer, O. L., Walker, B. J., Ziccardi, L. G., & Sharkey, T. D. (2021). The triose phosphate utilisation limitation of photosynthetic rate. Out of global models but important for leaf models. Plant, Cell and Environment, 44(10), 3223–3226. https://doi.org/10.1111/pce.14153
- Griffin, K. L., & Turnbull, M. H. (2012). Out of the light and into the dark. Post-illumination respiratory metabolism. New Phytologist, 195(1), 4–7. https://doi.org/10.1111/j.1469-8137.2012.04181.x
- Gupta, R. (2020). The oxygen-evolving complex. A super catalyst for life on Earth in response to abiotic stresses. Plant Signalling and Behaviour, 15(12), e1824721. https://doi.org/10.1080/15592324.2020.1824721
- Hampp, R., Goller, M., & Ziegler, H. (1982). Adenylate levels, energy charge, and phosphorylation potential during dark–light and light–dark transition in chloroplasts, mitochondria, and cytosol of mesophyll protoplasts from Avena sativa L. Plant Physiology, 69(2), 448–455. https://doi.org/10.1104/pp.69.2.448

- Han, M., Zhang, C., Suglo, P., Sun, S., Wang, M., & Su, T. (2021). L-aspartate. An essential metabolite for plant growth and stress acclimation. Molecules, 26(7), 1887. https://doi.org/10.3390/molecules26071887
- Harrison, E. P., Olcer, H., Lloyd, J. C., Long, S. P., & Raines, C. A. (2001). Small decreases in SBPase cause a linear decline in the apparent RuBP regeneration rate, but do not affect Rubisco carboxylation capacity. Journal of Experimental Botany, 52(362), 1779–1784.
- Haworth, M., Marino, G., Loreto, F., & Centritto, M. (2022). The evolution of diffusive and biochemical capacities for photosynthesis was predominantly shaped by CO2 with a smaller contribution from O2. Science of the Total Environment, 840, 156606. https://doi.org/10.1016/j.scitotenv.2022.156606
- Hazel, J. R., Williams, E. E., Livermore, R., & Mozingo, N. (1991). Thermal adaptation in biological membranes. Functional significance of changes in phospholipid molecular species composition. Lipids, 26(4), 277–282. https://doi.org/10.1007/BF02537137
- He, C., Berkowitz, O., Hu, S., Zhao, Y., Qian, K., Shou, H., Whelan, J., & Wang, Y. (2023). Co-regulation of mitochondrial and chloroplast function. Molecular components and mechanisms. Plant Communications, 4(1), 100496. https://doi.org/10.1016/j.xplc.2022.100496
- Heinz Walz GmbH. (2019). Handbook of Operation. Portable Gas Exchange Fluorescence System GFS-3000. Germany. www.walz.com
- Hernández, G. G., Winter, K., & Slot, M. (2021). Similar temperature dependence of photosynthetic parameters in sun and shade leaves of three tropical tree species. Tree Physiology, 41(5), 637–651. https://doi.org/10.1093/treephys/tpaa015
- Herrmann, H. A., Schwartz, J. M., & Johnson, G. N. (2020). From empirical to theoretical models of light response curves. Linking photosynthetic and metabolic acclimation. Photosynthesis Research, 145, 5–14.

- Heskel, M. A. (2018). Small flux, global impact. Integrating the nuances of leaf mitochondrial respiration in estimates of ecosystem carbon exchange. American Journal of Botany, 105, 815–818.
- Hermida-Carrera, C., Kapralov, M. V., & Galmés, J. (2016). Rubisco catalytic properties and temperature response in crops. Plant Physiology, 171(4), 2549–2561. https://doi.org/10.1104/pp.16.01846
- Heskel, M. A., O'Sullivan, O. S., Reich, P. B., Tjoelker, M. G., Weerasinghe, L. K., Penillard, A., Egerton, J. J. G., Creek, D., Bloomfield, K. J., Xiang, J., Sinca, F., Stangl, Z. R., Martinez-De La Torre, A., Griffin, K. L., Huntingford, C., Hurry, V., Meir, P., Turnbull, M. H., & Atkin, O. K. (2016). Convergence in the temperature response of leaf respiration across biomes and plant functional types. Proceedings of the National Academy of Sciences of the USA, 113(14), 3832–3837. https://doi.org/10.1073/pnas.1520282113
- Hildebrandt, T. M., Nunes-Nesi, A., Araújo, W. L., & Braun, H. P. (2015). Amino acid catabolism in plants. Molecular Plant, 8(11), 1563–1579. https://doi.org/10.1016/j.molp.2015.09.005
- Hobbs, J. K., Jiao, W., Easter, A. D., Parker, E. J., Schipper, L. A., & Arcus, V. L. (2013). Change in heat capacity for enzyme catalysis determines temperature dependence of enzyme-catalysed rates. ACS Chemical Biology, 8(11), 2388–2393. https://doi.org/10.1021/cb4005029
- Hodges, M. (2002). Enzyme redundancy and the importance of 2-oxoglutarate in plant ammonium assimilation. Journal of Experimental Botany, 53(370), 905–916. https://doi.org/10.1093/jxb/53.370.905
- Hoefnagel, M. H. N., Atkin, O. K., & Wiskich, J. T. (1998). Interdependence between chloroplasts and mitochondria in the light and the dark. Biochimica et Biophysica Acta, 1366(3), 235–255. https://doi.org/10.1016/S0005-2728(98)00126-1
- Holzwarth, A. R., Müller, M. G., Reus, M., Nowaczyk, M., Sander, J., & Rögner, M. (2006). Kinetics and mechanism of electron transfer in intact photosystem II

and in the isolated reaction centre. Pheophytin is the primary electron acceptor. Proceedings of the National Academy of Sciences of the USA, 103(2), 6895–6900. https://doi.org/10.1073/pnas.0505371103

- Huergo, L. F., & Dixon, R. (2015). The emergence of 2-oxoglutarate as a master regulator metabolite. Microbiology and Molecular Biology Reviews, 79(4), 419–435. https://doi.org/10.1128/MMBR.00038-15
- Huntingford, C., Atkin, O. K., Martinez-De La Torre, A., Mercado, L. M., Heskel, M. A., Harper, A. B., Bloomfield, K. J., O'Sullivan, O. S., Reich, P. B., Wythers, K. R., Butler, E. E., Chen, M., Griffin, K. L., Meir, P., Tjoelker, M. G., Turnbull, M. H., Sitch, S., Wiltshire, A., & Malhi, Y. (2017). Implications of improved representations of plant respiration in a changing climate. Nature Communications, 8, 1602.
- Igamberdiev, A. U., & Bykova, N. V. (2023). Mitochondria in photosynthetic cells. Coordinating redox control and energy balance. Plant Physiology, 191(4), 2104–2119. https://doi.org/10.1093/plphys/kiac541
- IPCC. (2023). Summary for Policymakers. In Climate Change 2023. Synthesis Report. Contribution of Working Groups I, II and III to the Sixth Assessment Report of the Intergovernmental Panel on Climate Change. IPCC, Geneva, Switzerland. https://doi.org/10.59327/IPCC/AR6-9789291691647.001
- Igamberdiev, A. U., & Eprintsev, A. T. (2016). Organic acids. The pools of fixed carbon involved in redox regulation and energy balance in higher plants. Frontiers in Plant Science, 7, 1042. https://doi.org/10.3389/fpls.2016.01042
- Igamberdiev, A. U., & Kleczkowski, L. A. (2006). Equilibration of adenylates in the mitochondrial intermembrane space maintains respiration and regulates cytosolic metabolism. Journal of Experimental Botany, 57(10), 2133–2141. https://doi.org/10.1093/jxb/erl006
- Ishijima, S., Uchibori, A., Takagi, H., Maki, R., & Ohnishi, M. (2003). Light-induced increase in free Mg2+ concentration in spinach chloroplasts. Measurement of free Mg2+ using a fluorescent probe and necessity of stromal alkalinisation. Archives

of Biochemistry and Biophysics, 412(1), 126–132. https://doi.org/10.1016/S0003-9861(03)00038-9

- Jastroch, M., Divakaruni, A. S., Mookerjee, S., Treberg, J. R., & Brand, M. D. (2010). Mitochondrial proton and electron leaks. Essays in Biochemistry, 47, 53–67. https://doi.org/10.1042/BSE0470053
- Jensen, R. G. (2000). Activation of Rubisco regulates photosynthesis at high temperature and CO2. Proceedings of the National Academy of Sciences of the USA, 97(24), 12937–12938. https://doi.org/10.1073/pnas.97.24.12937
- Johnson, J. E., & Berry, J. A. (2021). The role of cytochrome b6f in the control of steady-state photosynthesis. A conceptual and quantitative model. Photosynthesis Research, 148(3), 101–136. https://doi.org/10.1007/s11120-021-00840-4
- Jordan, D. B., & Ogren, W. L. (1984). The CO2/O2 specificity of ribulose-1,5-bisphosphate carboxylase/oxygenase. Dependence on ribulosebisphosphate concentration, pH and temperature. Planta, 161, 308–313.
- Jud, W., Vanzo, E., Li, Z., Ghirardo, A., Zimmer, I., Sharkey, T. D., Hansel, A., & Schnitzler, J. P. (2016). Effects of heat and drought stress on post-illumination bursts of volatile organic compounds in isoprene-emitting and non-emitting poplar. Plant, Cell and Environment, 39(6), 1204–1215. https://doi.org/10.1111/pce.12643
- Kaplan, F., Kopka, J., Haskell, D. W., Zhao, W., Schiller, K. C., Gatzke, N., Sung, D. Y., & Guy, C. L. (2004). Exploring the temperature-stress metabolome of Arabidopsis. Plant Physiology, 136(4), 4159–4168. https://doi.org/10.1104/pp.104.052142
- Katavouta, A., Williams, R. G., Jones, C. D., Brovkin, V., Friedlingstein, P., Schwinger, J., Bopp, L., Boucher, O., Cadule, P., Chamberlain, M. A., Christian, J. R., Delire, C., Fisher, A. R. A., Hajima, T., Ilyina, T., Joetzjer, E., Kawamiya, M., Koven, C. D., Krasting, J. P., … Ziehn, T. (2020). Carbon-concentration and carbon-climate feedbacks in CMIP6 models and their comparison to CMIP5 models. Biogeosciences, 17(16), 4173–4222. https://doi.org/10.5194/bg-17-4173-2020

- Khorobrykh, S., Havurinne, V., Mattila, H., & Tyystjärvi, E. (2020). Oxygen and ROS in photosynthesis. Plants, 9(1), 91. https://doi.org/10.3390/plants9010091
- Kitashova, A., Adler, S. O., Richter, A. S., Eberlein, S., Dziubek, D., Klipp, E., & Nägele, T. (2023). Limitation of sucrose biosynthesis shapes carbon partitioning during plant cold acclimation. Plant, Cell and Environment, 46(2), 464–478. https://doi.org/10.1111/pce.14483
- Knauer, J., Cuntz, M., Smith, B., Canadell, J. G., Medlyn, B. E., Bennett, A. C., Caldararu, S., & Haverd, V. (2023). Higher global gross primary productivity under future climate with more advanced representations of photosynthesis. Science Advances, 9, eade5460.
- Kirschbaum, M. U. F., & Farquhar, G. D. (1984). Temperature dependence of whole-leaf photosynthesis in Eucalyptus pauciflora Sieb. ex Spreng. Australian Journal of Plant Physiology, 11, 519–538.
- Kirschbaum, M. U. F., & Farquhar, G. D. (1987). Investigation of the CO_2 dependence of quantum yield and respiration in Eucalyptus pauciflora. Plant Physiology, 83, 1032–1036.
- Kitao, M., Agathokleous, E., Harayama, H., Yazaki, K., & Tobita, H. (2021). Constant ratio of Cc to Ci under various CO_2 concentrations and light intensities, and during progressive drought, in seedlings of Japanese white birch. Photosynthesis Research, 147, 27–37.
- Komenda, J., Sobotka, R., & Nixon, P. J. (2024). The biogenesis and maintenance of PSII. Recent advances and current challenges. Plant Cell, 36(10), 3997–4013. https://doi.org/10.1093/plcell/koae082
- Kositsup, B., Montpied, P., Kasemsap, P., Thaler, P., Améglio, T., & Dreyer, E. (2009). Photosynthetic capacity and temperature responses of photosynthesis of rubber trees (Hevea brasiliensis Müll. Arg.) acclimate to changes in ambient temperatures. Trees: Structure and Function, 23(2), 357–365. https://doi.org/10.1007/s00468-008-0284-x

- Kozuleva, M., Goss, T., Twachtmann, M., Rudi, K., Trapka, J., Selinski, J., Ivanov, B., Garapati, P., Steinhoff, H. J., Hase, T., Scheibe, R., Klare, J. P., & Hanke, G. T. (2016). Ferredoxin:NADP(H) oxidoreductase abundance and location influence redox poise and stress tolerance. Plant Physiology, 172(3), 1480–1493. https://doi.org/10.1104/pp.16.01084
- Kramer, D. M., & Evans, J. R. (2011). The importance of energy balance in improving photosynthetic productivity. Plant Physiology, 155(1), 70–78. https://doi.org/10.1104/pp.110.166652
- Kröner, Y., & Way, D. A. (2016). Carbon fluxes acclimate more strongly to elevated growth temperatures than to elevated CO_2 concentrations in a northern conifer. Global Change Biology, 22, 2913–2928.
- Kühlbrandt, W., Carreira, L. A. M., & Yildiz, Ö. (2025). Cryo-EM of mitochondrial complex I and ATP synthase. Annual Review of Biophysics. https://doi.org/10.1146/annurev-biophys-060724
- Kumarathunge, D. P., Medlyn, B. E., Drake, J. E., Tjoelker, M. G., Aspinwall, M. J., Battaglia, M., Cano, F. J., Carter, K. R., Cavaleri, M. A., Cernusak, L. A., Chambers, J. Q., Crous, K. Y., De Kauwe, M. G., Dillaway, D. N., Dreyer, E., Ellsworth, D. S., Ghannoum, O., Han, Q., Hikosaka, K., … Way, D. A. (2019). Acclimation and adaptation components of the temperature dependence of plant photosynthesis at the global scale. New Phytologist, 222(2), 768–784. https://doi.org/10.1111/nph.15668
- Kurek, I., Thom, K. C., Bertain, S. M., Madrigal, A., Liu, L., Lassner, M. W., & Zhu, G. (2007). Enhanced thermostability of Arabidopsis Rubisco activase improves photosynthesis and growth rates under moderate heat stress. Plant Cell, 19(10), 3230–3241. https://doi.org/10.1105/tpc.107.054171
- Lacis, A., Schmidt, G., Rind, D., & Ruedy, R. (2010). Atmospheric CO_2. Principal control knob governing Earth's temperature. Science, 330(6002), 353–356. https://doi.org/10.1126/science.1195475

- Lafta, A. M., & Lorenzen, J. H. (1995). Effect of high temperature on plant growth and carbohydrate metabolism in potato. Plant Physiology, 109(2)
- Laing, W. A., Ogren, W. L., & Hageman, R. H. (1974). Regulation of soybean net photosynthetic CO_2 fixation by the interaction of CO_2, O_2 and ribulose 1,5-diphosphate carboxylase. Plant Physiology, 54, 678–685.
- Laisk, A. (1977). Kinetics of photosynthesis and photorespiration in C_3 plants. Nauka, Moscow.
- Le, X. H., Lee, C. P., & Millar, A. H. (2021). The mitochondrial pyruvate carrier complex mediates one of three pyruvate-supplying pathways that sustain Arabidopsis respiratory metabolism. Plant Cell, 33(8), 2776–2793. https://doi.org/10.1093/plcell/koab148
- Le, X. H., & Millar, A. H. (2023). The diversity of substrates for plant respiration and how to optimise their use. Plant Physiology, 191(4), 2133–2149. https://doi.org/10.1093/plphys/kiac599
- Lee, Z., Lim, J. A., Harikrishna, J. A., Islam, T., Abd Rahim, M. H., & Yaacob, J. S. (2024). Regulation of plant responses to temperature stress. A key factor in food security and for mitigating effects of climate change. International Journal of Plant Production, 18(2), 141–159. https://doi.org/10.1007/s42106-024-00282-7
- Lefebvre, S., Lawson, T., Zakhleniuk, O. V., Lloyd, J. C., & Raines, C. A. (2005). Increased sedoheptulose-1,7-bisphosphatase activity in transgenic tobacco plants stimulates photosynthesis and growth from an early stage in development. Plant Physiology, 138(1), 451–460. https://doi.org/10.1104/pp.104.055046
- Lehmann, M. M., Rinne, K. T., Blessing, C., Siegwolf, R. T. W., Buchmann, N., & Werner, R. A. (2015). Malate as a key carbon source of leaf dark-respired CO_2 across different environmental conditions in potato plants. Journal of Experimental Botany, 66(19), 5769–5781. https://doi.org/10.1093/jxb/erv279
- Lehmann, M. M., Wegener, F., Barthel, M., Maurino, V. G., Siegwolf, R. T. W., Buchmann, N., Werner, C., & Werner, R. A. (2016). Metabolic fate of the carboxyl

groups of malate and pyruvate and their influence on $\delta^{13}C$ of leaf-respired CO_2 during light-enhanced dark respiration. Frontiers in Plant Science, 7, 739. https://doi.org/10.3389/fpls.2016.00739

- Leister, D. (2023). Enhancing the light reactions of photosynthesis. Strategies, controversies, and perspectives. Molecular Plant, 16(1), 4–22. https://doi.org/10.1016/j.molp.2022.08.005
- Li, G., Chen, T., Feng, B., Peng, S., Tao, L., & Fu, G. (2021). Respiration, rather than photosynthesis, determines rice yield loss under moderate high-temperature conditions. Frontiers in Plant Science, 12, 678653. https://doi.org/10.3389/fpls.2021.678653
- Li, H., Nakajima, Y., Nango, E., Owada, S., Yamada, D., Hashimoto, K., Luo, F., Tanaka, R., Akita, F., Kato, K., Kang, J., Saitoh, Y., Kishi, S., Yu, H., Matsubara, N., Fujii, H., Sugahara, M., Suzuki, M., Masuda, T., … Shen, J. R. (2024). Oxygen-evolving photosystem II structures during S1–S2–S3 transitions. Nature, 626(7999), 670–677. https://doi.org/10.1038/s41586-023-06987-5
- Li, Y., Si, D., Wang, W., Xue, S., Shang, W., Chi, Z., Li, C., Hao, C., Govindjee, G., & Shi, Y. (2023). Light-driven CO_2 assimilation by photosystem II and its relation to photosynthesis. Chinese Journal of Catalysis, 44, 117–126. https://doi.org/10.1016/S1872-2067(22)64170-6
- Li, Y., Song, X., Li, S., Salter, W. T., & Barbour, M. M. (2020). The role of leaf water potential in the temperature response of mesophyll conductance. New Phytologist, 225, 1193–1205.
- Li, Y., Zhou, K., Yang, X., Su, X., Ding, P., Zhu, Y., Cao, F., & Han, J. (2025). Leaf nitrogen allocation to non-photosynthetic apparatus reduces mesophyll conductance under combined drought–salt stress in Ginkgo biloba. Frontiers in Plant Science, 16, 1557412. https://doi.org/10.3389/fpls.2025.1557412
- Liang, L. L., Arcus, V. L., Heskel, M. A., O'Sullivan, O. S., Weerasinghe, L. K., Creek, D., Egerton, J. J. G., Tjoelker, M. G., Atkin, O. K., & Schipper, L. A. (2018). Macromolecular rate theory provides a thermodynamics rationale to underpin the

convergent temperature response in plant leaf respiration. Global Change Biology, 24(4), 1538–1547. https://doi.org/10.1111/gcb.13936

- Liao, Z., Zhou, B., Zhu, J., Jia, H., & Fei, X. (2023). A critical review of methods, principles and progress for estimating the gross primary productivity of terrestrial ecosystems. Frontiers in Environmental Science, 11, 1093095. https://doi.org/10.3389/fenvs.2023.1093095
- Lin, M., & Oliver, D. J. (2008). The role of acetyl-coenzyme A synthetase in Arabidopsis. Plant Physiology, 147(4), 1822–1829. https://doi.org/10.1104/pp.108.121269
- Lu, X., Ju, W., Li, J., Croft, H., Chen, J. M., Luo, Y., Yu, H., & Hu, H. (2020). Maximum carboxylation rate estimation with chlorophyll content as a proxy of Rubisco content. Journal of Geophysical Research: Biogeosciences, 125(8), e2020JG005748. https://doi.org/10.1029/2020JG005748
- Macherel, D., Haraux, F., Guillou, H., & Bourgeois, O. (2021). The conundrum of hot mitochondria. Biochimica et Biophysica Acta: Bioenergetics, 1862(2), 148348. https://doi.org/10.1016/j.bbabio.2020.148348
- Machino, S., Nagano, S., & Hikosaka, K. (2021). The latitudinal and altitudinal variations in the biochemical mechanisms of temperature dependence of photosynthesis within Fallopia japonica. Environmental and Experimental Botany, 181, 104248. https://doi.org/10.1016/j.envexpbot.2020.104248
- Maldonado, M., Fan, Z., Abe, K. M., & Letts, J. A. (2023). Plant-specific features of respiratory supercomplex I + III_2 from Vigna radiata. Nature Plants, 9(1), 157–168. https://doi.org/10.1038/s41477-022-01306-8
- Malnoë, A. (2018). Photoinhibition or photoprotection of photosynthesis? Update on the sustained quenching component qH. Environmental and Experimental Botany, 154, 123–133. https://doi.org/10.1016/j.envexpbot.2018.05.005
- Malone, L. A., Proctor, M. S., Hitchcock, A., Hunter, C. N., & Johnson, M. P. (2021). Cytochrome b_6f. Orchestrator of photosynthetic electron transfer. Biochimica et

Biophysica Acta: Bioenergetics, 1862(5), 148380. https://doi.org/10.1016/j.bbabio.2021.148380

- Mathieu, A., Tinel, C., Dailly, H., Quinet, M., & Lutts, S. (2018). Impact of high temperature on sucrose translocation, sugar content and yield in Cichorium intybus L. var. sativum. Plant and Soil, 432(1), 273–288. https://doi.org/10.1007/s11104-018
- Maxwell, K., & Johnson, G. N. (2000). Chlorophyll fluorescence. A practical guide. Journal of Experimental Botany, 51(345), 659–668.
- McClain, A. M., Cruz, J. A., Kramer, D. M., & Sharkey, T. D. (2023). The time course of acclimation to the stress of triose phosphate use limitation. Plant, Cell and Environment, 46(1), 64–75. https://doi.org/10.1111/pce.14476
- McDonald, A. E. (2023). Unique opportunities for future research on the alternative oxidase of plants. Plant Physiology, 191(4), 2084–2092. https://doi.org/10.1093/plphys/kiac555
- McLeod, M. J., Barwell, S. A. E., Holyoak, T., & Thorne, R. E. (2025). A structural perspective on the temperature-dependent activity of enzymes. Structure, 33, 924–934.
- Medlyn, B. E., Loustau, D., & Delzon, S. (2002). Temperature response of parameters of a biochemically based model of photosynthesis. I. Seasonal changes in mature maritime pine (Pinus pinaster Ait.). Plant, Cell and Environment, 25, 1155–1165. https://doi.org/10.1046/j.0016-8025.2002.00890.x
- Milrad, Y., Wegemann, D., Kuhlgert, S., Scholz, M., Younas, M., Vidal-Meireles, A., & Hippler, M. (2025). Insights into plastocyanin–cytochrome b_6f complex formation. The role of plastocyanin phosphorylation. Plant Physiology, 198(4). https://doi.org/10.1093/plphys/kiaf269
- Momayyezi, M., McKown, A. D., Bell, S. C. S., & Guy, R. D. (2020). Emerging roles for carbonic anhydrase in mesophyll conductance and photosynthesis. Plant Journal, 101(4), 831–844. https://doi.org/10.1111/tpj.14638

- Mondal, J., & Bruce, B. D. (2018). Ferredoxin. The central hub connecting photosystem I to cellular metabolism. Photosynthetica, 56(1), 279–293. https://doi.org/10.1007/s11099-018-0793-9
- Moreno, A., Quereda-Moraleda, I., Lozano-Vallhonrat, C., Buñuel-Escudero, M., Botha, S., Kupitz, C., Lisova, S., Sierra, R., Mariani, V., Schleissner, P., Gee, L. B., Dörner, K., Schmidt, C., Han, H., Kloos, M., Smyth, P., Valerio, J., Schulz, J., de Wijn, R., … Medina, M. (2024). New insights into the function and molecular mechanisms of ferredoxin-$NADP^+$ reductase from Brucella ovis. Archives of Biochemistry and Biophysics, 762, 110204. https://doi.org/10.1016/j.abb.2024.110204
- Moreno-Echeverry, D. L., Kirschbaum, M. U. F., Barbour, M. M., & Liáng, L. L. (2026). Estimating the photorespiratory CO_2 compensation point and CO_2 release in the light using the Laisk method combined with photosynthetic theory. Plant, Cell and Environment. https://doi.org/10.1111/pce.70195
- Moore, C. E., Meacham-Hensold, K., Lemonnier, P., Slattery, R. A., Benjamin, C., Bernacchi, C. J., Lawson, T., & Cavanagh, A. P. (2021). The effect of increasing temperature on crop photosynthesis. From enzymes to ecosystems. Journal of Experimental Botany, 72(8), 2822–2844. https://doi.org/10.1093/jxb/erab090
- Mueller-Cajar, O. (2017). The diverse AAA^+ machines that repair inhibited Rubisco active sites. Frontiers in Molecular Biosciences, 4, 31. https://doi.org/10.3389/fmolb.2017.00031
- Nawaz, M. A., Kasote, D. M., Ullah, N., Usman, K., & Alsafran, M. (2024). RuBisCO. A sustainable protein ingredient for plant-based foods. Frontiers in Sustainable Food Systems, 8, 1389309. https://doi.org/10.3389/fsufs.2024.1389309
- Needham, J. F., Dey, S., Koven, C. D., Fisher, R. A., Knox, R. G., Lamour, J., Lemieux, G., Longo, M., Rogers, A., & Holm, J. (2025). Vertical canopy gradients of respiration drive plant carbon budgets and leaf area index. New Phytologist, 246(1), 144–157. https://doi.org/10.1111/nph.20423

- Nicholls, D. G. (2021). Mitochondrial proton leaks and uncoupling proteins. Biochimica et Biophysica Acta: Bioenergetics, 1862(7), 148428. https://doi.org/10.1016/j.bbabio.2021.148428
- Niu, Z., Ye, Z. W. Y., Huang, Q., Peng, C., & Kang, H. (2025). Accuracy of photorespiration and mitochondrial respiration in the light fitted by CO_2 response model for photosynthesis. Frontiers in Plant Science, 16, 1455533. https://doi.org/10.3389/fpls.2025.1455533
- Noctor, G., & Foyer, C. H. (2000). Homeostasis of adenylate status during photosynthesis in a fluctuating environment. Journal of Experimental Botany, 51, 347–356.
- Numa, K. B., Robinson, J. M., Arcus, V. L., & Schipper, L. A. (2021). Separating the temperature response of soil respiration derived from soil organic matter and added labile carbon compounds. Geoderma, 400, 115128. https://doi.org/10.1016/j.geoderma.2021.115128
- Nunes-Nesi, A., Araújo, W. L., Obata, T., & Fernie, A. R. (2013). Regulation of the mitochondrial tricarboxylic acid cycle. Current Opinion in Plant Biology, 16(3), 335–343. https://doi.org/10.1016/j.pbi.2013.01.004
- Obata, T., & Fernie, A. R. (2012). The use of metabolomics to dissect plant responses to abiotic stresses. Cellular and Molecular Life Sciences, 69(19), 3225–3243. https://doi.org/10.1007/s00018-012-1091-5
- Oh, Z. G., Askey, B., & Gunn, L. H. (2023). Red Rubiscos and opportunities for engineering green plants. Journal of Experimental Botany, 74(2), 520–542. https://doi.org/10.1093/jxb/erac349
- O'Leary, B. M. (2021). Playing with Pyr. Alternate sources of mitochondrial pyruvate fuel plant respiration. Plant Cell, 33(8), 2519–2520. https://doi.org/10.1093/plcell/koab147
- Scafaro AP, Posch BC, Evans JR, Farquhar GD, Atkin OK. 2023. Rubisco deactivation and chloroplast electron transport rates co-limit photosynthesis above

optimal leaf temperature in terrestrial plants. Nature Communications 14: 3050. https://doi.org/10.1038/s41467-023-38496-4

- Scafaro AP, Fan Y, Posch BC, Garcia A, Coast O, Atkin OK. 2021. Responses of leaf respiration to heatwaves. Plant, Cell & Environment 44: 2090–2101. https://doi.org/10.1111/pce.14018
- Scheibe R. 2004. Malate valves to balance cellular energy supply. Physiologia Plantarum 120: 21–26. https://doi.org/10.1111/j.0031-9317.2004.0222.x
- Schertl P, Braun HP. 2014. Respiratory electron transfer pathways in plant mitochondria. Frontiers in Plant Science 5: 163. https://doi.org/10.3389/fpls.2014.00163
- Schipper LA, Petrie OJ, O'Neill TA, Mudge PL, Liáng LL, Robinson JM, Arcus VL. 2019. Shifts in temperature response of soil respiration between adjacent irrigated and non-irrigated grazed pastures. Agriculture, Ecosystems & Environment 285: 106620. https://doi.org/10.1016/j.agee.2019.106620
- Schmiege SC, Sharkey TD, Walker B, Hammer J, Way DA. 2023. Laisk measurements in the nonsteady state: tests in plants exposed to warming and variable CO_2 concentrations. Plant Physiology 193: 1045–1057. https://doi.org/10.1093/plphys/kiad305
- Scott DW. 2011. Box–Muller transformation. Wiley Interdisciplinary Reviews: Computational Statistics 3: 177–179. https://doi.org/10.1002/wics.151
- Sekiguchi T, Yoshida K, Wakabayashi K-i, Hisabori T. 2024. Proton gradient across the chloroplast thylakoid membrane governs the redox regulatory function of ATP synthase. Journal of Biological Chemistry 300: 107659. https://doi.org/10.1016/j.jbc.2024.107659
- Selinski J, Hartmann A, Deckers-Hebestreit G, Day DA, Whelan J, Scheibe R. 2018. Alternative oxidase isoforms are differentially activated by tricarboxylic acid cycle intermediates. Plant Physiology 176: 1423–1432. https://doi.org/10.1104/pp.17.01331

- Selinski J, Scheibe R. 2019. Malate valves: old shuttles with new perspectives. Plant Biology 21: 21–30. https://doi.org/10.1111/plb.12869
- Shameer S, Ratcliffe RG, Sweetlove LJ. 2019a. Leaf energy balance requires mitochondrial respiration and export of chloroplast NADPH in the light. Plant Physiology 180: 1947–1961. https://doi.org/10.1104/pp.19.00624
- Sharkey TD. 2016. What gas exchange data can tell us about photosynthesis. Plant, Cell & Environment 39: 1161–1163. https://doi.org/10.1111/pce.12641
- Sharkey TD, Bernacchi CJ, Farquhar GD, Singsaas EL. 2007. Fitting photosynthetic carbon dioxide response curves for C_3 leaves. Plant, Cell & Environment 30: 1035–1040. https://doi.org/10.1111/j.1365-3040.2007.01710.x
- Sharkey TD, Xu Y. 2025. Carbon dioxide release during photosynthesis: connecting gas exchange behaviour with biochemistry. Plant, Cell & Environment. Early view. https://doi.org/10.1111/pce.70216
- Shrestha A, Song X, Barbour MM. 2019. The temperature response of mesophyll conductance, and its component conductances, varies between species and genotypes. Photosynthesis Research 141: 65–82. https://doi.org/10.1007/s11120-019-00649-y
- Si L, Zhang S, Su X, Li M. 2024. Structural basis for the distinct core-antenna assembly of cryptophyte photosystem II. Nature Communications 15: 51206. https://doi.org/10.1038/s41467-024-51206-y
- Slot M, Rifai SW, Winter K. 2021. Photosynthetic plasticity of a tropical tree species, Tabebuia rosea, in response to elevated temperature and CO_2. Plant, Cell & Environment 44: 2347–2364. https://doi.org/10.1111/pce.14049
- Slot M, Winter K. 2017. In situ temperature relationships of biochemical and stomatal controls of photosynthesis in four lowland tropical tree species. Plant, Cell & Environment 40: 3055–3068. https://doi.org/10.1111/pce.13071

- Sluse FE, Jarmuszkiewicz W. 1998. Mitochondrial alternative oxidase. Brazilian Journal of Medical and Biological Research 31: 733–747. https://doi.org/10.1590/S0100-879X1998000600003
- Smith NG, Dukes JS. 2013. Plant respiration and photosynthesis in global-scale models: incorporating acclimation to temperature and CO_2. Global Change Biology 19: 45–63. https://doi.org/10.1111/j.1365-2486.2012.02797.x
- Smith K, Keenan T. 2020. Mechanisms underlying leaf photosynthetic acclimation to warming and elevated CO_2 as inferred from least-cost optimality theory. Global Change Biology 26: 5202–5216. https://doi.org/10.1111/gcb.15152
- Smith NG, Li G, Dukes JS. 2019. Short-term thermal acclimation of dark respiration is greater in non-photosynthetic than in photosynthetic tissues. AoB PLANTS 11: plz064. https://doi.org/10.1093/aobpla/plz064
- Sonawane BV, Cousins AB. 2019. Uncertainties and limitations of using carbon-13 and oxygen-18 leaf isotope exchange to estimate the temperature response of mesophyll CO_2 conductance in C_3 plants. New Phytologist 222: 122–131. https://doi.org/10.1111/nph.15585
- Song Q, Zhu XG. 2024. Techniques for photosynthesis phenomics: gas exchange, fluorescence and reflectance spectrums. Crop & Environment 3: 147–158. https://doi.org/10.1016/j.crope.2024.05.002
- Stirbet A, Lazár D, Guo Y, Govindjee G. 2020. Photosynthesis: basics, history and modelling. Annals of Botany 126: 511–537. https://doi.org/10.1093/aob/mcz171
- Stitt M, Zeeman SC. 2012. Starch turnover: pathways, regulation and role in growth. Current Opinion in Plant Biology 15: 282–292. https://doi.org/10.1016/j.pbi.2012.03.016
- Strand DD, Fisher N, Kramer DM. 2017. The higher plant plastid NAD(P)H dehydrogenase-like complex NDH is a high-efficiency proton pump that

increases ATP production by cyclic electron flow. Journal of Biological Chemistry 292: 11850–11860. https://doi.org/10.1074/jbc.M116.770792

- Suganami M, Suzuki Y, Tazoe Y, Yamori W, Makino A. 2021. Co-overproducing Rubisco and Rubisco activase enhances photosynthesis in the optimal temperature range in rice. Plant Physiology 185: 108–119. https://doi.org/10.1093/plphys/kiaa026
- Sun J, Guan D, Wu J, Jing Y, Yuan F, Wang A, Jin C. 2015. Day and night respiration of three tree species in a temperate forest of northeastern China. iForest 8: 25–32. https://doi.org/10.3832/ifor1213-007
- Sun YR, Ma WT, Xu YN, Wang X, Li L, Tcherkez G, Gong XY. 2023. Short- and long-term responses of leaf day respiration to elevated atmospheric CO_2. Plant Physiology 191: 2204–2217. https://doi.org/10.1093/plphys/kiac582
- Sweetlove LJ, Beard KFM, Nunes-Nesi A, Fernie AR, Ratcliffe RG. 2010. Not just a circle: flux modes in the plant TCA cycle. Trends in Plant Science 15: 462–470. https://doi.org/10.1016/j.tplants.2010.05.006
- Sweetlove LJ, Lytovchenko A, Morgan M, Nunes-Nesi A, Taylor NL, Baxter CJ, Eickmeier I, Fernie AR. 2006. Mitochondrial uncoupling protein is required for efficient photosynthesis. Proceedings of the National Academy of Sciences USA 103: 19587–19592. https://doi.org/10.1073/pnas.0607750103
- Takizawa K, Cruz JA, Kanazawa A, Kramer DM. 2007. The thylakoid proton motive force in vivo: quantitative, non-invasive probes, energetics and regulatory consequences of light-induced pmf. Biochimica et Biophysica Acta – Bioenergetics 1767: 1233–1244. https://doi.org/10.1016/j.bbabio.2007.07.006
- Tania SS, Utsugi S, Tsuchiya Y, Sasano S, Katsuhara M, Mori IC. 2025. Amino acid substitutions in Loop C of Arabidopsis PIP2 aquaporins alter the permeability of CO_2. Plant, Cell & Environment 48: 6835–6846. https://doi.org/10.1111/pce.15635
- Tasnim B, Borowski M, Villalta J, Bush K. 2021. Mitochondrial F_1F_0 ATP synthase determines the local proton motive force at cristae rims. EMBO Reports 22: e52727. https://doi.org/10.15252/embr.202152727

- Tcherkez G, Abadie C, Dourmap C, Lalande J, Limami AM. 2024. Leaf day respiration: more than just catabolic CO_2 production in the light. Plant, Cell & Environment 47: 2631–2639. https://doi.org/10.1111/pce.14904
- Tcherkez G, Atkin OK. 2021. Unravelling mechanisms and impacts of day respiration in plant leaves: an introduction to a Virtual Issue. New Phytologist 230: 5–10. https://doi.org/10.1111/nph.17164
- Tcherkez G, Cornic G, Bligny R, Gout E, Ghashghaie J. 2005. In vivo respiratory metabolism of illuminated leaves. Plant Physiology 138: 1596–1606. https://doi.org/10.1104/pp.105.062141
- Tcherkez G, Gauthier P, Buckley TN, Busch FA, Barbour MM, Bruhn D, Heskel MA, Gong XY, Crous KY, Griffin K, Way D, Turnbull M, Adams MA, Atkin OK, Farquhar GD, Cornic G. 2017. Leaf day respiration: low CO_2 flux but high significance for metabolism and carbon balance. New Phytologist 216: 986–1001. https://doi.org/10.1111/nph.14816
- Tholen D, Ethier G, Genty B, Pepin S, Zhu XG. 2012. Variable mesophyll conductance revisited: theoretical background and experimental implications. Plant, Cell & Environment 35: 2087–2103. https://doi.org/10.1111/j.1365-3040.2012.02538.x
- Tholen D, Zhu XG. 2011. The mechanistic basis of internal conductance: a theoretical analysis of mesophyll cell photosynthesis and CO_2 diffusion. Plant Physiology 156: 90–105. https://doi.org/10.1104/pp.111.172346
- Tikhonov AN, Vershubskii AV. 2020. Temperature-dependent regulation of electron transport and ATP synthesis in chloroplasts in vitro and in silico. Photosynthesis Research 146: 299–329. https://doi.org/10.1007/s11120-020-00777-0
- Tikkanen M, Aro EM. 2012. Thylakoid protein phosphorylation in dynamic regulation of photosystem II in higher plants. Biochimica et Biophysica Acta – Bioenergetics 1817: 232–238. https://doi.org/10.1016/j.bbabio.2011.05.005

- Timm S, Sun H, Huang W. 2024. Photorespiration: emerging insights into photoprotection mechanisms. Trends in Plant Science 29: 1052–1055. https://doi.org/10.1016/j.tplants.2024.07.001
- Tjoelker MG, Oleksyn J, Reich PB. 2001. Modelling respiration of vegetation: evidence for a general temperature-dependent Q10. Global Change Biology 7: 223–230. https://doi.org/10.1046/j.1365-2486.2001.00397.x
- Trinh MDL, Masuda S. 2022. Chloroplast pH homeostasis for the regulation of photosynthesis. Frontiers in Plant Science 13: 919896. https://doi.org/10.3389/fpls.2022.919896
- Ubierna N, Cernusak LA, Holloway-Phillips M, Busch FA, Cousins AB, Farquhar GD. 2019. Critical review: incorporating the arrangement of mitochondria and chloroplasts into models of photosynthesis and carbon isotope discrimination. Photosynthesis Research 141: 5–31. https://doi.org/10.1007/s11120-019-00642-5
- O'Leary, B. M., Asao, S., Millar, A. H., & Atkin, O. K. (2019). Core principles which explain variation in respiration across biological scales. New Phytologist, 222(2), 670–686. https://doi.org/10.1111/nph.15576
- O'Leary, B. M., Scafaro, A. P., & York, L. M. (2023). High-throughput, dynamic, multi-dimensional. An expanding repertoire of plant respiration measurements. Plant Physiology, 191(4), 2070–2083. https://doi.org/10.1093/plphys/kiac580
- Oliver, J.; Kim, T. D.; Trinugroho, J. P.; Cordón-Preciado, V.; Wijayatilake, N.; Bhatia, A.; Rutherford, A. W.; & Cardona, T. (2025). The evolution and evolvability of Photosystem II. Annual Review of Plant Biology, https://doi.org/10.1146/annurev-arplant-070522-
- Oliver, H.; Mercado, L. M.; Clark, D. B.; Huntingford, C.; Taylor, C. M.; Vidale, P. L.; McGuire, P. C.; Todt, M.; Folwell, S.; Shamsudheen Semeena, V.; & Medlyn, B. E. (2022). Improved representation of plant physiology in the JULES-vn5.6 land surface model. Photosynthesis, stomatal conductance and thermal acclimation. Geoscientific Model Development, 15(14), 5567–5592. https://doi.org/10.5194/gmd-15-5567-2022

- Onoda, Y., Hikosaka, K., & Hirose, T. (2005). Seasonal change in the balance between capacities of RuBP carboxylation and RuBP regeneration affects CO_2 response of photosynthesis in Polygonum cuspidatum. Journal of Experimental Botany, 56, 755–763.
- O'Sullivan, O. S., Heskel, M. A., Reich, P. B., Tjoelker, M. G., Weerasinghe, L. K., Penillard, A., Zhu, L., Egerton, J. J. G., Bloomfield, K. J., Creek, D., Bahar, N. H. A., Griffin, K. L., Hurry, V., Meir, P., Turnbull, M. H., & Atkin, O. K. (2017). Thermal limits of leaf metabolism across biomes. Global Change Biology, 23(1), 209–223. https://doi.org/10.1111/gcb.13477
- Parys, E., & Romanowska, E. (2000). Relationship between postillumination burst of CO_2 and enhancement of respiration in tall fescue leaves. Acta Physiologiae Plantarum, 22(2),
- Paul, M. J., & Foyer, C. H. (2001). Sink regulation of photosynthesis. Journal of Experimental Botany, 52(360), 1383–1400. https://doi.org/10.1093/jexbot/52.360.1383
- Pastorello, G., Trotta, C., Canfora, E., Chu, H., Christianson, D., Cheah, Y. W., Poindexter, C., Chen, J., Elbashandy, A., Humphrey, M., Isaac, P., Polidori, D., Ribeca, A., van Ingen, C., Zhang, L., Amiro, B., Ammann, C., Arain, M. A., Ardö, J., … Papale, D. (2020). The FLUXNET2015 dataset and the ONEFlux processing pipeline for eddy covariance data. Scientific Data, 7, 225. https://doi.org/10.1038/s41597-020-0534-3
- Peisker, M., & Apel, H. (2001). Inhibition by light of CO_2 evolution from dark respiration. Comparison of two gas exchange methods. Photosynthesis Research, 70, 291–298. https://doi.org/10.1023/A:1014827017936
- Perdomo, J. A., Capó-Bauçà, S., Carmo-Silva, E., & Galmés, J. (2017). Rubisco and Rubisco activase play an important role in the biochemical limitations of photosynthesis in rice, wheat, and maize under high temperature and water deficit. Frontiers in Plant Science, 8, 490. https://doi.org/10.3389/fpls.2017.00490

- Peterson, R. B. (1983). Estimation of photorespiration based on the initial rate of postillumination CO_2 release. II. Effects of O_2, CO_2 and temperature. Plant Physiology, 73.
- Pinelli, P., & Loreto, F. (2003). $^{12}CO_2$ emission from different metabolic pathways measured in illuminated and darkened C_3 and C_4 leaves at low, atmospheric and elevated CO_2 concentration. Journal of Experimental Botany, 54(388), 1761–1769. https://doi.org/10.1093/jxb/erg187
- Pons, T. L., Flexas, J., von Caemmerer, S., Evans, J. R., Genty, B., Ribas-Carbó, M., & Brugnoli, E. (2009). Estimating mesophyll conductance to CO_2. Methodology, potential errors, and recommendations. Journal of Experimental Botany, 60(8), 2217–2234. https://doi.org/10.1093/jxb/erp081
- Portis, A. R., Li, C., Wang, D., & Salvucci, M. E. (2008). Regulation of Rubisco activase and its interaction with Rubisco. Journal of Experimental Botany, 59(7), 1597–1604. https://doi.org/10.1093/jxb/erm240
- Prywes, N., Phillips, N. R., Tuck, O. T., Valentin-Alvarado, L. E., & Savage, D. F. (2023). Rubisco function, evolution, and engineering. Annual Review of Biochemistry, 92, 385–410. https://doi.org/10.1146/annurev-biochem-040320
- Qu, Y., Sakoda, K., Fukayama, H., Kondo, E., Suzuki, Y., Makino, A., Terashima, I., & Yamori, W. (2021). Overexpression of both Rubisco and Rubisco activase rescues rice photosynthesis and biomass under heat stress. Plant, Cell and Environment, 44(7), 2308–2320. https://doi.org/10.1111/pce.14051
- Quetin, G. R., Anderegg, L. D. L., Boving, I., & Trugman, A. T. (2024). A moving target. Trade-offs between maximising carbon and minimising hydraulic stress for plants in a changing climate. New Phytologist, 244(5), 1788–1800. https://doi.org/10.1111/nph.20127
- Raghavendra, A. S., & Padmasree, K. (2003). Beneficial interactions of mitochondrial metabolism with photosynthetic carbon assimilation. Trends in Plant Science, 8(11), 546–553. https://doi.org/10.1016/j.tplants.2003.09.015

- Raines, C. A. (2022). Improving plant productivity by re-tuning the regeneration of RuBP in the Calvin–Benson–Bassham cycle. New Phytologist, 236(2), 350–356. https://doi.org/10.1111/nph.18394
- Ranathunga, K. N., Evans, J., Toth, N., Brown, S., Van Eerd, L. L., & Wagner-Riddle, C. (2025). Net ecosystem carbon budget and net greenhouse gas emissions under diverse crop rotation using cover crops compared to a conventional crop rotation. Agriculture, Ecosystems & Environment, 381, 108786.
- Rawsthorne, S., & Hylton, C. M. (1991). The relationship between the post-illumination CO_2 burst and glycine metabolism in leaves of C_3 and C_3–C_4 intermediate species of Moricandia. Planta, 186, 122–126. https://doi.org/10.1007/BF00201507
- Reddy, M. M., Vani, T., & Raghavendra, A. S. (1991). Light-enhanced dark respiration in mesophyll protoplasts from leaves of pea. Plant Physiology, 96(4), 1368–1371. https://academic.oup.com/plphys/article/96/4/1368/6086787
- Ren, Y., Wang, H., Harrison, S. P., Prentice, I. C., Atkin, O. K., Smith, N. G., Mengoli, G., Stefanski, A., & Reich, P. B. (2024). Reduced global plant respiration due to the acclimation of leaf dark respiration coupled with photosynthesis. New Phytologist, 241(2), 578–591. https://doi.org/10.1111/nph.19355
- Rogers, A., Kumarathunge, D. P., Lombardozzi, D. L., Medlyn, B. E., Serbin, S. P., & Walker, A. P. (2021). Triose phosphate utilisation limitation. An unnecessary complexity in terrestrial biosphere model representation of photosynthesis. New Phytologist, 230(1), 17–22. https://doi.org/10.1111/nph.17092
- Rokka, A., Zhang, L., & Aro, E. M. (2001). Rubisco activase. An enzyme with a temperature-dependent dual function? Plant Jornal, 25(4), 463–471. https://doi.org/10.1046/j.1365-313X.2001.00981.x
- Rosa-Téllez, S., Alcántara-Enguídanos, A., Martínez-Seidel, F., Casatejada-Anchel, R., Saeheng, S., Bailes, C. L., Erban, A., Barbosa-Medeiros, D., Alepúz, P., Matus, J. T., Kopka, J., Muñoz-Bertomeu, J., Krueger, S., Roje, S., Fernie, A. R., & Ros, R. (2024). The serine–glycine–one-carbon metabolic network orchestrates

changes in nitrogen and sulphur metabolism and shapes plant development. Plant Cell, 36(2), 404–426. https://doi.org/10.1093/plcell/koad256

- Rott, M., Martins, N. F., Thiele, W., Lein, W., Bock, R., Kramer, D. M., & Schöttler, M. A. (2011). ATP synthase repression in tobacco restricts photosynthetic electron transport, CO_2 assimilation, and plant growth by over-acidification of the thylakoid lumen. Plant Cell, 23(1), 304–321. https://doi.org/10.1105/tpc.110.079111
- Ruban, A. V. (2016). Non-photochemical chlorophyll fluorescence quenching. Mechanism and effectiveness in protecting plants from photodamage. Plant Physiology, 170(4), 1903–1916. https://doi.org/10.1104/pp.15.01935
- Rühle, T., Leister, D., & Pasch, V. (2024). Chloroplast ATP synthase. From structure to engineering. Plant Cell, 36(10), 3974–3996. https://doi.org/10.1093/plcell/koae081
- Saidi, Y., Peter, M., Fink, A., Cicekli, C., Vigh, L., & Goloubinoff, P. (2010). Membrane lipid composition affects plant heat sensing and modulates Ca^{2+}-dependent heat shock response. Plant Signaling & Behavior, 5(12), 1530–1533. https://doi.org/10.4161/psb.5.12.13163
- Sage, R. F., & Kubien, D. S. (2007). The temperature response of C_3 and C_4 photosynthesis. Plant, Cell & Environment, 30(9), 1086–1106. https://doi.org/10.1111/j.1365-3040.2007.01682.x
- Sage, R. F., Way, D. A., & Kubien, D. S. (2008). Rubisco, Rubisco activase, and global climate change. Journal of Experimental Botany, 59(7), 1581–1595. https://doi.org/10.1093/jxb/ern053
- Saito, K., Rutherford, A. W., & Ishikita, H. (2013). Mechanism of proton-coupled quinone reduction in Photosystem II. Proceedings of the National Academy of Sciences, 110(3), 954–959. https://doi.org/10.1073/pnas.1212957110
- Sakata, T., Matsuyama, S., Kawai, K., Yasumoto, K., Sekikawa, S., & Ishida, A. (2024). Interspecific variation in Rubisco CO_2/O_2 specificity along the leaf economic spectrum across 23 woody angiosperm plants in the Pacific islands. New Phytologist, 243(3), 951–965. https://doi.org/10.1111/nph.19820

- Salvucci, M. E., & Crafts-Brandner, S. J. (2004). Relationship between the heat tolerance of photosynthesis and the thermal stability of Rubisco activase in plants from contrasting thermal environments. Plant Physiology, 134(4), 1460–1470. https://doi.org/10.1104/pp.103.038323
- Salvucci, M. E., DeRidder, B. P., & Portis, A. R. (2006). Effect of activase level and isoform on the thermotolerance of photosynthesis in Arabidopsis. Journal of Experimental Botany, 57(14), 3793–3799. https://doi.org/10.1093/jxb/erl140
- Sánchez-Baracaldo, P., & Cardona, T. (2020). On the origin of oxygenic photosynthesis and Cyanobacteria. New Phytologist, 225(4), 1440–1446. https://doi.org/10.1111/nph.16249
- Santarius, K., Heber, U., Ulrich, W., & Urbach, W. (1964). Intracellular translocation of ATP, ADP and inorganic phosphate in leaf cells of Elodea densa in relation to photosynthesis. Biochemical and Biophysical Research Communications, 9, 139–146.
- Scafaro, A. P., Atwell, B. J., Muylaert, S., Van Reusel, B., Ruiz, G. A., Van Rie, J., & Gallé, A. (2018). A thermotolerant variant of Rubisco activase from a wild relative improves growth and seed yield in rice under heat stress. Frontiers in Plant Science, 9, 1663. https://doi.org/10.3389/fpls.2018.01663
- Scafaro, A. P., Bautsoens, N., Den Boer, B., Van Rie, J., & Gallé, A. (2019). A conserved sequence from heat-adapted species improves Rubisco activase thermostability in wheat. Plant Physiology, 181(1), 43–54. https://doi.org/10.1104/pp.19.00425
- Scafaro, A. P., Gallé, A., Van Rie, J., Carmo-Silva, E., Salvucci, M. E., & Atwell, B. J. (2016). Heat tolerance in a wild Oryza species is attributed to maintenance of Rubisco activation by a thermally stable Rubisco activase ortholog. New Phytologist, 211(3), 899–911. https://doi.org/10.1111/nph.13963
- Ubierna N, Cernusak LA, Holloway-Phillips M, Busch FA, Cousins AB, Farquhar GD. 2019. Critical review: incorporating the arrangement of mitochondria and chloroplasts into models of photosynthesis and carbon isotope discrimination. Photosynthesis Research 141(1): 5–31. https://doi.org/10.1007/s11120-019-00635-8

- Ubierna N, Gandin A, Cousins AB. 2018. The response of mesophyll conductance to short-term variation in CO_2 in the C_4 plants Setaria viridis and Zea mays. Journal of Experimental Botany 69(5): 1159–1170. https://doi.org/10.1093/jxb/erx464
- Ubierna N, Holloway-Phillips M, Farquhar G. 2022. Commentary: scaling from fluxes to organic matter: interpreting ^{13}C isotope ratios of plant material using flux models. New Phytologist 236: 2003–2008. https://doi.org/10.5061/dryad.jm63xsjct
- Ulrich W, Neimanis S, Siebke K, Schönknecht G, Katona E. 1992. Chloroplast energization and oxidation of P700/plastocyanin in illuminated leaves at reduced levels of CO_2 or oxygen. Photosynthesis Research 34: 433–447.
- van Aken O. 2021. Mitochondrial redox systems as central hubs in plant metabolism and signalling. Plant Physiology 186(1): 36–52. https://doi.org/10.1093/plphys/kiab101
- Van Der Kamp MW, Prentice EJ, Kraakman KL, Connolly M, Mulholland AJ, Arcus VL. 2018. Dynamical origins of heat capacity changes in enzyme-catalysed reactions. Nature Communications 9(1): 1177. https://doi.org/10.1038/s41467-018-03597-y
- Vanlerberghe GC. 2013. Alternative oxidase: a mitochondrial respiratory pathway to maintain metabolic and signalling homeostasis during abiotic and biotic stress in plants. International Journal of Molecular Sciences 14(4): 6805–6847. https://doi.org/10.3390/ijms14046805
- Vanlerberghe GC, Dahal K, Alber NA, Chadee A. 2020. Photosynthesis, respiration and growth: a carbon and energy balancing act for alternative oxidase. Mitochondrion 52: 197–211. https://doi.org/10.1016/j.mito.2020.04.001
- van't Hoff JH. 1884. Études de dynamique chimique. Frederik Muller & Co.
- Vera-Vives AM, Novel P, Zheng K, Tan S-L, Schwarzländer M, Alboresi A, Morosinotto T. 2024. Mitochondrial respiration is essential for photosynthesis-

dependent ATP supply of the plant cytosol. New Phytologist 243(6): 2175–2186. https://doi.org/10.1111/nph.19989

- Viil J, Ivanova H, Pärnik T. 2012. Specificity factor of Rubisco: estimation in intact leaves by carboxylation at different CO_2/O_2 ratios. Photosynthetica 50(2): 247–253. https://doi.org/10.1007/s11099-012-0026-6
- Vines HM, Tu Z-P, Armitage AM, Chen S-S, Black CC. 1983. Environmental responses of the post-illumination CO_2 burst. Plant Physiology 73.
- Viveros R, Labra N, Anic V, Cavieres LA, Sáez PL, Fuentes F, Ramírez C. 2024. Mesophyll conductance limits photosynthesis and relates to anatomical traits in high-elevation plants in the Andes. Environmental and Experimental Botany 226: 105916. https://doi.org/10.1016/j.envexpbot.2024.105916
- von Caemmerer S, Quick W. 2000. Rubisco: physiology in vivo. In: Leegood RC, Sharkey TD, von Caemmerer S, eds. Photosynthesis: Physiology and Metabolism. pp. 85–113.
- Voon CP, Law YS, Guan X, Lim SL, Xu Z, Chu WT, Zhang R, Sun F, Labs M, Leister D, Pribil M, Hronková M, Kubásek J, Cui Y, Jiang L, Tsuyama M, Gardeström P, Tikkanen M, Lim BL. 2021. Modulating the activities of chloroplasts and mitochondria promotes adenosine triphosphate production and plant growth. Quantitative Plant Biology 2: e7. https://doi.org/10.1017/qpb.2021.7
- Vrábl D, Vašková M, Hronková M, Flexas J, Šantrůček J. 2009. Mesophyll conductance to CO_2 transport estimated by two independent methods: effect of variable CO_2 concentration and abscisic acid. Journal of Experimental Botany 60(8): 2315–2323. https://doi.org/10.1093/jxb/erp115
- Waheeda K, Kitchel H, Wang Q, Chiu PL. 2023. Molecular mechanism of Rubisco activase: dynamic assembly and Rubisco remodeling. Frontiers in Molecular Biosciences 10: 1125922. https://doi.org/10.3389/fmolb.2023.1125922
- Walker BJ, Cousins AB. 2013. Influence of temperature on measurements of the CO_2 compensation point: differences between the Laisk and O_2-exchange methods. Journal of Experimental Botany 64(7): 1893–1905. https://doi.org/10.1093/jxb/ert058

- Walker BJ, Ort DR. 2015. Improved method for measuring the apparent CO_2 photocompensation point resolves the impact of multiple internal conductances to CO_2 to net gas exchange. Plant, Cell & Environment 38(11): 2462–2474. https://doi.org/10.1111/pce.12562
- Walker BJ, Orr DJ, Carmo-Silva E, Parry MAJ, Bernacchi CJ, Ort DR. 2017. Uncertainty in measurements of the photorespiratory CO_2 compensation point and its impact on models of leaf photosynthesis. Photosynthesis Research 132: 245–255.
- Walker BJ, Strand DD, Kramer DM, Cousins AB. 2014. The response of cyclic electron flow around photosystem I to changes in photorespiration and nitrate assimilation. Plant Physiology 165(1): 453–462. https://doi.org/10.1104/pp.114.238238
- Walker BJ, Vanloocke A, Bernacchi CJ, Ort DR. 2016. The costs of photorespiration to food production now and in the future. Annual Review of Plant Biology 67: 107–129. https://doi.org/10.1146/annurev-arplant-043015-111709
- Walker EJ, Hamill CJ, Crean R, Connolly MS, Warrender AK, Kraakman KL, Prentice EJ, Steyn-Ross A, Steyn-Ross M, Pudney CR, van der Kamp MW, Schipper LA, Mulholland AJ, Arcus VL. 2024. Cooperative conformational transitions underpin the activation heat capacity in the temperature dependence of enzyme catalysis. ACS Catalysis 14(7): 4379–4394. https://doi.org/10.1021/acscatal.3c05584
- Wang Y. 2024. Improving photosynthetic efficiency in fluctuating light to enhance yield of C_3 and C_4 crops. Crop & Environment 3(4): 184–193. https://doi.org/10.1016/j.crope.2024.06.003
- Warren CR, Dreyer E. 2006. Temperature response of photosynthesis and internal conductance to CO_2: results from two independent approaches. Journal of Experimental Botany 57(12): 3057–3067. https://doi.org/10.1093/jxb/erl067
- Way DA, Aspinwall MJ, Drake JE, Crous KY, Campany CE, Ghannoum O, Tissue DT, Tjoelker MG. 2019. Responses of respiration in the light to warming in field-grown trees: a comparison of the thermal sensitivity of the Kok and Laisk methods. New Phytologist 222: 132–143.

- Wehr R, Munger JW, McManus JB, Nelson DD, Zahniser MS, Davidson EA, Wofsy SC, Saleska SR. 2016. Seasonality of temperate forest photosynthesis and daytime respiration. Nature 534(7609): 680–683. https://doi.org/10.1038/nature17966
- Weidner M, Fehling E. 1985. Heat modification of ribulose-1,5-bisphosphate carboxylase/oxygenase by temperature pretreatment of wheat (Triticum aestivum L.) seedlings. Planta 166(1): 117–127.
- Weston DJ, Bauerle WL, Swire-Clark GA, Moore BD, Baird WMV. 2007. Characterization of Rubisco activase from thermally contrasting genotypes of Acer rubrum (Aceraceae). American Journal of Botany 94(6): 926–934. https://doi.org/10.3732/ajb.94.6.926
- Wilson S, Ruban AV. 2020. Rethinking the influence of chloroplast movements on non-photochemical quenching and photoprotection. Plant Physiology 183(3): 1213–1223. https://doi.org/10.1104/pp.20.00549
- Xiao J, Zhou Y, Xie Y, Li T, Su X, He J, Jiang Y, Zhu H, Qu H. 2024. ATP homeostasis and signaling in plants. Plant Communications 5(4): 100834. https://doi.org/10.1016/j.xplc.2024.100834
- Xu Z, Jiang Y, Zhou G. 2015. Response and adaptation of photosynthesis, respiration, and antioxidant systems to elevated CO_2 with environmental stress in plants. Frontiers in Plant Science 6: 701. https://doi.org/10.3389/fpls.2015.00701
- Xu CY, Lin GH, Griffin KL, Sambrotto RN. 2004. Leaf respiratory CO_2 is ^{13}C-enriched relative to leaf organic components in five species of C_3 plants. New Phytologist 163(3): 499–505. https://doi.org/10.1111/j.1469-8137.2004.01153.x
- Xu M, Liáng LL, Kirschbaum MUF, Fang S, Yu Y. 2021. Short-term temperature response of leaf respiration in different subtropical urban tree species. Frontiers in Plant Science 11: 628995. https://doi.org/10.3389/fpls.2020.628995
- Xu Y, Schmiege SC, Sharkey TD. 2025. Time-resolved targeted metabolomics shows an abrupt switch from Calvin–Benson–Bassham cycle to

tricarboxylic acid cycle when the light is turned off. Photosynthesis Research 163(5). https://doi.org/10.1007/s11120-025-01173-2

- Yamaguchi DP, Nakaji T, Hiura T, Hikosaka K. 2016. Effects of seasonal change and experimental warming on the temperature dependence of photosynthesis in the canopy leaves of Quercus serrata. Tree Physiology 36(10): 1283–1295. https://doi.org/10.1093/treephys/tpw021
- Yamori W, Shikanai T. 2016. Physiological functions of cyclic electron transport around photosystem I in sustaining photosynthesis and plant growth. Annual Review of Plant Biology 67: 81–106. https://doi.org/10.1146/annurev-arplant-043015-112002
- Yamori W, Suzuki K, Noguchi K, Nakai M, Terashima I. 2006. Effects of Rubisco kinetics and Rubisco activation state on the temperature dependence of the photosynthetic rate in spinach leaves from contrasting growth temperatures. Plant, Cell & Environment 29(8): 1659–1670. https://doi.org/10.1111/j.1365-3040.2006.01550.x
- Yanhui C, Hongrui W, Beining Z, Shixing G, Zihan W, Yue W, Huihui Z, Guangyu S. 2020. Elevated air temperature damage to photosynthetic apparatus alleviated by enhanced cyclic electron flow around photosystem I in tobacco leaves. Ecotoxicology and Environmental Safety 204: 111136. https://doi.org/10.1016/j.ecoenv.2020.111136
- Yin X. 2021. No need to switch the modified Arrhenius function back to the old form. New Phytologist 231(6): 2113–2116. https://doi.org/10.1111/nph.17341
- Yin X, Amthor JS. 2024. Estimating leaf day respiration from conventional gas exchange measurements. New Phytologist 241(1): 52–58. https://doi.org/10.1111/nph.19330
- Yin X, Busch FA, Struik PC, Sharkey TD. 2021. Evolution of a biochemical model of steady-state photosynthesis. Plant, Cell & Environment 44(9): 2811–2837. https://doi.org/10.1111/pce.14070
- Yin X, Niu Y, van der Putten PEL, Struik PC. 2020. The Kok effect revisited. New Phytologist 227(6): 1764–1775. https://doi.org/10.1111/nph.16638

- Yin X, Struik PC. 2009. Theoretical reconsiderations when estimating the mesophyll conductance to CO_2 diffusion in leaves of C_3 plants by analysis of combined gas exchange and chlorophyll fluorescence measurements. Plant, Cell & Environment 32(11): 1513–1524. https://doi.org/10.1111/j.1365-3040.2009.02016.x
- Yin X, Sun Z, Struik PC, Gu J. 2011. Evaluating a new method to estimate the rate of leaf respiration in the light by analysis of combined gas exchange and chlorophyll fluorescence measurements. Journal of Experimental Botany 62(10): 3489–3499. https://doi.org/10.1093/jxb/err038
- Yokochi Y, Yoshida K, Hahn F, Miyagi A, Wakabayashi K, Kawai-Yamada M, Weber AP, Hisabori T. 2021. Redox regulation of NADP-malate dehydrogenase is vital for land plants under fluctuating light environment. Proceedings of the National Academy of Sciences USA 118(6): e2016903118. https://doi.org/10.1073/pnas.2016903118
- Zhang S. 2010. Temperature acclimation of photosynthesis in Meconopsis horridula var. racemosa Prain. Botanical Studies 51: 457–464.
- Zhang Y, Fernie AR. 2023. The role of TCA cycle enzymes in plants. Advanced Biology 7(8): 2200238. https://doi.org/10.1002/adbi.202200238
- Zhang T, Peng JT, Klair A, Dickinson AJ. 2023. Non-canonical and developmental roles of the TCA cycle in plants. Current Opinion in Plant Biology 74: 102382. https://doi.org/10.1016/j.pbi.2023.102382
- Zhang Z, Zhu G, Peng X. 2024. Photorespiration in plant adaptation to environmental changes. Crop & Environment 3(4): 203–212. https://doi.org/10.1016/j.crope.2024.07.001
- Zheng DM, Wang X, Liu Q, Sun YR, Ma WT, Li L, Yang Z, Tcherkez G, Adams MA, Yang Y, Gong XY. 2024. Temperature responses of leaf respiration in light and darkness are similar and modulated by leaf development. New Phytologist 241(4): 1435–1446. https://doi.org/10.1111/nph.19428

- Zheng K, Martinez M del P, Bouzid M, Balparda M, Schwarzländer M, Maurino VG. 2025. Regulation of plant glycolysis and the tricarboxylic acid cycle by posttranslational modifications. Plant Journal 122(1). https://doi.org/10.1111/tpj.70142
- Zhou Z, Zhang Z, van der Putten PEL, Fabre D, Dingkuhn M, Struik PC, Yin X. 2023. Triose phosphate utilization in leaves is modulated by whole-plant sink–source ratios and nitrogen budgets in rice. Journal of Experimental Botany 74(21): 6692–6707. https://doi.org/10.1093/jxb/erad329
- Zhu L, Bloomfield KJ, Asao S, Tjoelker MG, Egerton JJG, Hayes L, Weerasinghe LK, Creek D, Griffin KL, Hurry V, Liddell M, Meir P, Turnbull MH, Atkin O. 2021. Acclimation of leaf respiration temperature responses across thermally contrasting biomes. New Phytologist 229(3): 1312–1325. https://doi.org/10.1111/nph.16929

Appendix A

The co-authorship form related to the article included in this thesis is provided on the following page.